

Silica Surface Features and Their Role in the Adsorption of Biomolecules: Computational Modeling and Experiments

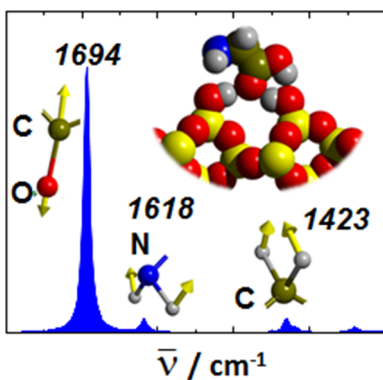
Albert Rimola,[†] Dominique Costa,[‡] Mariona Sodupe,[†] Jean-François Lambert,[§] and Piero Ugliengo^{*,†,‡}

[†]Departament de Química, Universitat Autònoma de Barcelona, 08193 Bellaterra (Cerdanyola del Vallès), Spain

[‡]Laboratoire de Physico-Chimie des Surfaces, UMR CNRS-ENSCP 7045, Ecole Nationale Supérieure de Chimie de Paris, Chimie-ParisTech, 11, Rue Pierre et Marie Curie, 75005 Paris, France

[§]Laboratoire de Réactivité de Surface, UMR CNRS 7197, Université Pierre et Marie Curie—Paris 6, Case 178, 3 Rue Galilée, 94200 Ivry-sur-Seine, France

[†]Dipartimento di Chimica, and NIS – Nanostructured Interfaces and Surfaces – Centre of Excellence, Università di Torino, Via P. Giuria 7, 10125 Torino, Italy



CONTENTS

- 1. Introduction
- 2. Structure and Polymorphism
 - 2.1. Synthesis of Silica Samples
 - 2.2. Silica Surfaces: Nomenclature of Surface Groups
- 3. Experimental Data
 - 3.1. Features of a Bare Silica Surface
 - 3.1.1. Bulk Data: Thermogravimetry (TG) and silanol surface Densities
 - 3.1.2. Bulk Data: Acid–Base Titration. How Many Negatively Charged Silanolate Groups Can There Be at the Interface?
 - 3.1.3. Vibrational Spectroscopies: IR and Raman
 - 3.1.4. NIR, Visible, and UV
 - 3.1.5. Solid-State NMR
 - 3.1.6. Paramagnetic Sites: EPR and Related Techniques
 - 3.1.7. Adsorption of Probe Molecules
 - 3.1.8. IRAS, STM, LEED: “Flat” Silica Surfaces
 - 3.1.9. Use of Molecular Analogues of Silica Surface Groups
 - 3.1.10. Silica in Aqueous Solutions: Existence of a Modified Water Region
 - 3.2. Adsorption of Biomolecules on Silica
 - 3.2.1. X-ray Diffraction
 - 3.2.2. Bulk Adsorption Data: Geochemical Models and Adsorption Enthalpies
 - 3.2.3. Vibrational Spectroscopies

3.2.4. NMR Techniques	R
3.2.5. Flat Surface Techniques	S
3.2.6. An Overview of Experimental Studies of Small Biomolecule/Silica Systems	S
3.2.7. From Oligopeptides to Proteins: Adsorption, Secondary Structure, and Selectivity	T
4. Different Approaches To Model Adsorption at Surfaces	T
4.1. The Periodic Boundary Conditions Approach	T
4.2. The Cluster Approach	W
4.3. The Embedded Cluster Approach	X
5. Theoretical Methods and Their Application to Silica Surface Modeling	Z
5.1. Wave Function Based Methods	Z
5.2. DFT-Based Methods	Z
5.3. Dispersion Corrections	AA
5.4. Basis Sets	AB
5.5. Molecular Dynamics Simulations	AB
5.6. Approximated Methods	AC
5.6.1. Semiempirical Methods	AC
5.6.2. SCC-DFTB Method	AC
5.6.3. Classical Force Fields	AD
6. Crystalline Silica Surfaces	AE
6.1. Surface Sites	AE
6.2. Surface Reconstruction	AF
6.3. Hydroxylated Surfaces	AG
7. Amorphous Silica Surfaces	AI
7.1. The Tielens Model	AI
7.2. The Ugliengo Model	AJ
7.3. Other Models	AM
7.4. The S2R Surface Defect	AM
8. Adsorption of Water on Silica Surfaces	AM
8.1. The Early Story: First Principles Cluster Based Calculations	AO
8.2. Water on Crystalline Hydroxylated Silicas	AP
8.2.1. The Low Coverage Case	AP
8.2.2. Intermediate Coverages	AR
8.2.3. The Case of the Water Dimer	AR

Special Issue: 2013 Surface Chemistry of Oxides

Received: July 30, 2012

8.2.4. Water Monolayer	AS
8.2.5. Water Multilayers	AU
8.2.6. Crystalline Silica–Liquid Water Interface	AV
8.2.7. Water on Hydrophobic Crystalline Silicas	AZ
8.2.8. Adsorption of Water on Crystalline Defects	BA
8.3. Water on Amorphous Hydroxylated Silicas	BB
8.3.1. Hydroxylated Amorphous Silica Models Obtained by Classical MD	BB
8.3.2. Hydroxylated Amorphous Silica Models Obtained by ab Initio Methods	BD
9. Interaction with Biomolecules	BE
9.1. Interaction with Amino Acids	BE
9.1.1. The Glycine Case	BN
9.1.2. Other Amino Acids	BR
9.1.3. General Trends Found in Amino Acid Adsorption on Silica Surfaces	BU
9.1.4. Thermally Induced Transformations of Adsorbed Amino Acids on Silica Surfaces	BV
9.2. Interaction with Peptides	BZ
9.3. Interaction with Nucleic Acid-Related Biomolecules	CB
9.4. Interaction with Drugs and Natural Products	CF
10. Summary and Perspectives	CI
Author Information	CI
Corresponding Author	CI
Notes	CI
Biographies	CJ
Acknowledgments	CJ
References	CT
Note Added in Proof	

1. INTRODUCTION

There are many reasons to report on silica interacting with biomolecules. The most obvious one is that on the Earth's crust, oxygen and silicon are the most abundant atomic species, with percentages of 45.5% and 27.2%, respectively, which manifests itself in a large variety of silica and silicate minerals so that the contact between living matter and these materials is ubiquitous.¹ The abundance originates from the stellar evolution of massive stars (>8 solar masses) in which Mg, Si, and O nuclei are formed in large amounts from the nuclear fusion reactions.² If the star is more massive than 10 solar masses, it will explode as a supernova inseminating deep space with its newly formed chemical elements. Therefore, silica based minerals in the rocky planets, like Earth, derive from the accretion of interstellar dust grains resulting from chemical reactions between the most electropositive elements and oxygen. More specifically, silica refers to silicon dioxide SiO₂, a solid compound present in many different crystalline or amorphous allotropic forms. In nature, it is usually found as quartz, or sand, but is also present in some plants and marine organisms like Radiolarians in which it is metabolized to provide the skeleton structure. The name derives from the Latin *Silex* and its use is known from the Stone age, as a constituent to manufacture flint tools. An enormous body of literature exists on silica itself and its applications, and excellent books and reviews are available on silica properties. In the following, many of the general concepts about silica will be borrowed from the classical book by Iler³ and the edited book

by Legrand,⁴ the well-known collection of papers on adsorption at silica surfaces in the book edited by Papirer,⁵ and, in particular, from contributions by El Shafei,⁶ Morrow and Gay,⁷ and Davydov.⁸ Another good point of reference is the book by Vansant.⁹

An additional reason to focus on this topic is that silica surfaces have a key role in many applications dealing with biomolecule interactions,¹⁰ for instance, in chromatography,¹¹ just to mention the most common one. Indeed, silica as stationary phase for liquid chromatography system is used in the pharmaceutical industry, in the analysis of contaminants, pesticides, bioanalytes, and drug residues in drinks and food samples, and in medical or environmental tests.

The physicochemical reasons behind the delicate equilibrium established between the adsorbed and the mobile phases are ultimately dictated by the specific interactions between silica surface functionalities and the adsorbate, resulting in different adsorption constants. The contact between a biomolecule or, more generally, an organic molecule and an inorganic oxide surface is also the key to understand how artificial implants based on bioglasses, a combination of CaO, Na₂O, and SiO₂ oxides (of which the latter is the dominant one), perfectly merge with the body bone tissue.^{12,13} Applications of pure silica in health care are found in porous glass, which can be designed to encapsulate a specific drug that is then released *in situ* by a degradation of the silica matrix so as to maximize therapeutic effects and reduce toxicological side effects.¹⁴ Mesoporous materials are the main example of "drug delivery systems" (DDSs) with two principal aims: the development of systemic-delivery systems, able to release drug at a controlled rate avoiding premature degradation of the active agents, and implantable local-delivery devices, able to release drug as a response to an external stress (for instance, the application of a magnetic field) or a change in internal conditions (for instance, pH).^{15,16} Molecular sieves, particularly MCM-41, have been proposed as DDSs starting from 2001¹⁷ and their interaction with ibuprofen, widely employed as anti-inflammatory and analgesic, has been intensively studied. For a DDS to work properly, it should show biocompatibility.¹⁸ Interestingly, the biocompatibility of amorphous silica particles with cellular systems has been proven,^{19,20} whereas crystalline silica manifests toxic effects in interaction with cellular systems. The toxicity of crystalline silica is derived from prolonged inhalation of micrometric dust of quartz and its polymorphs of major density, cristobalite and tridymite, provokes serious lung diseases like pulmonary fibrosis and silicosis,^{21–23} whereas amorphous silicas and silicic acid do not show pathogenic effects.²⁴ Many hypotheses have been proposed by scientists to explain the origin of silicosis, all of them involving the role of functionalities exposed at the silica surface in the adsorption of endogenous matter. Adsorption of biomolecules may, in principle, trigger toxicity by modifying their structure and activating the immune system in a sort of autoimmune defense mechanism. For instance, the arrangement of silanols and siloxane bridges, which manifests in the presence of hydrophilic or hydrophobic areas, can cause the unfolding of proteins, or the adsorption of phospholipids through the hydrophilic phosphate and may provoke cell membrane rupture.²²

Less relevant to the present context is the use of silica in heterogeneous catalysis and as a sensing device. The possibility to modify surface silanols to give Si—O—M, where M may be a catalytically active metal as V, W, Mo, Cr, or many other elements, or to host nanosized metal particles at the surface

makes silica an excellent material in catalysis.²⁵ Sensing with silica materials is based on surface binding or encapsulation of sensitive molecules. The change in one or more properties when the silica surface is in contact with the analyte is revealed by the device. An interesting feature of silica as a support for sensors is the possibility to manufacture it in various forms as required, so that doped glasses can be miniaturized and integrated in optics fiber²⁶ or arranged in sensor arrays for the detection of multiple analytes.²⁷ Furthermore, they can easily be prepared to be used as selective tagged systems.²⁸

Most forms of divided silicas are structurally amorphous, and therefore, few techniques can provide atomic resolution information. Exceptions are rare, and only very recently, elegant experiments using scanning tunneling microscopy in ultrahigh vacuum conditions²⁹ combined with quantum mechanical modeling revealed the atomic structure of a vitreous thin silica bilayer film grown on Ru(0001). The difficulty in getting accurate structural information further increases when considering the interaction with biomolecules, despite the fact that for the latter alone, the Protein Data Bank³⁰ contains >82000 biomolecule structures known with atomic accuracy from a variety of diffraction and NMR spectroscopy techniques. It is then clear that experiments alone cannot cope with the complexity of the silica/biomolecule interactions. Indeed, the missing information about atomistic details can be provided by computer simulation techniques of various kinds, which are becoming essential to provide detailed views of the interface regions in which the silica/biomolecule interaction is occurring. Computer experiments can be conceived as “virtual microscopes” because they are able to increase our understanding providing not only atomic details but also, most importantly, the energetic features of the adsorption process, vibrational frequencies, NMR chemical shifts, electron density maps, and electrostatic potentials, which are essential ingredients for the correct interpretation of the experimental data. Silica functionalities are mainly surface silanol groups (SiOH), and they interact with the polar groups of proteins or nucleic acids or with the phosphate groups of membrane phospholipids through relatively strong H-bonds. To reduce the complexity, one can resort to a bottom-up approach, by studying the isolated biopolymer constituents, that is, amino acids, DNA bases, phosphates, etc. but because water is also ubiquitously present in the biological context, it is very challenging to disentangle the silica/water, water/biomolecule, and silica/biomolecule components from the resulting interaction strength.³¹ As it will become clear in this review, much exciting work remains to be done in this field, as many important issues still need to be fully clarified. Just to focus on one of the most common aspects, it is known that silica surface features are sensitive to the thermal treatment suffered by the material as silanol groups are removed from the surface by mutual condensation. What appears to be a rather straightforward process is indeed a very complex phenomenon and neither experiments nor computer simulation have clarified why the surface of an amorphous silica sample heated at high T (>1000 K) will not return to the pristine situation after water adsorption of the thermally treated material, whereas this happens for lower treatment temperatures.^{32,33} Despite its being such a common material, the synthesis of silica, either in gaseous phase as pyrogenic silica or in solution, has only been achieved in the first half of the 20th century, with the development of the sol–gel synthesis technique.¹³ Starting from the 1960s, silica materials have

become the subject of intense academic research and industrial application.³⁴ Nowadays silica, in all its different forms and possible applications, is one of the most studied compounds in the fields of chemistry, physics, material science, biomaterials, and engineering.³⁵ Indeed, searching for “silica” in the ISI Web of Knowledge within the 2001–2011 period reveals a regular increase in the number of entries in article topics and titles during the years (see Figure 1).

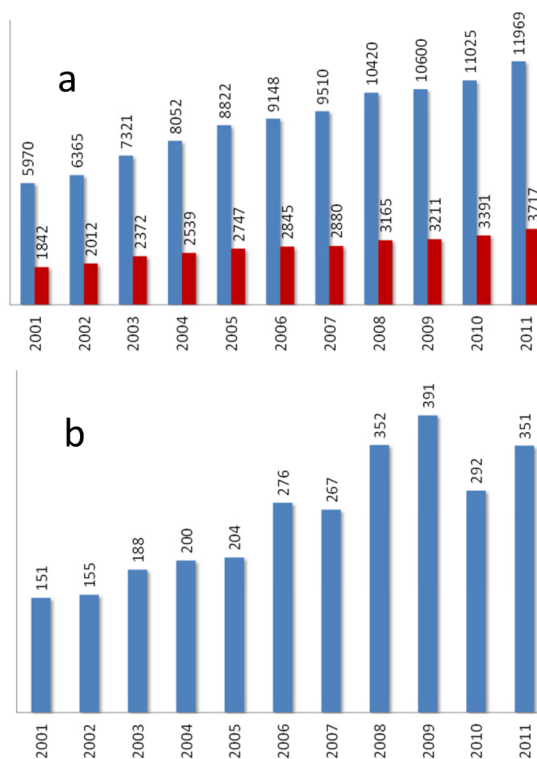


Figure 1. (a) Record count vs publication year (2001–2011) for the word “silica” in article topic (blue bar) and in title (red bar). (b) Record count vs publication year (2001–2011) for “silica” in review’s topic. Raw data obtained from ISI Web of Science, Databases=SCI-EXPANDED, SSCI, A&HCI, search date, 07-08-2012.

The name “silica” is also present more than 2500 times in review topics, and more than 60 new materials have been patented (silica in patent title) in the same period of time, confirming the importance of silica-based materials in a wide range of different fields.

In the present review, we only focus on the interaction between silica, either crystalline or amorphous, and biomolecules, restricting our attention to studies reporting a joint use of experiment and modeling techniques. We have also decided to include water as a special case, because H_2O is the most common biomolecule by election. In the spirit of a bottom-up approach, it resulted that amino acids, small peptides, nucleic acids, and a few important drug-related molecules have been studied so far in interaction with silica. The situation is similar to other materials like hydroxyapatite³⁶ and bioactive glasses.³⁷ Specific cases of molecules that are not, strictly speaking, biological are also included when they can play an important role in a biochemistry context. The pioneering and elegant work developed for a long time to characterize the interaction of small molecules, CO, CO_2 , NH_3 , etc., with silica surfaces from gas/solid adsorption experiments³⁸ is not the focus of the present contribution because it has already been reviewed³⁹ and

it has less relevance in the biological context. It will, however, be briefly reviewed in section 3 because some fundamental results on simple molecules are also relevant for the case of adsorption of more complex biomolecules.

2. STRUCTURE AND POLYMORPHISM

In the following, we very briefly summarize the silica surface features common to crystalline as well as amorphous silicas without claiming to be exhaustive (see, for instance, ref 40 for details). Silica is a solid material with a density between 2 and 3 g/cm³ and high melting point (ca. 1700 °C), whose chemical formula is SiO₂. In the structure of most crystalline polymorphs (except for stishovite, *vide infra*), a silicon atom is bound to four oxygen atoms, and each oxygen is bound to two silicon atoms. The silicon atoms are at the centers of regular tetrahedra of oxygen atoms, [SiO₄], connected through an oxygen vertex. Already in 1932, Zachariasen suggested that vitreous silica also consists of a continuous random network of corner-sharing [SiO₄] tetrahedra.⁴¹ The overall SiO₂ structure is neutral because the formal oxidation numbers for silicon and oxygen are (+4) and (-2), respectively, and each oxygen atom in the structure is the bridge between two [SiO₄] tetrahedra, so that the silicon–oxygen ratio is 1:2. Thus, the [SiO₄] tetrahedron represents the building block of almost all silica polymorphs, and they only differ in the connectivity of the tetrahedral framework. The different linking patterns for each polymorph translate into different structural, physical, and chemical properties.

The Si–O bond shows a predominantly covalent character, as proven by the electron density maps, obtained from X-ray diffraction, and by the bond population analysis obtained from quantum mechanical calculations. Both experimental and computational results assign a charge of ca. +1.4 on silicon atoms and -0.7 on oxygen atoms.^{42,43}

Since silicon has empty d orbitals at a relatively low energy, it can expand its coordination to become octahedrally coordinated. Stishovite, a high-temperature and high-pressure polymorph of silica, is the only form characterized by a framework in which the silicon atoms are octahedrally coordinated by six oxygen atoms, and it was discovered in Meteor Crater, Arizona, due to the favorable high *T* and *P* caused by the body impact,⁴⁴ and synthesized in the laboratory by Stishov and Popova.⁴⁵ Its X-ray structure revealed a rutile type SiO₂ framework.⁴⁶

The [SiO₄] unit is rigid, because changing the O–Si–O angle from the equilibrium value of 109° is an energetically expensive process. In contrast, the Si–O–Si angle that connects two tetrahedra can easily change, for instance, as a function of temperature or geometrical constraints. Indeed the flexibility of the Si–O–Si angle is very high, since it costs virtually no energy to change the angle value between 130° and 180°, as demonstrated in the past in a number of computational studies.^{47–49} For instance, the CISD/TZ+2d potential energy surface of H₃Si–O–SiH₃ as a cluster model (see section 3.2) of the siloxane Si–O–Si bond gave a minimum at 142°, while changing the angle from 130° to 180°, only costs around 6.7 kJ/mol.⁴⁷ The exact value of the barrier to bring the Si–O–Si to 180° from the actual minimum was shown to be difficult to compute because Bär and Sauer⁴⁸ showed a large sensitivity of the results to the quality of the adopted Gaussian basis set. For instance, MP2 calculations with basis sets including up to five d and four f polarization functions showed a minimum potential energy at a Si–O–Si angle value larger than 145° and a

linearization barrier of only 1.5 kJ/mol. Similar results have been reported in an exhaustive work by Tielens et al.⁵⁰ who adopted six different exchange–correlation functionals with very large Gaussian basis sets, confirming the extreme flexibility of the Si–O–Si angle in full agreement with the MP2 results by Bär and Sauer.⁴⁸ All these results are at variance with the case of organic ether in which the C–O–C angle is almost invariably found around 110° and there is a very high energy barrier to linearization. The Lewis basicity of the Si–O–Si siloxane bridges has also long ago⁵¹ been proven to be significantly smaller than the corresponding one measured for the C–O–C link found in organic ethers. Reasoning based on the oxygen *p* orbital back-donation through the empty d orbitals of Si has been put forward but more recent quantum mechanical calculations did not find any evidence for that and electrostatic interactions have been invoked to explain the relatively short Si–O bond length.⁴⁸

The high pliability of the Si–O–Si angle is the reason behind the large number of all-silica materials, envisaging all possible silica polymorphs, from dense crystalline and amorphous structures (quartz or glasses) to nonperiodic porous systems (aerogels and sponges) to microporous crystalline zeolites and mesoporous materials (see Figure 2).

Dense	Porous	
	Non-periodic	Periodic
• Quartz-like 	• Amorphous • Variable pore size • Irregular arrangement 	• Crystalline • Constant pore size • Regular arrangement
• Glass-like 	Sponges 	Aerogels
	Inert support, chromatography	Zeolites
		MCM's
		Catalysts, molecular sieves

Figure 2. Different silica structures based on corner-sharing [SiO₄] units.

Just for the limited case of zeolites, the structural database⁵² reports 201 different kinds of all-silica frameworks that can, at least in principle, be synthesized. In practice, most of them have only been synthesized as aluminosilicates (zeolites), because a small amount of substitutional aluminum stabilizes the framework. Zeolites are used as catalysts as well as adsorbent in a large number of technological applications.^{53,54}

The [SiO₄] arrangement that determines the formation of different dense polymorphs chiefly depends on the crystallization pressure (*P*) and temperature (*T*), and their relative stability changes with the values of *P* and *T*. The different polymorphic phases can be present out of their *P* and *T* stability range because the phase transformation between one polymorph and another is an extremely slow process. A phase that is maintained unaltered outside its stability conditions is named metastable. Zeolites are classical examples of metastable phases, and their stability can also depend on the presence of the template molecule. At room temperature and low pressure, the most stable silica phase is α -quartz followed by α -tridymite and α -cristobalite. These are the most common high-density crystalline polymorphs. Each one of them can exist also in a phase named β , which is stable at higher temperature and presents a more symmetric structure. At room conditions, α -quartz is the most stable phase, and every different crystalline or

amorphous, low- or high-density silica phase in these conditions is metastable at best.

The $[\text{SiO}_4]$ building blocks are joined via corner-sharing links in the vast majority of silica materials. Exceptions to this class of structures are stishovite (*vide supra*) and fibrous silica^{55,56} consisting of chains of edge-sharing $[\text{SiO}_4]$ tetrahedra. The existence of this material is important, as it will be shown later, since two-membered silicon rings $(\text{SiO})_2$ (hereafter called S2R) like those constituting the repeating unit in fibrous silica are also formed as isolated defects at the surface of amorphous silica subject to thermal temperature at $T > 800 \text{ K}$, imparting to the surface a reactive character.

2.1. Synthesis of Silica Samples

The formation of colloidal silicas, pyrogenic silica, silica xerogels, and precipitated silica has been largely studied in order to synthesize products of technological importance with reproducible properties. The preparation of silica samples can be made in anhydrous vapor phase at high temperature (such samples are trademarked Carb-O-sil in the USA or Aerosil in Europe), vaporizing SiO_2 in an arc or plasma jet and condensing it in a stream of dry inert gas or oxidizing and hydrolyzing silicon compounds (SiH_4 , SiCl_4 , HSiCl_3), or in aqueous solution (silica gel or precipitated silica) by condensation of simple monomers $\text{R}_x\text{Si}(\text{OH})_y$ ($x + y = 4$). Both methods produce porous structures: pyrogenic silica normally presents smaller pores than colloidal silica whereas Aerosil only exhibits interparticular porosity. All of these materials have high surface areas as measured by means of the adsorption isotherm obtained with N_2 as adsorbate⁵⁷ applying the Brunauer, Emmett, and Teller (BET) theory.⁵⁸ Such samples are overall amorphous structures, but pyrogenic silica may present crystal-like order in limited regions. This can be explained considering that at the high temperature required by the synthesis the rate of rearrangement of $[\text{SiO}_4]$ tetrahedra is very high, and since configurations with local order similar to those of crystals are the most stable, the tetrahedra tend to arrange locally in ordered networks.

In 1984, Avnir and co-workers⁵⁹ described the hydrolytic polycondensation of silicon alkoxides, $\text{Si}(\text{OR})_4$ or $\text{R}'\text{Si}(\text{OR})_{4-n}$, in solution to form highly porous organosilicates, where the organofunctional groups R' modifies the network of the product. The reaction was somehow revolutionary because it permits the entrapment of organic and bioinorganic molecules within the structure of glasses at low temperature, something that was not possible before due to the high temperature that the preparation of glasses normally requires.

The porosity of the gel structure changes with the organofunctional R and R' groups and other factors like the drying procedure applied after the synthesis or the use of drying agents like formamide, glycerol, oxalic acid, and other organic acids.⁶⁰ For instance, samples dried by natural evaporation (xerogels) present a minor porosity, whereas samples dried in an autoclave (aerogels), where the solvent is removed above its critical point, present a major porosity and a lesser density. The porosity strongly determines the features of the functionalities exposed at the surfaces and, thereby, the surface properties of the sample.^{59,61} Clearly, it is not possible within this review to report the innumerable applications of these silica-based hybrids especially since they involve a surface chemistry potentially very different from bare silica.

In 1992, researchers of the Mobile Oil Corporation developed a new family of ordered mesoporous silicas with

pore diameters tunable between 15 and 300 Å, using liquid crystal surfactants with long n-alkyl chains as templating agents.^{62,63} Such highly porous ordered silicas present pores with amorphous silica walls spatially arranged in periodic patterns. These compounds were named M41S (molecular sieves) and present very high specific surface areas ($\sim 700 \text{ m}^2/\text{g}$) and pore volumes. The M41S consist of a hexagonal phase ($P6m$) named MCM-41, a cubic phase ($Ia3d$), named MCM-48, and a lamellar phase named MCM-50 (see Figure 3).

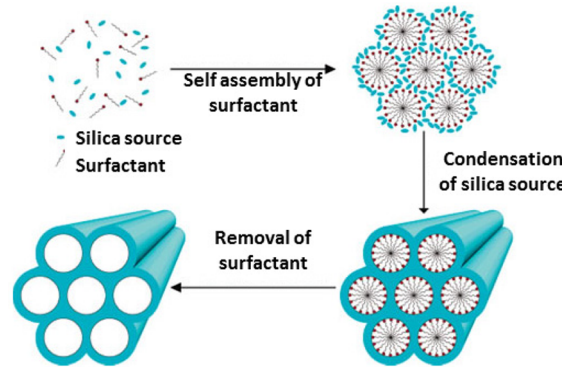


Figure 3. Schematic representation of the process giving rise to molecular sieves. Reprinted with permission from ref 64. Copyright 2005 America Chemical Society.

The pore dimension depends on the length of the alkyl chain, and the pore walls are amorphous overall. The pore diameter essentially determines the dimension of the molecules that can be entrapped inside the pores: tuning the pore dimension in a range that varies from a few nanometers to several tens of nanometers allows it to host small molecules or macromolecules, such as proteins. The presence of additives during the synthesis, which modify the functional groups exposed at the wall surfaces, may determine the adsorption properties of the molecular sieves. For this reason, such structures present a large number of potential applications.

The list would not be complete without mentioning biogenic silica, such as sponge spicules, radiolarian tests, and especially the frustules (silicified cell walls) of diatoms, whose accumulation yields diatomaceous earth or kieselguhr and siliceous ooze sediments. They have original middle-range organizations such as regular nanometric spheres of opal, and the micrometer-size structures of diatom walls are especially spectacular.⁶⁵ Biogenic silicas interact with biomolecules, almost by definition, but in a different way from what is considered in the present paper: specialized biomolecules such as the proteins silaffins and silicateins⁶⁶ pre-exist to the siliceous phase and strongly contribute to building it from molecular precursors. This is a fascinating subject, but it falls outside of the scope of this review. The question whether biogenic silicas differ from their synthetic counterparts at the molecular level is largely untouched.

2.2. Silica Surfaces: Nomenclature of Surface Groups

While an ideal solid, irrespective of its amorphous or crystalline nature, is by definition infinite, a real solid is always finite and therefore characterized by external surfaces. The surfaces represent the interface between a solid bulk and the external environment so that the physical and chemical features characterizing the interaction of (bio)molecules with the silica surfaces should be studied at the atomic level. To achieve that,

the first step is to highlight the structural properties of the bare silica surfaces.^{4,40}

When silica is fractured in the laboratory under ultrahigh vacuum conditions a complex reconstruction of the broken Si–O bonds occurs in order to self-heal the dangling bonds at the surface (see also sections 3.1.6 and 6). This can be attained by the formation of highly strained Si–O rings of small nuclearity or unusual defects like $>\text{Si}=\text{O}$ ones (silanones). It has, however, been measured that even a very low water partial pressure (of the order of 10^{-7} Torr) brings about a complete reconstruction of the silica surface giving rise to surface silanol groups, SiOH .⁶⁷ Therefore, at the silica surface, in normal laboratory conditions, the most common termination is given by two main functional groups: the siloxane links (Si–O–Si) and the silanol groups (Si–OH). The siloxanes are also present in the bulk structure, although not accessible, and result from the vertex sharing of the $[\text{SiO}_4]$ tetrahedra. Silanol groups either in the bulk or at the surface are the result of an incomplete condensation during the polymerization that forms the massive solid. The contact between silica and chemicals of various nature may break Si–O bonds at the surface of the material giving rise to unfilled valences. Water is normally present in the environment around the material, so that either protons or hydroxyl groups (OH) are the most suitable candidates to complete the valency of both atoms. Even in cases where the silica derives from combustion process, the final material is, nonetheless, exposed to the moisture. Hydrated surfaces, characterized by high population of surface hydroxyls, are therefore formed. The usual picture of a pure silica surface is, thus, a system composed by regions of siloxane links interrupted by sites exposing silanol groups. Silanols are responsible of the hydrophilic properties of silica, since they can interact with polar groups or molecules via hydrogen bond interactions.^{8,38}

In crystalline silica, ideally, the $[\text{SiO}_4]$ tetrahedra are stacked in an ordered design, which is repeated regularly, so that a regular distribution of the hydroxyls at the surface has to be expected. Despite this, experimental evidence suggests that silica samples are quite heterogeneous because of irregular packing and incomplete condensation during the synthesis process. On crystalline silica, the upper layers can present an amorphous character with a loss of the expected order.^{21,68} Nevertheless, within the scope of the present review, only regular surfaces have been considered when dealing with crystalline materials so that special surface features are expected due to the repeating nature of the SiOH groups.

As mentioned before, Si atoms in the bulk silica are mostly bound to four bridging oxygen atoms. This environment, clearly identifiable by NMR,⁷ is labeled as Q^4 in which the superscript indicates the number of neighboring $[\text{SiO}_4]$ groups attached to a given Si. On the other hand, silicon at the surface can bind to one or two hydroxyl groups to complete its valence, according to whether its binding to the bulk involves three or two Si–O–Si bridges: the corresponding environments are therefore denoted as Q^3 or Q^2 , respectively. Surface structures like surface silanone $>\text{Si}=\text{O}$ and $\text{Si}-(\text{OH})_3$ (Q^1) with the silicon bonded to only one bulk oxygen, can exist in principle, but the first one is thermodynamically and kinetically unstable toward water adsorption,^{69–71} whereas no evidence of the Q^1 species has been reported from NMR experiments (see also section 3).⁷²

Figure 4a shows a cartoon that helps to visualize different kinds of silanols exposed at silica surfaces. A single or terminal

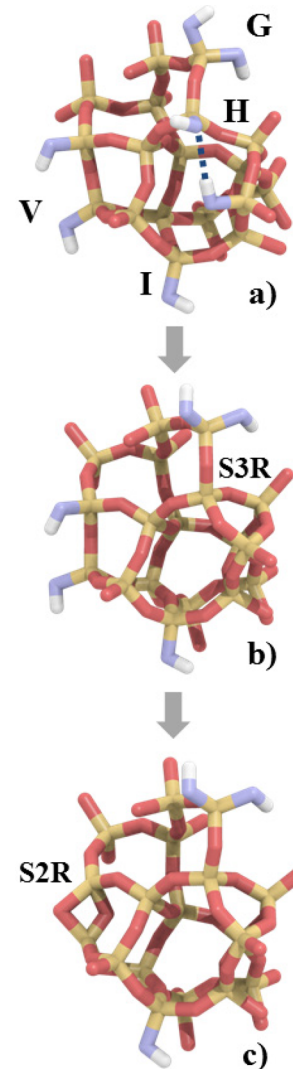


Figure 4. A cartoon of the possible silica surface sites: (a) isolated SiOH (I, Q^3), geminal SiOH (G, Q^2), vicinal SiOH (V, Q^3), and H-bonded SiOH (H, Q^3); (b) formation of the $(\text{SiO})_3$ ring (S3R) by condensation of the H pair; (c) formation of the $(\text{SiO})_2$ ring (S2R) by condensation of the V pair. Evolution from a to c is driven by increasing temperature. Color coding: oxygen (red), oxygen of the SiOH (blue), hydrogen (white), silicon (yellow). Molecular graphics rendered by Qutemol.⁷³

Si–OH group (Q^3) is called an *isolated* silanol SiOH (I) when the distance to the closest SiOH groups is such that they cannot be involved in H-bond interactions. Silanol groups that are separated by more than ~ 3.3 Å can be considered as unable to establish mutual hydrogen bond, and therefore as isolated. The isolated silanol groups are then free to establish H-bond interactions with adsorbates as both H-bond donors and acceptors. Pairs of silanols belonging to tetrahedra that share a common oxygen vertex are normally called *vicinals* (V). The two silicon atoms of vicinals are separated by a single oxygen so that the two hydroxyl groups are separated by less than 3 Å, but despite that, they are usually not involved in a H-bond, at least according to quantum mechanical calculations on cluster models.^{74,75} Nevertheless, local geometrical constraints may force a vicinal site to become weakly H-bonded. Two silanols that do not belong to directly connected tetrahedra but nonetheless are closer than ~ 3.3 Å will establish H-bonds and

are called *interacting* or H-bonded (H). The optimum O···O distance between the two OH involved in a H-bond lies between ~2.5 and ~2.8 Å. It is worth noting that the positions in space of surface SiOH groups in silica are constrained by the underlying solid structure, so that in many cases, they cannot give rise to strong H-bond interactions as would have occurred in a less constrained environment. Two OH groups linked to the same surface silicon atom (Q^2) to give the $\text{Si}-(\text{OH})_2$ moiety are called *geminals* (G), and since the silicon atom is attached in addition to two tetrahedra by Si—O—Si links, a pair of geminals necessarily correspond to a Q^2 Si. Even though they are very close, the two geminal OH are oriented in such a way that they cannot be involved in mutual H-bonds.

When a highly hydrated silica is heated, the main effect is the progressive condensation of pairs of surface silanols involved in H-bond interactions and the formation of a siloxane bridge, as showed in Figure 4b. Depending on the pair of H-bonded silanol groups, the condensation brings about $(\text{SiO})_n$ rings of distinct nuclearity n . For instance, in Figure 4b, the condensation of the H pair gives a three-membered silicon (SiO_3) ring (S3R), whereas when vicinal V pairs are involved a highly strained two-membered silicon (SiO_2) ring (S2R) is formed (Figure 4c). Their formation increases the structural tension of the outgassed surface during the heating process. Because the SiOH groups can give rise to H-bond interactions with adsorbates and, in particular, with the ubiquitously present water molecules, outgassing silica at high T decreases its hydrophilic character and increases the hydrophobic one. Thus, for high-temperature-treated silicas, the adsorption processes are dominated by hydrophobic interactions, mainly driven by dispersive forces. This means that thermal treatments are a very simple and convenient way to fine-tune the adsorption properties of silica-based materials. We will see in section 3 how infrared spectroscopy can be used to track the dehydroxylation process.

Silica samples prepared in the gas phase, known as Aerosil, are usually less hydrophilic than sol–gel silicas, because the high temperature of the preparation already causes a decrease of the number of OH groups, which condense during the synthesis process. In this case, it is important to consider the age of the sample to know the degree of surface hydroxylation.⁶ Samples of Aerosil tend, upon aging, to increase the total concentration of silanols, while reducing the concentration of isolated silanols. This is the result of the cleavage of strained siloxane bridges by water molecules in the surrounding environment.⁷⁶ Water breaks Si—O—Si to form a pair of mutually H-bonded silanol groups (apart from the opening of the S2R resulting in a vicinal pair), in the inverse process of that described in Figure 4, so that the total number of silanols increases while the fraction of isolated ones decreases.

Despite the complexity of silica surfaces, Zhuravlev has shown that the average number of Si—OH groups per square nanometer in a fully hydroxylated surface is a physicochemical constant amounting to 5 OH/nm², irrespective of the preparation method for a set of about 100 different silica aerogel samples.^{77–80}

More generally, if one considers surfaces that have been thermally activated or are not fully hydroxylated for any reason, the total concentration of silanol terminations (and their distribution between isolated, vicinal, and H-bonded or between terminal and geminal) can vary considerably.^{8,81,82} However, regularities are observable, and Zhuravlev⁷⁸ has proposed a “master curve” showing the concentrations of the

different types of silanols exposed at the surface as a function of the sample thermal treatment, which is reproduced in Figure 5.

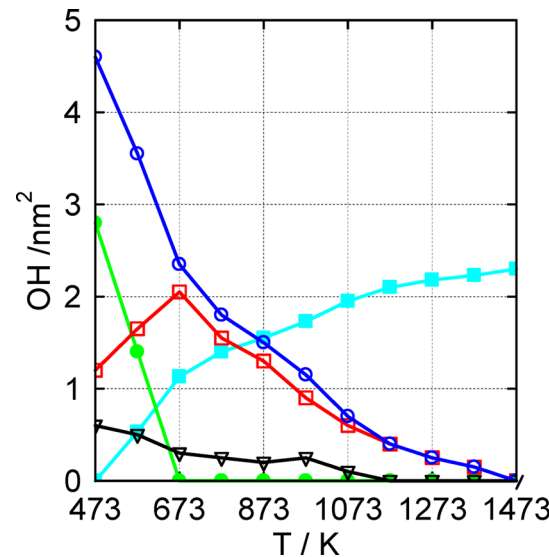


Figure 5. Distribution of the OH surface group per square nanometer as a function of the silica sample treatment temperature: (blue open circles) average concentration of total OH/nm²; (cyan solid squares) average concentration of Si—O—Si; (red open squares) average concentration of free OH groups; (green solid circles) average concentration of H-bonded OH groups; (black open downward pointing triangles) average concentration of geminal groups. Graph drawn using raw data from ref 78.

Thus, for instance, for the total density of 4.6 OH/nm² on a silica sample fully hydroxylated at 500 K, about 0.6, 1.2, and 2.8 OH/nm² are due to geminal, isolated, and H-bonded ones, respectively. Already at 700 K, all H-bonded silanols have disappeared, while the isolated silanols reach their maximum density of 2 OH/nm². At about 1000 K (see also Figure 5), only one isolated silanol per square nanometer remains, together with a small fraction of geminals, and at about 1500 K, the sample undergoes sintering with the elimination of all surface functionalities. This very last step brings about a complex restructuring of the silica sample making subsequent rehydration by water adsorption an extremely slow process.^{32,33} It is still unclear how it happens and what are the physicochemical steps controlling that process, which implies some sintering of silica.

An interesting aspect of silica surfaces in contact with water solutions of different ionic strength and pH is silanol deprotonation, which produces negatively charged surface groups ($\equiv\text{SiO}^-$), with relevant consequences for the adsorption of ions and polar molecules from the solution. What is known about this important point will be detailed in section 3.1.2.

3. EXPERIMENTAL DATA

3.1. Features of a Bare Silica Surface

Here we will only be concerned with silica features that can play a role in “realistic” conditions for biomolecule adsorption, that is, in conditions of high water activity. As discussed in section 2, this excludes some features such as silanone groups. We will list the experimental techniques that allow the observation and discrimination of silica surface groups and

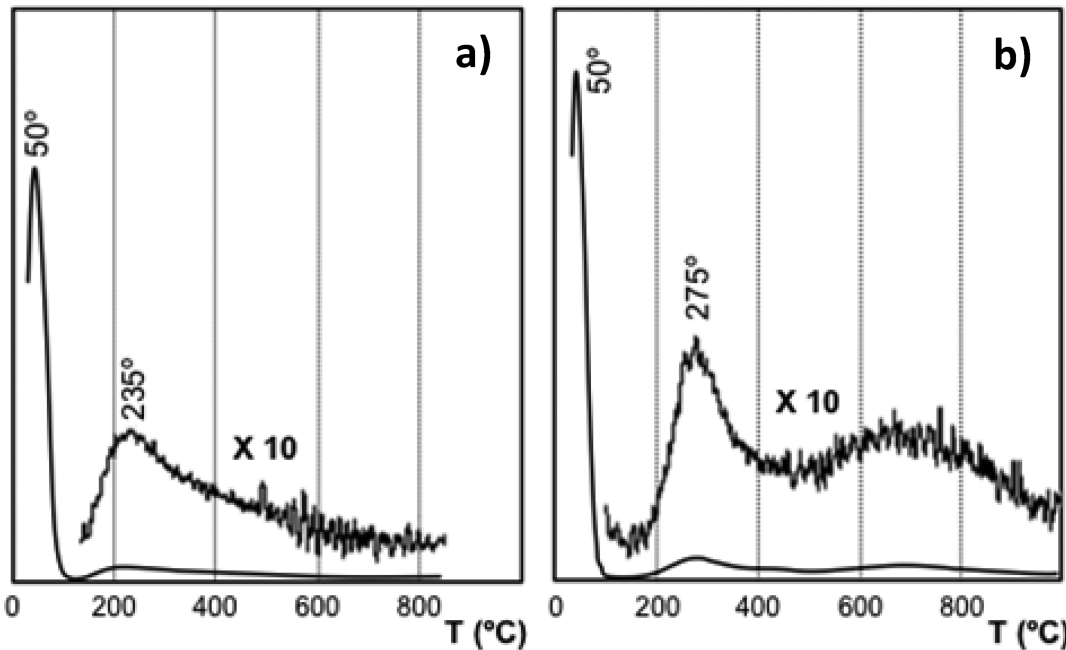


Figure 6. Typical TG traces (presented as first derivative, DTG) of (a) a fumed silica, Aerosil 380 (Degussa), (b) a mesoporous silica, MCM-41, under dry air flow, $\beta = 5\text{ }^{\circ}\text{C}/\text{min}$.

summarize the main results that have been safely established so far.

3.1.1. Bulk Data: Thermogravimetry (TG) and silanol surface Densities. Thermogravimetric analysis has been applied to amorphous silicas for a long time. TG traces usually show the elimination of physisorbed water at $T \leq 100\text{ }^{\circ}\text{C}$, followed by the condensation of different types of surface silanols up to $1000\text{ }^{\circ}\text{C}$. A huge amount of data has been analyzed in great detail and allowed what is sometimes called “Zhuravlev’s model” to be devised,^{78,80} of which the main feature is an almost constant value of the silanol surface density for maximally hydroxylated silicas at $4.6\text{--}4.9\text{ nm}^{-2}$ based on nonporous silicas such as Aerosils. For mesoporous silicas, a figure of 4 nm^{-2} has been reported by Trébosc et al.⁸³ from TG and ^{29}Si NMR (see section 3.1.5); also from TG and ^{29}Si NMR, Landmesser et al.⁸⁴ have evaluated the percentage of Si atoms bearing OH groups, and while there is some ambiguity regarding the surface area of their material, a figure in the range $4.2\text{--}4.6\text{ nm}^{-2}$ has been estimated.

It is generally accepted that precipitated silicas have significantly higher surface silanol densities. For instance, a figure of $7.7\text{ silanols nm}^{-2}$ (from TG alone) has been reported in ref 85.

Conversely, silicas with lower silanol densities⁸⁶ may be prepared if the thermal condensation process is correctly controlled. The only way for silanols to disappear is to condense in pairs, producing one siloxane and one water molecule. This generally results in the formation of strained cycles or rings, which can be observed by vibrational spectroscopy (cf. section 3.1.3). The evolution of the surface densities of various types of silanols with pretreatment temperatures has been mentioned in section 2 (Figure 4). Surface silanol densities significantly lower than 4 nm^{-2} have sometimes been reported for fully hydroxylated silicas without thermal treatment, for example, $2.2\text{--}2.7\text{ nm}^{-2}$ for precipitated silicas.⁸⁷ As it turns out, figures in this range are calculated from

LiAlH_4 titration of the silanols,⁷⁶ a method that has never been proven to be quantitative.

Note that the (111) face of β -cristobalite has a silanol density very similar to the average values mentioned above (4.55 nm^{-2}): this has spurred interest in the use of this surface as a model for that of amorphous silica.⁸⁸ However, the β -cristobalite (111) surface also has features significantly different from that of amorphous silicas, because the silanols cannot form H-bonds to each other (cf. section 3.1.3; much more on the topic of model crystalline surfaces will be found in section 6.3, see especially Table 4 for silanol densities).

Although TG curves could in principle be used to assess the distribution of surface silanols between populations of different reactivity toward condensation (such as isolated vs interacting), they are in fact quite featureless and attempts to extract further information from them are not fully convincing. Figure 6 shows the first derivative of the weight loss for a hydrated fumed silica; the first and most intense event peaking at 50° is due to the desorption of physisorbed water, and it is followed by a very broad feature corresponding to silanol condensation, peaking in the $230\text{--}280\text{ }^{\circ}\text{C}$ range and tailing smoothly up to $1000\text{ }^{\circ}\text{C}$ at least. DTG traces of mesoporous silica are only slightly different (Figure 6). For precipitated silicas, sharper peaks in the DTG may sometimes be observed, but they are likely due to the elimination of residual organic residues on the surface.

3.1.2. Bulk Data: Acid–Base Titration. How Many Negatively Charged Silanolate Groups Can There Be at the Interface? There are many ways to differentiate the reactivity of surface silanols, depending on what phase is in contact with the silica surface. If one is dealing with a silica–aqueous solution interface, simple acid–base titration can be useful. Most early studies, chiefly aimed at determining the value of the PZC (point of zero charge) of silica, and titration data were thus treated in the “1 site, 2 pK” model.^{89–91} In this model, all surface sites are supposed to be equivalent and can be either protonated or deprotonated; thus, the only significant differences would be between protonated silanols $\text{Si}–\text{OH}_2^+$,

neutral ones Si—OH, and deprotonated ones Si—O[−]. Duval et al.⁹¹ have analyzed their O 1s XPS results in this manner. But the appropriateness of the 1 site, 2 pK model may be questioned since only negative surface charges are observed for all tested pHs;^{92,93} besides, other techniques amply show the heterogeneity of surface silanols. Furthermore, when the total amphoteric site density is considered as an adjustable parameter and estimated from the titration curves, it provides values quite different from those estimated from TG.⁹³

Therefore it would seem more fruitful to consider that the silica surface exhibits different surface sites, all of them acidic but with different acidity constants, that is, to use “multisite, one pK” models.⁹⁴ With such models, the PAD (proton affinity distribution) could be extracted from acid–base titration curves. In practice, this approach is not widespread, and we are not aware of PAD curves for pure silica, although they have been reported for silica-containing mixed oxides.⁹⁵

On the other hand, some authors have observed the evolution of surface ionization by other means than measuring proton consumption. Ong et al.⁹⁶ followed the surface charging of a quartz surface by SHG (second harmonic generation) observation of polarized interfacial water. This technique does not allow an estimate of the absolute value of the surface charge. However, the existence of two successive jumps separated by 4 pH units is unmistakable (see Figure 7), and

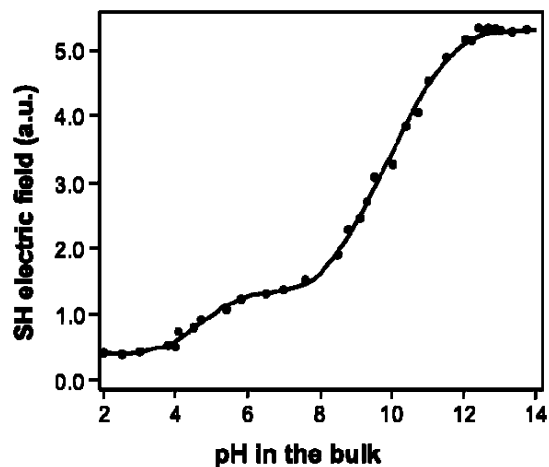


Figure 7. Intensity of the electric field (supposed proportional to the surface charge) at the silica–aqueous NaCl solution interface as a function of solution pH. Adapted with permission from ref 96. Copyright 1992 Elsevier.

therefore, the existence of two silanol populations with intrinsic acidities separated by a factor of 10 000 is established. The first population represents 15–20% of the total and has a $pK_a = 4.5$ (about the same as that for acetic acid), whereas the remaining one accounts for 80–85% and has a $pK_a = 8.5$; very similar conclusions were reached by Ostroverkhov et al. from SFG (sum frequency generation).⁹⁷

Evanescence wave cavity ring-down spectroscopy is another technique allowing researchers to probe the chemical state of a solid–liquid interface *in situ*,⁹⁸ and its application to the adsorption of cationic dyes on silica prisms as a function of pH confirmed the existence of two populations of sites with different acidity in about 3 to 1 ratio.^{99–101} This is an example of using the adsorption of a particular molecule in order to identify a corresponding site on the surface; that is, it is an

instance of probe molecule adsorption at the solid–liquid interface: more will be said on probe molecules in section 3.1.7.

While the authors of these studies did not provide specific assignments for the two silanol populations, a possibility is that they correspond to geminal and terminal silanols, respectively: the percentage of groups with the smaller pK_a value (more acidic) is of the same order as the percentage of geminal with respect to total silanols as measured by NMR. Other interpretations of the two populations could be possible, because the state of H-bonding may also influence the acidity of a silanol, and we will propose such an explanation in the conclusions (section 10). Some simplified models of surface groups, such as the MUSIC (multisite complexation) model and its refinements, have been proposed to theoretically predict these effects, but they seem to do a rather poor job at accounting for silica surfaces.^{102–104} Therefore, the molecular modeling of the surface acidity of silanol groups is currently an active field of research and will be discussed in detail in section 8.2.6 below.

Well-defined jumps are not apparent from classic pH-metric data (Figure 8). Whether this difference is simply due to an intrinsically lower resolution for the latter data remains unknown.

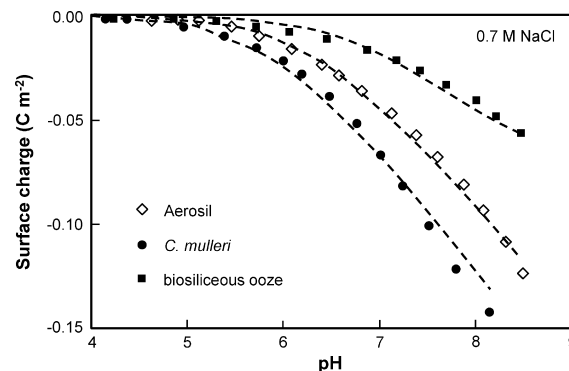


Figure 8. Charge densities from proton titration of three different silicas, one Aerosil and two biological silicas, as a function of pH. “C. mulleri” refers to a biogenic silica synthesized by the diatom *Chaetoceros muelleri*. Adapted with permission from ref 93. Copyright 2002 Elsevier.

A better assignment of pK_a values observed on amorphous silica would be possible if we knew more about the behavior of silanol groups on crystalline silica faces, which should expose silanols in well-known, uniform environments. Churchill et al.¹⁰⁵ estimated PZCs from AFM measurements at variable pH and found small but significant differences between the (100) face on the one hand (PZC = 2.9) and the (101) and (011) faces on the other hand (PZC = 2.7). Such studies are still rare.

A question of significance for modeling silica interfaces in the presence of an aqueous solution is the maximum density of negatively charged groups (silanolates, i.e., Si—O[−]). If one adopts the 1-site, 2-pK model, the answer should be fairly simple. In this model, all surface silanols are supposed to be chemically equivalent and amphoteric. At a pH value significantly superior to pK_{a2} , virtually all of them should be negatively ionized (dissociation rate $\alpha \approx 1$). If one were dealing with a solution of a weak acid, α would be about 0.99 at pH = $pK_{a2} + 2$; in fact for acid groups on a surface, α is smaller due to the adverse energetic effect of accumulating negative charges in close vicinity upon ionization, but it should still tend toward

unity at reachable pH values; that is, the silanolate density should approach the total silanol density. Now this type of reasoning is not very helpful in practice because there is no independent estimate of the pK_{a2} apart from the proton titration data and in addition the 1-site, 2-pK model is probably inadequate to account for the acid-base behavior of silica surface sites as mentioned above.

What we do obtain from experience with certainty is a value of the surface charge density as a function of pH. To give a few typical examples, for Aerosil 300 in KCl electrolyte, the surface charge varied from about 0.01 to about $0.08 \text{ C}\cdot\text{m}^{-2}$ as the pH was raised from 5 to 8,⁹³ corresponding, respectively, to 0.06 and 0.49 silanlates ($\equiv\text{SiO}^-$) per square nanometer. The earliest study by Bolt⁸⁹ reported a value of about $0.01 \text{ C}/\text{m}^2$ for a colloidal suspension of silica particles (with a surface area of $180 \text{ m}^2/\text{g}$), marketed as Ludox,¹⁰⁶ in a $1 \times 10^{-3} \text{ M}$ NaCl solution at pH = 7. Sonnenfeld¹⁰⁷ reported for spherical silica particles in a solution at pH = 7 and ion strength = $5 \times 10^{-3} \text{ M}$ a value of $0.02 \text{ C}/\text{m}^2$ ($0.12 \equiv\text{SiO}^- \text{ nm}^{-2}$). Behrens and Grier¹⁰⁸ measured a value of 4000 effective negative charges per square micrometer at pH = 7 and ion strength = $5 \times 10^{-6} \text{ M}$ for $1 \mu\text{m}$ silica spheres, that is, only $0.004 \equiv\text{SiO}^- \text{ nm}^{-2}$. For comparison, the same authors report for a glass plate in contact with a solution at the same pH and ion strength a value of 3000 effective negative $\equiv\text{SiO}^-/\mu\text{m}^2$, that is, $0.003 \equiv\text{SiO}^- \text{ nm}^{-2}$. Other studies provide silica surface charge data.^{109–112} Figure 8 shows the surface charge density as a function of pH for three different silicas.⁹³

These data, while incomplete, show how the actual electric state of the silica surface is crucially determined by the pH of the solution from which the adsorption is taking place. It also depends on the ion strength, although less sensitively. This has serious consequences if one wishes to model (bio)molecule adsorption from a solution: the surface density of negatively charged silanolate groups introduced in the model will only have a limited range of validity in terms of conditions in the solution. Note that ^1H NMR is a possible experimental approach to detect water in the vicinity of a silanolate, which has been reported to resonate at an unusually low chemical shift value.^{113,114}

3.1.3. Vibrational Spectroscopies: IR and Raman. IR spectroscopy has been applied to amorphous silica, in contact with either a gas phase or vacuum, for a long time. A comprehensive review of the literature until 1998 may be found in ref 40. A typical evolution of the IR spectrum of an Aerosil silica in the 2750 – 3800 cm^{-1} range is shown in Figure 9.

This range contains the stretching vibration of OH groups ($\nu_{\text{O}-\text{H}}$). If silica is observed under air without any pretreatment, the contribution of the OH of adsorbed water molecules is dominant. Because water molecules adsorbed in a multilayer are subject to a large range of inhomogeneous H-bond interactions, one observes a large bathochromic shift of the OH stretching frequency of their OH groups, together with a heterogeneous broadening. This results in a broad feature extending to about 1000 cm^{-1} lower than the reference frequency of 3747 – 3750 cm^{-1} (labeled I+G+V in Figure 9, since these three types of silanols are indistinguishable, cf. infra). Outgassing at $T = 300 \text{ K}$ already removes the largest fraction of the multilayer adsorbed water, leaving few adsorbed water molecules at the surface so that the absorption is due chiefly to silanol O–H, and at 450 K , dehydration is probably complete. Even then, this region shows a complex band structure. The narrow band at 3747 cm^{-1} becomes stronger and

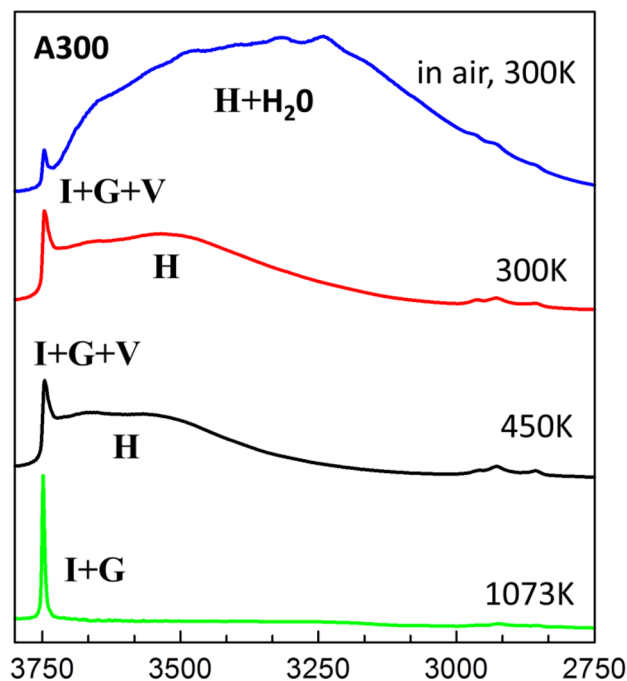


Figure 9. Infrared spectra of a sample of Aerosil 300 (A300, a fumed silica sample characterized by a surface area of $300 \text{ m}^2/\text{g}$) after sample pretreatment in vacuum at increasing temperatures. I, isolated; G, geminal; V, vicinal; H, H-bonded (see section 2.2).

more distinct after outgassing; it has been assigned to isolated silanols (denoted I), not interacting through H-bonds. Several red-shifted broad components are observed in addition. They correspond to variously H-bonded silanols. The energy of the stretching vibration is more deeply affected when the O–H group acts as an H-bond donor, when it falls down to about 3520 cm^{-1} ; acting as an H-bond acceptor will cause a smaller perturbation, of a few tens per centimeter. It has been claimed that both fumed and precipitated silica surfaces exhibit a density of isolated silanols of about 1.1 nm^{-2} .¹¹⁵ Other studies, however, would indicate that the balance between isolated and H-bonded silanols is variable and depends on the geometry of the silica particles, and most notably on their size. Namely, the smaller particles have a lesser number of isolated silanols, presumably due to constraints imposed by surface curvature,¹¹⁶ whereas on fully hydrated particles with a diameter $>30 \text{ nm}$, only H-bonded silanols were observed.

Sometimes, more precise assignments of the “H-bonded silanol bands” have been proposed, but they remain open to question. Quantification of IR absorption results is at best relative: the evolution of the densities of a given type of surface silanol can be followed along a series of treatments, such as thermal activation or chemical functionalization, but an absolute quantification is difficult due to the high variability of extinction coefficients. In silicalite, which is a kind of microporous silica, several signals including a strong band at 3500 cm^{-1} and a shoulder at 3450 cm^{-1} were assigned to small groups of Si–OH mutually interacting in “silanol nests”.¹¹⁷ These could in principle form the basis for band assignments on silica (see a similar remark below for ^1H NMR results).

Further heating and outgassing at $T = 1073 \text{ K}$ entirely removes the H-bonded pairs leaving on the surface only terminal (isolated and geminal) silanols. IR alone, in contrast to ^{29}Si NMR (vide infra), cannot discriminate between terminal

and geminal (G) groups.^{118,119} Takei et al.¹²⁰ attempted to create *de novo* geminal groups (corresponding to Q² Si) as well as “triple silanols” –O–Si(OH)₃ (corresponding to Q¹ Si) by grafting of chlorosilanes on the silica surface followed by their hydrolysis; they concluded that the frequencies of such groups are within 2 and 3 cm⁻¹, respectively, of that of isolated terminal silanols (Q³ Si), which is too small a difference for ordinary spectrometers to resolve.

Silica also shows several diagnostic vibrations outside of the OH stretching range.¹²¹ The strong Si–O–Si stretching vibrations in the 1000–1200 cm⁻¹ range and the bending modes under 800 cm⁻¹ are usually ill-resolved and mostly due to bulk and not to surface groups. An exception can be found in thin silica films obtained by superficial oxidation of Si wafers, where all Si–O–Si groups belong to the surface region. These systems can be observed by a variant of IR spectroscopy, namely GA-ATR (grazing incidence attenuated total reflectance). The asymmetrical Si–O–Si stretch undergoes a phonon splitting between longitudinal optic (LO) and transverse optic (TO) components. It has been shown^{122,123} that in a thin SiO₂ film, the TO vibrations are parallel to the film surface while the LO vibrations are perpendicular to it. Both components can be observed in GA-ATR; the band at 1230 cm⁻¹ has been assigned to the LO mode and the band at 1045 cm⁻¹ to the corresponding TO mode.^{124–130}

More specific vibrational bands can also give information on siloxane ring sizes. Strained rings give rise to breathing modes conspicuous in Raman spectra, at 605–607 cm⁻¹ for 3-rings (S3R), known as D2 defects,^{131–133} and 490 cm⁻¹ for 4-rings (S4R, called D1 defects; the latter is more difficult to interpret due to the overlap with another band). The 4-rings are only slightly strained. As already mentioned in section 2, strained rings can be seen in freshly calcined silicas but exposure to water will break the siloxane (Si–O–Si) bond.¹³⁴ The energy gain provided by strain relief seems more than sufficient to cause dissociative chemisorption of water, at least in the case of S3R. This process has been quantified in a thorough study on heat-treated silica gels,¹³⁵ and indeed the disappearance of one D2 defect is accompanied by the appearance of two newly formed silanols. Conversely, heating at high temperatures causes silanol pairs to condense giving rise to strained ring defects.

The 3-rings and 4-rings are found in some little-known natural crystalline silicates, which may serve as references (quoted in ref 136).

Then there is the important question of 2-rings or S2R, which have been mentioned in section 2; S2R are especially important for the present review because they have given rise to many molecular modeling studies. Two bands at 888–891 and 908–910 cm⁻¹ had been observed to be present in silicas activated at high temperature (fortunately, they lie in a narrow transparent window in the silica spectrum, between Si–O–Si bending and stretching modes) and to disappear upon adsorption of Lewis bases or Lewis acids¹³⁷ (see below, section 3.1.7). Michalske and Bunker¹³⁸ hypothesized that they were specifically attributable to S2R (which they called “edge-shared defects”), and they were able to substantiate this claim by comparing with the vibrational spectra of molecular disiloxanes¹³⁹ (Figure 10).

Thus, an experimental basis was available for this assignment, which has first been made before the era of molecular modeling. Some attempts have been made to quantify S2R: Grabbe et al.¹⁴⁰ reported a figure of 0.2–0.4 nm⁻² on an Aerosil

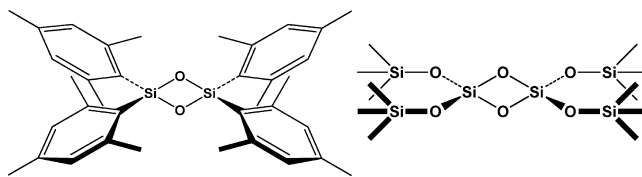


Figure 10. A molecular disiloxane (left) compared with the local structure of the S2R defect on the silica surface (right).

silica treated at 1075 °C. Of course, less harsh treatments are expected to generate a lower S2R concentration. Later, the IR bands typical of S2R were also observed on mesoporous silicas pretreated at 600 °C¹⁴¹ and silica thin films pretreated at 1130 °C in vacuo.¹⁴²

3.1.4. NIR, Visible, and UV. The NIR region contains overtones and combinations of stretching and bending modes involving OH groups of water and silanols. The most specific features associated with silica surface groups are bands at 4550 and 7310 cm⁻¹ (about 2200 and 1368 nm, respectively). The first one is a combination band ($\nu_{\text{OH}} + \delta_{\text{SiOH}}$), the second one is the 2 ν_{OH} harmonic.⁴⁰ The combination band in particular is useful because it can be observed even in the presence of adsorbed water, because it is energetically well separated from the ($\nu_{\text{OH}} + \delta_{\text{HOH}}$) combination of H₂O. It then shows two or three components that have been attributed to isolated silanols and H-bonded ones,⁴⁰ but some physicists still argue that the 4550 cm⁻¹ band has a more complex origin,¹⁴³ and this spectral region is not widely used to discriminate surface groups.

Silica is essentially transparent in the visible range and exhibits charge transfer bands in the UV (or band gap, depending on whether a localized or a delocalized bond description is adopted), like all solid oxides. It has been claimed¹⁴⁴ that the 50% UV cutoff wavelength can provide information on the distribution of siloxane ring sizes, but it is doubtful whether precise information can be obtained in this way.

3.1.5. Solid-State NMR. Since the first stages of its development, solid-state NMR has been a choice technique in the study of the local structure of silicates and silica polymorphs.⁷² Since ²⁹Si is a “good” nucleus for NMR because it has a 1/2 nuclear spin, it provides well-resolved spectra without the complications due to quadrupolar interactions, and ²⁹Si chemical shifts (δ) are highly sensitive to details of the molecular environment (for instance, a correlation between δ and the average Si–O–T angle was indicated early on). Thus, ²⁹Si NMR provides valuable information on the bulk structure. Whether it allows one to specifically observe surface groups depends first and foremost on the surface area: if this parameter is too low, surface-specific signals will be overwhelmed by bulk ones. For many amorphous silicas, the surface area reaches values on the order of several hundred square meters per gram, and in this case the proportion of total Si atoms that are exposed on the surface is high enough for their signal to stand out in the spectrum. Bulk Si all belong to Q⁴ tetrahedra and give rise to a broad signal centered at about -110 ppm. On the other hand, surface Si may belong to either Q², Q³, or Q⁴ tetrahedra, with maxima at about -90, -100, and -110 ppm, respectively, according to well-known assignments.¹⁴⁵ The signals are much broader than, for example, those in zeolites because of the large distribution of Si–O–Si angles, but they are well-resolved enough to allow unequivocal quantification (Figure 11). Now this quantification in terms of Qⁿ

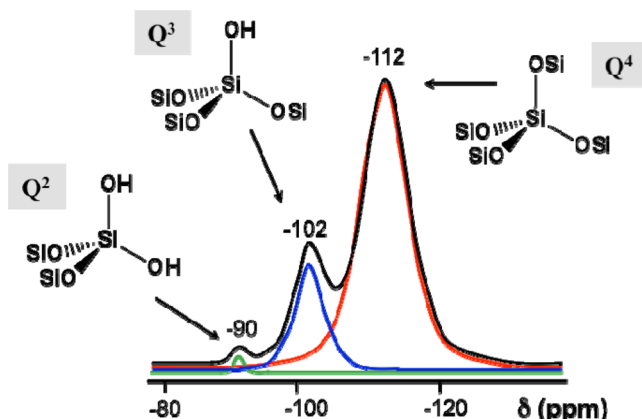


Figure 11. Typical (1-pulse) ^{29}Si MAS NMR spectrum of a fumed silica (PQ CS2040), with band assignments. Reprinted with permission from ref 146.

connectivity is correlated with the densities of the different types of silanol groups, since each Q^3 Si bears one terminal silanol, while each Q^2 Si bears two geminal ones. This is the most precise way of quantifying surface silanols, and the fact that it correlates well with the completely independent TG data as far as total silanol densities are concerned is encouraging.

Some authors have proposed that the Q^4 peak could be further decomposed into components corresponding to strained and unstrained rings, the former resonating at lower field, but since the hypothesized components of the Q^4 peak are never well resolved this probably cannot form the basis of a quantification of different size rings.

It is possible to selectively enhance the NMR signals of surface Si if desired. Detecting the ^{29}Si signals by proton cross-polarization ($\{\text{H}-^{29}\text{Si}\}$ CP) ensures that only those Si atoms in close vicinity of a proton will appear in the spectrum. Since the proton sources are silanols and adsorbed water molecules, this technique is surface-selective (it also has the advantage of being faster than single-pulse NMR); however, quantification of CP results is difficult since Si atoms in different environments will respond differently, according to the intensity of their coupling with protons, which determines the dynamics of polarization transfer. The most relevant data on this problem are summarized in ref 147, which proposes a CP quantification technique. Recently, an improvement in surface selectivity more spectacular than that observed with CP was shown using dynamic nuclear polarization (DNP), where a 100-fold enhancement of the surface ^{29}Si signals was observed for a mesoporous silica.¹⁴⁸ This technique involves contacting the sample with a small amount of radical-containing solution, which is not chemically innocuous, and it is too early to tell what impact it will have on the field.

^{17}O NMR data are much less frequent than ^{29}Si NMR because the natural abundance of the target isotope is lower, which makes it difficult to record spectra without isotopic enrichment. Natural abundance ^{17}O spectra were recorded for some silica polymorphs, notably in cristobalite at high temperature.¹⁴⁹ Potentially, signals specific for surface groups could be even more obvious than in ^{29}Si NMR, because the oxygen in a silanol lies in a very different environment from that in a siloxane bridge. A very different chemical shift is therefore expected and probably also a different quadrupole constant value (a parameter with no analogue for ^{29}Si , which determines the line shape). In addition, it may be possible to specifically

enrich the surface region by exchange with $^{17}\text{OH}_2$. ^{17}O spectra have indeed been recorded on 45% enriched sol–gel silicas,¹⁵⁰ but it turned out that the signals originating from silanol groups are difficult to detect due to very short relaxation times. Thus, ^{17}O NMR has not lived up to its promise so far.

^1H NMR is of course surface-selective because it “sees” silanol groups, which mostly exist on the surface. However the interpretation of spectra has been complicated by the difficulty to record solid-state NMR spectra on fully dried samples without exposure to room humidity. In most cases protons from adsorbed water molecules are interfering. This problem was specifically discussed in ref 151. On partially dehydrated silica surfaces, two main signals are generally observed.^{83,152} The first one at 1.8 ppm has been assigned to noninteracting silanols and progressively becomes prominent upon dehydration; some authors have hypothesized that these silanols are internal, but actually this is not necessary to explain the weak interaction with water. The second signal is observed in the 3–5 ppm range. As the surface is dehydrated, it becomes less intense and shifts to lower δ values. It has been assigned to the protons of silanols in fast exchange with water and therefore to the Si–OH that have the highest affinity for water, as will be mentioned in section 3.1.7, they correspond to H-bonded silanols. Thus, the situation is reminiscent of that observed by IR in the OH stretching region, with the ^1H NMR peak at 1.8 ppm evolving like the IR band at 3740 cm^{-1} . It must be underlined that both techniques are basically sensitive to the “isolated vs associated” silanols dichotomy, while ^{29}Si NMR provides information on the “terminal vs geminal” distribution.

Different protons may be distinguished on the basis of chemical shifts, but also of spin–spin and spin–lattice relaxation times.¹⁵² Dipolar dephasing experiments allowed Liu and Maciel to conclude that associated silanols are indeed strongly coupled to water but not isolated silanols.¹⁵³

Some advanced NMR techniques allow “spin counting”, that is, an evaluation of the number of nuclear spins present in an interacting network.¹⁵⁴ In the solid state, MQ (multiple-quantum) methods for spin counting have been developed since 1985.¹⁵⁵ On silica, proton MQ-NMR could be used in principle to count the number of silanols interacting in a “silanol cluster”. This technique has been applied to silica catalyst supports¹⁵⁶ but with rather trivial results, namely, that all ^1H spins exist in clusters of less than seven silanols. Yet it probably has some potential to identify silanol clusters, as shown by a study on high-silicic zeolite ZSM-12¹⁵⁷ where proton MQ-NMR revealed defects that were tentatively identified as three-silanol clusters.

Another intriguing possibility is 2-D spin–spin correlation, either between protons or between proton and ^{29}Si (HETCOR, heteronuclear correlation). These techniques have the potential to unravel neighboring relations between target nuclei in detail. They may provide an opportunity to overcome the “short-sightedness” of single-pulse NMR and other spectroscopic methods. In their study focused on MCM-41 mesoporous silica,⁸³ Trébosc et al. were led to propose various arrangements involving surface silanols and water molecules bound together by a well-defined lattice of H-bonds. Although their data were not sufficiently precise to discriminate among these arrangements, providing evidence for such structures is an attainable goal for future research.

3.1.6. Paramagnetic Sites: EPR and Related Techniques. In principle, this review is not concerned with high-temperature defects, which are quenched by exposure to water,

as stated in section 2.2. The question is of course exactly what defects are completely healed, and while silanone groups for instance are rarely claimed to play an important role in silica reactivity, there is abundant evidence that some radical defects are an essential feature in determining the biotoxicity especially of crystalline silica samples such as quartz and cristobalite.¹⁵⁸ A few words should therefore be said on these radical defects, which can be generated by cleavage of a macroscopic crystal, photochemically¹⁵⁹ or mecanochemically (by grinding of a powder), especially since they represent a challenge for molecular modeling and are therefore discussed to a small extent in sections 5.2 and 6.1.

Since they have unpaired electrons, they should be easily observable by EPR (electron paramagnetic resonance, or ESR, electron spin resonance). This technique allows quantifying paramagnetic defects, and can also give qualitative information from the line shape: signal anisotropy and hyperfine splitting constant (A) allow identification of the chemical nature of the paramagnetic center. Hyperfine splitting can yield valuable information on coupling with neighboring ^{17}O and ^{29}Si .^{160,161} For instance, hyperfine splittings were correlated with Si—O—Si in a recent study.¹⁶²

Simple (cw, continuous-wave) EPR is most frequently used. More advanced techniques such as pulsed EPR¹⁶³ or ESEEM (electron spin–echo envelope modulation)¹⁶⁴ have occasionally been applied.

Many radical defects exist and have received names based on their luminescence and optical properties. The most relevant ones for the adsorption of biomolecules correspond to $\equiv\text{Si}-\text{O}^\bullet$, $\equiv\text{Si}^\bullet$, peroxides, and species derived from interaction of the latter with dioxygen, belonging to the infamous ROS (reactive oxygen species). The formation of ROS is one consequence of the high reactivity of surface radical species. They are also reactive toward probe molecules and biomolecules themselves, which is the basis for indirect characterization techniques such as spin trapping and SDSL (site-directed spin labeling), which are mentioned in the review by Fenoglio et al.¹⁶⁵

As regards noncrystalline silicas, Inaki et al.¹⁴¹ have observed the EPR spectrum of mesoporous silicas activated at high temperatures in the frame of a study of surface sites active for photometathesis. They interpreted them as stemming from ($\equiv\text{Si}-\text{O}^\bullet$) defects. They only made use of the quantitative evolution of the signal intensity, without analyzing the signal line shape. It should be noted that their work led them to promote an unorthodox assignment of the IR bands at 890 and 910 cm^{-1} , mentioned in section 3.2.4 and generally attributed to S2R; in their view they can also be attributed to ($\equiv\text{Si}-\text{O}^\bullet$).

Mesoporous SBA-15 was also investigated by SQUID magnetometry¹⁶⁶ and found to exhibit a weak hysteresis at 2 K, indicative of ferromagnetic behavior. This was interpreted as due to the formation of ($\equiv\text{Si}-\text{O}^\bullet$) or ($\equiv\text{Si}^\bullet$) defects during the calcination step.

3.1.7. Adsorption of Probe Molecules. The present review exclusively focuses on the interaction between silica and biomolecules and does not intend to provide a general view of adsorption on silica. However, some adsorption studies are specifically aimed at identifying surface sites and probe molecule adsorption can be said to constitute a surface characterization technique in its own respect. Many important details about the structure of silica “surface active sites” have been obtained chiefly or exclusively from these studies; furthermore, they can form a basis for the interpretation of

the more complex phenomena resulting from the adsorption of biomolecules.

A probe molecule must have some kind of interactional complementarity with a certain type of surface site, giving rise to site adsorption. The data may be purely macroscopic: at least they must provide quantification of the amount of considered sites, either by volumetry of the adsorbed molecules from the gas phase or by thermal desorption following the adsorption step; they may also include an estimate of thermodynamic parameters, by calorimetry or from the temperatures of desorption, and in many cases they are complemented by spectroscopic information, providing a molecular-level view of the probe/site interaction. The spectroscopic technique of choice is generally IR.

In view of the importance of the problem for heterogeneous catalysis,¹⁶⁷ the most common use of probe molecules is to titrate Brønsted acidic sites (also known as Brønsted acidic centers, BACs), and in that case they must of course be Brønsted bases. Pure silica does not have strong Brønsted acidity. It adsorbs NH_3 by H-bond formation, without protonation.^{168,169} CO is another probe molecule that forms H-bonds with BACs, resulting in a blue shift of the ν_{CO} stretching band proportional to the acid strength, and it also reveals only weakly acidic sites. As CO is adsorbed, the OH stretching band of isolated silanols undergoes a -79 cm^{-1} red shift,¹⁷⁰ and they are therefore considered to be the adsorption sites.

Interestingly, comparing silicas with different thermal treatments showed that NH_3 preferentially adsorbs on H-bonded rather than on isolated silanols.¹¹⁷

Pyridine (Py) has been systematically used for many years as a probe of surface acidity for oxides of catalytic interest (e.g., refs 171 and 172), because adsorbed pyridine has several IR bands whose wavenumber is highly responsive to the adsorption mechanism: one can discriminate at the very least between H-bonded Py, Py interacting with BACs, and Py interacting with LACs (Lewis acidic centers). It was actually first observed by Morrow and Cody¹³⁷ that pyridine binds reversibly to LACs on the surface of silica activated at rather high temperatures, and the nature of these LACs can even be surmised, in fact, the silica bands of “strained siloxane bridges”, which were later attributed to S2R (cf. section 3.1.4) decrease upon pyridine adsorption. It has been hypothesized that in S2R sites the (SiO_4) tetrahedra are strained enough that a Si atom can make an additional bond to the doublet of pyridine (Figure 12).

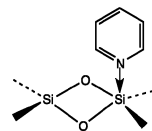


Figure 12. Pyridine bound by a coordinative bond to a S2R site.

Water is an intriguing molecule whose interaction with silica surfaces plays a key role for many applications including biomolecule adsorption. Since this will be the topic of section 8, there is no need to be exhaustive here. There are very precise works combining water adsorption volumetry and microcalorimetry, which provide information on the molar adsorption enthalpy for different silica surfaces.^{81,82,173} An (absolute) value of the molar adsorption enthalpy in excess of the latent heat of liquefaction of water (44 kJ mol^{-1}) indicates a

specific interaction with the silica surface. In practice, values as high as 170 kJ mol⁻¹ have been reported. These data are further discussed in section 8.1. By combining adsorption isotherms with IR, it is shown that the sites having strong affinity for water, in other words the hydrophilic sites, consist in patches of H-bonded silanols; isolated silanols are not hydrophilic⁴⁰ (the same was observed for NH₃ adsorption, see above). This may sound paradoxical in view of their better accessibility to molecules coming from the gas phase. One must realize however that at least the terminal members in a cluster of H-bonded silanols will become a stronger H-bond donor by cooperative effects.

At room temperature, water physisorption by H-bonding occurs immediately. Hydrolysis of strained bonds, which results in water chemisorption, has both fast and very slow components. They probably correspond, respectively, to the opening of highly strained S2R and of somewhat larger rings.

Alcohols share with water the presence of an X—OH moiety. Methanol was one of the first molecules whose adsorption on silica was studied by volumetry, calorimetry, and IR.^{174,175} Like water, it can be physisorbed at room temperature by H-bonding but also opens up strained siloxane rings, yielding easily recognizable methoxy groups (the corresponding reaction has also been reported with ethanol).^{176,177} It is interesting to note that in the latter study, the cooperative effect of several H-bonds resulted in rather strong adsorption, with adsorption enthalpies in the 78–100 kJ mol⁻¹ range.

The slow chemisorption by siloxane ring-opening in S2R involving water or alcohol decomposition can be represented as shown in Figure 13.^{139,178}

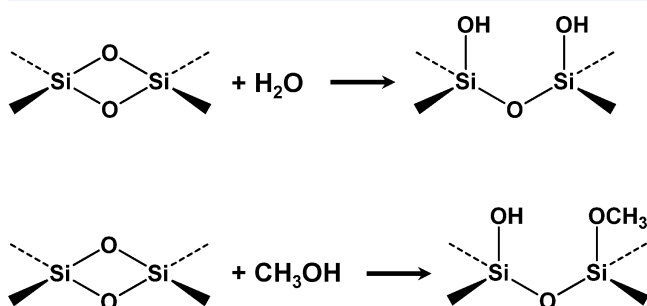
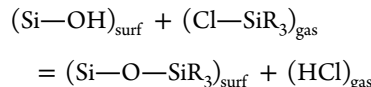


Figure 13. Opening a S2R defect with water (upper) or methanol (lower).

This could in principle happen on other siloxanes, but the dissociation of S2R siloxanes is 5 orders of magnitude faster than that of unstrained siloxanes.¹⁷⁸

Aldehyde, ester, and ketone adsorption was followed by calorimetry and IR spectroscopy, demonstrating H-bond formation with surface silanols: it was reported that upon acceptance of H-bond(s) from silanols, the C=O stretching vibration of these molecules could be weakened by several tens cm⁻¹ (as high as 80 cm⁻¹ in some cases),¹⁷⁹ which provides a point of comparison for similar studies on biomolecules.

There are a huge number of studies aiming at the modification of silica surfaces through grafting of silanes bearing organic functionalities, or of functional groups based on other metal centers such as titanium isopropoxide. Grafting is a form of chemisorption since it involves the formation of covalent bonds, most often with surface silanols, for example,



While we are not concerned in this review with the hybrid materials surfaces formed through these procedures, it has been suggested that grafting, as a selective reaction, might be used to obtain information on the specific groups exposed by the starting silica surface. In one study, it was shown that PTMS (propyltrimethoxysilane) preferably reacts with the hydrophobic regions of a mesoporous silica surface, namely those containing only siloxanes and isolated silanols.¹⁸⁰ Conversely, it seems that Ti isopropoxide grafting preferentially occurs on H-bonded rather than isolated SiOH;¹⁸¹ interestingly, to prove the latter point, the authors made use of two silicas, a Stöber microspheric silica, which has no isolated silanols, and an Aerosil where previous treatment by Si(CH₃)₂Cl₂ had selectively deactivated the isolated silanols, like in the previous case.

One should not be surprised if some grafting agents exhibited a more stringent selectivity toward silica surface sites than simply preferring isolated vs H-bonded or vice versa. Early on, it was suggested that terminal and geminal silanols may have different reactivities, for instance, toward tetramethylsilane (TMS) grafting.¹⁸² In fact, claims of high specificity may be found in the old literature: some Russian workers¹⁸³ used VOCl₃ grafting to titrate groups of two and of three neighboring silanols. They claimed to be able to separately monitor the evolution of monografted, digrafted, and trigrafted V centers, which followed a logical trend as a function of the total silanol density. Unfortunately this line of thought has not been pursued any further.

Recently, however, interesting data were obtained by grafting of Ga(CH₃)₃ from the gas phase on an Aerosil and a mesoporous silica previously heated at 800 °C.¹⁸⁴ The investigators deduced from a precise analysis of Ga K-edge EXAFS (extended X-ray absorption fine structure) that gallium atoms were preferentially grafted in pairs, these pairs being connected by two bridging silanolate groups. Integrating these results with bulk mass balance data on the adsorbed Ga and the methane molecules emitted upon grafting yielded an interesting model of the adsorption site, which would consist of a S2R bearing an additional silanol group, the so-called “d³ site” (Figure 14):

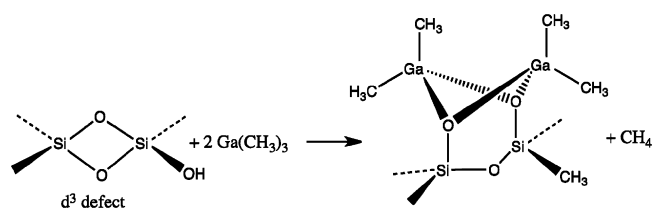


Figure 14. How the reactivity of dimethylgallium provides evidence for the existence of “d³ defects” (S2R bearing one OH group) on the silica surface, according to ref 184.

If unequivocal evidence of d³ defects is confirmed, experimental results would be significant, because it would constitute a step toward the identification of surface defects with more complicated structures, combining several functionalities. Note that the d³ defects would probably be formed at high temperatures from the condensation of Q²—Q³ vicinal silanol pairs (Figure 15).

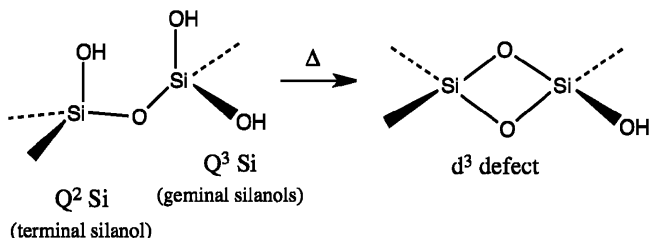


Figure 15. Formation of a “d³ defect” through high temperature silanol condensation.

It can be inferred from the data that there would be about 0.51 such sites per square nanometer on the surface of Aerosil 380.

All of the above results refer to adsorption of probe molecules from the gas phase. Adsorption from aqueous solutions could also help identify specific adsorption sites.

Attempts have been made to dose “completely isolated” silanols through the adsorption of a bulky molecule, CV or crystal violet.¹⁸⁵ A strong adsorption was assigned to CV cations lying flat on the silica surface, electrostatically bound to a silanolate and unimpaired by interaction with other silanols or silanolates. Since one CV molecule occupies an area of 120 Å², this means that CV would dose silanols that are separated by more than 10 Å from their nearest neighbors, and there are about 0.11 of them per square nanometer. This figure may be compared with the value mentioned above for isolated silanol densities, defined as those lying too far apart from other silanols to interact by H-bonding, which is about 10 times higher.

In a study of Ni^{II} complex adsorption (these are significant as precursors of supported catalysts), Boujday et al.^{186,187} measured adsorption isotherms for several polyamine-aqua complexes and observed well-defined and different saturation coverages, which were rationalized by postulating cooperative adsorption sites consisting of 1–3 silanols able to act as ligands to the metal ion, together with H-bond accepting groups in close vicinity.

3.1.8. IRAS, STM, LEED: “Flat” Silica Surfaces. Thin silica films have been grown on metal single crystal surfaces as model systems for studying the structural properties of SiO₂, providing access to surface science techniques such as IRAS (infrared reflection attenuation spectroscopy), STM (scanning tunneling microscopy), LEED (low-energy electron diffraction), etc. Mo(112),^{188–190} Ru(0001), and Pt(111)¹⁹¹ have been used as substrates for this purpose, and thin “silica” films were prepared by gas-phase Si deposition followed by oxidation. It can be questioned whether these surfaces are really comparable with those of pristine silicas because they are often only a few layers thick and thus strongly influenced by the substrate so that even the stoichiometry may significantly differ from SiO₂. However, spectacular results have recently been obtained for two-layer thick SiO_x films on Ru(0001)²⁹ where STM allowed for the first time visualization in real space the (SiO)_n rings that were so far only indirectly postulated, and thus obtainment of experimental histograms of ring size distribution.

On silicon wafers, SiO_x films can be developed by high-temperature oxidation in an oven but also by “wet” methods involving superficial oxidation, for example, by “piranha” treatment¹²⁸ and observed by ordinary FTIR (Si can be obtained in transparent form) or reflection attenuation IR, ellipsometry, contact angle,¹⁹² and SIMS (secondary ions mass spectroscopy).^{193,194} Work comparing SIMS and XPS and

using chemical derivatization has shown that the *m/e* = 45 (SiOH⁺) SIMS peak may be used to quantify total silanol surface densities, which was thus measured at 2.6 nm⁻² in ref 194. Reflection attenuation IR also allowed observation of S2R sites.¹⁴²

SiO_x films on silicon can grow up to at least 1 μm thick while still allowing the use of surface techniques such as specular X-ray reflectivity and SANS (small-angle neutron scattering),¹⁹⁵ and this would be expected to remove the structural influence of the substrate. Here again though, there are indications that the surface of these films may have properties substantially different from that of divided silica. SIMS and XPS Si 2p spectra¹⁹⁶ of films with 25 nm thickness indicate a significant amount of Si atoms surrounded by less than four oxygens, and they apparently do not belong to the deeply buried SiO_x/Si interface since both techniques are surface-sensitive. The reactivity of these systems also has peculiarities; for instance, SiO_x/Si was much more reactive toward methanol at RT than a mesoporous silica because decomposition reactions were observed instead of simple adsorption.¹⁹² In the same way, contacting ethanol with thin films surfaces resulted in the formation of acetaldehyde and ethylene,¹⁹⁴ which is quite unexpected based on the reactivity of divided silica. Thus, it is possible that flat SiO_x films present surfaces quite different from divided silicas; at the very least, more work is needed to obtain “normalized” silica adlayers.

3.1.9. Use of Molecular Analogues of Silica Surface Groups. We have already mentioned the role of cyclo-diloxanes in validating the existence of S2R defects on the silica surface. In fact organometallic chemists have synthesized a large variety of molecular compounds containing siloxane or silanol groups in well-defined geometries. Many of them could serve as molecular analogues of postulated silica surface groups (see ref 197 for a good review). This line of thought has indeed been explored, but mostly in the field of catalysis, to obtain analogues of silica-supported metal catalysts that are more uniform and energetically homogeneous (“homogeneous mimics”), especially from the silsesquioxane family of compounds^{198,199} (Figure 16). The similitude with surface

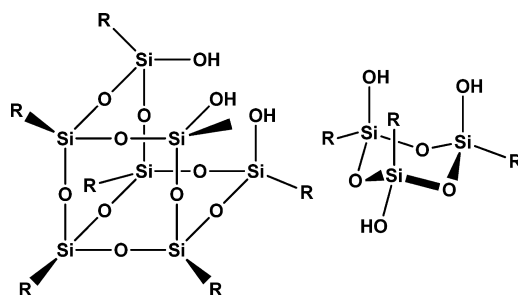


Figure 16. (left) A silsesquioxane bearing a group of three silanols in close vicinity and (right) a cyclotrisiloxane that could be used as a molecular mimic of a three-ring.

groups of silica, especially as regards the vibrational properties of silanols in well-defined environments, is sometimes put forward.²⁰⁰ It must be recognized however that in other respects, such as reactivity and ²⁹Si NMR spectroscopy, the existence of Si—C bonds in the silsesquioxane, as opposed to the all-Si—O environment on the surface of silica, will lead to very different properties.

Table 1. Most Significant Experimental Studies of Small Biomolecule/Silica Adsorption, Indicating the Main Techniques Used and Results in Each Case

oxide mineral	biomolecules	from gas or solution	main results or techniques used	ref
SiO ₂	Ala, Gly, Ile, Leu, Met, Phe, Val	G	IR	241
SiO ₂	Val, Gly, Ala, Leu, Ile, Pro, Phe, Met, Thr, Trp	G	analysis of organic products after desorption, condensation and analysis of gaseous products	242
SiO ₂	(Gly) ₂ , Gly-Ala, Gly-Leu, Gly-Val, Ala-Ala, Val-Val	G	condensation and analysis of gaseous products	222
SiO ₂	(Gly) ₂ , Ala-Ala, Leu-Leu, Val-Val, Pro-Pro	G	condensation and analysis of gaseous products	243
divided SiO ₂ (Aerosil380)	Gly	G	IR	223
SiO ₂ (quartz) single crystals	Ala, Asp, Glu, Gly, Leu, Lys, Tyr	S	AFM (atomic force microscopy)	105
fused silica prism	Asp, Glu, Phe	S	SFG	218
divided SiO ₂	pyroglutamic acid	S	IR	221
divided SiO ₂ (chromatographic)	dipeptides, cyclic and linear	S	free energies of adsorption	242
divided SiO ₂ (chromatographic)	AA, peptides, Krebs' cycle molecules, nucleosides, nucleotides	S	free energies of adsorption	244
divided SiO ₂ (chromatographic)	Ala, Asn, Asp, Cys, Gln, Glu, Gly, Ile, Leu, Met, Phe, Pro, Ser, Tyr, Thr, Trp, Val	S	free energies of adsorption	216
divided SiO ₂ (chromatographic)	Ala, Asn, Asp, Cys, Gln, Glu, Gly, Ser, Tyr, Thr, Trp, Val	S	free energies of adsorption	207
SiO ₂	Gly, (Gly) ₂	S	wetting-and-drying cycles	245
SiO ₂	Ala (Ala + Gly) (Ala + (Gly) ₂) (Ala + DKP)	S	wetting-and-drying cycles	245
SiO ₂	Gly, Ala, Pro, Val, Leu (Ala + Gly), (Ala + (Gly) ₂) (Pro + Gly) (Pro + (Gly) ₂) (Val + Gly) (Val + (Gly) ₂) (Leu + Gly) (Leu + (Gly) ₂) (Ala + Pro), (Ala + Val)	S	wetting-and-drying cycles	246
divided SiO ₂ (Aerosil 380)	Gly	S	IR, macroscopic data	210
divided SiO ₂ (Kalush A-300)	Arg, His, Lys	S	macroscopic modeling of adsorption data	214
divided SiO ₂ (Aerosil 380)	Gly, Lys	S	IR, macroscopic data	247
modified SiO ₂	Gly, Leu, His, Lys	S	adsorption isotherms	248
glass, hydrophilic and hydrophobic	Leu, Ser	S	isotopic labeling	249
divided SiO ₂ (Kalush A-300)	Ala, Leu, Phe, Trp, Tyr, Val, coadsorption with Cu ²⁺	S	macroscopic data, adsorption isotherms	250
"chromatographic grade" divided SiO ₂ (SRL)	His, Trp	S	adsorption isotherms, macroscopic modeling	251
mesoporous SiO ₂ MCM-41	(Ala) ₄	S	deuterium NMR	252
mesoporous SiO ₂ MCM-41	Lys	S	adsorption isotherms, macroscopic modeling	215
mesoporous SiO ₂ SBA-15	Phe, Glu, Arg, Leu, Ala	S	adsorption isotherms, effect of pH, ion strength	253
divided SiO ₂ , 615 m ² /g (Wakosil 25SIL)	Lys	S	ATR	217
mesoporous SiO ₂ MCM-41 and SBA15	Ala	S	² H NMR on deuterated molecules	225
mesoporous SiO ₂ SBA15	Met (and Ala-Ala)	S	¹ H and ² H MAS NM	226
mesoporous SiO ₂ SBA-15	Ala	S	NMR: SLF and REDOR	227
mesoporous SiO ₂ SBA-15	Gly	S	NMR: REDOR, TEDOR, SLF, 2D-HETCOR	228
mesoporous SiO ₂ , AA-templated	Pro, Ile, Val, Leu, Hyp, Phg	S	macroscopic adsorption data	254
mesoporous SiO ₂ , AA-templated	L-Pro, D-Pro	S	adsorption isotherms	255
mesoporous organosilica	Gly, Lys, Ile	S	adsorption isotherms, effect of pH	256
mesoporous SiO ₂ thin layers on silicon (111) wafers	Trp (and proteins)	S	adsorption isotherms	257
	adenine	S	XPS, NEXAFS	258

3.1.10. Silica in Aqueous Solutions: Existence of a Modified Water Region. Physical chemists have long realized that inorganic oxide surfaces are able to induce dramatic changes in the structure of water (ref 201; this is a capability that they share with large biomolecules, incidentally). In the presence of silica, ^1H NMR relaxation times were used to evidence surface-induced water structures characterized by a preferred spatial orientation of the water molecules and a lower molecular density (compared with bulk water).²⁰² These surface-induced structures extend at least 8 nm from the surface. It follows that for a suspension of divided silica with a surface area in the range of several hundred meters squared per gram, the amount of modified water will represent several times the weight of the silica. In fact, it is easy to observe that colloidal silica suspensions tend to form gels when the weight concentration of SiO_2 exceeds about 10% by weight. This has undesired consequences when one tries to study the adsorption of biomolecules, or any molecules for that matter, on divided silica from an aqueous phase. It will not be possible to obtain the pure solid phase by ordinary separation techniques such as filtering or centrifugation: instead, it will retain a large amount of solution, containing dissolved molecules that do not directly interact with the surface. If the resulting gel is dried, these molecules will either precipitate as bulk compounds or establish new interactions with the dry surface, and they will interfere with the molecules that were already adsorbed at the solid/solution interface.

3.2. Adsorption of Biomolecules on Silica

A highly commendable short monograph on the subject is the one of Basiuk,²⁰³ which asks many of the right questions especially concerning the biomolecule adsorption mechanisms. Other relevant data can be found in several more general reviews, such as Parida et al.²⁰⁴ (small organic molecules on silica, including some biomolecules), Lambert²⁰⁵ (amino acids on divided oxides, written in a prebiotic perspective), or Fenoglio et al.¹⁶⁵ (interaction of biomacromolecules with inorganic surfaces).

There are many experimental results from the fields of controlled release/controlled delivery,²⁰⁶ chromatography,²⁰⁷ biosensors and biocatalysts,²⁰⁸ and immobilized enzymes.²⁰⁹ Here, as for bare silica surfaces (subsection 3.1), we will first discuss the different techniques that have been used to study the interaction of small biomolecules with silica and the type of information each one is able to provide; more specific experimental results are discussed in section 9, together with relevant molecular modeling studies. We will also give a (hopefully) exhaustive list of the research papers that have been devoted to the most frequently studied systems, namely, amino acids on silica.

3.2.1. X-ray Diffraction. Molecules adsorbed on divided silica, or on divided matter in general, do not in principle give rise to diffraction patterns because the surface of the particles has no three-dimensional periodicity; this is actually one great difficulty of adsorbed species characterization. However, performing XRD on biomolecule/divided silica systems is useful at least in a negative way. The amount of biomolecules that can establish a specific interaction with a silica surface is limited and *a priori* unknown. If the deposition procedure results in retaining a larger amount, excess biomolecules will probably form three-dimensional crystals. It is necessary to be aware of that if one wishes to interpret correctly the results of other characterization techniques. For instance, bulk amino acid

crystals were evidenced both in glycine/ SiO_2 ²¹⁰ and glutamic acid/ SiO_2 .²¹¹ An interesting phenomenon that will be discussed in section 9.1.1.2 is that in the case of glycine, excess glycine precipitated as the metastable β polymorph, while the α form is normally observed upon precipitation from a clean solution.

In contrast to XRD, LEED (low-energy electron diffraction) is a surface-specific diffraction technique that can only be applied to single crystal surfaces. It is possible to obtain LEED results on crystalline SiO_2 surfaces, notably quartz,²¹² but this is technically difficult. So far, this technique has not been applied to biomolecules on crystalline silica, although on other substrates such as copper it provides unique information, for example, on the formation of chiral structures²¹³ (see also section 3.2.5).

3.2.2. Bulk Adsorption Data: Geochemical Models and Adsorption Enthalpies. Geochemists have long developed models of adsorption on oxide surfaces from aqueous solutions, such as the double layer and triple layer models. They are most often used to rationalize metal ions adsorption but can be applied to biomolecules as well. The decrease of amino acid concentration in the solution upon contact with, for example, a divided silica is measured by spectrophotometry or HPLC. The evolution of adsorbed quantities as a function of pH and ion strength can then allow identification of the adsorption mechanism, either physisorption (through H-bond or electrostatics) or chemisorption (grafting). In this way, Vlasova and Golovkova²¹⁴ proposed for basic amino acids (arginine, histidine, lysine, and ornithine) the formation of outer-sphere complexes with silanolates, $\text{Si}=\text{O}^-(\text{H}_2\text{X})^+$, where X denotes the deprotonated form of the amino acid. In a mesoporous silica, the adsorption of lysine was through a combination of electrostatic and outer-sphere $\text{Si}=\text{O}^-(\text{H}_2\text{Lys})^+$ complex formation.²¹⁵

The measurement of adsorption isotherms (adsorbed amount vs activity in solution, at constant pH and ion strength) can yield interesting information. If they can be fitted by a Langmuir model (single site adsorption without lateral interaction), two parameters can be extracted from the isotherm, namely, the saturation coverage, which is equal to the surface density of adsorption sites, and the adsorption equilibrium constant, K_{ads} , which gives access to the adsorption thermodynamics; if isotherms are recorded at different temperatures, the entropic and enthalpic parts can be unraveled by plotting $\ln(K_{\text{ads}})$ against $1/T$ (van't Hoff plot). Adsorption isotherms are sometimes recorded (see examples in Table 1), but unfortunately their discussion often remains trivial. Neither are there good instances of the application of other model isotherms, such as the FFG (Frumkin–Fowler–Guggenheim) model, which might account for the site adsorption of positively or negatively charged amino acids accumulating charge on the surface.

Thermodynamic data on biomolecule adsorption reactions have been obtained at the silica–water interface however. This was done with the aim to predict separative properties of silicas or modified silicas as chromatographic phases: the retention times of different adsorbates are directly related to the corresponding K_{ads} values. Free energies of adsorption were estimated by Basiuk^{207,216} for most amino acids and some oligopeptides on a (bare) chromatographic silica. For monomeric amino acids, they are almost always positive (0 to +4 kJ mol⁻¹) and a compensation effect is observed between $\Delta_{\text{ads}}H^\circ$ and $\Delta_{\text{ads}}S^\circ$:²¹⁶ while the adsorption of most amino acids is exothermic, the entropic contribution is unfavorable. As

longer oligopeptides are tested, adsorption becomes more and more favorable. For some series of chemically similar amino acids, a linear correlation of $\Delta_{\text{ads}}H^\circ$ with the number of carbon atoms was observed, which draws the attention to the possible role of dispersion interactions (see section 5.3).

3.2.3. Vibrational Spectroscopies. Most biomolecules have functional groups with a conspicuous IR signature. However, since they normally represent a minority component in biomolecule/silica systems, only those that fall in a range where the silica support is transparent will be observable. This includes C=O stretching and NH₂/NH₃⁺ bending vibrations that are present in all amino acids and amide ($-\text{CO}-\text{NH}-$) bands of peptides and proteins. OH and NH stretching vibrations are also observable if the surface is dehydrated (otherwise they are lost in the broad background of water OH stretching). Conventional transmission IR spectroscopy has indeed been applied to several amino acid/silica systems in the dry state (see Table 1). Technical developments also allow observation of *in situ* vibrational spectra of amino acids at the aqueous solution/silica interface by ATR^{211,217} or, for interfaces with planar silica, by SFG.²¹⁸ This is extremely important in view of the importance of water in defining the amino acid–surface interaction, a point that will be discussed in section 9.1.1: the application of a drying step is very likely to modify the state of the adsorbed amino acids.

Raman spectroscopy does not seem to have been applied to amino acids on silica. Surface-enhanced Raman scattering (SERS) depends on a resonance with electronic plasma oscillation and is not applicable on silica in principle. IRAS, which is adapted to planar reflecting surfaces (e.g., ref 219 for glycine on Cu), would be applicable to SiO₂ thin films deposited on substrates such as Mo (see section 3.1.3), but it has not been applied so far to biomolecule adsorption; neither has GA-ATR.

On flat surfaces of fused silica, SFG has recently been used in the hope of detecting amino acids at the silica–solution interface.^{218,220} The results are still limited as regards the amino acid itself, but the advantage is that this technique allows water in the interfacial region to be observed *in situ* as well during the adsorption phenomenon.²²⁰

Vibrational spectroscopy gives unequivocal results as regards the protonation state of the amino acid because $-\text{COO}^-$ is rather easily distinguished from $-\text{COOH}$ and NH₂ from NH₃⁺. It would be expected that it also would provide information on the adsorption mechanism, since even rather weak bonding with a functional group will affect its characteristic vibrations (cf. section 3.1.7). In fact, early studies on amino acid adsorption on silica from the gas phase observed important shifts of the carbonyl band, which were interpreted, after similar studies on kaolin clays,²²¹ as meaning that the carboxylic acid terminal had condensed with surface silanols to give what was variously referred to as “anhydride with surface hydroxyl groups”, “surface acyl”, or “surface ester”, Si–O–CO–CH_(NH₂)–R. It is in fact difficult to reach a definite conclusion from IR only, and the conditions of possible formation of such covalently grafted species constitute a testing ground for molecular modeling studies, of which more will be said later. We shall note here that according to Basiuk et al., they only form on thoroughly dehydrated surfaces and may be destroyed when these surfaces are reexposed to water.²²² In other studies, shifts in the $-\text{NH}_x$ and CO bands were interpreted as indicative of H-bond formation with the surface.^{210,223}

3.2.4. NMR Techniques. Biomolecules contain several nuclei amenable to NMR study, the most important of which is ¹³C. ¹H, ²H, and ¹⁵N might also be useful. Multinuclear NMR is a workhorse of organic chemistry, and one benefits from a considerable amount of accumulated data to help interpretations, although solid-state NMR spectra are considerably less well-resolved than those of solutions. Despite this, the application of solid-state NMR to understand biomolecule adsorption on silica is recent.^{211,224–228} This is due to the low intrinsic sensitivity of the ¹³C nucleus. In conjunction with the fact that the biomolecule is a minority species in the samples, it causes NMR signals to be very weak, so that long accumulation times are necessary, unless one uses expensive isotopically enriched biomolecules. The rewards are high however because the ¹³C isotropic shifts are very sensitive to the molecular environment: for instance, it has been demonstrated that the C=O signal position responds in a predictable way to the different H-bonding states of Hgly[±] zwitterions in the three polymorphs α -, β -, and γ -glycine,²²⁹ and for glycine/Aerosil, a specific signal was attributed to glycine zwitterions adsorbed by H-bonding.²²⁴ A word of caution is in order again about the difficulty in quantifying ¹³C{¹H} CP spectra (since one-pulse acquisition of ¹³C spectra would be very slow). If the adsorbed biomolecule is highly mobile, its CP signal may be totally undetectable.

However the potential of NMR techniques goes beyond chemical identification through chemical shifts, as underlined by Ben Shir et al.²²⁸ These authors used REDOR (rotationally enhanced double resonance) NMR to demonstrate neighboring relations between nuclei from the biomolecule and those from the silica surface. More precisely, the joint use of ²⁹Si{¹⁵N} and ¹⁵N{²⁹Si} REDOR revealed intermolecular interactions between the ammonium group of alanine adsorbed on mesoporous silica and three to four predominantly Q³ surface Si species, and N–Si distances could even be evaluated.²²⁷ In addition, ¹⁵N{¹³C} REDOR provided information on the state of mobility of adsorbed alanine as a function of temperature, allowing discrimination between immobile and rapidly reorientating alanine populations. Later on, for the related glycine/mesoporous silica system, the same techniques were applied together with HETCOR, a 2-D NMR technique already mentioned for bare silica surfaces in section 3.1.5; ¹H{¹³C}, ¹H{¹⁵N}, and ¹³C{¹⁵N} HETCOR were investigated here in addition to ¹H{²⁹Si}, giving access to the corresponding neighboring relations. Here too, two immobile and one freely reorienting glycine populations were demonstrated.

The mobility of the functional groups of adsorbed amino acids is an important question, because it will indicate what groups, if any, are strongly bound with the surface. Amitay-Rosen et al.²²⁵ used deuterium line shape analysis (or rather, for samples rotating at the magic angle, sidebands analysis) of CH₃-deuterated alanine on mesoporous silica, in comparison with ¹H spectra. They rationalized their observations on the basis of a two-site exchange model. Although their conclusions were not fully compatible with those of Ben Shir et al. on the same system, this may be due to a different hydration state.

Despite these divergences, the studies just mentioned represent a breakthrough in that they started investigating dynamic processes in adsorbed biomolecules systems instead of providing a static picture; the very strong dependence of the adsorption behavior upon the hydration state of the surface revealed in this way and the experimental determination of new

observables such as dipolar coupling strengths represent new challenges for molecular modeling.

For adsorbed peptides, NMR can provide rich structural information. Advanced NMR techniques have long been applied to the in-depth study of proteins and peptides, and they can be transferred to peptides on surfaces despite the additional complexities induced by working in the solid state or in suspensions. Thus, 2-D NOESY (two-dimensional nuclear Overhauser) experiments based on through-space spin–spin coupling can reveal spatial relations between the different residues of a peptide chain. Mirau et al.²³⁰ have applied 2-D NOESY to suspensions containing fumed silica particles and specific SiO₂-binding peptides. By use of programs making use of distance constraints to determine peptide conformations, they could propose structural models of several peptides adsorbed on silica, which contained common structural elements. As seen in Figure 17, these common elements were

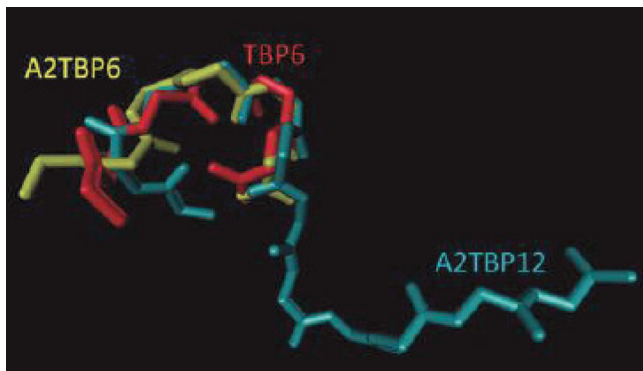


Figure 17. Secondary structures adopted by three related peptides adsorbed on silica. Reprinted with permission from ref 230. Copyright 2011 American Chemical Society.

observed to fold in very similar ways on the surface, which is a strong argument in favor of the reliability of the results. Note however that the techniques used provide exquisitely detailed information on the adsorbed peptide, but none at all on the silica surface, which appears as a featureless background.

3.2.5. Flat Surface Techniques. As for bare silica surfaces, one is limited by the nonconducting nature of SiO₂. Thus, in keeping with remarks in section 3.2.1, LEED would be very hard to apply to adsorption on crystalline silica phases. Other surface techniques however can be applied to silica overlayers deposited on a sensing chip.

Thus, QCM (quartz crystal microbalance) allows quantification of adsorption phenomena on flat surfaces and can provide *in situ* kinetic data. The quartz crystals may be covered by a layer of amorphous-like silica and the adsorption of “heavy” biomolecules such as proteins may be followed. In this way, it was found that streptavidin has a silica adsorption behavior strongly different from avidin or neutravidin, two closely related proteins.²³¹ Smaller molecules such as penta-²³² or heptapeptides^{233,234} or longer peptides²³⁵ have occasionally been studied in this way; application to monomers such as amino acids exist but are still limited on silica so far.²²⁰ In a significant study, lysine and proline adsorption on flat silica were compared with the adsorption of the corresponding oligomers both quantitatively by QCM and qualitatively by SFG, which yielded vibrational spectra.²³⁶

The SPR technique that has allowed in-depth thermodynamic studies of peptide adsorption on gold²³⁷ is not easily

applicable on silica. To obtain thermodynamic data for peptide adsorption on silica, Thyparambil et al.²³⁸ developed a protocol using a special AFM (atomic force microscopy) technique: the AFM tip was functionalized with the oligopeptide to be investigated (forming a single-molecule force sensor²³⁹), and the desorption force curve allowed extraction of a $\Delta_{\text{ads}}H^{\circ}$ value, on quartz (100) and fused glass among other surfaces.

One study of protein adsorption on surfaces of varying wettability, including SiO_x on Si wafers (cf. section 3.1.8), used contact angle measurements with drops of solutions of the biomolecule to assess the adsorption free energy.²⁴⁰ This study underlined again the role of water in adsorption phenomena: on very hydrophilic surfaces, almost no protein adsorbed because it cost too much energy to displace water molecules.

3.2.6. An Overview of Experimental Studies of Small Biomolecule/Silica Systems. Table 1 summarizes the most important experimental studies of small biomolecule adsorption on silica surfaces, indicating the type of silica surface, the interface from which adsorption was carried out, and the main characterization techniques that were used. A quick glance at this table indicates that despite the rather large number of reported studies, much remains to be done.

While many studies bear on the essential amino acids (the list of 20 AAs that has been selected by biochemistry for building proteins), far fewer have been devoted to other small biomolecules. In particular, one would expect to find some investigations on the adsorption of nucleotides, the monomers of RNA or DNA, since rather long DNA or RNA sequences have occasionally been adsorbed on silica for technological reasons.²⁵⁹ In fact, the only example that we are aware of is a comparative study of nucleotide and nucleoside adsorption with other small molecules possibly involved in prebiotic chemistry,²⁴⁴ where the former were found to adsorb more strongly than most AAs at neutral pH. One communication was also devoted to the adsorption on a flat silica surface of adenine,²⁵⁸ a nucleobase that is a component of the corresponding nucleotide but is not expected to adsorb in the same way, since they have very different acid-base speciations (nucleotides and their polymers accumulate negative charges due to deprotonation of the polyphosphate groups).

Most amino acids on the other hand have been studied at least once, but comparative studies are rare. For instance, it is not possible to find adsorption isotherms of all natural AAs on silica in controlled conditions, nor systematic studies of pH effects. The most valuable comparisons are the extensive thermodynamic data of Basiuk et al. (ref 207 and references therein). Reference 253 considered the hydrophilic/hydrophobic nature of AAs; the authors concluded that differences in adsorption parameters could be explained by a combination of electrostatic attraction/repulsion between the AA and the surface, which is pH-dependent,²⁰⁵ and hydrophobic effects.

Unsurprisingly, the biomolecule most widely studied in this context is one of the simplest, namely, glycine. It is also for this molecule that the most precise questions start being asked in recent publications, for example, the identification of H-bonding lattices with the surface.

Other molecules may be worth mentioning, which, although they are not biomolecules in a strict sense, share some functional group similarities with, for example, amino acids and can therefore help explain the adsorption behavior of the latter. Such examples are provided by the field of drug delivery, and the most relevant ones will be discussed in section 9.4.

3.2.7. From Oligopeptides to Proteins: Adsorption, Secondary Structure, and Selectivity. The preceding paragraphs mentioned a few oligopeptides. When the peptide chain grows longer, the number of spatial conformations accessible to it grows exponentially. It is well-known that the proper functioning of a protein such as an enzyme depends on its adoption of the right tertiary structure, which corresponds to a tiny fraction of the available phase space and the realization of which depends on fine details of energetics (interactions between amino acid residues and between amino acids and solvent molecules). Therefore it is of crucial importance for many biological and biomedical applications to know whether the protein structure will be conserved upon adsorption.^{260,261}

The conventional answer is negative: adsorption, in particular on silica, changes the folding pattern of the protein chain; in other words it causes denaturation. We cannot discuss here the many results that have been obtained for protein/silica systems; a good source for these is a recently published and already mentioned review paper.¹⁶⁵ The situation is very complex for proteins due to their long chains, and computationally they are only amenable to low-level modeling, mostly by MD. Short-chain peptides on the other hand may achieve some elements of secondary structure such as the α -helix or the β -sheet, and some of them fall within the limits of high-level modeling methods.

Techniques used to determine adsorbed peptide structures include NMR (cf. section 3.2.4 and ref 262), CD (circular dichroism²⁶³), which is applied directly to colloidal suspensions containing the peptide and the silica nanoparticles, IR (analysis of IR spectra in the amide bands region allows identification of motifs such as the α -helix²⁶⁴), or ToF-SIMS (time-of-flight secondary ion mass spectrometry), probably better suited for adsorbed proteins;²⁶⁵ in this technique, the protein fragments that are eroded first are those that were furthest removed from the silica surface. Ellipsometry and AFM can be used to demonstrate the formation of larger-scale structures such as fibrils.²⁶⁶

The effect of adsorption on the secondary structure of adsorbed peptides has been investigated for at least a dozen years. It is reported that in general there is a loss of α -helicity (e.g., for the 13-mer DDDDAAAAARRRR^{267,268}) and concomitant formation of β -sheets.^{269,270}

This is no absolute rule however. Some peptides have been specifically designed that strongly adsorb to silica particles and form helices on the surface,²³⁵ while they were not structured in solution. This was achieved by introducing at regular spacings in the polymer chain amino acids with basic side chains such as arginine (R), for example, YARQQRAEARQQRAHARQK-RAEARQQRA. The basic AAs are protonated, and since the silica surface is negatively charged, the peptide folds in such a way as to direct all arginine chains toward the surface.

In the preceding example, the silica binding peptide was designed from first principles and chemically synthesized, but there is another approach. Biocombinatorial techniques that were developed to select the “best” peptide sequences binding to a particular biochemical target have been applied to choose the best sequences for adsorption on inorganic surfaces.²⁷¹ In this way, quartz-binding peptides have been engineered²⁷² and sequences specific for amorphous silica have also been produced.²⁷³ These studies are quickly generating a database of specific peptide sequences having more or less strong affinity with silica surfaces. There is of course a strong incentive to understand the structural basis for this affinity; at present it

seems that many results can be understood by combining an electrostatic interaction between positively charged amino acid side chains and negatively charged silanoles on the silica surface and also hydrophobic interactions between apolar side chains²⁷³ and siloxanes, a rationalization similar to that put forward to explain the silica selectivity of a natural protein that was called a “Si-tag”.²⁷⁴ These explanations are still sketchy: obviously much remains to be elucidated in order to understand the interactions of specific protein moieties with specific silica surface sites, their cooperativity, and by way of consequence their effect on protein structuring. Molecular modeling techniques can play a precious role in unraveling these phenomena.

4. DIFFERENT APPROACHES TO MODEL ADSORPTION AT SURFACES

4.1. The Periodic Boundary Conditions Approach

In the context of this review, we focus on reporting modeling data obtained for surfaces belonging to crystalline and amorphous silica. The starting material, irrespective of its aggregation state, is a solid so that the most natural approach to model its features in a computer is to enforce periodic boundary conditions (PBC) and to solve the corresponding Schrödinger equation accordingly.^{275–277} For a crystalline bulk material, this is a rigorous procedure, and more details are provided in section 6. In essence, besides the level of the adopted theory, to work with PBC, one has to define a unit cell, a straightforward step for genuine crystalline materials like α -quartz, because it is the natural outcome of X-ray or neutron diffraction studies of any crystalline material. Crystallographic databases are available that contain the unit cell atomic coordinates of the most important silica polymorphs, both dense and microporous.²⁷⁸ The atomic positions in the unit cell are related to each other, as a function of the considered system, by symmetry elements dictated by the crystallographic space group.²⁷⁹ This, in turn, can be exploited to greatly reduce the computational cost as many components of the unit cell total energy are related by simple symmetry rules and should not be recomputed. For the particular case of silica, one element of difficulty is that silica is also found as an amorphous material. In that case, the fine details of its structure remain inaccessible because diffraction techniques only provide averaged information like the radial distribution function.²⁷⁹ The way in which the structure of an amorphous bulk silica (but this is in general true for other glass-like materials) is arrived at, in a computer simulation, follows strategies that bring a crystalline starting phase (whose structure is known) toward the amorphous one by decreasing the long-range atomic order. Silica, as already described in section 2, is made of rigid $[\text{SiO}_4]$ building blocks joined together by very floppy Si–O–Si angle defining the siloxane bond. This means that in the amorphous silica, the local order within the $[\text{SiO}_4]$ building block is preserved whereas the long-range symmetry relationships between $[\text{SiO}_4]$ groups are lost. This kind of disorder can be achieved with a variety of techniques, for instance, a Monte Carlo bond-switching²⁸⁰ or molecular dynamics carried out at very high T in order to melt the material followed by a quenching step to kinetically freeze the structure in a glassy state.^{281–287} This procedure can be repeated a convenient number of times until physicochemical features of the bulk material (density, Si–O–Si ring nuclearity and distribution, radial Si–O distribution function, etc.) are in good agreement

with experiments. Irrespective of the adopted methods, this is a time-consuming step that is needed to achieve the proper topology of the material. To be representative of the real amorphous material, the simulation should adopt a large enough unit cell to ensure structural richness in the local environment of each $[\text{SiO}_4]$ block. For these reasons, the simulation of amorphous materials is usually much more expensive than that of crystalline ones, particularly when quantum mechanical techniques are adopted. One should also check the dependency of the results on the cell size, a task that is rarely done due to the high cost of the calculation. Nevertheless, results obtained by optimizing at B3LYP a silica bulk derived from the heat/cool procedure gave properties in very good agreement with experiments even for a unit cell content of less than 100 atoms.^{280,288–290}

The key point within the present context is how to move from silica bulk to surfaces, because the properties of the latter are the relevant ones when adsorption of (bio)molecules is considered. Usually, surfaces are modeled using slabs of finite thickness cut out from the bulk structure along a given Miller (hkl) crystallographic plane.^{276,291} The surface unit cell should then be defined accordingly through a matrix transformation of the original bulk one. At variance with the bulk, the periodic boundary conditions should only be enforced by translation vectors parallel to the surface, because periodicity is now lost in the noncrystallographic direction perpendicular to the slab plane. Technical reasons bound to the adoption of plane waves based methods (*vide infra*) enforce the adoption of a tridimensional unit cell for slabs as well. Thus, one needs to define a large enough empty space above and below the true slab to avoid mutual fictitious interactions between the periodically repeated slabs. This is different from periodic quantum mechanical calculations carried out using a Gaussian type basis set, in which the definition of the true bidimensional slab is completely rigorous, that is the electrostatic potential above and below the slab decays exponentially with the distance from the slab.^{276,291} In all cases, the adequacy of the adopted slab must be checked by considering convergence of geometry, energy, and electronic properties as a function of the increasing number of atomic layers included in the slab and, for plane-waves based calculations, also of the size of the empty space separating the repeating slabs. For both true oxides and metals, the geometrical cut completely defines a given (hkl) plane that can then be modeled by a variety of techniques. For oxides, extra care should be exerted in order to avoid either charged slabs or slabs with a large dipole moment across the slab itself, because in this case they are electronically unstable.^{292,293} For a covalent material like silica, bond cutting brings about the formation of a variety of surface defects, the most relevant being the $\text{Q}^3(\bullet)$ silyl $\equiv\text{Si}\bullet$, the $\text{Q}^3(\text{O}^\bullet)$ siloxy $\text{E}' \equiv\text{SiO}^\bullet$, the $\text{Q}^2(:) >\text{Si}$; and the $\text{Q}^2(\text{O})$ silanone $>\text{Si}=\text{O}$. The nature and stability of these defects has been discussed in the literature^{69–71,294–305} showing that all of them, without exception, are thermodynamically unstable with respect to water hydroxylation. Because water is ubiquitously present during biomolecule adsorption these defects should not play an important role in that case. In practice, the above defective sites are all “healed” by extraction of H or OH groups from the water environment in a real material or by manual addition of H (to $\equiv\text{SiO}^\bullet$) and OH (to $\equiv\text{Si}\bullet$) in the simulated one. The “healing” process does not lead, however, to a unique surface termination, because different kinds of SiOH groups are known to exist at the silica surface (see section 2) as a function of their

local environment. For instance, when dealing with surfaces derived from a crystalline silica the height at which the geometrical cut is carried out does indeed matter, because it defines the resulting type of SiOH, that is, the sole specification of the (hkl) crystallographic family plane does not uniquely define the kind of SiOH termination.

As an example, in Figure 18 the same (010) crystallographic face of α -quartz can be terminated by either geminal or vicinals

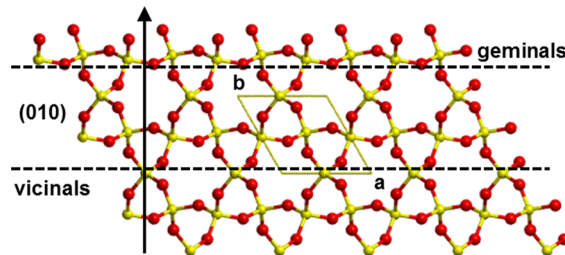


Figure 18. Different geometrical cut planes defining different silica surface terminations for the same (010) crystal plane. Possible cut planes are represented by dotted lines.

SiOH groups as a function of the cut height along the axis perpendicular to the slab. Therefore, for a crystalline surface, both the (hkl) crystallographic plane and the kind of SiOH termination chosen should be clearly specified to completely define the system under study. Some subtle effects are possible, however, because for instance, the fully hydroxylated (001) and (010) surfaces of α -quartz and the (001) and (110) ones for α -cristobalite all envisage geminal terminations, but they are all different from each other, because different H-bond interactions (defining them as “interacting pairs”)³⁰⁶ are taking place (see Figure 19).

Therefore, a further step is needed in the calculations to find the best arrangement of the surface SiOH in order to maximize

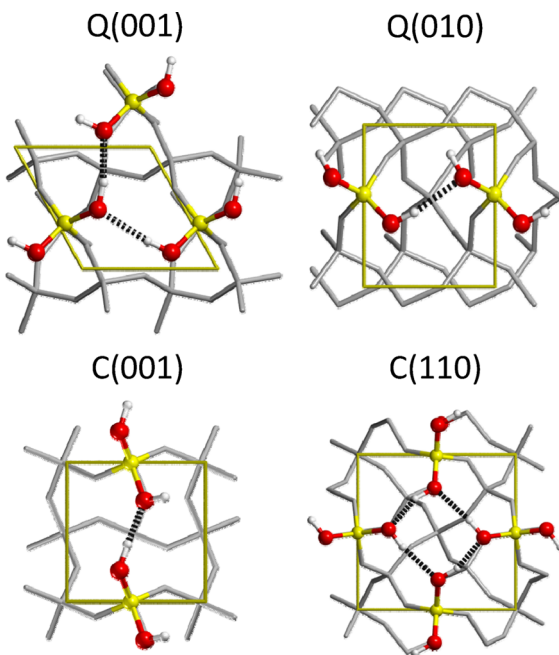


Figure 19. Different H-bond patterns between geminal SiOH sites at the surfaces of α -quartz (Q(001) and Q(010)) and cristobalite (C(001) and C(110)).

the H-bond interaction and, consequently, to reduce the surface formation energy computed as the energy of reaction of the bulk crystal with water molecules.

The very same approach can be followed to define the surface of an amorphous silica material, starting from an “amorphized” bulk prepared with some of the procedures described above. In this case, the geometrical meaning of a particular crystallographic (*hkl*) plane is lost due to the amorphous nature of the material and less freedom is left in positioning the cut plane, because electroneutrality should always be enforced. Because the unit cell is neutral, this can be automatically accounted for by using slab thickness, which is an integer multiple of the unit cell size with geometrical cuts along the three main (100), (010), and (001) crystal planes. It is worth noting that, contrary to crystalline surfaces, the upper face is no longer equivalent to the lower face of the slab after the hydroxylation step due to the amorphous nature of the material. Figure 20 shows the case of the equivalent faces for

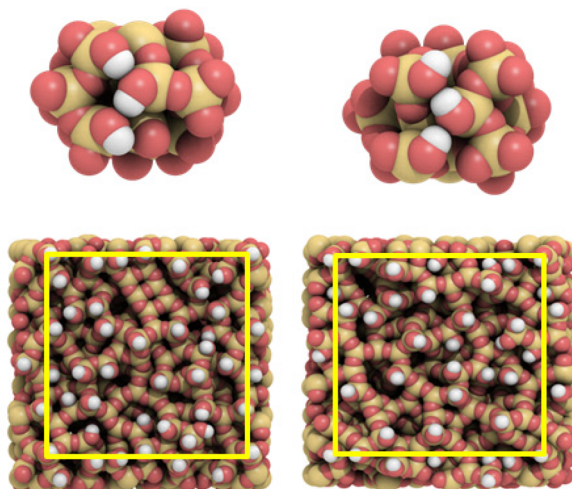


Figure 20. Upper and lower (top) fully hydroxylated (101) faces of cristobalite and (bottom) fully hydroxylated faces of the silica amorphous surfaces from refs 285 and 307. Molecular graphics rendered by Qutemol.⁷³

the (101) cristobalite and the nonequivalent ones for a model of amorphous silica surface recently proposed by Colombi Ciacchi and co-workers.^{285,307}

This is an advantage for the simulation of amorphous materials because the two different hydroxylated surfaces enrich the variability of the SiOH surface groups to be studied. For instance, calculation of the OH vibrational features will be improved due to the increasing variability of the local surrounding of each OH group at the upper/lower face of the same slab. Also, at variance with what happens for the crystalline silica surfaces, for the amorphous ones different kinds of SiOH groups are present in the same surface unit cell.

When dealing with adsorption of (bio)molecules there is one important caveat. The adopted unit cell, irrespective of whether one is dealing with a crystalline or an amorphous silica system, should be large enough to avoid lateral interactions between adsorbates. This forces the surface unit cell to become very large for even small biomolecules like short peptides, preventing the adoption of first principle calculations. For instance, Schneider and Colombi Ciacchi adopted a $44 \times 44 \text{ \AA}^2$ unit cell size of a partially oxidized Si surface to study the

adsorption of a fully solvated RKLPA hexapeptide by classical force field molecular mechanics methods.³⁰⁸ An even larger unit cell ($98 \times 98 \text{ \AA}^2$) was used to simulate the adsorption of the NC1(84–116) domain of collagen VIV on the natively oxidized silicon surface.³⁰⁷ Nevertheless, lateral interactions can be easily computed, at least within the local Gaussian basis set approach, and their contribution (either repulsive or attractive) can be subtracted to the total adsorption energy.^{309–312} A number of detailed examples on this point will be discussed in the following sections devoted to adsorption of water and amino acids on silica surface models. Care should also be taken to study not only the adsorption but also the properties of the pristine surfaces, because the adoption of a too small unit cell would impose geometrical constraints biasing the true potential energy surface. An example is the recent study by Sautet and co-workers³¹³ on dehydroxylation processes at the surface of crystalline cristobalite as a model of the amorphous silica surface, in which large enough cells have been chosen to ensure enough flexibility in the multistep simulation of the dehydroxylation process.

In the recent past, it has been customary to adopt a specific surface derived from a crystalline silica polymorph to mimic some of the specific features of the hydroxylated amorphous silica surfaces. This originates from the seminal work by Peri³¹⁴ in which the (100) hydroxylated surface of β -cristobalite was chosen as a model system to interpret the dehydroxylation process occurring at the amorphous silica surface either by heating and outgassing the sample or by specific reactions. At that time, to reference to a crystalline model was a clever idea in order to figure out possible models of the more complex amorphous silica whose modeling was technically unfeasible. In the last 20 years, the very same idea was adapted to the computer simulation of amorphous silica surface.^{315,316} As it was recalled in section 2.2, the real amorphous silica surface exhibits different kinds of surface silanols, a fact that cannot be simulated by a single crystalline surface, which exhibits only one kind of OH group (*vide supra*). The idea is to consider different surfaces derived from the same crystalline silica polymorph and then merge the results to mimic the more complex behavior of the real amorphous system (see Figure 21).

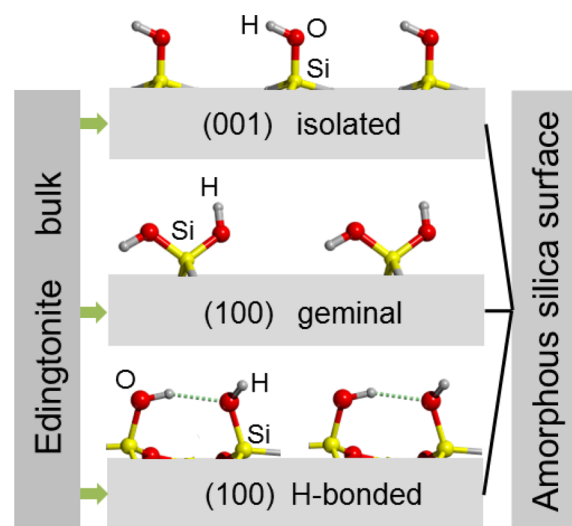


Figure 21. Amorphous silica surface simulated by merging different surface terminations of the edingtonite bulk.

The easiest system to simulate is an amorphous silica outgassed at high temperature in which only isolated silanol groups remain at the surface. In that respect, Civalleri et al.³¹⁶ were the first to propose the (001) surface of edingtonite, a microporous all-silica polymorph particularly suitable to quantum mechanical calculations due to its structural rigidity and simplicity, to model the isolated silanols on an amorphous silica surface. Tosoni et al.³¹⁷ extended the model to include the (100) surface exhibiting either H-bond interacting or geminal sites to model both clean and water-interacting surfaces. The infrared spectra were constructed by merging the results of the three independent surfaces obtaining excellent agreement with the experimental ones. The same model has been adopted in a number of studies devoted to studying adsorption of simple molecules to silica^{318–320} as well as to studying the adsorption of glycine^{309,321–323} and alanine.^{324,325} This approach has obvious limitations, and it is preferable to rely on amorphous silica models, which is now feasible with the development of highly parallelized computer programs³²⁶ at the modern high-performance computing facilities.

In summary, the advantage of the PBC approach is that the extended nature of the material is naturally taken into account at the expense of using a large enough unit cell for modeling amorphous silica or to avoid spurious lateral interactions. The disadvantage is that the maximum level of theoretical method applicable to periodic systems is limited to the DFT approach due to the difficulty of extending the higher correlated methods based on the wave function expansion to solid state treatment. Recent progress has, however, been made both in the direction of the periodic implementation of the MP2 method in its localized definition³²⁷ in the CRYSCOR program³²⁸ and methods based on the random phase approximation associated with exact exchange³²⁹ coded in the VASP program.³³⁰ In general, these approaches are rather expensive and the geometries cannot be coherently optimized because the analytical energy gradient has not yet been implemented. Nonetheless, the applicability of MP2 to molecular crystals of chemical interest and medium size has been recently carried out,³³¹ as well as recent parallelization of the CRYSCOR code³³² opening the possibility for applications dealing with adsorption of large molecules on silica surfaces.

4.2. The Cluster Approach

The PBC approach focuses, first, on the definition of the bulk structure to reach to a specific hydroxylated silica surface, either crystalline or amorphous. The cluster approach, instead, focuses on the surface first and in particular on the kind of SiOH groups to be modeled by (i) cutting out a representative piece of matter around a specific site from an underlying silica material, (ii) expanding the size of the cluster around the active site using topologies reminiscent of the silica secondary building units found in microporous all-silica zeolites, or (iii) adopting a tree-like cluster grown around the active site whose extension mimics the underlying solid. In all cases, the Si–O bonds at the border of the cluster are saturated by either H or OH groups, giving rise to Si–H and Si–OH terminations, respectively.³⁹ Care should be taken to avoid spurious structural and electronic effects of the terminations on the core zone of the cluster where the “active” SiOH is modeled by enforcing structural constraints at the frontier atoms and bonds. With all dangling bonds properly healed, the cluster becomes a regular molecule so that standard quantum mechanical methods using highly sophisticated quantum chemistry computer programs

can be applied to characterize its physicochemical features. This is a real advantage over the PBC method, because the level of sophistication in the adopted theoretical method is only limited by the available computing resources, so that CCSD(T), the gold standard for quantum chemical calculations,³³³ can be adopted. Furthermore, solvation methods based on the continuum approach³³⁴ can also be included as a first approximation to study solvent effects on the adsorptive properties of the surface “active site”, which is particularly important in the context of biomolecule adsorption. This is a feature entirely missing from the present computer codes devoted to run periodic calculations. In practice, the cluster method was the only option available in the 1990s when computer resources and programs apt to solve the Schrödinger equation for crystalline systems were still in their infancy. The state of this matter until 1994 has already been reviewed.^{39,335} In essence, subminimal and minimal clusters (shell-0 and shell-1 clusters in ref 39) were adopted in which only the first neighbor atoms around the SiOH group were included in the cluster definition. In principle, a shell-*n* cluster, grown in a “tree-like” fashion, would provide a better representation of the local environment of the “active” SiOH by increasing the *n* value. Unfortunately, this approach is impractical, due to the large number of geometrical constraints needed to avoid large distortion of the cluster geometry caused by the interactions between terminal groups. The large number of terminal atoms also biases the adsorption of molecules, in particular for those of larger size (see Figure 22).

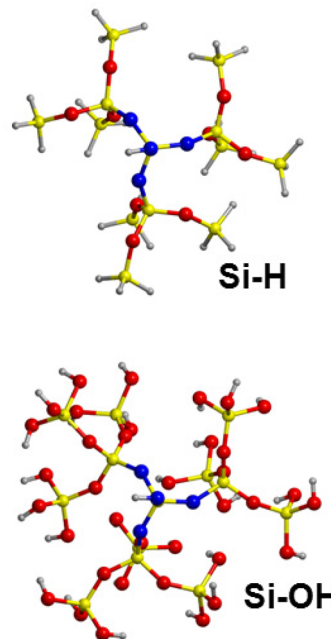


Figure 22. Tree-like models for the isolated SiOH group at the silica surface terminated by Si–H and Si–OH groups. The SiO_3OH moiety representing the surface SiOH group is depicted in blue.

Later on, clusters based on Si–O secondary building units, the main constituents of silica frameworks,³³⁶ were proposed³³⁷ (see Figure 23).

These studies focused on the dependence of the features of the SiOH on the cluster ring topology and geometrical tension meant to model the isolated SiOH at the amorphous silica surface. Specifically, they have been successful in simulating the

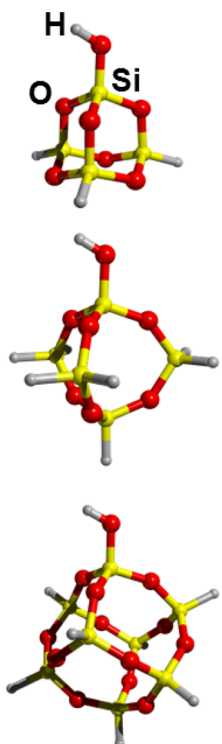


Figure 23. Cage-like cluster models for the isolated SiOH group at the silica surface.

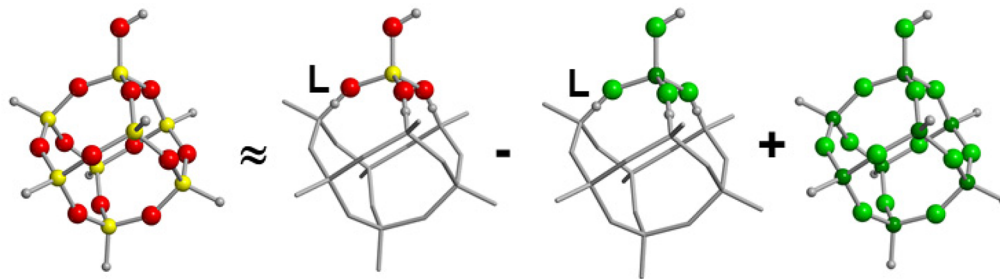
vibrational features of the Si–OH moiety,³³⁸ the $\delta(^1\text{H})$ and $\delta(^{29}\text{Si})$ NMR chemical shifts,³³⁹ and the adsorption of NH₃ on the isolated³⁴⁰ and interacting hydrogarnet SiOH sites³⁴¹ or for studying H₂O adsorption on external surfaces of zeolite ZSM-5³⁴² and CH₃OH on Ca-rich silica surfaces.³⁴³ The advantage of the “cage-like” models over the “tree-like” ones are their natural structural rigidity, which avoids the use of geometrical constraints, and the near absence of spurious effects at the core SiOH site due to cluster terminations. The isolated cluster method has gradually lost momentum in recent years, the PBC approach being now the most widespread one. Nevertheless, the cluster approach can be extremely useful to check whether the specific level of theory, which is usually limited to DFT in PBC calculations, is adequate by comparing the DFT results with higher levels of theory run on representative clusters cut out from the periodic model. This is particularly important, for instance, for open-shell systems for which it is known³⁴⁴ that functionals based on the generalized gradient approximation (GGA) provide too delocalized spin density with respect to well correlated methods. A recent application to modeling crystalline silica surfaces rich in radical siloxy $\equiv\text{SiO}^\bullet$ terminations has adopted this approach to establish the Becke-Half&Half functional as the best choice by comparing its performance with CCSD(T) ones run on small clusters.³⁴⁵ Another application is for the development and checking of new empirical potentials based on analytical expression. Very recently Colombi Ciacchi and co-workers have run MP2 calculations on silica clusters cut out from a PBC model to develop a new force-field to model the interaction of water with protonated (SiOH) and deprotonated (SiO⁻) amorphous silica surfaces.²⁸⁵ This is obviously extremely relevant in the present context, because the silica surface is known to become negatively charged at pH values higher than 6. It should be clear, however, that the cluster approach remains physically

sound only when the properties under study are local in nature and do not depend on long-range interactions or on structural features specifically due to the extended nature of the system (i.e., infinite H-bond chains). Furthermore, collective properties of the adsorption, like water restructuring close to the silica surface compared with bulk liquid water, which are extremely important to our understanding of the wettability of silica based materials, cannot be simulated by the cluster approach.³⁴⁶

4.3. The Embedded Cluster Approach

In the mid-1990s, it was realized that it would be interesting to merge the advantages of the cluster approach, in which a high level of theory is applicable, with the geometrical constraints naturally imposed by the PBC, but without actually making use of the periodicity. In principle, the PBC can be avoided by adopting a large enough cluster to properly mimic the surroundings of the active site. Unfortunately, this approach brings about an exponential growth in the number of atomic orbitals with the cluster size despite the interesting chemistry being localized at one particular active site. A number of methods have been developed to describe with a higher level of theory the chemically relevant part while leaving the outside region to be described by a lower (and computationally cheaper) method. Among others, the connecting bond approach by Bakowies and Thiel,³⁴⁷ the pseudobond scheme by Zhang and co-workers,³⁴⁸ and the effective group potential (EGP) by Poteau et al.^{349,350} may be mentioned. Another technique, inspired by the pseudobond scheme of Zhang et al.,³⁴⁸ is the transfer Hamiltonian^{351,352} that employs a newly parametrized pseudoatom to describe the short-range interaction.³⁵³ Special pseudoatoms have been derived to account for the physicochemical properties of the external chemical part connected to the central site. The pseudoatoms are then used to cap the central site to arrive at a classical cluster model (see section 4.2). This has been achieved by defining a pseudopotential for the link atoms in such a way that the properties computed for the smaller capped cluster are as close as possible to those for a larger model treated with the highest level of available theory (CCSD(T)). A recent application of the transfer Hamiltonian has been reported⁸⁷ to model the adsorption of H₂O, NH₃, and NO at the silica isolated, geminal, and vicinal surface sites obtaining excellent agreement with the experimental results for both SiO–H frequency shifts and adsorption energies. The efficiency of the method allowed the authors to treat the capped cluster at MP2/6-311++G(d,p) level. Interestingly, the results computed for the adsorption of NH₃ on isolated silanol groups are in excellent agreement with that computed by Armandi et al.¹⁶⁹ using periodic boundary conditions calculations (see section 4.1) based on the density functional plus dispersion corrections PBE-D method (see section 5.3).

A more general solution of the problem has been suggested by Morokuma and co-workers who proposed the “integrated molecular orbital molecular mechanics”, IMOMM, in which the interesting zone of the cluster was treated at a higher level (quantum mechanics) while adopting a low level (classical force fields) for the external part.³⁵⁴ Later on, the method eventually became an internal feature of the Gaussian98 program,³⁵⁵ known as the ONIOM2 method in which the lower level of theory was no longer restricted to molecular mechanics but can be any quantum mechanical method.^{356–358} It was immediately clear that this approach was ideal to treat active sites present at the silica surfaces. Particularly relevant in that respect is the



$$E[\text{High:Low}] \approx E(\text{High, Model}) - E(\text{Low, Model}) + E(\text{Low, Real})$$

Figure 24. Definition of the ONIOM2 scheme for a cage cluster model representing the isolated SiOH group at the silica surface. Color coding identifies the level of calculus. L identifies the link atoms.

QMPot method developed by Sauer and co-workers, which was specifically designed to model silica and zeolite materials.³⁵⁹ In brief, the ONIOM2 approach subdivides the system of interest into two parts or layers, each of which is described at a different level of theory.³⁶⁰ The most important part of the system is the innermost layer, the “model system”, which is described at the highest level of theory. Obviously, the values of the computed properties are a function of the size and topology of the model system. The whole system is called the “real system”. One delicate step is to define the cut between the model system and the rest of the system. Usually this is attained by adding a set of fictitious atoms, usually hydrogen atoms (called “link atoms”), along the pre-existing chemical bonds extending from the model system toward the exterior layer.

In the ONIOM2 approach, the energy $E[\text{High/Low}]$ of the system, subdivided into the two layers, is written as (see Figure 24):

$$\begin{aligned} E[\text{High/Low}] &\approx E[\text{High/Real}] \\ &= E(\text{High, Model}) - E(\text{Low, Model}) \\ &\quad + E(\text{Low, Real}) \end{aligned}$$

in which $E(\text{High, Model})$, $E(\text{Low, Model})$, and $E(\text{Low, Real})$ are the total energies of the model and real systems at the high and low levels of theory. The nice feature about the ONIOM2 formulation is that the method is self-embedding by definition; that is, if the low level of calculation is increased to reach the highest adopted level or if the model system is enlarged up to the real system, one rigorously gets $E[\text{High/High}] = E(\text{High, Real})$, for model → real as well as for low → high.

The first application of the ONIOM2 method to model the adsorption of NH_3 at the isolated hydroxyl groups on a highly dehydrated silica surface was discussed in ref 361. The purpose was to establish which level of theory, within the ONIOM2 framework, was optimum to provide internally consistent data for the prediction of a number of physical observables like the OH vibrational features and the NMR $\delta(^1\text{H})$ and $\delta(^{29}\text{Si})$ chemical shifts and to characterize the adsorption of NH_3 . A cage-like cluster was adopted, which was considered as the real system, and subportions of different sizes cut out around the SiOH group were adopted to define the model system. Results were very satisfactory, because all properties converged quicker than pure cluster calculation to those computed for the real system. Other applications of the ONIOM2 approach to model silica surface features include the adoption of the same cage cluster used to mimic the isolated SiOH in ref 361 to compare the adsorption energies of N_2 , CO , H_2O , NH_3 , and CH_3CN .

with clusters representative of Lewis and Brønsted sites in zeolites³⁶² and the simulation of the hydrogarnet in all-silica silicalite.^{117,363} In the latter case, the silica hydrogarnet in the all-silica silicalite was represented by a $\text{Si}_{56}\text{O}_{90}\text{H}_{52}$ real system and by the $\text{Si}_4\text{O}_{16}\text{H}_4$ model zone computed with ONIOM-[B3LYP/6-31G(d,p):PM3] (Figure 25) to model the fine vibrational features in the OH stretching region of the hydrogarnet.

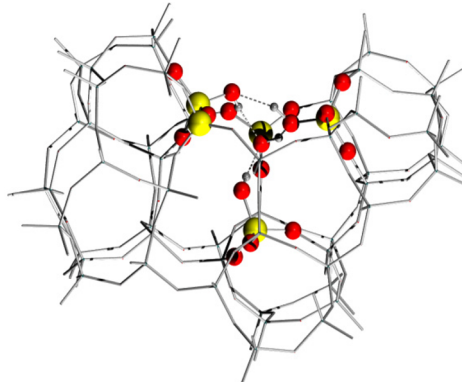


Figure 25. Model of the hydrogarnet in all-silica silicalite structure. The balls identify the model region treated at B3LYP/6-31G(d,p) level.

The mechanical embedding scheme, in its QMPot implementation as proposed by Sauer and co-workers,³⁶⁴ has reached a high popularity in the study of Brønsted sites (both acidic and cation exchanged ones) in zeolites.^{365,366} More recently, thanks to the increased computing power, the method has been extended to adopt DFT to treat the real system within the PBC. In the applications, PBE functional and plane waves as implemented in the VASP code have been adopted as the low level of calculus. The model system is usually treated at the MP2 high level with a large Gaussian basis set, which ensures that dispersive interactions are also taken into account, at least in the model system.³⁶⁷ Recent applications of this modern version of QMPot are the study of H_2 adsorption on metal organic frameworks³⁶⁸ or the benzene ethylation catalyzed by the adsorption in H-ZSM-5.³⁶⁹ To the best of our knowledge, no applications have been published to date to model adsorption at silica surfaces even if nothing should hinder their success in that respect. In the original implementation of the ONIOM method, neither direct charge transfer nor polarization were possible between the exterior layer and the

model system. Only indirect effects on the model system occur due to the equilibration of energy gradients acting on the link atoms, which force the atoms of the model system to follow those of the exterior layer and vice versa. In the modern implementation of the ONIOM method, the charge distribution of the MM region interacts with the actual charge distribution of the QM region. In this case, the partial charges from the MM region are included in the QM Hamiltonian, which provides a more accurate description of the electrostatic interaction and, in addition, allows the wave function to respond to the charge distribution of the MM region. This approach is referred to as electronic embedding.³⁷⁰

5. THEORETICAL METHODS AND THEIR APPLICATION TO SILICA SURFACE MODELING

An accurate description of the properties of silica surfaces and, in particular, their role on adsorption and reactivity processes at the atomic level requires the use of quantum chemistry methods. These methods are based on the resolution of the time-independent, nonrelativistic Born–Oppenheimer electronic Schrödinger equation and can be classified into two major groups: methods based on the wave function and those based on density functional theory. It is not our goal to provide a detailed description of the existing electronic structure methods, which can be found in various textbooks,^{371–373} and its current state is nicely reviewed in a recent *Chemical Reviews* thematic issue devoted to quantum chemistry.³⁷⁴ Instead, we attempt to provide a general overview of the methods that have been and can be applied to study silica surfaces and their interaction with biomolecules, while mentioning their strengths and weaknesses.

5.1. Wave Function Based Methods

The simplest ab initio wave function based method, the Hartree–Fock (HF) method, is based on a single Slater determinant. It has limited accuracy since it neglects the electron correlation energy, which can significantly influence the results, particularly when comparing situations with different electron correlations or when describing radical defects or H-bond and dispersion interactions, aspects that are of great importance to the present topic. Electron correlation can be taken into account by expanding the wave function through the inclusion of excited state configurations. Derived methods are called post-Hartree–Fock and include, for instance, the configuration interaction (CI), Møller–Plesset (MP_n) and coupled cluster (CC) methods.^{371–373} Wave function based methods have the advantage that they can be applied hierarchically to obtain increasingly more accurate values converging to the exact solution. Among them, the CCSD(T) with single, double, and triple T excitations (the latter estimated through perturbation theory) extensively includes electron correlation and, when combined with basis set extrapolation techniques, is considered the “gold standard” in quantum chemistry.³³³ Applicability of CCSD(T) is, however, hampered by the size of the modeled system and is limited to the cluster approach. Indeed, the main disadvantage of wave function based correlated methods is the high scaling of the computational cost with the size of the system. Local correlation methods^{375–383} allow exploitation of the fundamental local character of dynamical electron correlation, leading to methods that may scale linearly with the size of the system and thus largely reducing the computational costs of post-Hartree–Fock methods. As already anticipated in section 4.1, it

is worth mentioning that local-MP2 has been implemented for extended systems by exploiting the translational and point symmetry properties of crystalline structures³⁸⁴ with the periodic boundary conditions as implemented in the CRYSCOR program³²⁸ and in the VASP program³³⁰ through the random phase approximation associated with exact exchange.³²⁹ These methods are, in general, very expensive when applied to extended systems, but the development of codes apt to exploit the power of the high-performance computing architectures³³² will soon make this kind of calculation available to the scientific community.

5.2. DFT-Based Methods

Since the mid-1990s, approaches based on electron density (see ref 344 for a nice introduction to DFT and for the technical nomenclature) rather than on the wave function have become attractive alternatives because, while including electron correlation, they are computationally cheaper than post-Hartree–Fock methods. In general, DFT methods based on generalized gradient approximation (GGA) functionals such as PBE, PW91, or BLYP are usually implemented in codes running periodic calculations based on a plane-waves basis set (*vide infra*). Hybrid functionals like B3LYP and PBE0 contain a fraction of exact exchange in the functional definition, which allows improvement of the already good performance of GGA functionals for systems where the self-interaction error may become important.³⁸⁵ At variance with the GGA case, the implementation of hybrid functionals is easier using localized basis functions (Gaussian-type orbitals, *vide infra*). To show an example of the DFT performance with respect to the present topic, the structural data and relative stabilities of α -quartz, α -cristobalite, and α -tridymite^{386,306} are very well reproduced with B3LYP with a 6-31G(d) Gaussian basis, as illustrated in Table 2.

Table 2. Structural Data and Relative Stabilities of α -Quartz, α -Cristobalite, and α -Tridymite^a

	α -quartz		α -cristobalite		α -tridymite	
	expt ^b	B3LYP	expt ^c	B3LYP	expt ^d	B3LYP
space group	P3 ₁ 2 ₁	P3 ₁ 2 ₁	P4 ₁ 2 ₁ 2	P4 ₁ 2 ₁ 2	C222 ₁	C222 ₁
<i>a</i> (Å)	4.902	4.971	4.969	5.024	8.756	8.869
<i>b</i> (Å)	4.902	4.971	4.969	5.024	5.024	4.968
<i>c</i> (Å)	5.399	5.467	6.926	6.989	8.213	8.267
<i>V</i> (Å ³)	112.4	117.0	171.0	176.4	45.2	45.5
$\langle \text{Si}–\text{O} \rangle$ (Å)	1.612	1.632	1.603	1.629	1.559	1.626
$\langle \text{Si}–\text{O}–\text{Si} \rangle$ (deg)	142.6	142.7	146.7	144.5	179.7	176.8
relative stability, ΔH (kJ/mol)	0.0 ^e	0.0	10.9 ^e	10.5	12.1 ^e	12.6

^aCell parameters as *a*, *b*, and *c*; cell volume as *V*; $\langle \text{Si}–\text{O} \rangle$ and $\langle \text{Si}–\text{O}–\text{Si} \rangle$ average values. ^bReference 387. ICSD no. 93974. ^cReference 388. ICSD no. 77452. ^dReference 389. ^eReference 390.

The agreement between experimental and computational data for the three polymorphs is excellent. Even the B3LYP $\langle \text{Si}–\text{O}–\text{Si} \rangle$ angle inside the cell, whose value is very sensitive to small perturbations due to its high flexibility, is in good agreement with experimental data, the largest deviation being 2.9°. Calculated ΔH values associated with the relative stability of the silica polymorphs are also in excellent agreement with calorimetric data.³⁹⁰ The GGA PBE and PW91 functionals provide consistent results³⁹¹ but with slightly larger expanded

lattices due to larger Si–O–Si angles computed at these levels of theory. The hybrid B3LYP functional also appears to be superior to GGA in the calculation of vibrational frequencies of α -quartz,³⁹² with mean absolute deviations of only 6 cm^{−1}, which validates the B3LYP functional as a reliable method to study silica materials.

Point defects on silica, such as the common nonbridging oxygen hole center, $\equiv\text{Si}–\text{O}^\bullet$, can also be reasonably described with DFT methods.^{345,393–396} In these cases, however, where radical species are present, the use of hybrid functionals is especially important to get accurate results. GGA functionals tend to delocalize the spin density because these situations are overstabilized^{397,398} due to a bad cancellation of the self-interaction part by the exchange functionals. This can significantly influence the $\equiv\text{Si}–\text{O}^\bullet$ bond length, the computed EPR data,^{345,393} or the optical properties.^{302,396} Indeed, quantitative agreement between measured and computed hyperfine coupling constants and *g* factors is only found with hybrid functionals including 50% of exact exchange.³⁹³ GGA functionals, such as BLYP, fail in describing these defects. Spin density delocalization also influences the H-bonding in a surface containing radical defects and the kinetics of the $\equiv\text{Si}–\text{O}^\bullet + \text{H}_2\text{O} \rightarrow \equiv\text{Si}–\text{OH} + \text{OH}^\bullet$ reaction.³⁴⁵ The energy barrier is significantly smaller with GGA than with hybrid functionals, BH&HLYP including 50% of exact exchange being the one that best compares to CCSD(T) calculations.

Hydroxylated silica surfaces exhibit H-bonding between surface silanols and with the adsorbed molecules. It is, therefore, important to assess whether DFT methods are capable to properly describe H-bonded interactions of medium strength.³⁹⁹ This topic has been largely investigated in the last two decades, the water dimer being probably the most intensively studied hydrogen bonded system.³⁴⁴ Among the standard density functionals frequently used in periodic calculations, B3LYP and BLYP have been shown to slightly underestimate the binding energy and the $R_{\text{O}–\text{O}}$ distance, while both slightly overestimate the O–H stretching frequency shift in an H-donor OH, compared with MP2 and experimental data.^{400–404} The PBE functional, while providing accurate interaction energies,⁴⁰⁵ underestimates the $R_{\text{O}–\text{O}}$ distance somewhat more and predicts larger frequency shifts,⁴⁰¹ and its reliability is closely connected to the bond directionality.⁴⁰⁶ For the most specific case of hydroxyl groups in ionic crystals like $\beta\text{-Be(OH)}_2$ and Mg(OH)_2 it was proven⁴⁰⁷ that B3LYP OH frequency shifts are in better agreement with experiment than those resulting from PW91 functional, which were definitely overestimated. In general, it can be safely stated that functionals based on Becke's exchange formulation provide better frequency shifts than those resulting from Perdew's one for bonds acting as H-bond donors. These results show that, on the whole, the properties (binding, geometry, and frequency shifts) of systems (molecular and crystalline) with moderately strong H-bonds (dominated by electrostatics³⁹⁹) are reasonably well described by standard GGA and hybrid functionals.

5.3. Dispersion Corrections

Standard density functionals are, however, unable to cope with long-range dispersion interactions,^{408–411} which are essential to properly describe the adsorption of biomolecules on silica surfaces (see, for instance, refs 321, 412, and 413). Moreover, accounting for dispersion interactions appears to be important to describe the structure and dynamics of liquid water,⁴¹⁴ which

otherwise becomes overstructured,^{415,416} especially when using GGA functionals.⁴¹⁷

To account for dispersion, it has been proposed^{418–421} to use an atom–atom additive damped empirical potential of the form $-\mathcal{f}(R)C_6R^{-6}$ to include long-range dispersion contributions to the computed ab initio DFT total energy and gradients:

$$E_{\text{DFT-D2}} = E_{\text{DFT}} + E_{\text{DISP}}$$

where E_{DISP} is the empirical potential:

$$E_{\text{DISP}} = -s_6 \sum_{i < j} f(R_{ij}) \frac{C_6^{ij}}{R_{ij}^6}$$

Here, C_6^{ij} is the dispersion coefficient for the pair of atoms *i* and *j*, s_6 is a scaling factor that depends on the adopted DFT method, and R_{ij} is the interatomic distance between atoms *i* and *j* in the molecular system. The damping function $f(R_{ij}) = 1/(1 + e^{-d(R_{ij}/R_{\text{vdw}}^{-1})})$ was used to avoid near-singularities and double-counting for small interatomic distances by using the sum of the van der Waals atomic radius of atoms *i* and *j* and the steepness of the damping function as determined by the value of the *d* parameter. Values of the van der Waals radii, atomic C_6 coefficients from which the C_6^{ij} are computed as geometrical mean, and the s_6 values for specific functionals are provided in ref 420. The coding of the above formulas for energy and gradient are very simple and the computational cost with respect to a plain DFT calculation is negligible. The above formulas have been promptly extended to correct energy and gradient for crystalline systems as it was reported in ref 422.

The beauty of the DFT-D2 approach is that it leaves unaltered the original accuracy of the DFT functional for short-range interactions (bond breaking/making), while it dramatically improves the long-range tail of the interaction dominated by London forces.^{420,423–425} Inclusion of dispersion interactions is mandatory when computing the adsorption energies of biomolecules on silica surfaces, since they can account for up to 40–50% of the total adsorption energy (see, for instance, ref 321). Moreover, when adsorption is determined by dispersion interactions with siloxane groups and less by H-bonding, such a correction also becomes essential to determine the proper geometry and adsorption energy of the adsorbed adduct. An example of that is the work of Rimola et al.⁴²⁶ who studied the interaction of benzene, which can be considered as a partial analogue of the phenylalanine molecule, with a hypothetical hydrophobic silica surface constituted by only Si–O–Si bonds, that is, with no SiOH surface groups. Calculations were run adopting periodic boundary conditions (see section 4.1) using B3LYP and B3LYP-D* methods, the latter inclusive of the dispersion contribution properly reparametrized⁴²² to account for the condensed matter nature of the system. At the B3LYP level, the calculated BSSE-corrected adsorption energy (ΔE^{C}) was found to be slightly repulsive (+2 kJ mol^{−1}), becoming attractive and as large as −32 kJ mol^{−1} when dispersion was included at the B3LYP-D* level. Significant changes also resulted in the optimized geometries due to the role of dispersion. That is, at the B3LYP level, the optimum benzene distance from the surface was about 4.5 Å, which decreased to 3.3 Å at the B3LYP-D* level (see Figure 26a). When benzene was adsorbed on a highly hydroxylated (5.2 OH nm^{−2}) silica surface model (Figure 26b), the optimum structure revealed specific OH···π interactions. At the B3LYP level, the strength of this interaction, ΔE^{C} , was −10 kJ mol^{−1}, which increased (in absolute terms) to −48 kJ mol^{−1} at the B3LYP-D* level; that is,

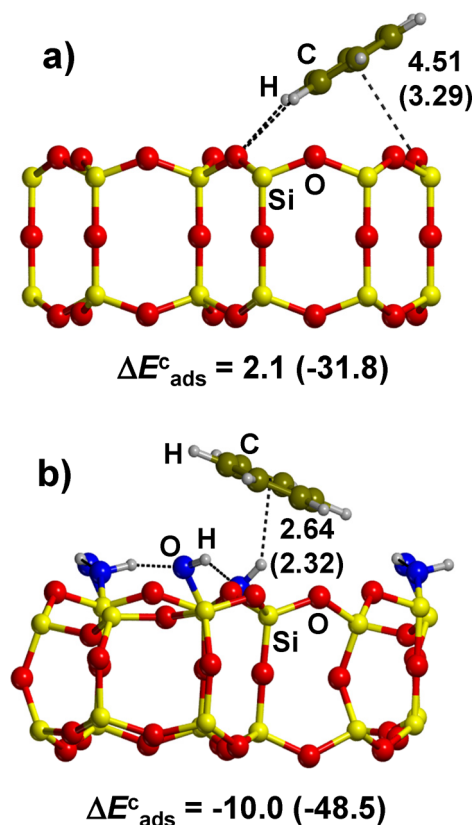


Figure 26. Optimized structures and adsorption energies for benzene adsorbed on (a) a hydrophobic and (b) a hydrophilic silica surface at the B3LYP (B3LYP-D*) levels of theory. Distances are in Å and energies in kJ mol^{-1} . Drawn with structural and energetic data from ref 426.

dispersion provides an almost five times increase in the adsorption energy. For this system, the geometry differences between B3LYP and B3LYP-D* were less accentuated than those observed for the hydrophobic silica surface; however, a significant decrease of the $\text{OH}\cdots\pi$ distance (~ 0.3 Å) was observed upon dispersion inclusion.

The DFT-D2 scheme has recently been reformulated as DFT-D3 method⁴²¹ by including atom-pairwise specific dispersion coefficients and cutoff radii that are both computed from first principles. Moreover, a new nonempirical method to obtain C_6 coefficients from ground state electron density of a molecule or solid has also been proposed.⁴²⁷ Other approaches to account for dispersion corrections have been developed, for instance, those based on adding effective atom-centered potentials^{428–430} or explicitly including nonlocal terms in the correlation functional as in the vdW-DF method.⁴³¹ Alternatively, a new suite of M06 hybrid functionals based on meta-generalized gradient approximation, have been proposed by the Thrular's school^{432,433} and shown to be promising in handling noncovalent interactions. However, these functionals represent an improvement only up to medium range contacts and, to the best of our knowledge, are not implemented in codes running periodic calculations.

5.4. Basis Sets

Besides the errors associated with the chosen functional, one must also consider the errors due to the basis set expansion of the Kohn–Sham orbitals. Two major kinds of basis sets are currently used: localized Gaussian-type orbitals (GTO) and

plane waves (PW). Gaussian orbitals have the advantage that the number of basis functions depends on the number of atoms included in the crystalline cell but not on the dimension or shape of the cell. Moreover, due to the local nature of Gaussian functions, the true dimensionality of the system (0D, molecules; 1D, chains; 2D, slabs; 3D, crystals) is always obeyed. Transferability of GTO basis functions to periodic systems, however, should be done with care, particularly in the case of diffuse functions, to avoid an exponential increase in the number of bielectronic integrals to be evaluated due to the long-range nature of the tail of diffuse functions. This, in turn, also may lead to linear dependence in the definition of the wave function. On the other hand, the use of a limited number of basis functions entails the so-called basis set superposition error (BSSE), that is, a spurious stabilizing contribution arising from the improved description of a fragment in a complex due to the assistance of the basis sets of the other fragments. This error is normally corrected *a posteriori*, at the uncorrected geometries, with the counterpoise method.⁴³⁴

Plane wave basis sets are mainly used in solid-state simulations, along with pseudopotentials or projector augmented wave method to account for core electrons. Plane wave calculations are free of BSSE since they are not centered on the atomic nuclei, thereby describing any point in the supercell with the same quality. Moreover, energy and gradient calculations are more efficient than with GTO for GGA functionals. The reverse is true for hybrid functionals because the calculation of the exact exchange using plane waves is very expensive and applications of B3LYP based on plane waves started to appear only very recently⁴³⁵ compared with B3LYP with Gaussian-type orbitals, which were first run for studying the relative stability of silica polymorphs⁴³⁶ already in 1998. This prevents the use of hybrid functionals, which, on many occasions, are more accurate than standard GGA functionals. Another disadvantage of PW basis sets is that calculations are intrinsically periodic in three dimensions (3D), regardless of whether one is dealing with a molecule, a polymer, a slab, or a crystal, the 3D box being uniformly filled with plane waves. The quality of PW basis sets is specified by the electronic kinetic energy cutoff E_{kin} ; i.e., the higher E_{kin} the better the basis.

With the aim of analyzing the differences arising from using GTO and PW basis sets for hydrogen bonded systems, the formic acid molecule, its dimers, and the molecular crystal were computed with different GGA functionals. This study shows that, irrespective of the functional, PW and GTO results converge smoothly as a function of the quality of the basis set.⁴³⁷ Moreover, in an attempt to bridge the gap between methods routinely applied in materials science using PW basis sets and quantum chemical methods using local GTO basis sets, the behavior of PBE and PBE0 (including one-quarter of exact exchange to PBE) to determine geometries and atomization energies of molecules in the G2-1 data set was assessed using both basis sets. This study shows that discrepancies are very small. Indeed, both approaches yield identical results if convergence is carefully checked and reached for both methods.⁴³⁸

5.5. Molecular Dynamics Simulations

Exploring the potential energy surface, that is, solving the electronic Schrödinger equation at different nuclei positions, allows determination of thermodynamically stable structures (minima) and transition structures (first-order saddle points) at 0 K. For noninteracting rigid molecules, temperature effects can

be reasonably incorporated by assuming the rigid rotor-harmonic oscillator approximation and standard statistical methods from frequency calculations at the minimum energy structure. However, for large molecules, with soft torsional modes, or in solution, thermal effects must be estimated from a representative sampling of the phase space by using simulation techniques such as Monte Carlo and molecular dynamics. In Monte Carlo methods, the phase space sampling is attempted by random displacements of the relevant coordinate (Cartesian or internal coordinates) with the corresponding energy evaluation. The exploration is usually conditioned through a Boltzmann weighting scheme (Metropolis Monte Carlo), which ensures a reasonable efficiency in the search for local minima.⁴³⁹ Many millions of steps are needed, however, in order to ensure a statistically meaningful ensemble, as a result of the potential energy sampling.

The Monte Carlo steps cannot be considered as an evolution in time of the system. The latter can be rigorously achieved by a technique known as molecular dynamics. Introduced by Alder and Wainwright in 1959⁴⁴⁰ and extended by Rahman in 1964,⁴⁴¹ this method allows the study of the evolution in time–space phase of the atomic positions subject to the internal forces of chemical nature and to the kinetic energy due to the temperature of the system. To ensure energy conservation, however, the time step used to integrate the Newton equations should be smaller than that associated with the fastest vibration of the system, resulting in values close to 0.1 fs (10^{-16} s). Obviously, realistic applications of molecular dynamics imply a huge computational effort to explore the system behavior even for a very short time window. For that reason, molecular dynamics was developed to use a description of the internal forces resulting from classical force fields (see section 5.6.3), which ensures a fast evaluation of the energy and forces at the price of lower accuracy. The situation dramatically changed when the Car–Parrinello⁴⁴² (CP) method was introduced in 1985. In this method, forces are evaluated “on the fly” as resulting from a plane waves based density functional calculation in which electron density is not computed at each time step but estimated through the time integration of a cleverly defined Lagrangian operator. Since then, the CP method has enjoyed an enormous popularity in many different fields of molecular physics and chemistry.⁴⁴³ Among the cases in which molecular dynamics is beneficial are the adsorption of biomolecules on silica surfaces in solution, because this technique accounts for temperature effects, which are essential to understand their chemical behavior. Indeed, several studies presented in the frame of this review (e.g., section 9.1.1.2) have used molecular dynamics simulations to study surface reconstruction, water–silica interfaces, or biomolecule adsorption. While molecular dynamics (MD) simulations may be essential to afford detailed structural and dynamical insights, they can also become computationally prohibitive for relevant time scales. However, due to the continuous improvement of the power of high-performance computers, molecular dynamics simulations with on-the-fly computation of interatomic potentials from electronic structure theory can nowadays reach hundreds of picoseconds whereas classical molecular dynamics, based on predefined classical force fields, derived either from empirical data or from quantum chemical calculations, can extend up to the microsecond time scale. The reliability of these force fields, however, is a critical aspect that should be carefully analyzed, particularly when entering into large time scales (see section 5.6.3).

5.6. Approximated Methods

As seen in the previous sections, density functional theory is a formidable and general tool to treat, at least in principle, any kind of molecular or extended system. Limitations are, besides the intrinsic inaccuracy of the DFT itself, due to the rather steep rise in the computational resources needed to simulate systems containing hundreds or thousands of atoms. This is particularly relevant for the present topic because both biopolymers and silica surfaces imply a large number of atoms. For instance, the need for realistic models of the amorphous silica surface inevitably implies the adoption of very large surface unit cells without internal symmetry, which prevents the straightforward application of DFT based methods (see section 7). A further issue is the need to run molecular dynamics calculations when configurational entropy becomes a key ingredient for describing the system, as in all cases in which liquid water plays a key role. Another example in which molecular dynamics is mandatory is when modeling the bulk amorphization process with increasing temperature and reconstructions and relaxation of silica surfaces. To address the above points, a number of approaches have been developed in the literature to reduce the computational burden.

5.6.1. Semiempirical Methods. A possibility to speed up a calculation, by at least 3 orders of magnitude with respect to a DFT reference calculation, is to adopt semiempirical methods, which are all based on the neglect of differential overlap approximation by Pople et al.⁴⁴⁴ The evolution of the earlier CNDO and INDO through the MNDO method⁴⁴⁵ of the early 1980s continued up to the most recent PM6 and PM7 methods available in the MOPAC2012 computer code,⁴⁴⁶ maintained by James Stewart. Basically, no applications of the semiempirical methods to adsorption of molecules or biomolecules on silica have appeared due to the known weakness of these methods in dealing with H-bond and dispersive interactions, which are the dominant components of the adsorption energy for these cases. Nevertheless, the present status of the semiempirical methods can change the matter dramatically, due to important improvements addressed by the PM6-DH2^{447,448} and PM7 model Hamiltonians, which allow modeling of both H-bond interactions and London dispersive forces much more accurately than in the past.

5.6.2. SCC-DFTB Method. A level of theory that is intermediate between the semiempirical and the full DFT approach is based on the tight-binding approach originally suggested for periodic systems by Koster and Slater.⁴⁴⁹ The modern version is known as self-consistent charge density functional tight-binding method (SCC-DFTB) mainly developed by Elstner’s group^{450–454} and is an approximation to density functional theory (DFT), where the Kohn–Sham (KS) total energy is expanded up to the second order in the charge density fluctuations, δn , about a reference density, n_0 . The SCC-DFTB total energy is

$$E = \sum_i^{\text{occ}} \langle \psi_i | \hat{H}_0 | \psi_i \rangle + \frac{1}{2} \sum_{\alpha\beta} \gamma_{\alpha\beta} \Delta q_{\alpha} \Delta q_{\beta} + E_{\text{rep}}$$

where Δq_{α} is the Mulliken net charge on atom α and $\gamma_{\alpha\beta}$ is a function that depends on the $\alpha-\beta$ interatomic distance and on the Hubbard parameters U_{α} and U_{β} , calculated within the generalized gradient approximation with the Perdew–Burke–Ernzerhof (PBE) formalism. E_{rep} is the repulsion energy approximated as the sum of pairwise repulsive potentials adjusted to DFT calculations on reference systems. SCC-DFTB

Table 3. Most Common Classical Force Fields for Modeling Silica Material.

potential	year	description	ref
BMH	1988	Born–Mayer–Huggins 2-body potential plus 3-body terms for O–Si–O and Si–O–Si	472
TTAM	1988	2-body potential derived from Hartree–Fock calculation on SiO_2 model clusters.	473
BKS	1990	2-body potential derived from Hartree–Fock calculations on H_4SiO_4 and supplemented with experimental α -quartz elastic constants.	457
SSLCT	1992	2- and 3-body shell–ion model potential for silica and Al-substituted zeolites	474
HS	1994	consistent force field from Hartree–Fock calculations on small silica clusters	475
SS96	1996	shell–ion model potential for silica and zeolites from Hartree–Fock calculations on small silica clusters	476
SS97	1997	shell–ion model potential for silica and zeolites from B3LYP calculations on small silica clusters	477
ReaxFF	2003	reactive force field with DFT parametrization based on bond length/bond order and bond order/bond energy concepts	470
FFSiOH	2008	shell–ion model potential for silica with a 3-body term for H-bonding from periodic B3LYP calculations on α -quartz	467
GGMG	2008	rigid water modified Guillot–Giussani model potential ⁴⁷⁸ merged with specific SiO_2 potential to allow bond breaking/making	465

KS equations are obtained by applying the variational principle to the energy functional by expanding the KS orbitals into a suitable set of localized atomic orbitals, $\psi_i = \sum_v c_v^i \phi_v$. The KS equations are transformed into a set of self-consistent algebraic equations in which the Hamiltonian and overlap matrix elements are approximated in order to evaluate the calculation of bielectronic integrals. This results in the SCC-DFTB approach being comparable to semiempirical methods as far as computational efficiency is concerned. The energy can also be supplemented by a dispersion correction term⁴⁴⁸ not accounted for by the level of theory. The method has been recently used to study biological systems of large complexity.⁴⁵⁵ Specific applications to silica/amino acid interactions³²³ are reviewed in section 9.

5.6.3. Classical Force Fields. Another 3 orders of magnitude with respect to semiempirical and SCC-DFTB methods can be gained by representing the molecular structure by means of “mechanical springs” whose features (length, strength, etc.) mimic the different interactions occurring within the molecule and between different molecules. The set of parameters associated to the springs is known as “force field” and the relaxation of the mechanical energy is the result of a “molecular mechanics calculation”. The method has enjoyed enormous success starting from the first public force field for hydrocarbons, MM2 by Norman Allinger.⁴⁵⁶ The same approach has been extended to inorganic solids and, in particular, to the silica bulk. The complexity of inorganic materials and the paucity of experimental data needed to derive the force field parameters forced the adoption of simple two-body potentials for the description of each spring, compared with the most sophisticated terms (three-body and four-body terms) used for molecular cases. For silica, despite the success of the classical two-body potential by van Beest, Kramer, and van Santen (BKS),⁴⁵⁷ the accurate description of the highly flexible Si–O–Si bond (see section 2) required three-body terms involving O–Si–O and Si–O–Si bending modes. Also, the semi-ionic nature of the Si–O bond^{42,43} suggested to adopt a shell–ion model potential in which the electronic charge on the oxygen atoms is split into an inner (core) and an outer (shell) components linked by a mechanical spring^{458,459} to take the electronic polarizability of the oxygen atom into account. Many of the calculations on silica and oxides have been run using the General Utility Lattice Program (GULP) developed by Julian Gale.⁴⁶⁰ Along the above general lines, a large number of force fields for modeling the silica bulk have been developed, and a separate review would be needed to describe all of them in detail. Here we only summarize the most widely used force fields for silica through Table 3, while the interested reader may read the review by Schaible⁴⁶¹ on silicon and silica force fields

for more details. The majority of the studies focused on the silica bulk properties, the surfaces being limited to studies devoted to understanding the geometrical relaxation due to the bond cutting with respect to the bulk; water reactions involving the classical SiOH surface terminations were usually not considered (see sections 7.3 and 7.4). In other words, the state of the fully hydroxylated silica surfaces, either crystalline or amorphous, the latter being the most common for real silica surfaces (see section 2) has hardly been addressed with these force fields (as exceptions, see refs 462–466), because these studies were not concerned with the description of the silanol groups and their mutual H-bonding interactions. To specifically address the H-bonded features at the silica surface, the FFSiOH force field has recently been proposed, demonstrating excellent performance for both the bulk and the surface of silica materials as regards structures and energetic and phonon spectra, including the OH stretching region.⁴⁶⁷ FFSiOH is based on a shell–ion model potential to which a specific three-body term has been added to describe the H-bonding interaction between SiOH groups.

Extension of silica force fields to model the interaction with adsorbates is much more difficult due to the complexity of the potential energy surface characterizing the surface/adsorbate interaction. The need for a much more extended set of parameters to deal with the interactions between the biomolecule and the surface has prevented this kind of study from appearing in the literature. For the silica/water system (see section 8 for a deeper discussion), Garofalini et al.,^{464,465} Singer et al.,^{462,463} and Du et al.⁴⁶⁶ have extended the silica force field to include the interaction with water. A recent example of the problems that can be addressed with such an extended force field is the very recent work by Colombi Ciacchi’s group who developed a force field for the interaction of H_2O on a partially deprotonated silica surface.²⁸⁵ This is particularly relevant because SiOH groups at the hydroxylated silica surfaces transform to Si–O[−] in solution as a function of pH and ionic strength (see section 3), a kind of situation very common when studying protein adsorption.

The classical force fields are not fit for describing chemical reactions because the analytical expressions are not flexible enough to allow changes in the atomic connectivity during chemical reactions with the need for “on the fly update” of the corresponding parameters. Recently, a different approach has been suggested by van Duin and co-workers who developed ReaxFF for hydrocarbons,⁴⁶⁸ a reactive force field that was designed to model equilibrium structures as well as reaction intermediates and activated complexes in chemical reactions. The idea is to correlate bond lengths with bond orders and the latter with bond energies, following old insights from Linus

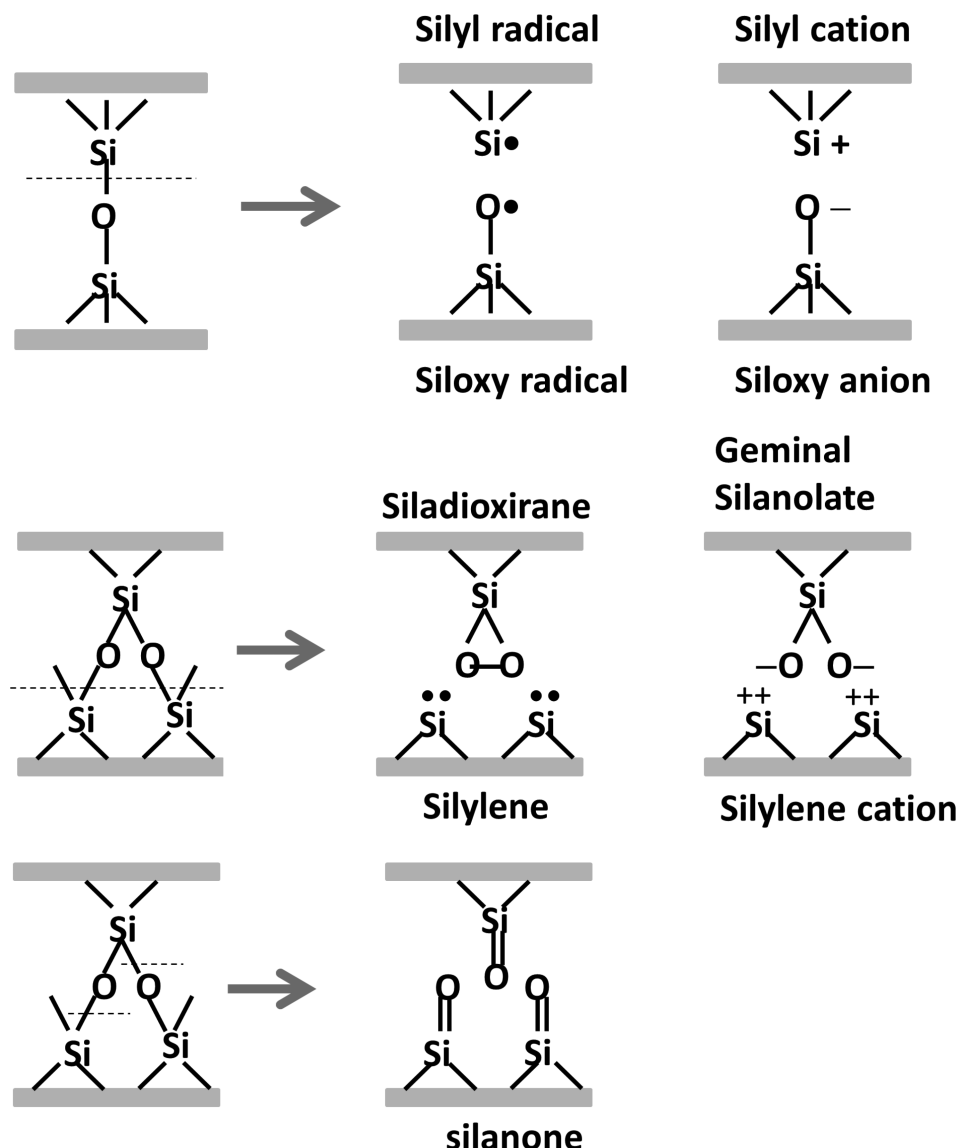


Figure 27. Silica surface sites derived from cleavage. Redrawn after ref 294.

Pauling's work.⁴⁶⁹ The same methodology was then extended to model silicon and silica materials.⁴⁷⁰ At the moment, ReaxFF has been very successfully applied to study the reaction of water on a freshly cleaved silica surface⁴⁷¹ (see also Table 3). While this approach is very powerful and promising, the development of new parameters is a rather cumbersome and a time-consuming process because they have to be calibrated against results from quantum mechanical calculations on test systems.

6. CRYSTALLINE SILICA SURFACES

6.1. Surface Sites

Crystalline silica surfaces are constructed by cutting a slab of a given thickness along a chosen crystallographic plane from the corresponding optimized bulk structure (see section 4.1). Cutting a silica structure involves breaking, homolytically or heterolytically, highly covalent Si–O bonds to form surface sites²⁹⁴ (see Figure 27), which are to a large extent responsible for the physicochemical processes on silica surfaces. In the homolytic cleavage, the pair of electrons of the broken chemical bond is divided evenly between the Si and O atoms, leading to the formation of two radicals. The possible surface sites

generated by homolytic cleavage of Q³ include the silyl ($\equiv\text{Si}^\bullet$) and siloxy ($\equiv\text{Si}-\text{O}^\bullet$) radicals. For Q², this cleavage can lead to silanone ($>\text{Si}=\text{O}$), silylene ($>\text{Si}^{\bullet\bullet}$) and siladioxirane (cyclo- $>\text{Si}(\text{O}_2)$) sites. In the heterolytic cleavage, the pair of electrons is transferred to the more electronegative oxygen atom, leading to the formation of charged species. The cleavage of Q³ sites produces surfaces with silyl ($\equiv\text{Si}^+$) cations and siloxy ($\equiv\text{Si}-\text{O}^-$) anions, whereas that of Q² would lead to silanone sites, doubly charged silylene cations ($>\text{Si}^{2+}$), and deprotonated geminal diols ($>\text{Si}(\text{O}^-)_2$).

Silica sites have been investigated with ab initio cluster calculations at the B3LYP level of theory and its bonding patterns characterized by natural bond order analysis.²⁹⁴ This work suggests that silanone sites and a pair of silyl/siloxyl radicals, resulting from homolytic cleavage, are the most stable Q² and Q³ sites, respectively, on a pristine silica surface. The heterolytic cleavage, entailing charge separation, is significantly less favorable than the homolytic one.²⁹⁴

Surface sites can be investigated by different experimental techniques. Radical sites such as the $\equiv\text{Si}-\text{O}^\bullet$ centers, also called nonbridging oxygen (NBO),^{296,479,480} are characterized

by photoluminescence^{481–487} and electron spin resonance (ESR) spectroscopy.^{480,488–491} From a theoretical point of view, both siloxyl and silyl surface defective centers have been analyzed in different surfaces: edingtonite (100), quartz (0001), and cristobalite (111), using embedded cluster models and the B3LYP functional.^{394,395} DFT (BLYP, B3LYP, and BH&HLYP) periodic calculations have also been carried out to analyze the siloxyl defect on three hydroxylated quartz surfaces ((001), (100), and (011)) in cristobalite (101) and tridymite (001),³⁴⁵ for siloxyl results show that the singly occupied orbital is mainly centered on one of the 2p orbitals of the nonbridging oxygen^{345,394} and that theory is able to reproduce the essential EPR properties of these centers,^{345,395} particularly when using hybrid functionals. Moreover, the overall absorption spectra calculated with time dependent DFT are in qualitative agreement with the experimental data.³⁹⁵ On the other hand, results show that computed properties of siloxyl sites are almost independent from the surface structure,^{345,395} confirming the strong local nature of this defect. If embedded in a hydroxylated surface, the surface features that change the most with the presence of this radical defect are the surface H-bonds, which tend to become weaker.³⁴⁵ For silyl sites, the unpaired electron is also localized in a sp^3 orbital of the three coordinated silicon, but the EPR properties, particularly a_{iso} , are more sensitive to the surface structure, mostly to the O–Si $^\bullet$ –O angle and the Si $^\bullet$ –O distance.³⁹⁵ Remarkably, calculations have also shown that these two well-known paramagnetic centers of silica surface are deep electron traps able to form stable negatively charged surface centers,³⁹⁴ which may have important consequences on their physical–chemical properties.

Silanone and siladioxirane surface sites, both diamagnetic, can be identified by optical⁴⁹² and vibrational spectroscopies.^{296,297} Moreover, detailed analysis of the low-lying excitations in these surface sites can be obtained from high-level ab initio quantum chemical methods,^{487,493} which can help to identify the bands on photoadsorption and photoluminescence spectra. For instance, the computed values associated with the lowest fully allowed singlet → singlet vertical transitions, found at ≈ 3 and ≈ 5 eV for siladioxirane and at ≈ 5.7 eV for silanone, are in good agreement with the experimental data (≈ 3 and ≈ 5 eV for siladioxirane and 5.65 eV for silanone), thereby providing support to the conclusion that the observed transitions in the optical spectra of the activated silica surface are due to silanone and siladioxirane sites.⁴⁹³ The photoluminescence properties of silanone and siladioxirane have also been investigated by quantum chemical methods,^{302,487} both surface sites constituting possible candidates for green- and red-light emitters. For silanone, the photoluminescence energies from the two lowest excited singlet states are calculated to appear at 2.3 and 1.6 eV, around 3.4–4.0 eV lower than the vertical excitation energies, due to a significant geometry relaxation in the excited states. Indeed, the Si=O double bond is highly elongated in the excited state, being transformed into a single bond, which leads to a loss of planarity of the >Si=O fragment. For siladioxirane, the excitation initiates the cleavage of the O–O bond and radiative transitions contribute to photoluminescence in the ranges 2.1–2.3 and 1.7–1.8 eV.

6.2. Surface Reconstruction

Freshly cleaved surfaces contain under-coordinated (also called “coordinatively unsaturated”) reactive sites. To investigate surface properties of fractured silica, models of low-index

unrelaxed surfaces of quartz were constructed and analyzed using periodic density functional theory calculations.^{295,494,495} Surface energies, defined as $E_{\text{surf}} = (E_{\text{slab}} - nE_{\text{bulk}}/(2A))$ with E_{slab} being the energy of a pristine slab, E_{bulk} the energy of SiO_2 in the bulk, n the number of SiO_2 in the supercell, and $2A$ the total surface area (top and bottom), were computed considering both spin-paired and spin-polarized calculations to describe heterolytic and homolytic cleavage, respectively. Noticeably, in nine out of ten cases, the specific surface energy differences between results of spin-polarized and spin-paired calculations was less than 2%.⁴⁹⁵ This is in contrast to cluster calculations,²⁹⁴ which suggest that the homolytic cleavage of a Si–O bond is energetically more favorable than the heterolytic one. The stabilization of surfaces with charged sites was attributed to intersite electrostatic interactions,^{295,494} which are not taken into account in cluster calculations. From this study, it was suggested that cuts with a more uniform distribution of surface sites at the opposite sides of the cleavage plane were associated with lower surface energies. Moreover, cuts with a more uniform distribution of oxygen atoms among the ruptured geminal surface sites, favoring neutral sites over the charged ones, also exhibited lower surface energies. The calculated unrelaxed surface energies of quartz range from 0.161 to 0.200 eV Å $^{-2}$ (2.6 to 3.2 J m $^{-2}$);^{295,495} these are high values, rendering these surfaces very reactive. As a result, they quickly reconstruct or, in the presence of water, become hydrolyzed leading to geminal Q 2 >Si(OH) $_2$ and terminal Q 3 ≡Si–OH silanol groups.

Several computational studies have been carried out to characterize the major features of surface reconstruction on different silica surfaces.^{295,496,497} First principles DFT (LDA) molecular dynamics simulations for (0001) α -quartz⁴⁹⁷ indicate that the most favorable surface reconstruction presents an unexpected densification of the two uppermost layers of SiO_2 tetrahedral units, with three- and six-membered rings, at 300 K. Similar results are obtained with interatomic potential based calculations at 400 K.⁴⁹⁶ During the reconstruction of the surface, the initial under-coordinated silicon and oxygen atoms of the cleaved surface recover full coordination, forming six-membered rings (S6R) parallel to the surface and three-membered rings extending into the bulk (see Figure 28).

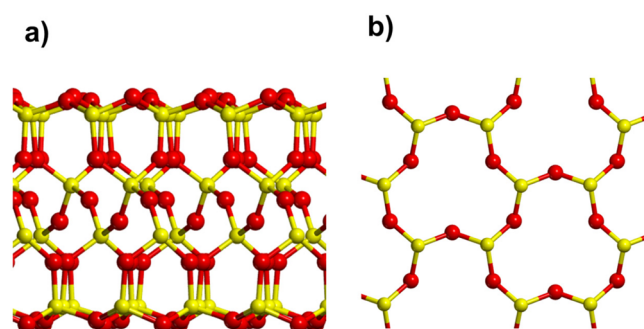


Figure 28. Most stable reconstruction of (001) α -quartz: (a) side view; (b) top view. Drawn with data from ref 391.

Reconstruction of most common pristine surfaces (101), (102), (112), (100), (111), (110), and (001) of α -quartz was also investigated with periodic DFT(GGA) and plane wave calculations.²⁹⁵ Four types of reconstruction were found: (a) formation of strained two-membered silicon rings (S2R) from silyl and siloxy sites, (b) formation of (S2R) $^+$ structures with

two side sharing S2R, (c) formation of three-membered silicon rings (S3R), and (d) transformation of silanone sites into siloxane sites. Energies of cleaved unrelaxed surfaces range from 0.161 to 0.200 eV Å⁻² (2.6 to 3.2 J m⁻²),^{295,495} whereas those associated to reconstructed surfaces range from 0.071 to 0.142 eV Å⁻² (1.1 to 2.3 J m⁻²). Relaxation energies are determined by the kind of reconstruction, the formation of S2R to saturate the valencies of undercoordinated oxygens exhibiting larger values than relaxation of silanone sites. Relaxation energies computed in ref 295, however, are smaller, and thus, reconstructed surface energies are higher, than those reported in other studies,^{391,497} because in the former reference relaxation was limited to a single silica tetrahedral layer, while in fact it can extend as deep as six SiO₂ molecular layers.⁴⁹⁷ Full relaxation, however, can lead to an overstabilization of the slab. Indeed, a recent study on the (001) α -quartz surface has revealed the importance of the slab thickness on the reconstructed surface energy, showing that a layer slab made of six [SiO₄] groups is needed to achieve converged values.³⁹¹

DFT(LDA) molecular dynamics simulations have also been performed recently on the (011) surface of α -quartz at room temperature.⁴⁹⁸ Reconstruction leads to the formation of a fused seven-member ring through the reaction of two adjacent O[•] radicals, followed by linking one of the reactive O with a nearby silicon. Remarkably, in the newly formed structures some of the silicon atoms exhibit a pentacoordinated environment, usually distorted between pure trigonal bipyramidal and square pyramid geometries. Moreover, in a few cases, oxygen atoms also became tricoordinated (see Figure 29).

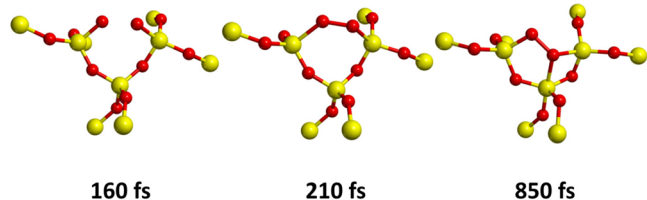


Figure 29. Process occurring during reconstruction of the (011) surface of α -quartz. Drawn with data from ref 498.

6.3. Hydroxylated Surfaces

Fractured silica is very hydrophilic so that exposure to water results in the hydrolysis of the surface sites with the formation of silanol groups. In principle, hydrolysis can lead to single silanol sites (Q³(OH)), to silanediols, that is, geminal silanols (Q²(OH)₂), and to silanetriol centers (Q¹(OH)₃). The latter ones, however, are thermally unstable and have not been detected in NMR studies as already mentioned. Previous calculations for (001) α -quartz have shown that the cleaved surface reacts exothermally with water until it becomes fully hydroxylated.^{497,499,500} When a water molecule approaches the surface, its oxygen atom binds to an under-coordinated Si atom, while one of its hydrogen atoms is transferred to a neighboring nonbridging oxygen, leading to the formation of two silanols (see Figure 30).⁵⁰⁰ Car–Parrinello ab initio molecular dynamics (CP-MD) simulations for the α -quartz–water interface at 1000 K and 0.3 GPa show that dissociation of H₂O molecules into H⁺ and OH[−] at the Si-terminated surface takes place on a very short time scale of about 2 ps.⁵⁰¹ On the other hand, calculations on cluster models⁵⁰² suggest that the energy barrier of this process is only 12–13 kJ mol^{−1} and, thus, that it will readily proceed under ambient conditions of

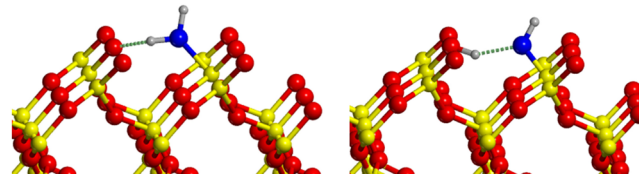


Figure 30. Hydration mechanism for the cleaved (0001) α -quartz. Drawn with data from ref 500.

temperature and humidity. As the surface becomes hydrated, hydrogen bond chains start appearing. The fully hydroxylated (001) α -quartz exhibits zigzag hydrogen bond networks with alternating strong and weak hydrogen bonds. Remarkably, the dense (reconstructed) surface, characterized by three-membered and six-membered rings with siloxane bonds at the top,⁴⁹⁷ is shown to be hydrophobic, suggesting that surfaces formed by nonstrained siloxane bonds are essentially hydrophobic.⁵⁰³

The hydrogen bonding features in the hydroxylated surfaces of quartz,^{295,306,391,499,500,504} cristobalite,^{306,315,492,505,506} tridymite,³⁰⁶ and amorphous silica^{507–509} have been analyzed in several studies with periodic DFT calculations. Among them, the study of Musso et al.³⁰⁶ provides a very systematic study of many different hydroxylated surfaces of quartz, cristobalite, and tridymite polymorphs. In particular, five surfaces were considered for quartz, Q(001), Q(100), Q(010), Q(011), and Q(101), four for cristobalite, C(001), C(100), C(101), and C(110), and three for tridymite, T(001), T(100), and T(110). Since hydrolysis of freshly cut surfaces proceeds very quickly in the presence of water vapor, surfaces were generated by cutting a slab of a given thickness along the chosen crystallographic plane from the corresponding optimized bulk structure and saturating the unfilled valencies with H and OH. This leads to different kinds of silanols (vicinal, geminal, or interacting, see section 2.2) and OH densities depending on the polymorph and crystallographic plane. The thickness of the slab was carefully chosen to avoid an excessive deformation as a result of considering a surface that is too thin. This is important since the slab thickness determines its rigidity and, thus, it can largely influence surface H-bonds.^{306,391} The distribution and pattern of OH groups as well as the H-bond features of each surface are displayed in Figure 31.

Optimized structures show different H-bond patterns depending on the distribution of the hydroxyl groups on the surface. C(100) and T(001) models, with the highest slab rigidity and the latter with the smallest OH density as well, only show isolated surface silanols. Q(010), Q(011), C(001), and T(100) surfaces exhibit a single H-bond interaction inside the crystalline cell, whereas C(110) shows four silanols interacting through a four-membered H-bond ring. The remaining surfaces, Q(001), Q(100), Q(101), C(101), and T(110) present infinitely extended H-bond chains.

In order to evaluate the stability of each slab model, the surface energy was computed according to the following reaction $aB_{\text{SiO}_2} + b\text{H}_2\text{O} \rightarrow cS_{\text{SiOH}}$, where B_{SiO₂} refers to the bulk unit cell and S_{SiOH} to the slab unit cell. The formation energy per unit cell and the surface energy were defined as $\Delta E_{\text{cell}} = cE_{\text{cell}}^{\text{cell}} - (aE_{\text{bulk}}^{\text{cell}} + bE_{\text{H}_2\text{O}})$ and $\Delta E_{\text{surf}} = \Delta E_{\text{cell}}/(2A)$, respectively, where A is the surface unit cell area. Computed values for each surface, as well as structural data, are given in Table 4. It can be observed that in almost all cases surface energies are negative, resulting in a thermodynamically favored surface formation.

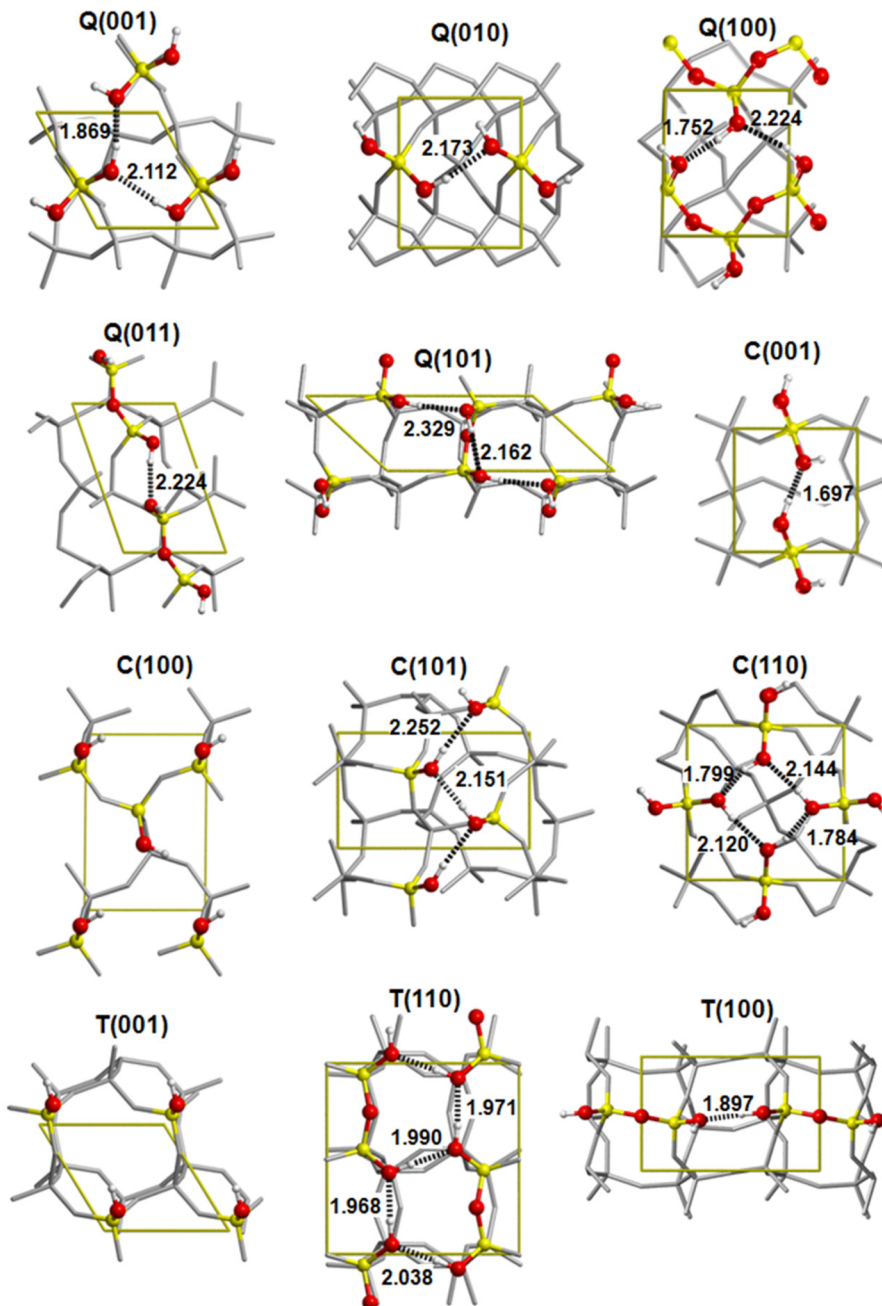


Figure 31. B3LYP-optimized structures of fully hydroxylated α -quartz, α -cristobalite, and α -tridymite surfaces (top face representation). Hydrogen bond distances ($\text{H}\cdots\text{O}$) in \AA as dotted lines. Reprinted with permission from ref 306. Copyright 2009 American Chemical Society.

Table 4. Structural Data for Quartz (Q), Cristobalite (C) and Tridymite (T) Slabs^a

	Q(001)	Q(010)	Q(100)	Q(011)	Q(101)	C(001)	C(100)	C(101)	C(110)	T(001)	T(100)	T(110)
<i>a</i> (\AA)	4.866	4.841	4.972	5.003	10.202	4.969	5.019	8.255	6.856	5.078	5.080	8.030
<i>b</i> (\AA)	4.963	5.565	5.361	7.290	4.983	5.002	6.873	5.014	6.733	5.076	7.923	7.951
γ (deg)	119.1	90.0	90.0	110.1	137.3	90.0	89.5	90.0	90.0	121.5	89.9	90.1
<i>A</i> (\AA^2)	21.1	26.9	26.7	34.3	34.5	24.9	34.5	41.4	46.2	22.0	40.3	63.9
τ (\AA)	11.0	8.6	8.9	8.0	7.4	20.0	13.2	9.3	7.6	9.3	10.7	11.0
$\langle \text{Si-O} \rangle$ (\AA)	1.633	1.635	1.632	1.636	1.636	1.631	1.631	1.633	1.637	1.629	1.630	1.632
$\langle \text{O-H} \rangle$ (\AA)	0.980	0.970	0.980	0.968	0.972	0.973	0.965	0.974	0.979	0.964	0.971	0.979
$\rho(\text{OH}/\text{nm}^2)$	9.5	7.4	7.5	5.8	5.8	8.0	5.8	4.8	8.7	4.5	5.0	6.3
ΔE_{surf} (J m^{-2})	-0.35	-0.12	-0.27	-0.01	-0.06	-0.21	0.00	-0.06	-0.28	0.01	-0.08	-0.24

^aCell parameters (*a*, *b*, γ), cell area (*A*), slab thickness (τ), $\langle \text{Si-O} \rangle$ and $\langle \text{O-H} \rangle$ bonds, the surface OH density (ρ), and surface energy (ΔE_{surf}).

Exceptions are observed for T(001) and C(100) for which no surface H-bonds are present, thereby suggesting that H-bonding between surface silanols is the key factor that drives the surface energy. Indeed, the surface energy is the result of three different factors: (i) the rupture of Si—O—Si bonds of the bulk followed by the formation of surface silanols; (ii) the structural relaxation of the interior of the slab, and (iii) the formation of H-bonds between the surface silanols. Process i is common to all considered surfaces and can be treated as a fixed contribution per Si—OH group to the surface energy. Its local covalent nature should lead to a near independence of the corresponding value on the considered slab. Processes ii and iii are intermingled; however, the fact that the bathochromic shift of the OH donor stretching frequency, which can be considered a measure of the H-bond strength, exhibits an inverse correlation with the surface energy³⁰⁶ (see Figure 32) suggests that H-bonding is probably the most representative contribution to the differences observed.

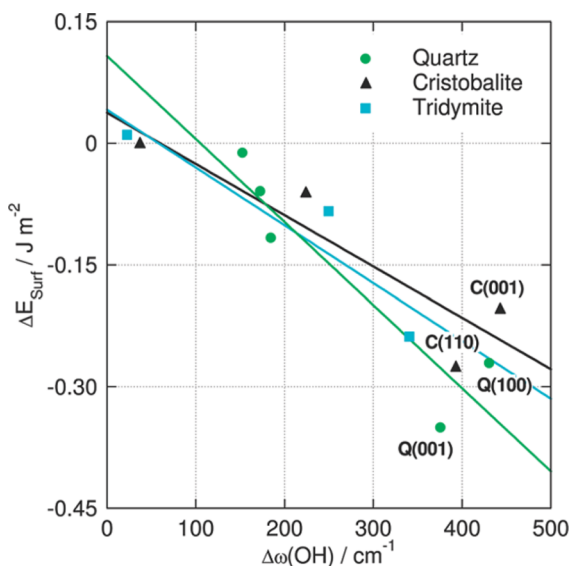


Figure 32. Surface energies, ΔE_{surf} , vs the largest bathochromic harmonic OH frequency shift, $\Delta\omega(\text{OH})$, calculated for all polymorph surfaces with respect to the value of 3904 cm^{-1} for the isolated OH groups of the T(001) surface. Reprinted with permission from ref 306. Copyright 2009 American Chemical Society.

Overall, hydroxylated silica surfaces are characterized by different types of OH groups (geminal, vicinal, and isolated) and by different H-bonding patterns that result from the interaction between hydroxyl groups. The H-bond pattern strongly depends on the disposition and on the density of the OH groups at the surface. Although the majority of the crystalline models exhibit infinitely connected H-bond chains, small local H-bonded rings or isolated pairs through completely free OH groups have also been found, depending on the OH density and the rigidity of the silica framework.

7. AMORPHOUS SILICA SURFACES

As we have seen in section 4, the most common way to deal with silica simulations is to adopt the periodic boundary condition method. Still, the problem of modeling the surface of amorphous silica is an open one, because no reference to experimental structural data can be made due to the lack of information about the fine details of the bulk and even more

seriously of the surface itself. As we have already mentioned, a proper combination of different hydroxylated surfaces derived from crystalline silica can be used to mimic the complexity of the amorphous silica surface. In this section, we only focus on models of amorphous silica surface exclusively derived from a true amorphous bulk within the PBC that have been characterized in detail in terms of their surface physicochemical features. We are also referring here to surfaces that have healed their main structural and electronic defects (see section 2), that is, surfaces only exhibiting Si—O—Si bridges and Si—OH groups, the main functionalities present in a water environment. We have singled out two models obtained using quantum mechanical methods based on DFT: the first one from Tielens et al.⁵¹⁰ and the second one from Ugliengo et al.,⁵⁰⁹ respectively.

7.1. The Tielens Model

This model derives from an amorphous silica bulk originally proposed by Garofalini⁴⁶⁴ who adopted molecular dynamics based on a specifically derived SiO_2 empirical potential for the simulation (see section 5.6.3). The usual procedure based on PBC, as described in section 4, was adopted by the authors who carefully avoided unstable defects at the surface by transforming three-coordinated Si atoms and nonbridging oxygen atoms, derived from the geometrical cut of the SiO_2 bulk in SiOH groups, by manual addition of H_2O molecules. To be able to adopt DFT-based methods the starting slab model was about 10 \AA thick, with an in plane cell size of $13 \text{ \AA} \times 17.5 \text{ \AA}$, which resulted in $\text{Si}_{26}\text{O}_{65}\text{H}_{27}$ composition (118 atoms as a whole). Ab initio molecular dynamics based on plane waves basis set was carried out at 400 K using the PBE functional at the Γ point for 5 ps. Spontaneous dehydroxylation was observed, resulting in the formation of small silica rings. Subsequent optimization at 0 K with higher accuracy in the number of k points and the kinetic cutoff was carried out. Results shows that the surface is very thin (about three layers thick) with thickness varying between 5 and 8 \AA (see Figure 33 for details).

The film thickness is not uniform and at the thinnest point, the upper side is separated from the lower one by just one HO—Si—O—Si—OH link. The full set of harmonic frequencies have been computed, as well as the NMR shielding constants, by means of the GIPAW⁵¹¹ approach, which ensures good quality of the results. Ring nuclearity peaked around four-, five-, and six-membered rings, with seven-, eight-, nine-, and ten-membered rings being only a minor feature. Interestingly, the model does not show either two- or three-membered rings, the former being unstable with respect to reaction with H_2O . The Si—O—Si angle distribution is very broad, covering a $130\text{--}180^\circ$ range, without a distinct maximum, in agreement with the high pliability of this bond (see section 2 on this point). The OH density of 5.8 OH nm^{-2} is the same for the upper and the lower face, and it is higher than the value of 4.5 and 4.9 OH nm^{-2} reported by Zhuravlev.⁷⁸ A relatively high population of geminal silanols has been found, with an uneven distribution between the two surfaces (23% and 46% for the upper and lower face, respectively). Due to the high OH density, the population of H-bonded SiOH groups is more than $1/3$ of the total (38% and 31% for the upper and lower face, respectively). Table 5 shows the distribution of the various kinds of SiOH groups. The absolute deprotonation energy of the OH groups has been computed, showing a higher acidity of the Q^3 sites compared with the Q^2 ones, resulting in a theoretical difference of 2.5 units of $\text{p}K_a$ in favor of the geminal sites. The NMR

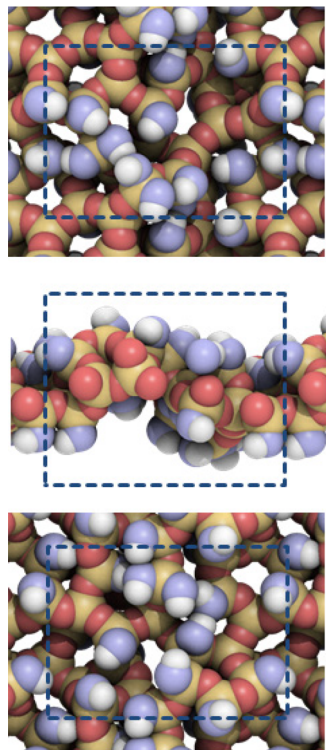


Figure 33. The top, lateral, and bottom views of the Tielens model. Oxygen atoms of the surface OH groups are colored in blue. Molecular graphics rendered by Qutemol.⁷³

Table 5. Properties of the Ugliengo Amorphous Silica Surfaces⁵⁰⁹

ρ [OH nm ⁻²]	OH (geminals) ^a	H-bond contacts ^b		free OH	% free OH
		OH···OH	OH···OSi ₂		
7.2	28 (8)	16	1	4	14
5.8 ^c	24 (6)	7	1	4	17
5.4	20 (3)	7	1	7	35
4.5	16 (1)	3	3	7	43
2.4	8 (1)	2	0	4	50
1.5	4 (1)	0	1	3	75

^aThe total number of OH groups (for the upper and lower surfaces) and, in parentheses, the number of geminal SiOH groups. ^bH-bond cutoff: 2.15 Å. ^cData for the Tielens surface.⁵¹⁰

$\delta(^{29}\text{Si})$ chemical shift has been found in nice linear correlation with the Si–O–Si angle for values belonging to the three Q², Q³, and Q⁴ families in agreement with experimental data.^{512,513} In light of the relevance of the OH vibrational features for silica surfaces (see sections 2 and 3), the ab initio harmonic OH stretching frequency values have been computed and shown to linearly correlate with the OH bond length. Calculations report a rather high difference between the two internal OH stretching frequency values for a Q² site, about 36 cm⁻¹, large enough to be distinguishable experimentally. This is in disagreement with both experimental evidence, which shows that the OH frequency values for Q² and Q³ sites are almost indistinguishable (ref 118 and section 3.1.4), and quantum mechanical calculations on the (001) hydroxylated surfaces of edingtonite, for which the B3LYP (scaled) harmonic frequencies were 3737, 3733, and 3735 cm⁻¹ for the Q³ and Q² sites, respectively. The discrepancy between the amorphous model and the one

derived from a crystalline bulk is probably due to the high OH density of the amorphous model, which forces almost all SiOH groups to “feel” their neighboring groups with a consequent perturbation of the OH stretching frequency, known to be very sensitive to local electric fields. In light of this result, it has to be established whether the acidity difference between the Q³ and Q² sites is not the consequence of different intermolecular interactions rather than being an intrinsic electronic effect of the Q² moiety (see also section 10 on this question).

In conclusion, the Tielens model, due to the addressed limitations, should be used with some caution to mimic the behavior of a fully hydroxylated amorphous silica surface (4.5 and 4.9 OH nm⁻²). The number of atoms still allows the adoption of normal computational resources to run plane waves based DFT calculations. Its main weakness is the exceedingly small thickness, which may render the model too flexible when adopted to simulate adsorption phenomena. This model has been used to study the adsorption of water and glycine, and these studies are reviewed in sections 8 and 9, respectively.

7.2. The Ugliengo Model

This model was derived starting from a bulk cristobalite with 192 atoms in the unit cell. Classical empirical partial charge rigid ion model potential⁵¹⁴ has been used to run molecular dynamics at very high T and then cooled down to room temperature. This process ensured an amorphization of the starting material without introducing defects (two-membered rings, >Si=O, and others) in the final structure. The bulk was then cut along one of the cell axes and the surface unfilled valencies (above and below) were automatically saturated by an algorithm encoded in the graphical program MOLDRAW.⁵¹⁵ Basically, a double-bonded Si is transformed into a Q² site by attaching two OH groups, whereas a single-bonded Si is removed, leaving the only bonded oxygen atoms singly bonded to the underneath slab. This is to avoid the creation of Q¹ sites (by attaching three OH groups to the singly bonded Si atom) because Q¹ sites are not found at the silica surface (see sections 3.1.4 and 3.1.5). A triple-bonded Si atom is transformed into a Q³ site by attaching a single OH group. All singly bonded oxygen atoms are transformed into OH groups. Because these transformations are operated in a geometrical fashion, they do not require any quantum mechanical calculations. The healed structure showed a silanol density of 7.2 OH nm⁻², typical of values for a sol–gel amorphous silica, was 14.5 Å thick, and consisted of 222 atoms. It was fully relaxed (internal and cell size) at B3LYP/6-31G(d,p) level using a massive parallel version of CRYSTAL06 code.^{291,516} The final structure is shown in Figure 34.

The number of geminal silanols amounts to 29% of the total OH population, not too far from the value for the Tielens model. With this structure as a starting model, the dehydration process occurring by outgassing the silica at high T was simulated by geometrically removing one water molecule from the closest OH···OH pairs and making a new Si–O–Si silanol bridge. The new resulting structure was fully relaxed, and this process was repeated in order to get OH densities of 5.4, 4.5, 2.4, and 1.5 OH nm⁻², respectively. This simulates different stages of the dehydroxylation process. Three representative structures are shown in Figure 34, and the corresponding data on the SiOH populations are reported in Table 5, together with the data for the Tielens model.

Data of Table 5 shows that the number of OH···OH H-bonds decreases dramatically with the drop in OH density. For

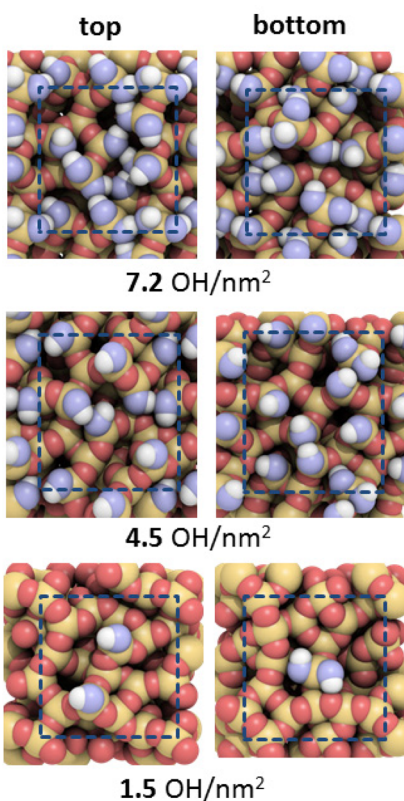


Figure 34. Top and bottom views of the Ugliengo model with variable OH densities. Oxygen atoms of the surface OH groups are colored in blue. Unit cell as dashed lines. Molecular graphics rendering by Qutemol.⁷³

the most representative case, 4.5 OH nm^{-2} , it corresponds to 19% of the total OH groups. Interestingly, the same percentage resulted for the H-bonds between OH and the siloxane Si—O—Si bridge. This is somehow surprising because the Si—O—Si is a very weak Lewis base. In the present case, the distortion introduced in the structure in the simulated dehydroxylation process brings about Si—O—Si angles much smaller than the normal 145° value (see also section 2 for the flexibility of the Si—O—Si bond) thereby increasing the associated basicity. B3LYP calculations of the dehydroxylation processes that bring the 7.2 OH nm^{-2} toward the 1.5 OH nm^{-2} model confirm the expected endothermic nature of the process as schematically shown in Figure 35.

The values also confirm that the endothermicity dramatically increases with the degree of dehydroxylation up to 359 kJ/mol to reach the 1.5 OH nm^{-2} case. The infrared spectrum in the OH region for a hypothetical surface exhibiting 4.5 OH nm^{-2} is given in Figure 36 (see original work⁵⁰⁹ for technical details). In order to account for the nonuniform OH density of a real silica surface, the spectral contributions from each of the considered models have been merged, with weights reflecting the expected experimental populations, obtaining a very good agreement with the experimental spectrum recorded for an Aerosil 300 from Degussa outgassed at 450 K in the OH stretching region (see Figure 36).

The 1.5 OH nm^{-2} Ugliengo model (albeit with some reduction in the slab thickness to decrease the computational burden) has been recently chosen to simulate the energetic and vibrational features of adsorbed ammonia and compared with experimental results.¹⁶⁹ The same approach was adopted to

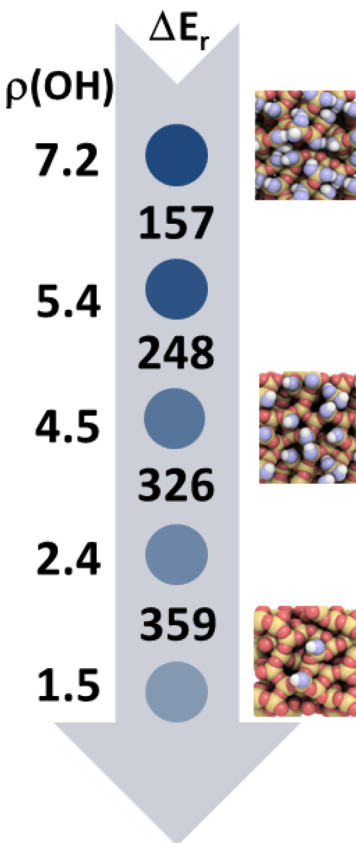


Figure 35. (left of the arrow) Silica surface OH density $\rho(\text{OH nm}^{-2})$; (within the arrow) dehydration reaction energies (kJ/mol) for reducing the OH density; (right of the arrow) cartoon of the silica surface for $\rho(\text{OH nm}^{-2}) = 7.2, 4.5$, and 1.5 , respectively. Oxygen atoms of the surface OH groups are depicted in blue. Molecular graphics rendering by Qutemol.⁷³

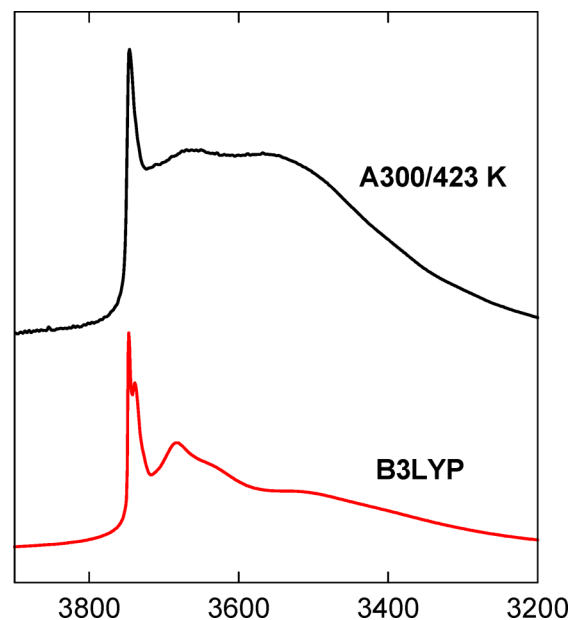


Figure 36. (top) Experimental infrared spectrum of silica Aerosil 300 outgassed at 423 K. (bottom) Simulated B3LYP infrared spectrum for the Ugliengo models. The range of wavenumbers (units in cm^{-1}) covers the OH stretching region.

Table 6. Different Methods and Target for the Simulation of Amorphous Silica Surfaces^a

method	studied systems	ref
MD with an effective three-body potential specific for SiO ₂	bulk silica and surfaces without water reconstruction; detection of S2R only at the surface; NBO defects coherent with the experimental SiOH density	518
MD with modified TTAM potential ⁴⁷³ for SiO ₂ and SPC ⁵¹⁹ for H ₂ O	simulation of a fully hydrophobic silica surface; the MD protocol was tweaked in order to minimize the formation of S2R, Si(3), and NBO; hydrophobicity was defined with respect to the heat of liquefaction of H ₂ O; a silica surface free from S2R, Si(3), and NBO was found hydrophobic	520
MD with van Beest–Kramer–van Santen (BKS ⁴⁵⁷) empirical potential	silica clusters (14, 19, 27 Å) and film (29 Å thick); density of surface S2R = 0.6 nm ⁻² ; no surface SiOH.	521
BLYP CPMD ⁴⁴² on BKS ⁴⁵⁷ generated surface	study of the reaction of S2R with H ₂ O and NH ₃	507
comparison between MD BKS ⁴⁵⁷ and BLYP CPMD ⁴⁴²	study of the distribution of rings and geometrical parameters as a function of the adopted method; CPMD disfavors the S2R formation over BKS	522
MD with Born–Mayer–Huggins empirical potential ⁵²³	silica surface without SiOH groups rich in NBO and Si(3); electrostatic potential maps of silica surface to establish reactivity with H ₂ O	524
MD with Buckingham, Coulomb, and Morse, three-body term to Si–O–H	silica surface with NBO, Si(3), and S2R reacted with H ₂ O; concentration of 4.5 OH nm ⁻² ; surface reactivity, separated NBO and Si(3) > NBO + Si(3) > S2R > S3R	466
BLYP CPMD ⁴⁴² on BKS ⁴⁵⁷ generated periodic SiO ₂ surfaces	exothermic reaction of H ₂ O with S2R at the silica surface	525
MD with Cerius ² GLASSFF 2.01 and GLASSFF [–] 1.01 ⁵²⁶ force fields to silica and CHARMM ⁵²⁷ developed parameters for water interaction	silica slabs and pores produced by annealing an amorphous bulk; care to avoid NBO, Si(3), and S2R at the surface and to convert them to SiOH groups; SiO [–] also included in the simulation; study of the wettability as a function of surface hydroxylation	528
MD with an extension of BKS ⁴⁵⁷ and SPC/E ⁵²⁹ force fields to silica/H ₂ O interactions	hydrated and hydroxylated silica surfaces; ab initio parametrization of the force field; hydrophilic and hydrophobic patches resulted as a function of SiOH density; heat of immersion in good agreement with experiment	462,463
MD with modified Stillinger–Weber potential ⁵³⁰ for Si and Vashishta et al. ⁵³¹ for SiO ₂	oxidized Si surfaces compared with full amorphous SiO ₂ model; heat of immersion and water structuring higher for the oxidized Si surfaces than for the amorphous SiO ₂	307
MD with water modified Guillot–Giussani model potential ⁴⁷⁸ merged with specific SiO ₂ potential to allow bond breaking and making	atomistic mechanism to the healing of Si(3) and NBO; silica surface models with 3.8 OH nm ⁻² ; proton transfer allows penetration of water up to 7 Å within the surface	465
MD with SiO ₂ reactive force field, SERIAL-REAX ⁴⁷⁰	simulation of very large SiO ₂ surface unit cells and their reaction with H ₂ O; spontaneous reconstruction by H ₂ O reaction in 250 ps	471
MD using specific SiO ₂ /H ₂ O force field ^{532,533}	simulation of water adsorbed in Vicor glass nanopores with fully hydroxylated internal walls; no bulk H ₂ O features for 1–4 nm pores	534
MD, ab initio and refinement of the Cole et al. ³⁰⁷ potential for SiO ₂ /H ₂ O system	simulation of the fully hydroxylated/H ₂ O interaction; improved parameters by MP2 calculations on clusters to treat Si–O [–] /H ₂ O interaction	285

^aS2R refers to the two-membered (SiO)₂ ring, Si(3) to the three-coordinated silicon, and NBO to the non-bridging oxygen of silanone.

Table 7. Different Methods to Model the Reactivity of S2R Defects towards H₂O and Glycine^a

model and methods	$\Delta_r E$	$\Delta_a E$	ref
BLYP/DZP on H ₂ (SiO) ₂ H ₂ as a cluster model of the S2R defect; S2R IR prediction of D2 modes	-134	27	537
BLYP β -cristobalite (111) reconstructed surface with periodic formation of S2R defects; amorphous silica model from BKS ⁴⁵⁷ simulation to simulate isolated S2R defects	-127		506
ONIOM2[B3LYP/6-31G*:UHF/STO-3G] on clusters containing the S2R defect cut out from SiO ₂ silica models from MD with polarizable ion model potential based on extension of WAC potential ⁵³⁸	68; ^b 107 ^c		502,539
BLYP CPMD ⁴⁴² on BKS ⁴⁵⁷ generated periodic surfaces	-168	34	507
PBE/plane waves mechanically embedded		40	540
MD with Buckingham, Coulomb and Morse, three-body term to Si—O—H; periodic surface models	-458		466
ONIOM2[B3LYP/6-31+G(d,p):MNDO] on Si ₁₀ O ₁₆ H ₁₂ (SiO) ₂ cluster model; IR prediction of S2R modes	-122	82	75
B3LYP/6-31+G(d,p)//ONIOM2[B3LYP/6-31+G(d,p):MNDO] on Si ₁₀ O ₁₆ H ₁₂ (SiO) ₂ cluster model; interaction and reactivity with glycine	-109	0.5	541

^a $\Delta_r E$ and $\Delta_a E$ are the reaction and activation energies for the opening of the S2R defect, respectively. Units in kJ/mol. ^bGas-phase molecule.

^cEmbedded in the silica matrix.

define a thinner 4.5 OH nm⁻² surface and to study the interaction of aspirin and ibuprofen on both surfaces.⁵¹⁷

7.3. Other Models

A number of authors have provided models for the amorphous silica surface. Since many of them focused on the surface defects, we will not discuss all of them in detail. Table 6 collects a brief summary of the considered models together with the methods for their simulations.

7.4. The S2R Surface Defect

As was discussed in sections 2 and 3, the defects remaining at the silica surface are, in principle, three-coordinated Si(3), nonbridging oxygen NBO, >Si=O, and strained rings, S2R or (SiO)₂. At ambient conditions, due to the presence of moisture, the Si(3) and NBO defects can hardly survive the reaction with H₂O (see also references in Table 6). The S2R is an exception, because it naturally results from the vicinal site condensation during the thermal treatment of silica at $T > 900$ K. As already reported in sections 2, 3.1.4, and 3.1.7, the S2R concentration is rather small (in the initial works,^{137,535,536} it was reported to be around 0.1 S2R nm⁻², although more recent data after severe activation steps suggest that it can reach up to 0.5 S2R nm⁻²). Interestingly, the formation of S2R surface defects is quite general because they have also been identified by their IR fingerprint in crystalline all-silica silicalite.³⁶³ S2R defects are very reactive toward molecules with hydrogen attached to electronegative elements like oxygen and nitrogen (section 3.1.7): H₂O, MeOH, and NH₃ react very fast with S2R defects, forming new surface functionalities, that is, two SiOH groups, SiOH and Si—O—Me, and SiOH and SiNH₂, respectively. Due to their relevance, a number of studies have been especially aimed at modeling S2R, and they are summarized in Table 7.

The majority of these studies focused on the calculation of the reaction of S2R with H₂O, for which both the reaction energy, $\Delta_r E$, and the energy barrier, $\Delta_a E$, have been computed. Data from Table 7 reveal that there is no general consensus on the values associated with the two quantities. In our opinion, there are two main reasons for that: (i) different procedures to define the amorphous silica surface; (ii) different computational methods. The first issue is responsible for a variable degree of geometrical tension on the S2R defect, which depends not only on the internal Si—O—Si angles (which are close to 90°) but also on the distortion of [SiO₄] tetrahedra surrounding the S2R defect. This, in turn, is determined by the model adopted (cluster or periodic, see section 4) and by the procedure to arrive to the S2R defect starting from a given bulk silica model (see section 4). For instance, adoption of small clusters like in

refs 75 and 537 decreases the tension outside the S2R zone because no constraints can be enforced as the rest of the surface is missing. Some further geometrical constraints imposed on the larger cluster adopted by Rimola et al.⁷⁵ showed their relevance to the computed value of the $\Delta_a E$. When PBC are adopted to make a dehydroxylated SiO₂ surface, the heat-and-cool MD procedure to arrive at the S2R defect also matters because it is difficult to ensure that the internal geometrical tension has been properly equilibrated. Reproducibility of the calculations can also be critical. The second issue is even more critical because the level of adopted theory has a deep influence on both $\Delta_r E$ and $\Delta_a E$. Even considering DFT as more reliable than empirical force fields, the adopted functional is very important. For instance, data from Table 7 reveal that functionals based on Perdew exchange like PBE and PW91 tend to underestimate the value of $-\Delta_a E$ compared to MP2 and Becke based functionals like B3LYP and BLYP. In summary, what is lacking is a systematic investigation of both aspects in order to provide a more robust picture of this important class of reactions.

The interaction between S2R defects and glycine has been modeled by Rimola et al.⁵⁴¹ since it has been argued that they may be present at the surface of the silica grains that are the core of the interstellar dust particles. This means that glycine, eventually formed under prebiotic conditions within the icy mantle surrounding the core grain, can react with the S2R defect, thus remaining firmly attached to the grain dust. Because comets are the results of accretion of dust grains, this can be one mechanism to seed the primordial Earth with glycine by comet bombardment. Rimola et al.⁵⁴¹ also showed that glycine can then be released from the grain by the action of at least four water molecules at room temperature.

8. ADSORPTION OF WATER ON SILICA SURFACES

The interaction of silica with water occurs in a great number of situations, either natural, as in geochemistry, prebiotic chemistry or biomineratization, because water and silica are the two most common terrestrial compounds, or derived from human activity, as in the fields of sensors, biomedical devices, or chromatography. Silicon is spontaneously covered with a SiO₂ layer, so that SiO₂–water interactions also occur on electronic devices. Water adsorption on hydrophilic surfaces induces large differences in the adhesion of species in solution at the nanoscale. Indeed, at the local scale, water organization (or lack of organization) at the surface has a major influence on the adsorption mode of species in solution. At a larger scale, it can

provide surface and dissolved species charge screening in the form of a dielectric.⁵⁴²

Before entering into the details of the main contributions, it is worth mentioning the major experimental data that shed light on the influence of the hard matter (silica) on the soft one, even at short length scales (1 nm or less): Shen et al.⁵⁴³ reported that water at the interface with Q(0001) organizes in an ice-like structure in a certain pH range (Figure 37a). At the opposite, Engemann et al.⁵⁴⁴ evidenced that amorphous silica induces a liquid-like layer at the silica–ice interface (Figure 37b).

However, experiments do not (or not yet) give information on the local H-bond breaking or making between silanols and water. Theoretical work is needed to disentangle those local aspects and help interpret spectroscopic data.

Here we focus on the influence of the hydroxylation structure in the energetics and structure of adsorbed water and on the interplay between the preexisting H-bond network between silanol groups and the formation of a new network between silanols and water. In this chapter, only fully hydroxylated surfaces are considered in interaction with water. Theoretical works on the reaction of water with defects like S2R that are known to be healed in the presence of water^{507,75,140} are not considered in this part (with the exception of the $\equiv\text{SiO}^\bullet$ species, which is possibly responsible for crystalline silica toxicity); neither are works focusing on the first steps of silica dissolution (see refs 501 and 545–549 for a nonexhaustive list) that can occur for instance on rough surfaces.^{547,550,551} Complex interface processes such as dissolution/precipitation and polymerization reactions in solution^{552,553} are not discussed here. In addition, whereas crystalline or amorphous plane surfaces are reviewed, confined spaces in nano- or mesoporous silicas (e.g., see ref 534) are not treated.

The bulk of the literature available may be partitioned into several categories that are illustrated in Figure 38 and detailed in Tables 8–12. Two axes have been considered: they correspond to increasing complexity of the silica model and increasing amount of water adsorbed, respectively. The zones of intensive research have been the clusters/isolated water/high level of theory, the crystalline and amorphous silica/water/classical molecular dynamics, and crystalline silica/isolated to bulk water/*ab initio*. One may note two facts: (i) there are only two systems that have been covered integrally with *ab initio* methods from the isolated water molecule to bulk liquid interface, Q(001) and C(100), and (ii) the amorphous silica/liquid water interface has not yet been investigated by means of *ab initio* techniques. Surprisingly, the reactivity of thin SiO_2 films on Si with water (section 3.1.8) has not been a subject of investigation, with a single exception.³⁰⁷

A strong evolution of the research topics and methods with time is noticed: many works have been performed in the last years of the 20th century using cluster calculations at a high level of theory. Indeed, the first attempts to study water interactions with silanols were performed using cluster calculations. Since 2000, more and more works have been devoted to crystalline surfaces with *ab initio* periodic calculations; meanwhile, force fields have been developed to mimic silica (crystalline and amorphous) properties. In the past few years, significant breakthroughs in the understanding of crystalline and amorphous silica–water interactions, with discrete molecules and with bulk water, have been achieved with DF-based methods.

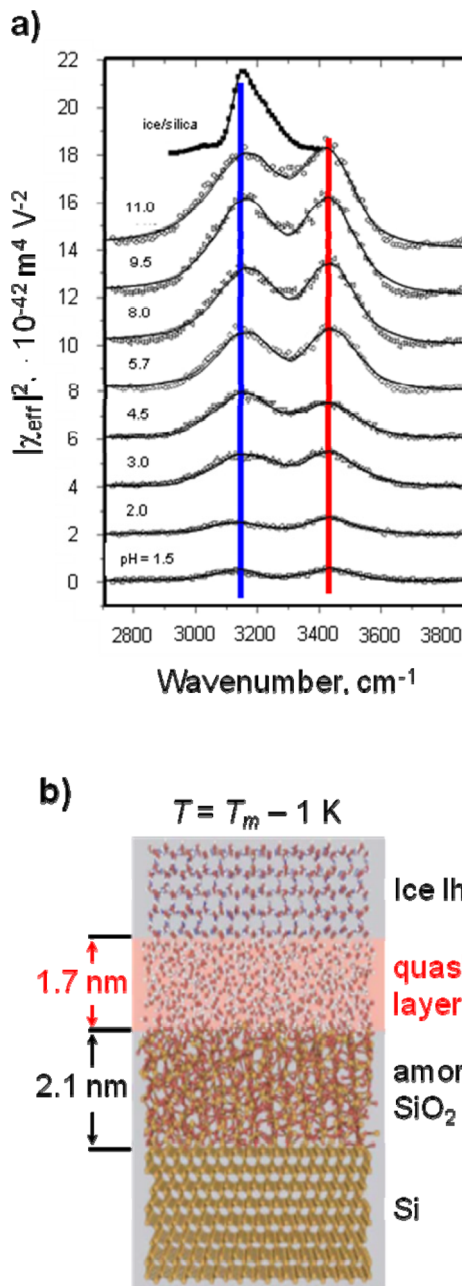


Figure 37. (a) SF vibrational spectra of water/α-quartz (001) at various bulk pH values. The ice/fused-silica spectrum is shown for comparison; adapted with permission from ref 543, Copyright 2004 Elsevier. (b) Real space model of the ice– SiO_2 interface associated with $T = T_m - 1 \text{ K}$. T_m = melting temperature of ice. The densities used in this representation correspond to the values deduced from the measurement. Reprinted with permission from ref 544. Copyright 2004 American Physical Society.

For obvious reasons, several periodic *ab initio* works have been devoted to the interaction of crystalline surfaces, mainly quartz surfaces, with water. In contrast, because several methods have been developed to generate bulk amorphous silica with force fields, works on amorphous silica surface are more numerous with classical methods.

Ab initio works on crystalline silica surfaces have been reviewed by Yang and Wang in 2006.⁵⁵⁴ Since then, a significant number of important studies based on electronic structure methods have appeared, including the comparison of

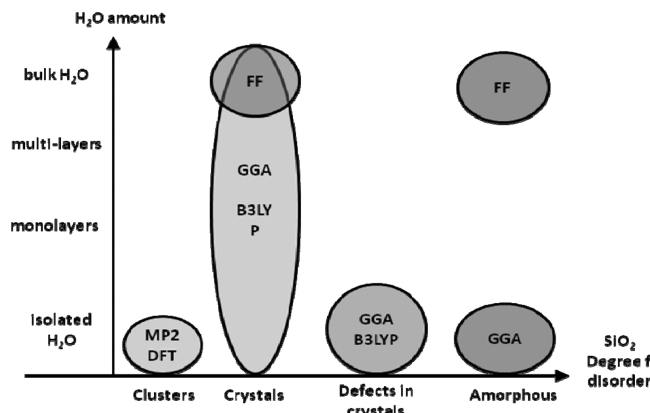


Figure 38. Main theoretical studies performed on the silica/water system.

several crystalline polymorphs and terminations, new crystalline surface analyses, new ab initio based amorphous silica models, and the properties of silica–water interface, such as pK_a calculations (see section 3.1.2).

8.1. The Early Story: First Principles Cluster Based Calculations

In the early days, water–silanol interactions were studied using a cluster approach.⁵⁵⁵ These cluster calculations were reviewed³⁹ in 1994 as mentioned in section 4.2 and continued by some authors until the end of the 1990s and early 2000,^{223,294,338–340,556,557} Here we do not aim to perform an exhaustive presentation of the work done but to describe the average trends. Generally the quantitative data (adsorption energies) are compared with experimental calorimetric data^{8,82,173,342,558–563} and gas chromatography.⁸⁷ The measured heat of water adsorption has been reported around -60 kJ/mol , but heterogeneity of hydrophilic patches caused adsorption enthalpies ranging from -90 to -44 kJ/mol . The calculated frequencies were also compared with vibrational spectroscopic

data.⁵⁶⁴ As a general rule, water interacts with silanols more strongly as a H-bond acceptor than as a H-bond donor, due to the rather low basicity of surface OH and Si–O–Si groups. Most studies focus on two types of silanols: isolated⁵⁶⁵ and geminal,⁵⁶⁶ because the differences between these two types is easily modeled through cluster calculations. In particular, the reactivity of geminal silanols was addressed to understand the cytotoxic reactivity of quartz, a surface that exhibits a high density of geminal silanols.⁵⁶⁷

The configurations obtained for the adsorption of a single water molecule on different types of silanols with cluster calculations are reported in Figure 39. The isolated silanol acts as H-bond donor to water^{338,339} with a value of $\Delta E_{\text{ads}} = -40\text{ kJ/mol}$, compared with -46.5 kJ/mol on the geminal silanols,³³⁹ where H_2O bridges the two species, as calculated at the B3LYP/DZP level. Other authors calculated room temperature enthalpies of -21.4 and -23.2 kJ/mol for water adsorption on the isolated and geminal species at the B3LYP/6-311++G(3df,2pd) level.⁵⁶⁸ Highly accurate calculations (MP2/aug-cc-pVTZ) on minimal clusters provide an adsorption energy of water on an isolated silanol of -27.3 and -17.3 kJ/mol , without and with the counterpoise correction for BSSE included, respectively.³³⁸ Note that in the work ZPE correction was not accounted for. Note that the BSSE error cannot be neglected. Water adsorption enthalpies at the MP2/6-311++G** level at 350 K were calculated to be -45.7 , -56.9 , and -46.7 kJ/mol on the isolated, vicinal, and geminal silanols, respectively,⁸⁷ clearly showing the same H-bond donor capability of Q^3 and Q^2 sites. Water adsorption on siloxane is athermic (calculations performed at the MP2/6-311++G** level).⁴⁶² To the best of our knowledge, cluster calculations of water adsorption on associated silanols are rare, because of the lack of structural information. Cyprik⁵⁶⁹ studied the interaction of several silanol clusters with water, from the isolated silanol to H-bonded vicinal silanols. On those silanols, the adsorption of water (calculated at the MP4/6-31G* level) is two times more exothermic (-60.2 and -30.3 kJ/mol with BSSE correction)

Table 8. Theoretical Works Based on Electronic Calculations, Using Periodic Conditions, Devoted to Water at Crystalline Silicas: Nature of the Surface Studied, Method, and Water Coverages Investigated

polymorph	surface	method	water coverage	ref
Q	(001)	PW91 UPP 350 eV	isolated water to monolayer	504
		B3LYP TZ polarization	isolated water	574
		PW91 PAW 400 eV	one to five water layers	576
		B3LYP Lanl2dz	isolated water	542
		PBE 400 eV, AIMD	bulk water	584
		BLYP TZVP2 + AGTH, 280 Ryd, BOMD	bulk water	585
		CPMD PBE Vanderbilt 25 Ry, 1000 K	water film (2–3 water layers)	501
	(100)	B3LYP TZ polarization	isolated water	574
	(011)	B3LYP TZ polarization	isolated water	574
	(101)	PBE PAW 400 eV	isolated water to monolayer	575
C	(010)	PW91, 680 eV cutoff	bulk water	587
	(100)	PW91 UPP 350 eV	isolated water to monolayer	346
	(100)	rPBE and PW91	one water monolayer	600
	(101)	B3LYP TZ polarization	isolated water	574
	(111)	PW91 UPP 350 eV	isolated water to monolayer and frequency analysis	573
E	(001)	B3LYP GTO	isolated water and monolayer and frequency calculations	317
	(100)			
T	(001)	B3LYP 6-31G*	one and two water molecules in acid and basic media	583
	(100)	DFT-TB MD 15 ps	bulk water	323,586
	(001)	B3LYP TZ polarization	isolated water	574

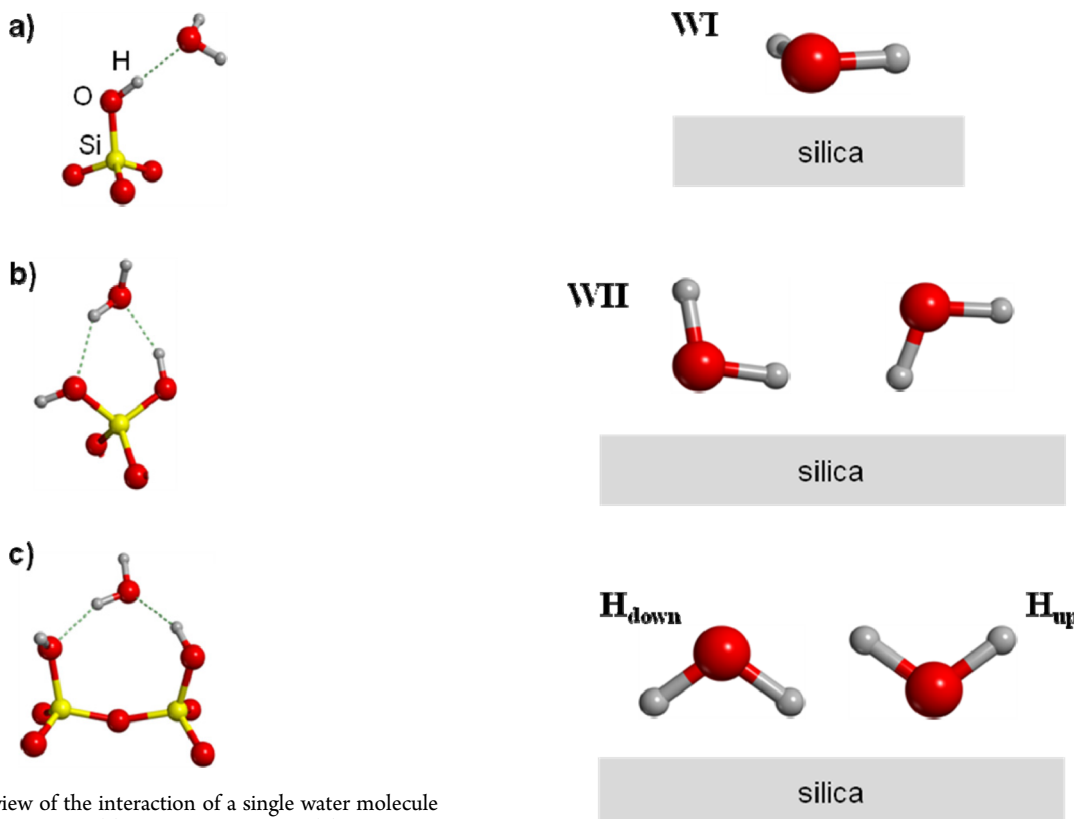


Figure 39. Synthetic view of the interaction of a single water molecule with silica clusters representing (a) an isolated silanol, (b) a geminal pair, and (c) vicinal silanols.

than that of water on isolated silanol (-30.1 and -19.7 kJ/mol).

8.2. Water on Crystalline Hydroxylated Silicas

Periodic studies of water at crystalline surfaces originate either from the chemists or the physicists communities; chemists are mostly interested in crystalline surfaces as potential models for amorphous silicas, whereas physicists are interested in the crystalline phases per se, for example, on reactivity at defects. Another difference lies in the studied coverages: in the chemistry community, strong attention has been put on low water coverage and frequency calculations, in order to assign IR spectra recorded on amorphous silica polymorphs.^{317,503,566,568,570–572} In contrast, even if low coverages are also investigated in the physics community, a strong effort is devoted to characterize complete water layers.^{346,504,573–576} Whereas numerous IR data are available on amorphous silicas,^{82,577–581} calculations of vibrational frequencies^{317,346,504,573,575,582} are more difficult to compare with experimental data recorded on crystalline samples⁵⁴³ because of the lack of data. It is interesting to notice that IR can help to estimate the amount of bulk water contained in a glassy silica.⁵⁸¹

Hydroxylated crystalline silica has a hydrophilic character. Water always interacts with silanol groups through H-bonding. Figure 40 shows the nomenclature generally adopted to describe water orientation versus the surface, which will also be used here.

There are different possible orientations for water: In type I (WI, see Figure 40), water is adsorbed parallel to the surface. Consequently, water can only act as a H-bond acceptor from the surface. In type II (WII), water is not parallel to the surface; it may be placed either with one H pointing away from the

Figure 40. Nomenclature adopted for designing water orientation at silica surface. See text for description.

surface (water then acts as a H-bond acceptor) or with an H pointing toward the surface (water acts as a H-bond donor). In some particular cases, water is oriented with both H pointing toward the surface (H_{down}). In other cases, water has the two protons directed away from the surface (H_{up}).

Some first principles works have explored the adsorption of water molecules beyond saturation (full monolayer),^{542,574,583} and of increasing numbers of water molecules on hydroxylated silica surfaces, from one isolated water to one monolayer,^{317,346,504,573,575} from one monolayer to several layers,^{501,576} and finally at the interface with bulk water^{501,582,584–588} (see Tables 8–11). Calculations using force fields have been devoted to the interface with water thin films and bulk water,^{542,559,589–599} with only two exceptions where a single water layer was investigated.^{594,600}

8.2.1. The Low Coverage Case. At low coverage, the water–hydroxyl interaction is predominant. The adsorption of one isolated water molecule has a very local effect.

Few crystalline surfaces exhibit isolated silanols, or rather noninteracting ones, E(100) and C(111) being the main ones. In the most stable configuration of E(100), water acts as a single H-bond acceptor and may be H-donor to a siloxane oxygen (Figure 41a).⁵⁷⁴ The same was found using cluster models.³⁴⁰ In contrast, on the C(111) surface, which exhibits noninteracting silanols (separated by 5 Å), water adsorbs in a hollow site and is double proton donor and proton acceptor.⁵⁷³ This example shows the limits of cluster models to mimick noninteracting silanols.

Geminal silanols cover the Q(001),^{295,499} Q(010),^{499,599} C(100),⁵⁷³ and E(001)^{317,601} surfaces. On Q(001) water does not adsorb above a geminal pair but rather in a bridging

Table 9. Theoretical Works Based on Classical Force Fields, Using Periodic Conditions, Devoted to Water at Crystalline Silicas: Nature of the Surface Studied, Method, and Water Coverages Investigated

polymorph	surface	method	coverage, water layer thickness and properties studied	ref.
Q	(0001)	CLAYSFF	isolated water to bulk liquid	542
Q	(0001)	PW91 300 eV cutoff ultrasoft pseudopotentials and Sanders, Baram, and Parker potentials	dissociative adsorption of water on a dry surface	589
Q	(0001)	Sanders, Baram, and Parker	bulk water at the nonhydroxylated and fully hydroxylated surface and quartz dissolution	590
Q	(100), (0001), (011)	CHARMM	bulk water	591
Q	(100), (001), (011)	CHARMM	bulk water	595
Q	(111)	COMPASS	water and oil mixture adsorption competition	597
Q	(010)	Cerius2	bulk water, diffusion coefficient study in water near the surface	599
C	(100)	COMPASS	water monolayer	600
C	(111)	SCP and LJ	bulk water interaction with surfaces of different OH coverages	592
C	(100), (111)	SPC and PN-TrAZ	bulk water, simulated adsorption isotherm	559
Q	(100), (011)	CHARMM	bulk water	593
C	(100)	CHARMM	water monolayer	594
C	(111)	ClayFF	bulk water	596
C	(111)	ClayFF	bulk water	598

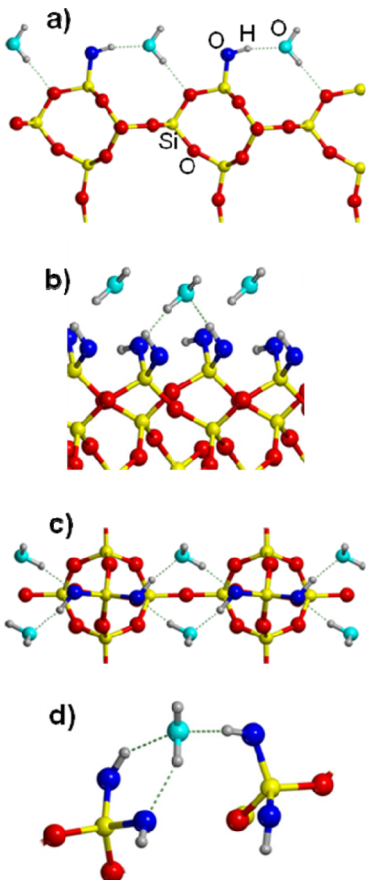


Figure 41. Water at low coverage on crystalline silicas (periodic DFT calculations): (a) isolated silanols on edingtonite; adapted with permission from ref 317, Copyright 2008 Institute of Physics; (b) water on geminal silanols of Q(001); adapted with permission from ref 574, Copyright 2011 American Chemical Society; (c) water on geminal silanols of E(001); adapted with permission from ref 317, Copyright 2008 Institute of Physics; (d) water on C(100); drawn with data from ref 573.

position between two geminal pairs (Figure 41b,c).^{306,504} Among the two possible sites, a weakly and a strongly H-bonded site, adsorption is more stable on the weakly H-bonded site, because breaking this bond is less energetically expensive than breaking a strong H-bond. A similar result is found on E(001)³¹⁷ (Figure 41b,c). An even more complex pattern occurs on the C(100) surface with water bridging the geminal silanol pairs and accepting an additional H-bond from a silanol (Figure 41d).⁵⁷³ The complexity of these surface structures cannot be easily modeled by a cluster approach. To our knowledge, no ab initio study is available on the Q(010)/water interaction.

The Q(101)⁵⁷⁵ surface exhibits vicinal silanols. Water interacts with a vicinal pair as a H-bond donor and also as a H-bond acceptor from a surface silanol (Figure 42).

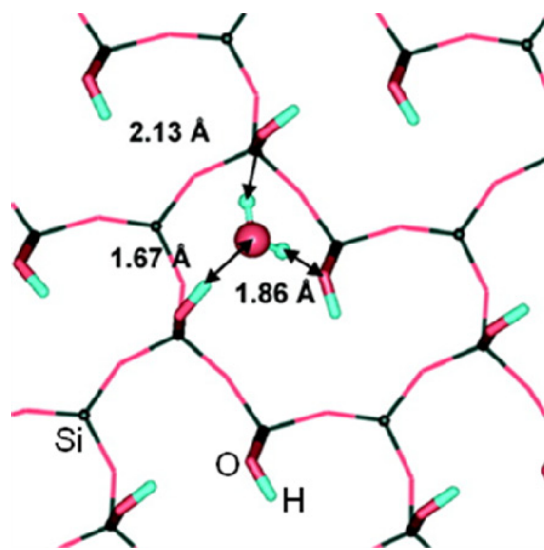


Figure 42. Snapshot of an isolated water adsorbed on vicinal silanols of Q(101) surface. Reprinted with permission from ref 575. Copyright 2011 American Chemical Society.

Finally, nonvicinal silanols able to bind to a water molecule are present on all but the E(100) surface. The situation is complex because the possible adsorption sites are not unique and a preexisting H-bond network may be broken. Water always acts as H-bond acceptor from a silanol and as H-bond donor to one or two silanols. Water binds to Q² silanols belonging to different geminal pairs on Q(001), E(001), and C(100), and Q³ silanols on the other surfaces, with the exception of E(100) (isolated silanol). Figure 43 illustrates the

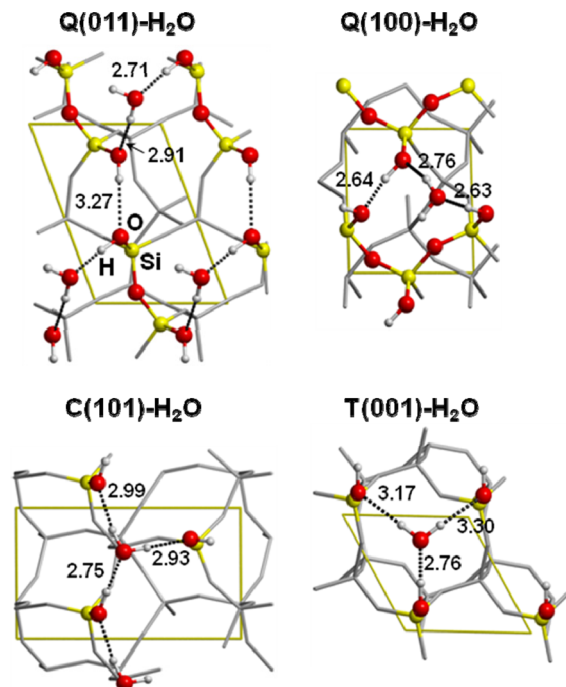


Figure 43. Adsorption of water at low coverage on adjacent silanols: (a) Q(011), (b) Q(100), (c) C(101), and (d) T(001). Reprinted with permission from ref 574. Copyright 2011 American Chemical Society.

configuration obtained for the Q(011), Q(100), C(101), and T(001) surfaces.⁵⁷⁴ Remarkably, in all cases, rows of H-bonds involving silanols and water are formed at the surface. In other

words, water on the crystalline surface helps the formation of the H-bond network.

The absolute adsorption energies recorded in the literature at low coverage (or isolated in the case of cluster calculations) are all within the 48–58 kJ/mol range, when water forms one or two H-bonds. A higher value of 77 kJ/mol is obtained for water inside a cycle of silanols, as on the (111) cristobalite surface, with the formation of three H-bonds.

8.2.2. Intermediate Coverages. The situation is also intricate at intermediate coverages because, on the one hand, stabilizing H-bond structures between water molecules and between water and silanols are formed, and on the other hand, preexisting H-bonds between silanols must be broken in order to establish these interactions. Table 10 shows that there is no apparent coherence between the calculated water adsorption energy and either the water coverage or the number of H-bonds formed per water molecule.

It is not an easy task to disentangle this question. This was addressed in ref 574, where it is shown that the water–surface binding energy shows an inverse correlation with the OH surface density (Figure 44). This interesting result somewhat contradicts, at least for low water coverages, the general view that surface hydrophilicity increases with the OH density. This study also demonstrates that the adsorption occurs at the cost of breaking the preexisting H-bond network (Figure 44). For T(001) and Q(011), the adsorption process does not imply the rupture of pre-existing H-bonds between silanols, which are absent in the former case and maintained on the silica/water molecule adduct in the latter, whereas in the case of Q(100) and Q(001), the adsorption process implies breaking pre-existing infinite chains of H-bonds. The C(101) surface exhibits an intermediate behavior with a weak H-bond (O…O distance is equal to 3.363 Å) being disrupted upon adsorption of water.

The computed adsorption enthalpy values for the quartz surfaces (at $T = 303$ K), which span the –51 to –70 kJ/mol range, are in reasonable agreement with experimental data.⁸² For cristobalite outgassed at 423 K, an experimental value of –55 kJ/mol for $\theta(\text{H}_2\text{O}) = 2.2$ has been measured,⁵⁶⁰ to be compared with the computed enthalpy value of –73 kJ/mol (at 0 K) for the adsorption on the C(101) surface at the same H_2O coverage.

8.2.3. The Case of the Water Dimer. Some authors have studied the interesting case of the water dimer adsorption,

Table 10. DFT Studies of Water Adsorption on Hydroxylated Crystalline Silicas at Low and Intermediate Coverages: Energetics and H-Bonding

polymorph	surface	hydroxyl type	method	adsorption mode of water	water density (molecule nm ⁻²)	absolute adsorption energy (kJ/mol)	ref
Q	(0001)	geminal	PW91 UPP 350 eV	1 H _{acc} , 1 H _{don}	1.2	52.1	504
	(0001)	geminal	B3LYP TZ basis + polarization	1 H _{acc} , 1 H _{don}	4.5	56.4	574
	(100)	vicinal	B3LYP TZ basis + polarization	1 H _{acc} , 1 H _{don}	3.5	64.9	574
	(011)	interacting silanols	B3LYP TZ basis + polarization	1 H _{acc} , 1 H _{don}	2.8	77.5	574
	(101)	vicinal	PBE PAW 400 eV	1 H _{acc} , 2 H _{don}	0.7	60.8	575
	(100)	geminal	GGA, Vanderbilt, 350 eV	1 H _{acc} , 1 H _{don}	1.9	51.1	346,573
C	(101)	vicinal	B3LYP TZ basis + polarization		2.2	81.4	574
	(111)	isolated	PW91 UPP 350 eV	1 H _{acc} , 2 H _{don}	3.7	74.3	573
E	(001)	geminal	B3LYP GTO		3.5	55.0	317
	(100)	isolated		1 H _{acc} , 1 H _{don} to a O	2.2	46.0	
T	(001)	isolated	B3LYP GTO	1 H _{acc} , 2 H _{don}	4.3		574

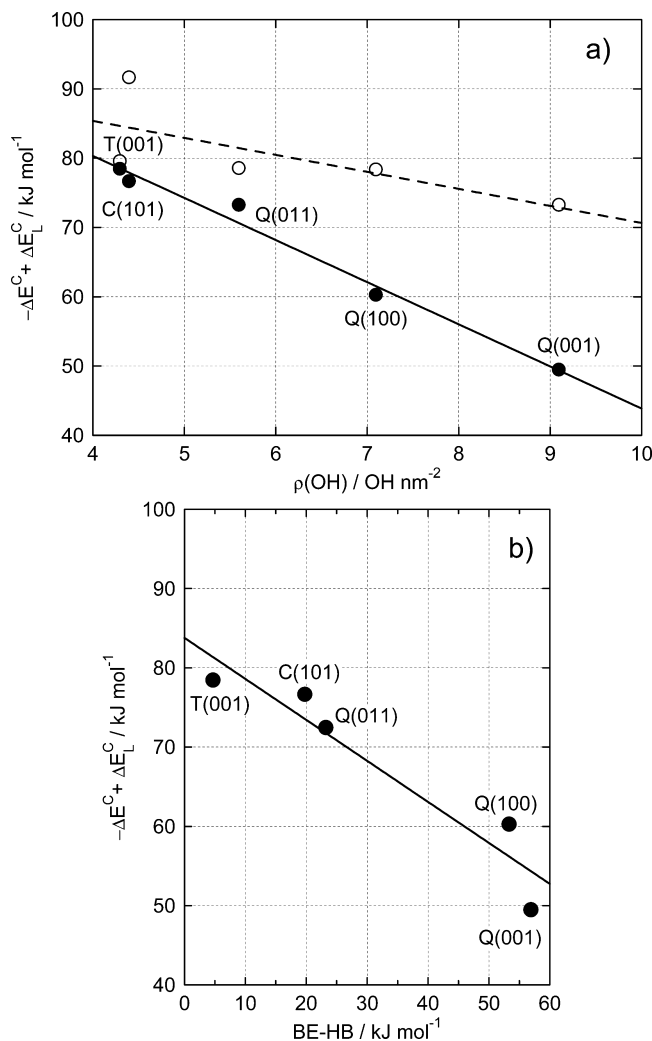


Figure 44. Water–surface binding energy (kJ/mol) (i.e., total interaction energy minus lateral interactions between adsorbates) reported for water on several crystalline surfaces (a) as a function of the OH surface density or (b) as a function of the initial H-bond binding energy between surface silanols. Reprinted with permission from ref 574. Copyright 2011 American Chemical Society.

because this is the simplest case where the lateral water–water interactions as well as H-bond formation with the surface contribute in the adsorption process.

On $\text{Q}(0001)^{504}$ the water dimer retains its configuration and adsorbs on top of two vicinal silanols, forming a bridge (Figure 45a). As for the monomer, adsorption is stronger on the weak H-bond site. The adsorption is slightly less energetic than in the monomer case, -45.3 kJ/mol , due to the decreased number of H-bonds between water and the surface. In the adsorbed dimer, the two types of water molecules, WI and WII, are identified. WI (see Figure 40), adsorbed parallel to the surface, shares H-bonds with neighboring water molecules and acts as H-bond acceptor from surface silanols, while WII is either H_{up} (H pointing out of the surface) or H_{down} (H pointing toward the surface) directed. The much reduced O–O distance of 2.63 \AA in the adsorbed dimer, compared with the computed value of 2.90 \AA for the free dimer clearly indicates that adsorption enhances H bonding of the water dimer.

Yang et al.^{346,504} found that on β -cristobalite (100), the most stable state for water dimer adsorption (with an adsorption

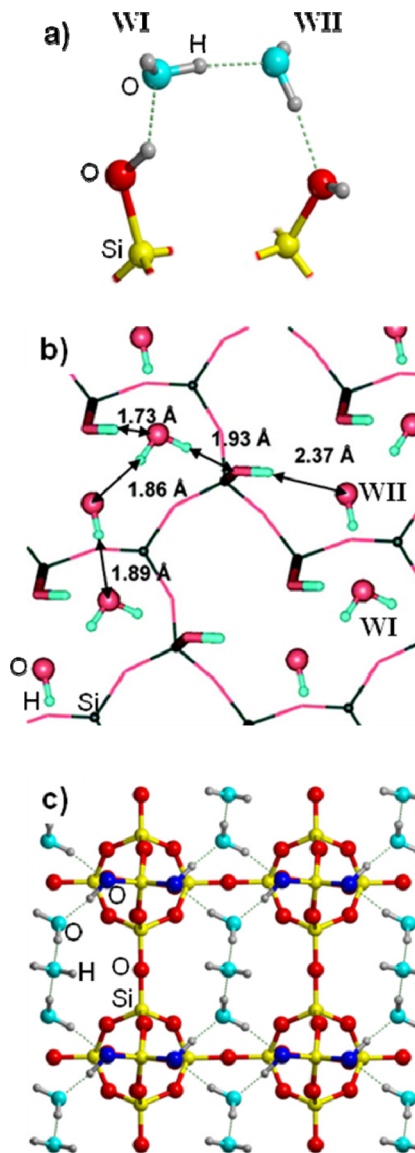


Figure 45. (a) Scheme of water dimer adsorption on $\text{Q}(0001)$, showing WI and WII types, (b) water dimer on $\text{Q}(101)$ (reprinted with permission from ref 575, Copyright 2011 American Chemical Society) and (c) water trimer on E (reprinted with permission from ref 317, Copyright 2008 Institute of Physics).

enthalpy of -72 kJ/mol) is in a bridge configuration between two pairs of geminal silanols. Interestingly, the H-bond in the adsorbed dimer is enhanced compared with the free, gas phase dimer. A similar result was found by Bandura et al.⁵⁷⁵ on $\text{Q}(101)$ for which the most stable water dimer configuration is found with an adsorption energy of -55 kJ/mol (Figure 45b).

In contrast, Tosoni et al. report the adsorption of a water trimer on edingtonite that has no increased adsorption energy compared with a single water molecule adsorption (-44 kJ/mol) (Figure 45c).³¹⁷

8.2.4. Water Monolayer. At increasing coverage, a water monolayer may be formed on the surface. Electron density profiles for all measured interfaces are consistent with a single layer of adsorbed water on (001) and (101) quartz surfaces at ambient conditions.⁶⁰² Etzler and Fagundus⁶⁰³ postulated that interfacial structuring of water would result in a decrease of the water density close to the silica surface. Schlegel et al.⁶⁰²

measured by X-ray reflectivity that the number of adsorbed water molecules is consistent with the number of silanol groups per unit cell, suggesting that the driving force for the formation of this layer is likely to be the hydrogen bonding of water molecules to surface silanol groups. This conclusion fully agrees with calorimetry data^{604,605} recorded on amorphous and crystalline silicas, which conclude that the differences in immersional heats of silicas in water significantly depend on the interaction of hydrogen bonds between water molecules and surface hydroxyl groups. It was concluded that hydrogen-bonded hydroxyl groups interact with water molecules more strongly than free hydroxyl groups.

However, if morphologically flat crystal surfaces adsorb only a single layer of water (monolayer), it was also proposed that corrugated surfaces have a disordered and random distribution of adsorbed H₂O molecules.⁶⁰⁶

The formation of a stable water monolayer on flat surfaces was later confirmed by ab initio works, which characterized the water monolayer on crystalline surfaces such as Q(0001)^{542,554,574,576,590} (Figure 46a,b) and C(100) (Figure 47a).^{346,573} Thanks to a “smooth epitaxy” mechanism⁶⁰⁷ between water and silanols, ice-like structures are formed on the surfaces. The WI/WII ratio on quartz (0001) and cristobalite (100) is 50/50. WII is always found H-down oriented. This type of water monolayer adsorption will fully saturate the hydrogen bonds of water molecules and hydroxyl groups on the surface: each water molecule shares three H-bonds with neighboring waters and one H-bond with surface silanols. Accordingly, the cohesion in the water layer is more important than the water–surface interaction. A WI water molecule is twice H-bond donor to water neighbors and twice H-bond receiver, from one silanol and one neighboring water. WII is twice H-bond receiver from water, and twice H-bond donor to silanol and water. However the crystalline structures of the layers formed on the different surfaces are reminiscent of the surface hydroxyl structure, as detailed hereafter.

Water forms a hexagonal ice layer on Q(001).⁵⁰⁴ The Q(001) surface has a hexagonal lattice constant of 4.91 Å, which is comparable with the periodicity in bulk ice Ih, 4.52 Å. The adsorption energy of this layer is −62.7 kJ/mol, which is higher in absolute value than the value for adsorption as isolated molecules, namely, −55.6 kJ/mol. Most of the adsorption energy gain in the layer structure is due to the formation of lateral H-bonding interactions between molecules. Accordingly, the water–surface interaction is reduced with respect to the adsorption as single water molecules. An interesting combined DFT (geometry optimization at the B3LYP/Lanl2DZ) and classical MD (using the CLAYFF force field) study was performed for one water monolayer (10 H₂O nm^{−2}) on hydroxylated (001) quartz.⁵⁴² The authors studied the effects of temperature (through MD simulation) on this monolayer. The dynamic picture has only partial occupation of the structure obtained at 0 K (S1, Figure 46c). Another configuration (S2), less stable at 0 K, with the two water hydrogens donating H-bonds to the surface SiOH groups is clearly thermally accessible. Water molecules coalesced on the surface to form a droplet of water (S3) that corresponding to multilayer adsorption is also demonstrated.

For Q(101),⁵⁷⁵ Bandura et al., using the PBE GGA with PAW pseudopotentials and a cutoff of 400 eV, calculated that water adsorption at the monolayer is exothermic by 59.2 kJ/mol. Several stable structures were investigated, with differences in energy ranging from 5 to 20 kJ/mol with respect to the most

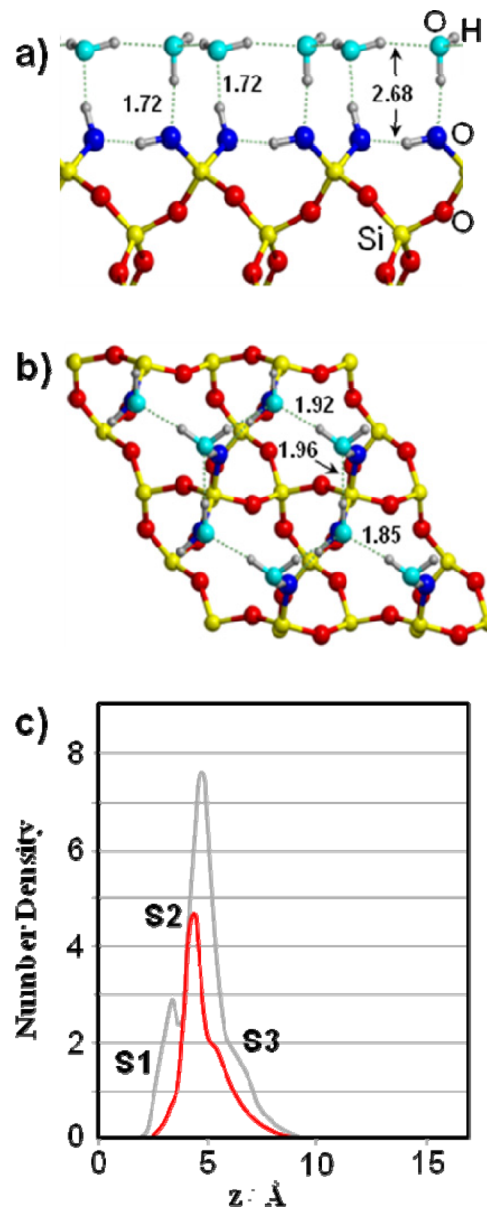


Figure 46. Water monolayer structure on Q(001) (adapted with permission from ref 576, Copyright 2011 American Physical Society): (a) side view and (b) view from above. (c) MD vertical water profiles for water/Q(0001) interfaces at coverage 1 H₂O/10 Å²; adapted with permission from ref 542, Copyright 2008 American Chemical Society.

stable structure. On this surface, because there is no distinct adsorption site on the hydroxylated surface, the amount of water adsorbed may reach the density of bulk water.⁶⁰² In this structure, a stable bilayer is found (Figure 47b). Again, WI and WII types are identified. Type WI sits nearly parallel to the surface by accepting a H-bond from one lifted surface hydroxyl group, and type WII points one of its protons down to the O atom of another surface hydroxyl. Each H₂O molecule is H-bonded with its three neighbors and a surface hydroxyl.

On cristobalite (100) and (111), a quadrangular/octagonal ice phase structure was demonstrated by Yang et al.^{346,573} The elementary water dimer structure formed on geminal silanols, with one WI and one WII, is retained at high coverage. The adsorption energy in the water layer is −68.5 kJ/mol. A different adsorption energy for the same structure was calculated by Lu et al.⁶⁰⁰ This ice tessellation was calculated

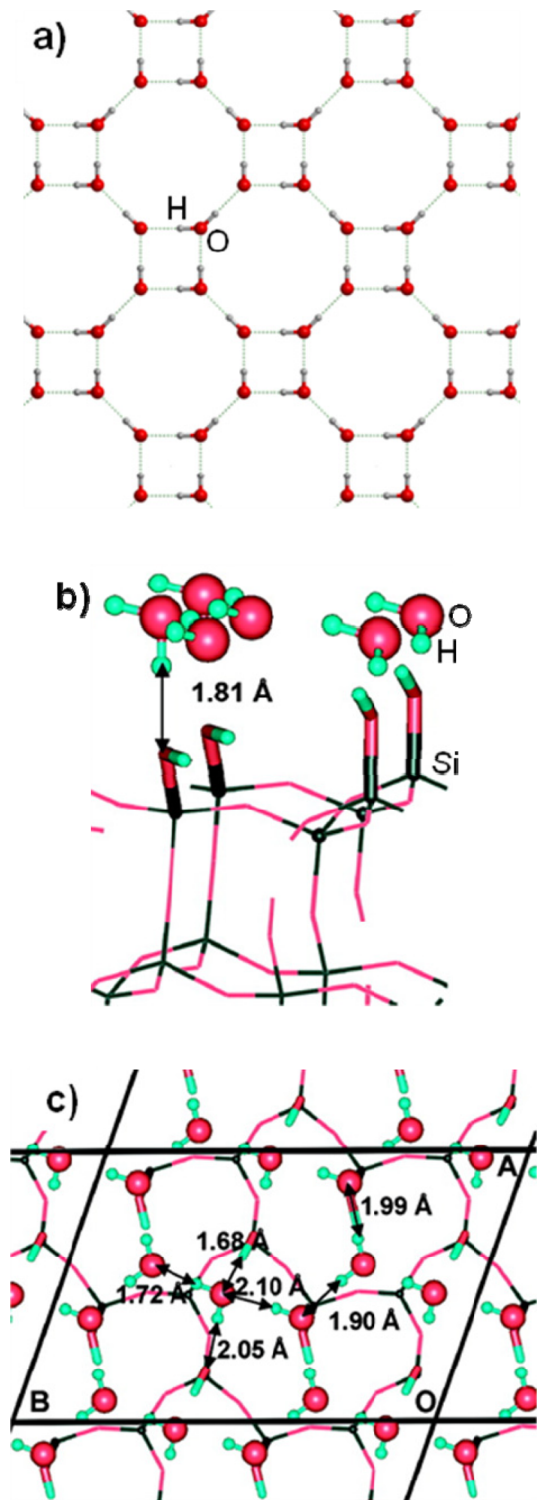


Figure 47. Water monolayer structures of (a,b) C(100), view from above and side view (adapted with permission from ref 346 Copyright 2004 American Physical Society) and (c) Q(101) (reprinted with permission from ref 575, Copyright 2011 American Chemical Society).

to be stable until 150 K by classical MD simulation (COMPASS), in contrast to a temperature desorption near 300 K calculated by Yang et al. in AIMD using the PW91 pure GGA.⁵⁷³ Lu et al.⁶⁰⁰ attribute this discrepancy to the overestimation of the H-bond interaction between water and the surface with PW91 (near -70 kJ/mol), whereas the value

calculated with rPBE (-48.7 kJ/mol) is more realistic. Indeed rPBE accounts better than PW91 for bulk water description.⁶⁰⁸

Few theoretical works using classical MD have been devoted to the adsorption of a single water monolayer on crystalline silica surfaces (see Table 9). An interesting screening of 40 cristobalite surfaces was performed by Nangia et al.⁵⁹⁴ who modeled different cristobalite surfaces with the multibody potential proposed by Feuston and Garofalini⁴⁷² and CHARMM⁵⁹³ and the adsorption of water thereon. First, the results using empirical potentials are validated by comparison to ab initio results on the C(100) surface,^{346,554} and then, the work is extended to other, less explored cristobalite surfaces. Indeed, quartz and cristobalite surfaces have no preferred crystallographic cleavage plane, and therefore, grounded samples have a complex structure composed of the combination of low index Miller planes. The results indicate that the surfaces with ordered topology and hydroxyl groups in planes parallel to the surface, for example, the (100) and (111) hydroxylated surfaces of cristobalite, have accessible hydroxyl groups that can adsorb water molecules through H-bonds. This result is in agreement with the X-ray reflectivity experimental data reporting that flat quartz surfaces adsorb a single water monolayer in a highly oriented way.⁶⁰² In contrast, surfaces that are corrugated or have less ordered topology do not have the hydroxyls in one plane to adsorb water effectively and thus to form a stable monolayer. Depending on the local topology of the corrugation, the surface can adsorb single water molecules with very different adsorption energies and stabilities.

To the best of our knowledge, only one study of water monolayer formation on isolated silanols is reported in literature, for the edingtonite (001) surface (Figure 48).³¹⁷ Here, the water–water interactions are still more important than in the Q and C cases, because the silanol density is lower. Adsorbed water molecules form tetramers H-bonded to the surface. The ratio WI/WII is 50/50 as for other surfaces, but interestingly, type II molecules are now equally distributed between H_{up} and H_{down} orientations. In other words, the lesser silanol density induces a lesser water layer–surface interaction, and the first water layer is bulk water-like, although with a less random orientation. The adsorption energy (-43 kJ/mol) in the water layer is also less negative than on other surfaces, because the type I molecules do not act as H-bond acceptors from silanol groups.

8.2.5. Water Multilayers. Wander and Clark,⁵⁴² in a classical MD study of the quartz–water interface, found no drastic change of the interfacial water layer when a second water layer is present on the surface. Very recently, layer-by-layer water adsorption on fully hydroxylated Q(0001) was performed by DFT.⁵⁷⁶ The first water layer has a strong energy of adsorption (-63.7 kJ/mol in this work), as shown in the preceding paragraph. When the second water layer is deposited on the first water layer on HY-Q(0001), the structure of the first water is almost unaffected, the hydrogen bonds between the first and second water layers being relatively long (about 2 Å; Figure 49a). The adsorption of the second water layer is less exothermic than the first one, -51.4 kJ/mol, and the bonding energy between the two water layers is only 0.093 J/m², indicating that the interaction between the two water layers is relatively weak and that the first water layer effectively shields the long-range surface–water interaction. When the third water layer is deposited onto the water bilayer, the out-of-plane protons in the second water layer reverse their orientations from pointing down to pointing up. As a result, the optimized

Table 11. DFT Studies of Water Adsorption on Crystalline Surfaces at Full Coverage

polymorph	surface	nature of hydroxyls	method	water density ($\text{H}_2\text{O nm}^{-2}$)	water organization	ref
Q	(0001)	geminal silanols	PW91 ^{504,576} B3LYP ⁵⁷⁴	9.1	hexagonal, planar, type I parallel and type II H_{down}	504,574,576
	(101)	no strong H bonds	PBE ⁵⁷⁵ PW91 ²⁹⁵	2.8 water/unit cell = bulk water	ice-like structure similar to (0001)	295,575
C	(100)	zig-zag with vicinal OH	PW91		quadrangular tessellation structure	346
E	(100)	isolated	B3LYP GTO	10	monolayer	317

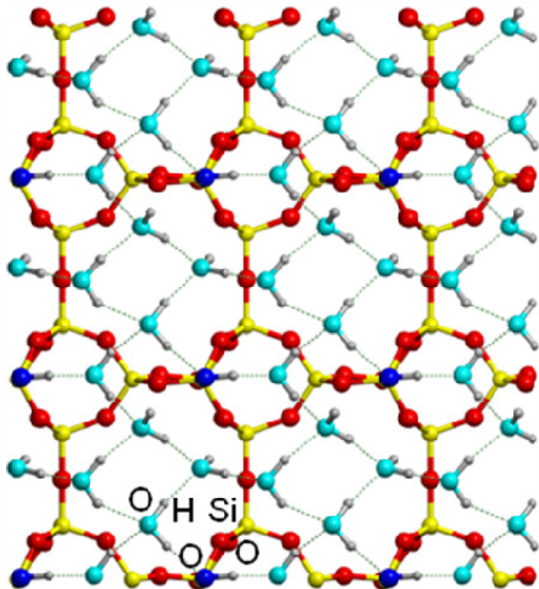


Figure 48. Water monolayer structure on E(001). Reprinted with permission from ref 317. Copyright 2008 Institute of Physics.

structure consists of the first layer structure and a water bilayer structure (Figure 49b). Accordingly, the adsorption energy of the third layer is higher than that of the second layer, -68.0 kJ/mol . When the fourth water layer is deposited a trilayer structure is obtained with an adsorption energy of -48.9 kJ/mol (Figure 49c). Results of trilayer and quadlayer adsorptions confirm that the bilayer-like structure at the silica–water interface effectively shields the interaction between the hydroxyl groups on the silica surface and water layers beyond the first layer.

8.2.6. Crystalline Silica–Liquid Water Interface. The quartz/water interface has been intensively studied experimentally. Quartz has a point of zero charge (PZC) of about 2 (ref 609 and section 3.1.2), which implies that at pH > 2, the surface is negatively charged.^{91,102,609–612} A few experimental studies allow characterization of the quartz–water interface at the atomistic level. Measurements of interfacial pK_a (defined as $-\log_{10} K_a$, where K_a is the acid dissociation constant) have been revolutionized by surface-sensitive second-harmonic generation (SHG) and sum-frequency vibrational spectroscopy (SFVS or SFG) techniques.^{613,614} We may recall here results already mentioned in section 3.1.2 (ref 96) demonstrating that 19% of silanol groups on fused silica surfaces exhibit a pK_a of 4.5 while the remaining 81% exhibit pK_a of 8.5. Other authors¹⁸⁵ estimate the density of strong acid silanols at only 0.83 OH nm^{-2} , only about 20% of the total silanol density. SFVS experiments on α -quartz reached similar conclusions and further suggested that the low-acidity silanol groups reside in regions with strong water–water hydrogen bonds.⁹⁷ As mentioned in section 3.1.2,

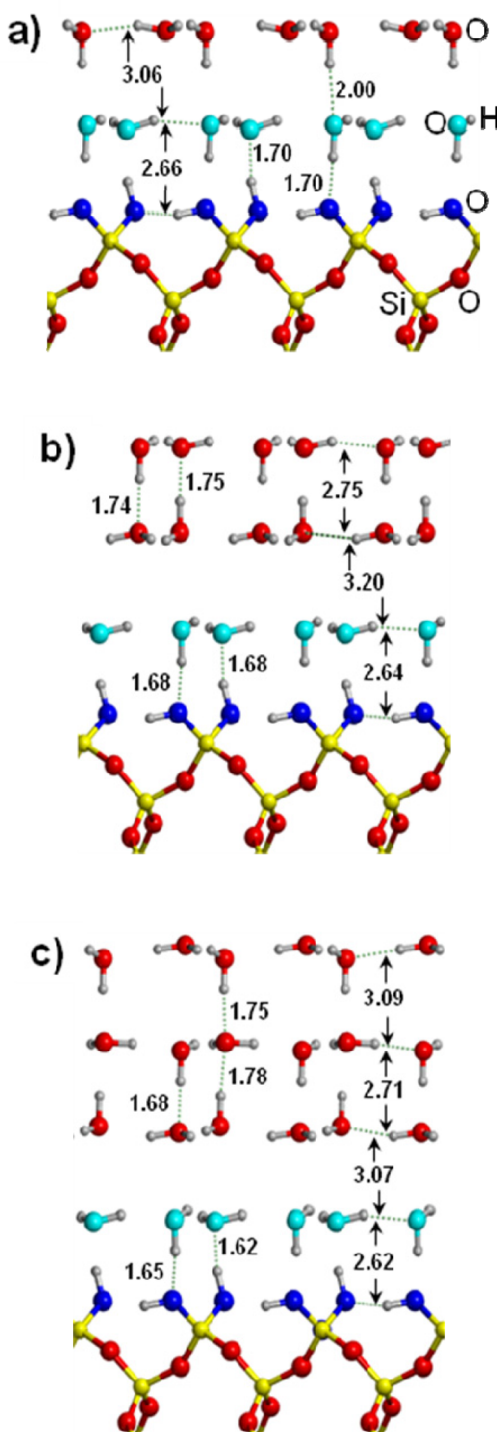


Figure 49. Water multilayers on Q(0001). Drawn with data from ref 576.

many titration curves are not precise enough to discriminate silanols of different acidities, yet at least one titration study on silica gel (amorphous silica)⁶¹⁵ and X-ray photoelectron spectroscopy measurements on quartz⁹¹ also independently suggested the existence of SiOH groups with pK_a between 4 and 5.5. Such qualitative agreement on different forms of silica is expected because liquid water is known to react slowly with crystalline silica to form an amorphous layer.⁶⁸ Indeed, in the presence of water even at pH 7, water molecules slowly generate an amorphous layer, which weakens the strong hydrogen bond network of the near-surface water molecules.

SFG experiments on the neutral (low pH) quartz–water hydrophilic interface give two bands located at ~ 3200 and $\sim 3400\text{ cm}^{-1}$.^{97,543,564,616} The 3200 cm^{-1} band occurs at the same frequency as in the IR and Raman of ice,^{617,618} while the 3400 cm^{-1} band is found approximately at the same frequency as in the IR and Raman spectra of liquid water. Note that the 3200 cm^{-1} band gains in intensity at higher pH. Assignment of these two SFG peaks is still debated, with two conflicting views in the literature: (1) The peak at 3200 cm^{-1} arises from a H-bond network of water molecules with an “ice-like” ordering, representative of O–H stretch of tetrahedrally coordinated water molecules, while the peak at 3400 cm^{-1} comes from a “liquid-like” arrangement of the water molecules, that is, more disordered H-bond network. (2) Another interpretation is that contributions to the 3400 cm^{-1} band mainly arise from water molecules directly adjacent to the surface while the 3200 cm^{-1} peak comes from water molecules in the more distant water layers.

Crystalline silica–bulk water interactions have been studied by classical methods and, very recently, with AIMD investigations. All the studies mentioned consider a neutral, uncharged surface. This is justified because, at pH 7, the surface charge is expected to be $-1\text{ }\mu\text{C}/\text{cm}^2$ (ref 89), that is, one negative SiO_4^{4-} group every 16 nm^2 ; thus large areas of the surface have a neutral character.

Force field studies have focused on quartz,^{68,457,473,499,542,587,588,590–593,619,620} and cristobalite.^{559,594} De Leeuw et al. studied the α -(0001) hydroxylated quartz–water interface.⁵⁹⁰ They found that interfacial water molecules loosely associate with the surface via hydrogen bonding between the oxygen atoms of the interfacial water molecules and hydrogen atoms of the surface Si–OH groups. In terms of configuration and bonding, the surface Si–OH groups resemble water molecules themselves and a relatively disordered three-dimensional interfacial water region forms near the surface, similar to bulk liquid water. The authors conclude that this liquid-like behavior is in agreement with experimental findings on interfacial water near the quartz surface at low pH.^{97,543} However, experimentally, at neutral pH water was observed to structure near the surface.⁹⁷

Wander and Clark⁵⁴² found a loss of water specific orientation for interfacial water layers more distant than the first one, in which for the most part, the H_{up} -oriented waters are above the SiOH groups, and the H-down are between them. When structure is present in the second layer, it appears to be more diffuse than that observed in first one.

Lopes et al. developed a force-field for silica, which was applied to the (011) and (100) quartz–water interface.⁵⁹³ Q(011) was modeled with single silanols (hydrophilic side) on one face and single silanes (hydrophobic side) on the other face. Q(100) was modeled similarly, having geminal silanols instead of single groups. The density profile of water between

quartz slabs was described (Figure 50). On the (011) surface, there is an accumulation of water near the silanol groups. Water

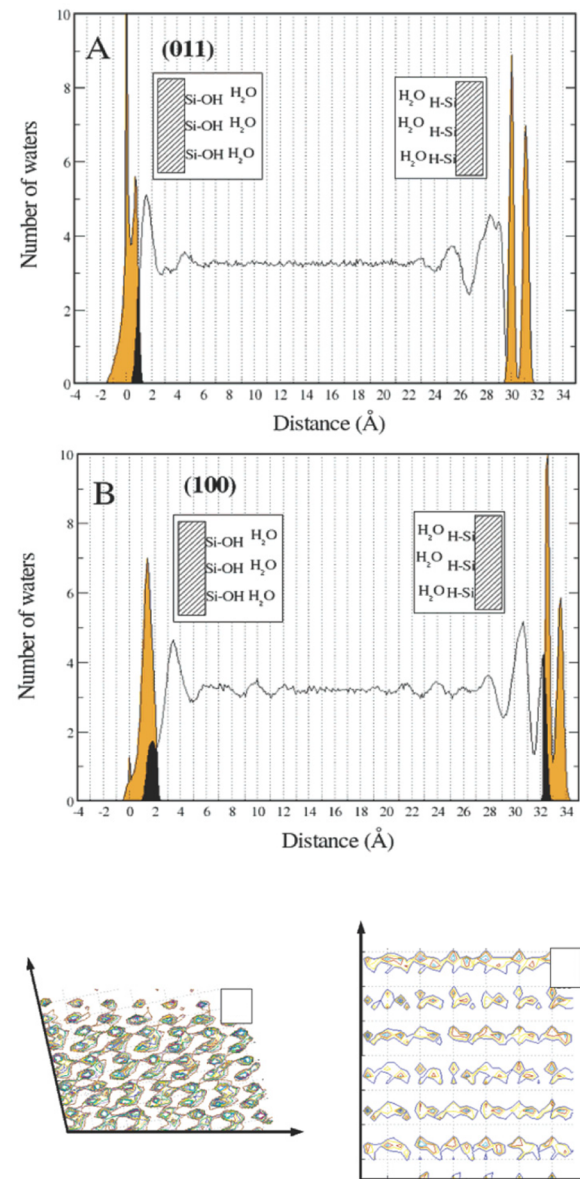


Figure 50. Density profiles for water adsorbed on quartz (A) (011) and (B) (100) surfaces. Orange represents the surface hydrogen atoms and the black areas mark the layers where surface hydrogen atoms coexist with water oxygens. (bottom) Probability density of silanols for Q(011) (left, single silanols) and Q(100) (right, geminal silanols) surfaces. Reprinted with permission from ref 593. Copyright 2006 American Chemical Society.

has some overlap with the surface silanols, and this is represented by the black area of Figure 50a, starting approximately at 0 Å. After this area of accumulation, there is a smaller area of depletion followed by a very small area of accumulation before reaching the bulk density at about 7 Å from the hydroxyl hydrogens. On Q(100) (Figure 50b), there is a significant penetration of water in the interstices formed by the surface hydroxyls. These waters form a distinct first layer although its density is about half of that of the bulk phase (black region on the bottom left of Figure 50b). Contrary to (011), the region of strong water accumulation is not

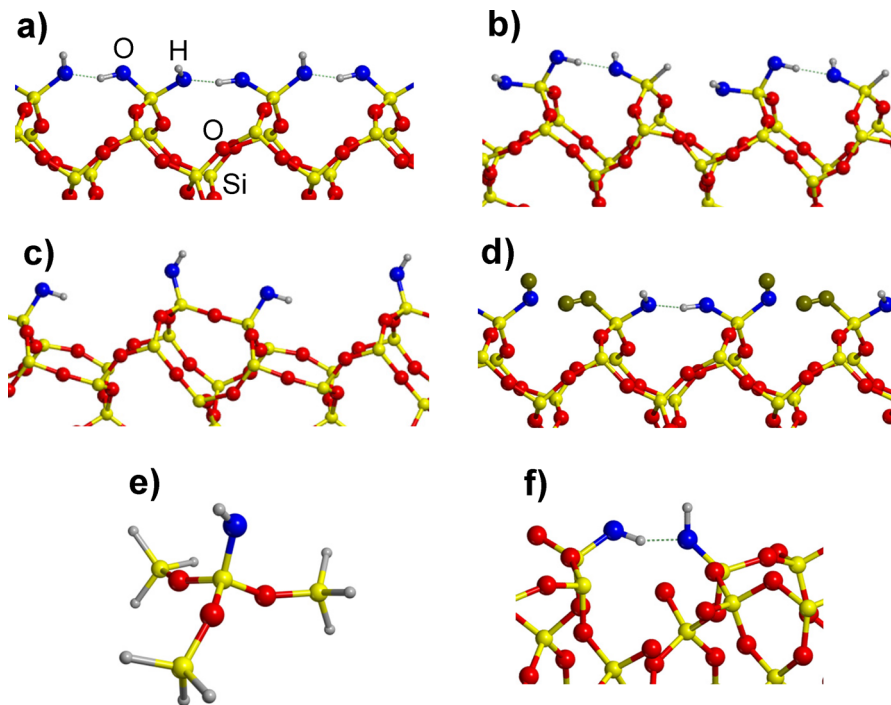


Figure 51. Systems studied in ref 584: (a) Hydroxylated β -cristobalite (100) surface. The SiOH groups (O indicated in deep blue) have $\rho(\text{SiOH}) \approx 8 \text{ nm}^{-2}$ and are all Q^2 and H bonded. The calculated pK_a is 7.6 ± 0.3 . (b) Hydroxylated (100) β -cristobalite surface with one OH group replaced by a H to break the chain of hydrogen bonds. The SiOH near this defect (Q^2 and isolated) exhibits $pK_a \approx 8.9 \pm 0.3$. (c) Reconstructed (100) β -cristobalite surface, $\rho(\text{SiOH}) \approx 4 \text{ nm}^{-2}$, Q^3 , and isolated; $pK_a \approx 8.1 \pm 0.5$ (six layers of water) and 7.0 ± 0.4 (four layers). (d) The structure in panel c comes from removing atoms shown here in black and linking the resulting undercoordinated Si and O atoms. Panels a–d show the side view of ~ 1.5 simulation cells. (e) $(\text{H}_3\text{SiO})_3 \text{ SiOH}$, which is Q^3 and isolated, exhibits $pK_a \approx 7.9 \pm 0.5$. (f) Top half of a reconstructed (0001) quartz surface model containing cyclic silica trimers $(\text{Si}-\text{O})_3$, $\rho(\text{SiOH}) \approx 2.3 \text{ nm}^{-2}$, Q^3 , and H-bonded; the SiOH on the trimer ring exhibits $pK_a \approx 5.1 \pm 0.3$, while the other has $pK_a \approx 3.8 \pm 0.4$ and 4.8 ± 0.4 depending on whether a nearby trimer ring breaks (see text). Si, O, and H atoms are in yellow, red, and white, respectively. (b, e) Finite-temperature AIMD snapshots with water molecules omitted for clarity; (a, c, f) Shown at $T \approx 0 \text{ K}$.

contiguous to the hydroxyl hydrogen atom layer but is located about 2 \AA away. The regions of accumulation and depletion are more extensive than those on (011), and water only reaches its bulk density 12 \AA from the hydroxyl hydrogen layer. These results were explained by considering the differences in surface group densities between quartz (011) and quartz (100): on quartz (011) (Figure 50a) the density of silanol groups is much higher than on quartz (100). On quartz (011), there is a significant overlap between water and quartz slabs, and this is due to the formation of H bonds between surface hydroxyls and water molecules. The situation on quartz (100) is reversed. The distribution of surface groups allows for sufficiently large areas into which water molecules can adsorb on the surface. This originates the distinct black peak in Figure 50b. Water is able to occupy the void spaces bounded by the protruding silanols. Interstitial water molecules are then stabilized by water–water and silanol–water H bonds.

The dynamic properties of confined water have been investigated. Water molecules close to the surface can travel smaller distances than bulk water molecules, as a result of the increased difficulty to break H-bonds with the surface or even leave the confinement areas.

The interfaces between several crystalline quartz surfaces, (100), (001), and (011), and water has been investigated by Walsh et al.^{591,595} The water density and orientation near the surface were studied. It was found that water is rather weakly ordered and the orientation of water molecules relative to the plane of the bilayer is always close to random. Common features appear among the three crystalline planes: they include

a favored water orientation WII, with one H pointing toward the surface in the interfacial water layer. This structural effect is lost at around 1.2 nm from the surface. Examining the interface in more detail, however, one can note differences between the three cases under study. Water penetrates into interstices between silanols on the (100) surface but not on the (001) one, due to a higher silanol density and thus, to the presence of a H-bond network on the latter. The lateral ordering of water on quartz was found to be strongly dependent on the surface, because the positions of water molecules are closely correlated to the positions of the surface silanol groups. On the (100) surface, water forms striations that run diagonally across the surface, along the direction of the [011] vector. Water on the (001) surface is arranged in rings that correspond to the underlying Si–O rings of the surface. The first water layer is denser on the (011) than on the other surfaces. Accordingly, the most pronounced lateral ordering occurs in this surface. A contributing factor may be the interactions of water with the bridging Si–O–Si oxygen atoms, which are present in the surface plane. Lateral diffusion coefficients of the first layer of water were found to be lower than in bulk water, yet the water molecules still have some degree of mobility.

Puibasset and Pellenq⁵⁵⁹ studied four different cristobalite surfaces, the (111) and (100) surfaces, and the (111) covered with a low (LD) and high (HD) silanol density. They found that the heat of adsorption of water at low coverage becomes less negative with increasing silanol content, with values of -68 , -61 , -50 , and -45 kJ/mol for silanol densities of 13.5 , 7.8 ,

5.5, and 4.5 OH nm^{-2} (surfaces (111-HD), (11 $\bar{1}$), (100) and (111-LD)).

Argyris et al.^{592,621} performed a study of the C(111) water interface using the SPC model for water and a 12–6 Lennard-Jones potential for Si–water interaction. Several degrees of hydroxylation were considered. In all cases, the perturbation of the water structure due to the surface interaction decreases as the distance from the solid substrate increases, bulk water properties being recovered for distances greater than $\sim 14 \text{ \AA}$. The fully hydroxylated surface with 13.6 OH nm^{-2} is more hydrophilic, as evidenced by the first water layer–surface average distance (2.15 \AA), than the partially hydroxylated and anhydrous surfaces (2.75 and 2.95 \AA , respectively). On this surface, the first water layer is found massively H_{down} directed toward the surface. The second water layer has an opposite orientation. This is the signature of layering of water molecules with opposite orientation and is indicative of an attempt to maximize water–water hydrogen bonds. The solid substrate affects the structural properties of water but also strongly alters its dynamic behavior: Interfacial water molecules at the fully hydroxylated surface remain longer on average in the interfacial region than water molecules at partially and nonhydroxylated surfaces. Zeitler et al.⁵⁹⁶ recently proposed a new method to calculate the accessible volume to water for complicated surfaces (e.g., those with kinks or hydroxyl groups). Zhao^{323,586} used a hybrid approach (DFTB) to model a (100) edingtonite surface in vacuum and at the interface with water. In vacuum, a significant reconstruction is observed, where silanols form H-bonds with each other. This is not the case in water, which prevents surface deformation.

More recently AIMD calculations were performed on the (0001) α -quartz surface^{584,501,582} and cristobalite surfaces.⁵⁸⁴

Adeagbo et al. studied the Q(001) water interface with PBE functional and Vanderbilt pseudopotentials.⁵⁰¹ They showed that the originally clean quartz surface is rapidly hydroxylated by chemical reaction with the water layer and that geminal silanol groups [Si(OH)₂] are formed predominantly.

The bimodal acid–base behavior of the water–silica interface (exhibiting two sites of respective pK_as of 8.5 and 4.5 with a ratio of 4:1) was investigated by Leung et al.⁵⁸⁴ To take into account the surface heterogeneity of amorphous silicas, as well as the lack of information of the crystalline silica–water structural modifications at the interface, six different silanol environments were compared: hydroxylated cristobalite (100) (Figure 51a), hydroxylated cristobalite (100) with one SiOH removed (Figure 51b), reconstructed cristobalite (100) (Figure 51c,d), a molecular system (Figure 51e), and two distinct SiOH's on reconstructed quartz (0001) (Figure 51f).

On the C(100) surface, with a silanol density of 8 OH nm^{-2} , the SiOH are all chemically equivalent. The zigzag surface H-bond features between silanols are preserved in the finite-temperature aqueous phase simulation. The umbrella sampling method was used to compute the $W(R)$ associated with SiOH deprotonation using a four-atom reaction coordinate R (Figure 52a).

On this surface, silanols exhibit pK_a values of 7.5 and 7.7. The other surfaces, containing isolated, H-bonded, and geminal silanols, all exhibit a pK_a > 7.0. The isolated SiOH group on cristobalite (Figure 52b) has a pK of 8.9 and is less acidic by 1.2–1.4 pH units than when the SiOH hydrogen donor is present. In Figure 52c, a reconstructed cristobalite surface exhibits isolated silanols (4 OH nm^{-2}), with pK_a = 8.1. The authors deduced that in the range $4 < \rho(\text{OH}) < 8 \text{ OH nm}^{-2}$,

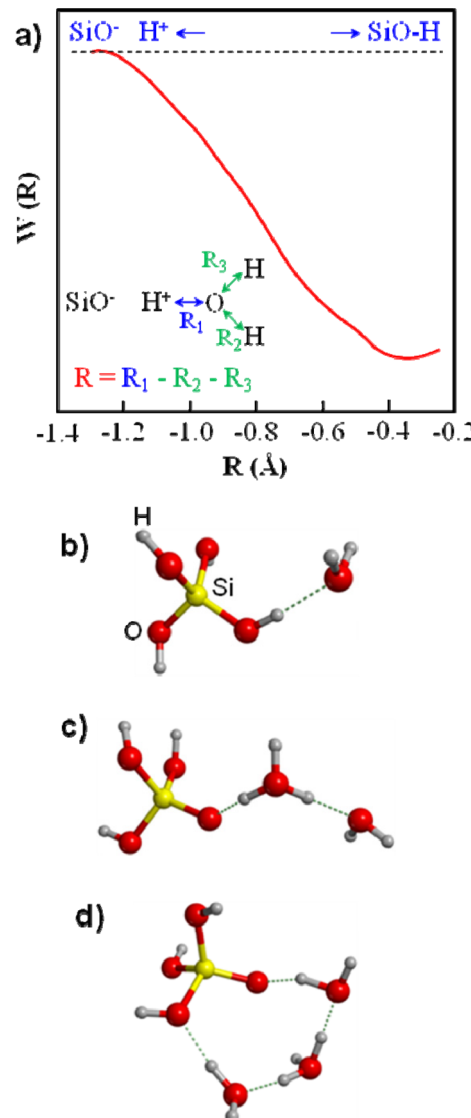


Figure 52. Umbrella method: Four-atom reaction coordinate R , illustrated for silicic acid in water, but is similar for all silanol-containing species. (b–d) Snapshots from AIMD deprotonation simulations with outershell H_2O molecules removed for clarity. As deprotonation proceeds, R progresses from intact $\text{SiO}-\text{H}$ (R around -0.4 \AA , panel b), to the $\text{SiO}^-/\text{H}_3\text{O}^+$ contact ion pair (R about -1.0 \AA , panel c), and then via a Grothuss proton transfer to a solvent-separated $\text{SiO}^-/\text{H}_3\text{O}^+$ pair (R around -1.32 \AA , panel d). Yellow, red, and white spheres represent Si, O, and H, respectively. Adapted with permission from ref 584. Copyright 2009 American Chemical Society.

the OH density has no effect on pK_a. All those silanol models may explain the experimental value of 8.5. To model a high-acidity silanol, a reconstructed quartz (0001) model, featuring $(\text{Si}-\text{O})_3$ (S3R), was used. It presents 2.3 SiOH nm^{-2} with two types of silanol groups that are hydrogen bonded to each other; one member of the pair resides on a cyclic trimer, while the other does not (Figure 51f). These SiOH groups on the strained surface exhibit $\text{p}K_a \approx 5.1$ and 3.8 respectively, close to the experimental value of 4.5. This study highlights the role of defective regions as the most promising candidates to explain the elusive bimodal acid–base behavior of silica surfaces.

The (001) quartz–water interface has also been recently investigated by Sulpizi et al.⁵⁸² using BLYP, who confirm that the H-bond network on this surface is partially maintained: two

types of silanols, “in plane” and “out of plane”, are present on the surface (Figure 53). The “in plane” silanols are H-bond

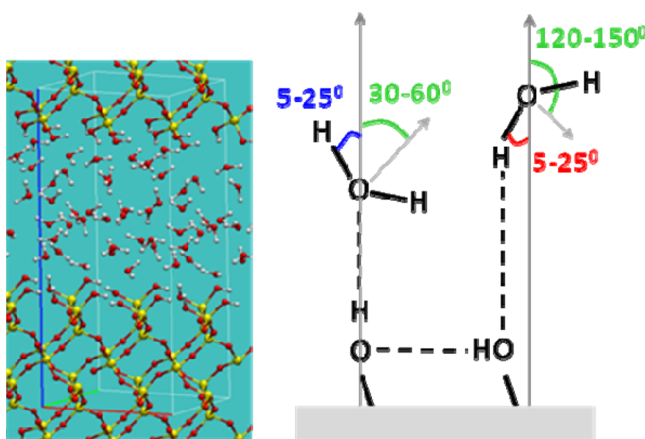


Figure 53. Quartz slab quartz–water interface and water orientation at the surface. Reprinted with permission from ref 582. Copyright 2012 American Chemical Society.

donor to a silanol (strong H-bond), and the “out of plane” ones are H-bond donor to water (Figure 53b). The strong in plane H-bond is maintained. Water in the interfacial layer is now only of type II, with half being strong H-bond acceptors from silanols and half weaker H-bond donors to silanols. In the local structure formed, a reminiscence of the dimer adsorption is observed, where, however, the H-bond between water molecules is lost. Water in the subsequent layer has a random orientation. From the ice bilayer found by Yang et al.,⁵⁰⁴ only the water–silanol interaction is retained, while all water–water interactions are lost. Thus, strictly speaking, the interfacial layer cannot be referred as ice-like, because no water–water favorite lateral interactions are present. A noticeable difference between results from classical and ab initio calculations is that the former does not predict the structuring of the first water layer compared with the latter. Another AIMD study shows that the water orientation at the surface is lost at the increased temperature of 1000 K.⁵⁰¹

The acidity constants of surface silanols and silicic acid are computed using the reversible proton insertion/deletion method. The most acidic silanol species, out of plane, has a calculated pK_a of 5.6, while $pK_a = 8.5$ for the in-plane silanol. The authors conclude that there is a bimodal distribution of silanols. However, the 1:1 ratio of the considered species does not fit the experimental value of 1:4.

To summarize, the final word on the nature of the acidic species on silica has not yet been written. Whereas Leung et al. open the route to defects of low silanol density and especially strained (S3R) rings on the surface, the Sulpizi et al. results suggest that H-bonds are responsible of the increase of acidity of otherwise equivalent silanols.

The “methodological gap” between AIMD and FF was bridged in the case of the (101) quartz surface. AIMD (PW91) was compared with X-ray reflectivity (XRR) experiments and with three force fields, LFF,⁵⁹³ ClayFF,⁶²² and CWCA.⁵²⁸ Discrepancies between the force fields but also between AIMD and experimental data were demonstrated. ClayFF was found to better agree with AIMD; however AIMD did not allow total recovery of the XRR data. This is likely due to the overestimation of H-bonds by pure GGA and by the absence

of van der Waals forces in these AIMD calculation. One reason for the discrepancy between FF and ab initio methods is the absence of dispersion in the latter (usually included in FF) so that it is mandatory to address the above problems with a level of theory of DFT-D quality, at the least.

One can remember from this section that water and crystalline silicas modify each other at the interface. On the one hand, strong silanol–silanol H-bonds are not disrupted by water even at the quartz–liquid interface at room temperature. Indeed, a recent PBE AIMD study of water–crystalline silica interfaces⁶²³ shows that the interaction between crystalline silica surfaces and water does not necessarily cleave the pre-existent H-bonds between the surface silanol groups. On the contrary, in some cases such as Q(100) and C(001), it is observed that SiOH...OH_{Si} H-bonds are even strengthened as a result of a mutual cooperative H-donor/H-acceptor enhancement between silanols and water molecules. In consequence, on those crystalline surfaces, the interaction with water is highly dependent on the preexisting H-bond network. On the other hand, the surface tends to impose a preferred orientation to the first water layer, thus giving rise to water surface layer properties closer to those of solid ice than that of bulk liquid. Studies at the silica–liquid interface (generally quartz) all conclude that the effect of the surface is lost beyond three layers.

8.2.7. Water on Hydrophobic Crystalline Silicas. It is well established that whereas fully hydroxylated surfaces (surface density of 4–5 Si–OH nm⁻² as measured by Zhuravlev⁷⁸) have a hydrophilic character, highly dehydroxylated surfaces (around 1–2 Si–OH nm⁻²) manifest hydrophobic character.⁸²

Du et al. showed that the reconstructed dry α -quartz (0001) surface is hydrophobic with respect to the interaction with a water molecule.⁵⁸⁹ Rignanese et al.⁵⁰⁰ showed with the PW91 GGA associated with a 50 Ry cutoff that the reconstructed dry α -quartz (0001) surface is stable and hydroxylation of such a surface by a water molecule is energetically unfavorable.⁵⁰⁰

Tosoni et al.,⁵⁰³ with B3LYP, used a completely dehydroxylated crystalline silica surface to model adsorption processes on highly dehydrated silica materials. The structure envisages only unstrained siloxane Si–O–Si bridges, a model not easy to devise. To do this, the authors have used a siloxane face of a 1:1 layered phyllosilicate as found in kaolinite. The surface exposes regular 6R rings (Figure 54). Its hydrophobic/hydrophilic character has been characterized by simulating the adsorption of water, from low to high water coverage. Three H₂O loading has been simulated as adsorbates: (i) a single H₂O molecule (one H₂O/cell); (ii) a hexagonal C-ice layer derived from a proton order form of ice XI (two H₂O/cell); (iii) a water monolayer (three H₂O/cell). At low coverage, the oxygen atom of the adsorbed water molecule lies on the silicon atom of the slab, whereas the water protons are directed toward the siloxane oxygen atoms without a clear indication of hydrogen bonding. Adsorption is athermal. The interaction energy of H₂O with the siloxane layer is indeed negligible at any coverage and for cases ii and iii the dominant factor is the lateral H₂O–H₂O interaction. When dispersion is included at the B3LYP-D* level, a weak interaction is established between the siloxane slab and the adsorbed water layer. Water does indeed prefer to move away from the siloxane surface to maximize the H-bond interactions within the ice-like layer. The H-bond features resemble those of a pure ice-like layer, although the mismatch between the siloxane unit cell and that of the free water layer

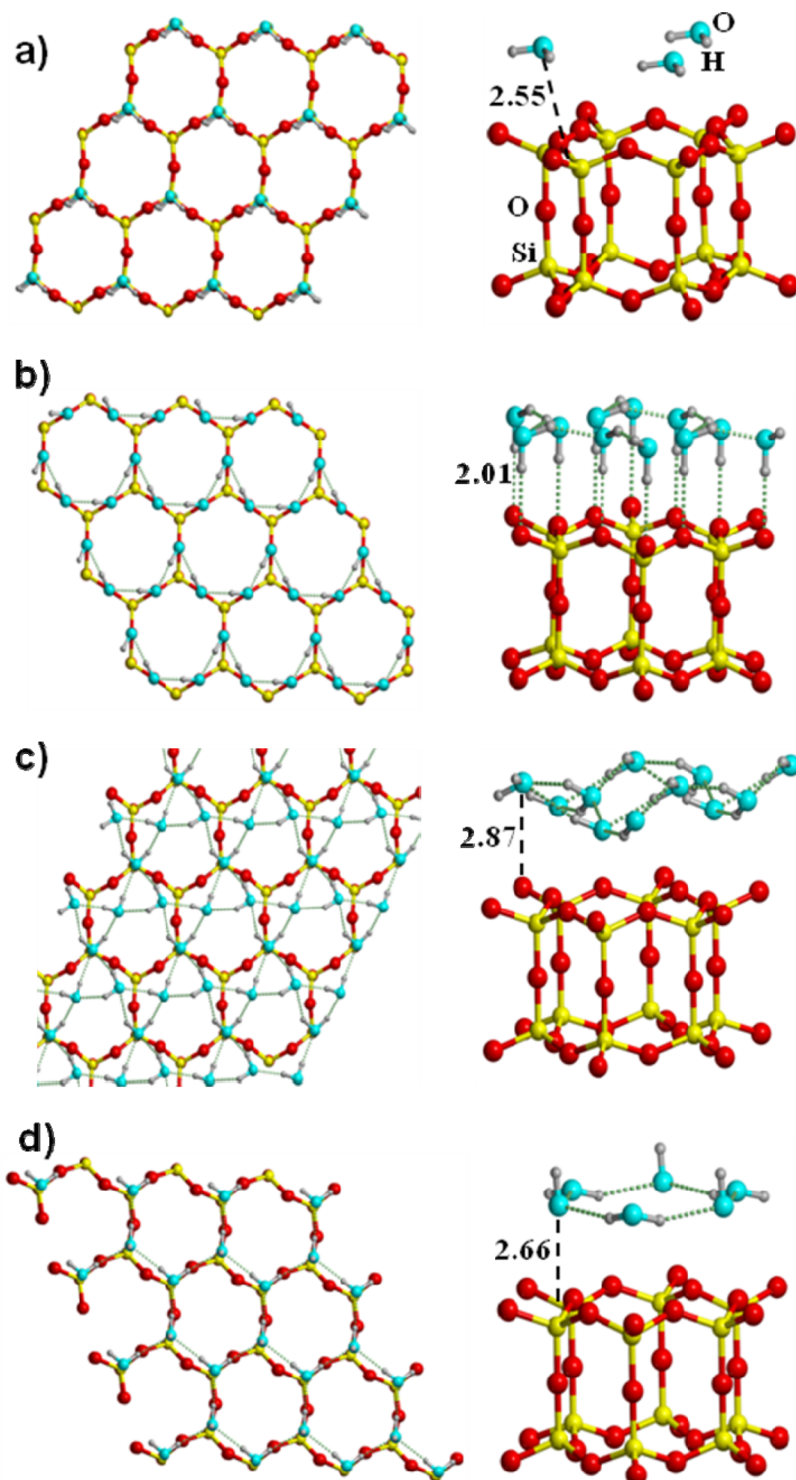


Figure 54. Water on hydrophobic surfaces. Reprinted with permission from ref 503. Copyright 2010 American Chemical Society.

causes a lengthening/weakening of the H-bonds, and the interaction energy per H_2O molecule is well below that in water ice (in absolute value). The free energy of adsorption at $P = 1$ atm for cases ii and iii remains indicative of an exothermic process until the thermal energy of the molecules is high enough to break the order of the ice layer at $T = 298$ K, according to the calculations. This is in qualitative agreement with IRAS and TPD measurements concerning water adsorbed on thin silica layers grown on Mo(112),⁶²⁴ where at 140 K an

ordered ice monolayer film was detected that becomes completely desorbed above 160 K.

8.2.8. Adsorption of Water on Crystalline Defects. As explained earlier, we will not consider in this section crystalline defects that are healed in reacting with water, such as, the two-membered ring, S2R. Theoretical^{75,625} studies converge with experimental ones (sections 3.1.3 and 3.1.7, for example, ref 178) in suggesting the disappearance of the S2R upon reaction with water at room temperature (see section 7.4 for a discussion of this question). However, some defects of

crystalline silicas that are not healed by water adsorption are mentioned here, as well as the reactivity with water of the $\equiv\text{SiO}^\bullet$ defect, which has been reported as possibly responsible for quartz toxicity.

Chen and Cheng⁶²⁶ have used DFT (PW91) method to study dry (1×1) α -quartz (0001) surfaces that have Frenkel-like defects such as oxygen vacancies. Single water molecules, water clusters, and water films were adsorbed on four defective surfaces.

According to the calculated adsorption and bonding energies, the hydrogen bonds within water clusters or water films are stronger than the defect–water interaction. In cases of water cluster adsorption on surfaces, the defect sites do enhance the interaction between water clusters and surfaces compared with the perfect surface. In the case of a single molecule adsorption, the molecule–surface defect interaction is larger than that on the perfect surface. The situation is opposite in water dimer–surface adsorption: adsorption energies on defective surfaces are smaller than on the perfect surface.

When water films are deposited on surfaces, the energy contributions from the hydrogen bond network and from the water–silica interaction differ by an order of magnitude. Neither the single-point defect of oxygen vacancies nor the oxygen displacements alter the basic water adsorption geometry on a (1×1) α -quartz (0001) surface. The calculations indicate that at low temperature and low defect density (oxygen vacancy and oxygen displacement), α -quartz (0001) surfaces are basically hydrophobic. Therefore, a surface with a low number of strained Si–O bonds and a low density of Frenkel defects is highly stable and not easily hydroxylated. The high stability of the water bilayer further reduces the water–defect interaction. Interestingly the dimer and the bilayer share a common feature, namely, the fact that defect/surface interaction is weakened because of their intrinsic stable hydrogen bond patterns. In a review article, Yates⁶²⁷ made a similar conclusion for water adsorption on silica surfaces with low defect density.

Radicals on crystalline silicas were elucidated through EPR spectroscopy (see section 3.1.7). Murashov et al.⁴⁹⁵ demonstrated the facility of quartz cleavage into several faces exhibiting radicals. Musso et al.³⁴⁵ have performed a periodic DFT study of the properties of the $\equiv\text{SiO}^\bullet$ radical defect on quartz, cristobalite, tridymite, and amorphous surface models. The radical defect is constructed by removing a hydrogen atom from a silanol of the surface while conserving the other features of the crystalline polymorph. Comparison between the hydroxylated and the radical slab shows that the radical defect at the surface does not induce significant tension at the crystalline structure, the Si–O bond distance associated with the radical defect being the only geometrical parameter that varies significantly (~ 0.04 Å). The spin density analysis shows that, regardless of the surface, the unpaired electron is mainly localized on the radical defect and, thus, does not provide a clue to understand the different behavior between crystalline and amorphous silica regarding the $\equiv\text{SiO}^\bullet + \text{H}_2\text{O} \rightarrow \text{SiOH} + \text{OH}^\bullet$ reaction. The enthalpy of this reaction is linearly dependent on the strength of the H-bond formed at the surface after the reaction (Figure 55). Finally, the enthalpy of reaction is two times less energetic on amorphous silica than on quartz, suggesting an explanation for the toxicity of quartz. However, the presence of water molecules smoothes the differences out to some extent.

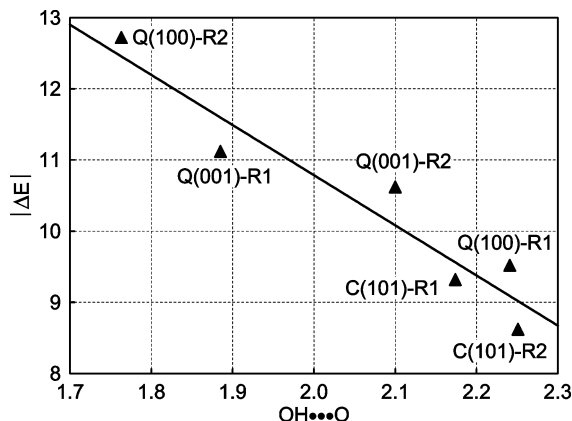


Figure 55. BHandHLYP correlation between ΔE of reaction $\text{SiO}^\bullet + \text{H}_2\text{O} \rightarrow \text{SiOH} + \text{OH}^\bullet$ (kcal mol⁻¹) and the length (Å) of the H-bond (H...O distance) formed as product in the case of Q(001), Q(100), and C(101) surfaces. Reprinted with permission from ref 345. Copyright 2010 American Chemical Society.

8.3. Water on Amorphous Hydroxylated Silicas

Remember that amorphous silicas are reported to have a hydroxyl group surface density of about 4.6 OH nm^{-2} (section 3.1.1). In recent years, a great amount of effort has been devoted to generate models of amorphous silica that are easy to handle with periodic ab initio methods. Chuang and Maciel⁸⁸ proposed a generalized β -cristobalite model of plane alternance where single silanols are situated on (111)-type surface segments and geminal silanols are situated on (100)-type surface segments.⁶²⁸ This allows mimicking of a large panel of H-bonding situations, which is not possible on homogeneous crystalline surfaces. However to our knowledge, the reactivity toward water has not been envisaged on this model.

In contrast to the water/crystalline silica interface, the water/amorphous silica interface is not expected to induce an ordering of water in an ice-like structure. Actually, it has been shown that the ice–amorphous silica (native oxide film grown on Si) interface already has a “quasiliquid structure” at a temperature close to the interfacial melting point.⁵⁴⁴ In other words, interfacial melting occurs at the ice–amorphous SiO_2 contact, just the opposite of the phenomenon mentioned for crystalline silica interfaces. The thickness of the interfacial layer within which the chemical and physical properties of the solution are affected by the amorphous silica surface was estimated to be 0.5 nm.⁶²⁹

For amorphous silica, the main challenge is, and remains, to describe to what extent and how the H-bond breaking may occur in the preexisting H-bond surface network to form a new network with water. Another question concerns the well-known heterogeneity of amorphous silicas, exhibiting hydrophilic and hydrophobic zones, and finally, the link between nanoscopic reactivity and large scale measurements such as contact angles.

8.3.1. Hydroxylated Amorphous Silica Models Obtained by Classical MD. The first works on water adsorption on amorphous silicas were performed by Garofalini et al. to study the adsorption mechanisms and the effect of water on the relaxation of surfaces.^{464,639} However, no water adsorption on hydroxylated silica was considered. Later on, Lee and Rossky⁶³¹ studied the structural and dynamic properties of water above two hydrophobic (rough and flat) surfaces and one hydrophilic silica surface (Table 12). Warne et al.⁶³⁴ studied the effects of increasing the ionic strength of water confined between two

Table 12. Theoretical Works Based on Classical Force Fields, Devoted to Bulk Water at Amorphous Silicas: Nature of the Surface Studied and Methods

silica surface properties	method	ref
hydrophobic and hydrophilic silica fully hydroxylated	LMCCR force field ⁶³⁰	631
SiO and SiOH units with a 3:1 ratio	Collins–Catlow force field ^{632,633}	634
silanol density 3.33 OH nm ⁻² and SiO ⁻ deprotonation sites	Stillinger–Weber potential ⁵³⁰ for Si and Vashista et al. ⁵³¹ for SiO ₂	285,307
surfaces of different silanol density	BKS (see Table 3)	462,635
surface with 1.3 OH nm ⁻²	BMH (see Table 3)	524,636
silanol density from 1 to 3.2 OH nm ⁻²	CC force field	528
silanol density 3.2 OH nm ⁻²	CC Force field	637
surface with 1.8 OH nm ⁻²	BMH (see Table 3)	638

amorphous silica surfaces. Unfortunately, in these works no details are given about the nature (terminal or geminal) of silanols, the OH density, the distribution of silica rings, or the silica H-bond network. Cruz-Chu et al.⁵²⁸ simulated wetting angles of water adsorbed on silicas surfaces with 0, 1, and 3.2 SiOH nm⁻². They showed that the presence of silanols induces hydrophilicity. However, it was not possible to identify differences in wetting angles (that were equal to zero) between the surfaces with silanol densities 1 and 3.2 nm⁻². Colombi Ciacchi et al.³⁰⁷ proposed two amorphous silica models, one obtained from bulk silica and one ultrathin SiO₂ layer on metal Si, both having a SiOH density of 3.33 OH nm⁻². The two surfaces, when immersed in water, induce a structuring of water in layers of higher and lower densities with respect to the bulk. Water penetration into the relatively open structure of the hydroxylated surfaces was also observed. The bulk water density is reached at 4–5 Å from the surfaces. Heat of immersion values of 166 and 203 mJ/m² for the amorphous silica and native oxide, respectively, were calculated. The first of the two values may be compared with experimentally measured values of 157 and 158 mJ/m² for surfaces with estimated densities of terminal SiOH groups of 2.3 and 3.4 nm⁻².^{604,605} Water in the first layer above amorphous silica forms on average 2.54 H-bonds with water, 0.14 H-bonds with siloxane O, and 0.3 donor and 0.3 acceptor bonds with silanol groups. On the ultrathin film, the water–siloxane H-bond is increased to 0.24. We note, as for crystalline surfaces, the occurrence of donor H bonds from water to siloxane that were not confirmed with ab initio studies on crystalline surfaces. However an ab initio study of an amorphous silica surface/water interface is still lacking. More recently, the same group proposed a theoretical study of water adsorption on a periodic model of amorphous silica (see Figure 56), from which a cluster containing a negatively charged SiO⁻ group is cut.²⁸⁵ Ab initio preliminary calculations show that water preferentially adsorbs on a SiO⁻ group with the protons pointing toward the negative charge. Force field parameters have been parametrized to fit an onset of ab initio MP2 benchmark. It is found that the heat of immersion of the negatively charged surface is highly dependent on the surface charges and of the chosen water model.

Hassanali and Singer^{462,463,635} generated an amorphous silica surface exhibiting a silanol density of 6.4 OH nm⁻² with 70% of geminal silanols and 30% of vicinal groups and a surface with 4.0 OH nm⁻² and 40% geminal and 60% vicinal silanols, which

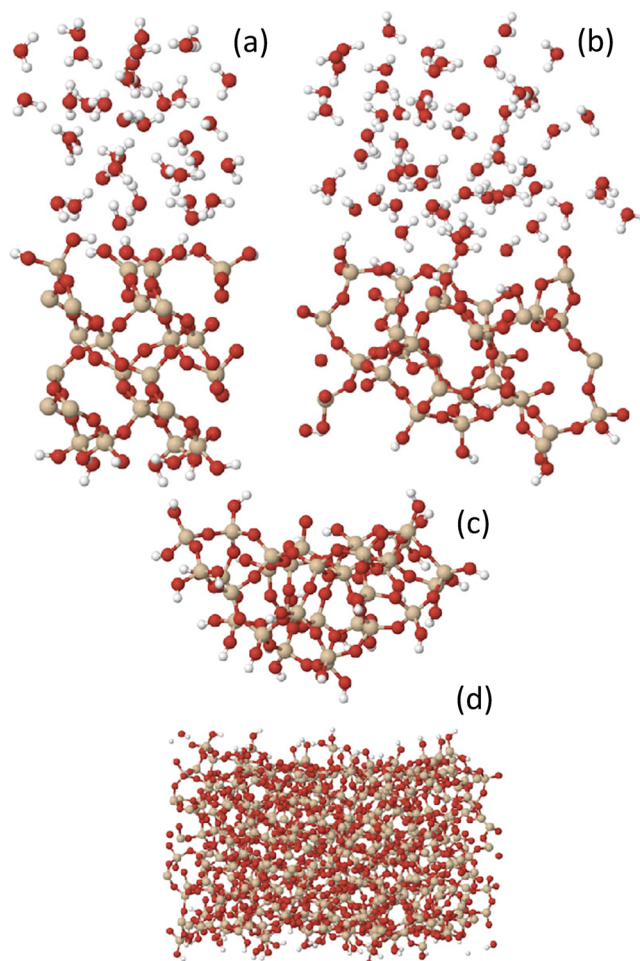


Figure 56. Model systems used for the calculation of atomic charge differences after the deprotonation of a terminal silanol group: (a) The (0001) surface of α -quartz in contact with liquid water. (b) A small periodically repeated amorphous SiO₂ slab in contact with liquid water. (c) A deprotonated amorphous SiO₂ cluster carved out from the large amorphous SiO₂ slab shown in panel d and terminated with OH groups to saturate the artificial dangling bonds. Reprinted with permission from ref 285. Copyright 2011 John Wiley and Sons.

also had strained S2R rings. The calculated heats of immersion are 0.832 and 0.279 J/m², respectively, suggesting an increased hydrophilicity of the high OH density silica. This was confirmed by the analysis of the surface heterogeneity, in which patches of siloxane-covered surfaces exhibit a hydrophobic character, whereas zones of high silanol densities have an increased hydrophilic character, a trend confirmed by the radial density analysis (Figure 57).

Floess and Murad⁶³⁷ studied the competitive adsorption of PDMS and water on amorphous silica. The generated amorphous silica surface features are unfortunately not described. The adsorption of water vapor is found to be stronger than that of PDMS, with penetration into the silica network. Water seems to cluster on the surface rather than form a continuous film.

Leed and Pantano^{524,636} generated an amorphous silica surface containing a hydroxyl concentration of 1.3 OH nm⁻², a rather low OH content. No local information on the OH distribution at the surface is provided. The heat of water adsorption on this surface ranged from -75 to -40 kJ/mol, and

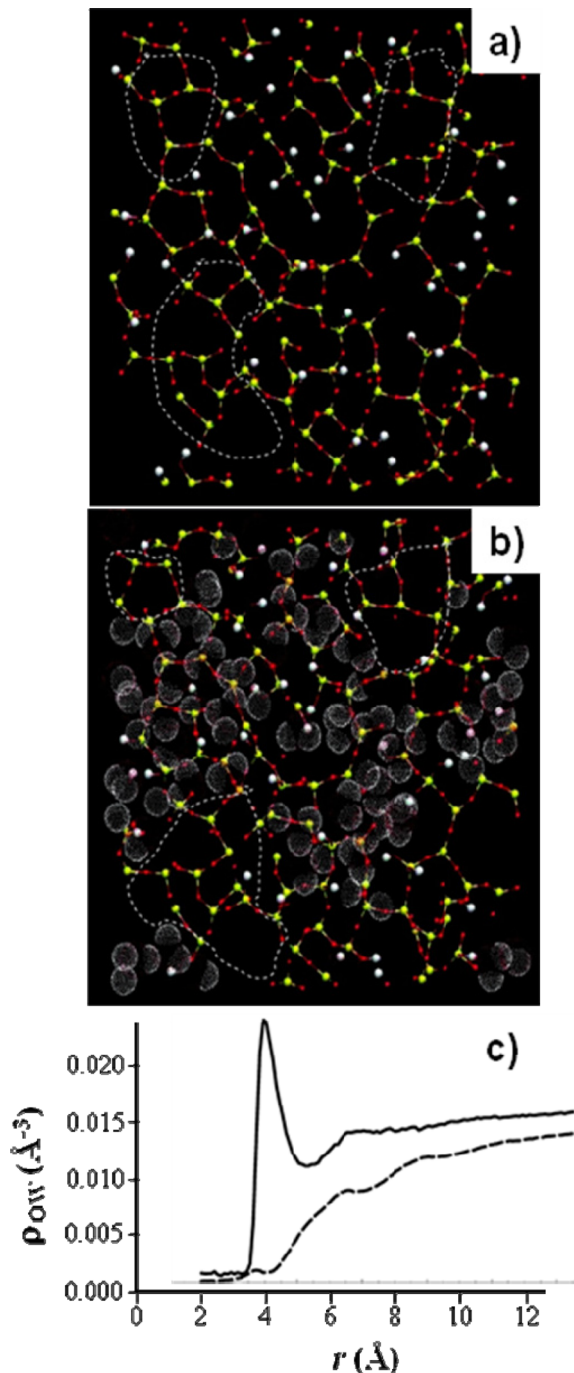


Figure 57. (a) Hydrophobic and (b) hydrophilic zones on amorphous silica and (c) radial density of water molecules surrounding silanol oxygens (solid curve) and surface siloxane (dashed curve). Reprinted with permission from ref 462. Copyright 2007 American Chemical Society.

50% of the surface sites exhibit an interaction with water more negative than -44 kJ/mol , the heat of water liquefaction.⁵⁶²

Chai and Yang⁶³⁸ modeled water/amorphous silica interaction and the wetting angle (Figure 58).

8.3.2. Hydroxylated Amorphous Silica Models Obtained by ab Initio Methods. In recent years, ab initio amorphous silica models have been proposed. Minibaev et al.⁶⁴⁰ proposed a silica surface with a silanol density of 6.9 OH nm^{-2} . Ab initio studies of adsorption of simple molecules on this silica gel surface allowed the most preferential adsorption

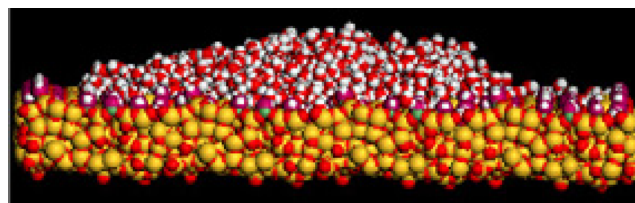


Figure 58. Wetting of amorphous silica by water. Reprinted with permission from ref 638. Copyright 2009 Elsevier.

positions to be found. The energies of adsorption of water with the silica gel surface ranged from -19.3 to -77.2 kJ/mol ; in the most stable configuration, water is twice H-bond acceptor from silanols and once H-bond donor.

Adsorption energies of isolated water molecules on the Tielens' model are -46 and -50 kJ mol^{-1} on the terminal and geminal silanols, respectively, showing no significant reactivity differences between terminal and germinal silanols.⁵¹⁰ A more favorable energy of adsorption is calculated for water adsorption on silanol nests: a study of discrete water molecule adsorption on amorphous silica was performed by Costa et al.⁶⁴¹ The amorphous silica surface model is inspired by the model of Masini and Bernasconi.⁵⁰⁷ This surface presents a high silanol density of 7.66 OH nm^{-2} , partitioned in 66% geminal silanols and 34% terminal-associated ones. AIMD of water molecules evenly spread on the whole silica surface resulted in water clustering and concentration on the parts of the surface richest in silanols (Figure 59). The mean energy of

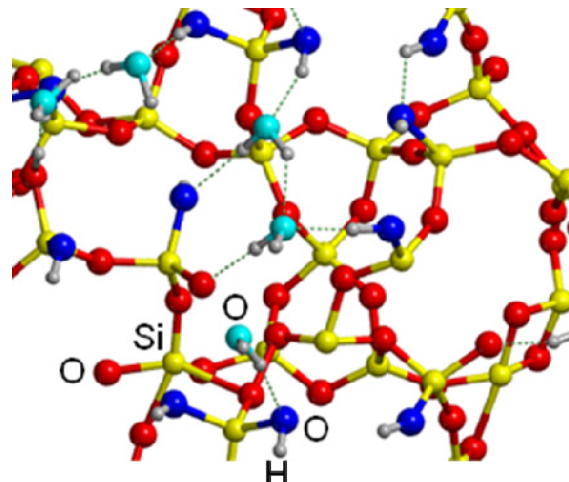


Figure 59. Water cluster adsorbed on amorphous silica. Drawn with data from ref 641.

adsorption of water on this surface is -61 kJ mol^{-1} , slightly more negative than that found on isolated silanols. Poly-H-bonded silanols have been reported to exhibit an increased acidic character by comparison with mono- and di-H-bonded silanols.^{200,642}

In conclusion, the silica–water interface represents a complex system to be studied because of the subtle interplay between complementary and competing forces (hydroxyl–hydroxyl network vs water–hydroxyl interactions) on one hand, and intricate H-bond patterns occurring at the amorphous silica surfaces on the other hand. One clear point is that Q^2 and Q^3 develop the same attitude to H-bond with adsorbed water molecules and can be considered to exhibit the

same Brønsted acidity. Experimental data reveal that the silica interface has a structuring effect on the adsorbed water layer. Ab initio studies show that water adsorption is efficiently described by its interactions with the preexisting H-bond pattern: water may either break or cooperatively reinforce this pattern. The OH density and nature are two factors affecting the preexisting H-bond pattern. Ab initio MD appears to be the most promising tool to reveal silica surface properties related to the acid/base character of its surface sites. Furthermore, results from AIMD allow development and validation of new force fields, which in turn permit study of the properties of more complex model systems and for a longer time evolution.

9. INTERACTION WITH BIOMOLECULES

Understanding the interaction between biomolecules and inorganic materials is of extraordinary relevance due to its direct implications in several fields such as biotechnology, nanotechnology, biomaterials, biominerization, and drug delivery as mentioned in the Introduction.²⁶¹ The practically relevant properties of, for instance, a protein/surface system, are mediated by protein adhesion at the surface, which in turn is dictated by molecular recognition. Deep knowledge of the biomolecule/surface interactions would indeed allow the design or the functionalization of biocompatible materials in a more rational fashion, since they could then be prepared with a particular target in mind. Silica surfaces are particularly suitable for these purposes. Furthermore, in a prebiotic chemistry context, it was suggested long ago and reviewed recently²⁰⁵ that mineral surfaces could have played a role in the polymerization of biomonomeric building blocks to form the first biopolymers. Although Si in the Earth's crust is primarily found in silicates that contain cations of crucial relevance in the condensation processes, studying the biomolecule/silica surface interactions constitutes the first step in understanding the role of such surfaces in concentrating, immobilizing, selecting, and organizing the relevant raw biomolecules in the reactions. Additionally, peptide/silica surface interactions may induce conformational changes, which may stimulate the peptide to show a specific bioactivity lacking in its unfolded state. Such an activation of the potentially "hidden" bioactivity might have triggered the first biocatalytic reactions in a primordial Earth, hence giving rise to the emergence of metabolic cycles, a crucial aspect for the origin of life.⁶⁴³

Useful information for the above-mentioned purposes can be provided by answering the following questions: (i) Which regions of the biomolecule are responsible for the biomolecule/silica surface interactions, and why? ii) Is the biomolecule/surface contact direct or through solvent water molecules? (iii) Among the different surface sites present in a given biocompatible material, does the biomolecule show any preferential interaction and why? (iv) Does the biomolecule undergo significant conformational changes upon adsorption? Most of this information can be obtained by carefully analyzing the biomolecule/silica interface region.

From the modeling point of view, works purporting to study the interactions between full biomacromolecular systems and silica surfaces, which normally include the presence of water solvent, were carried out with classical molecular dynamics. Studying these kinds of systems at an ab initio level, despite the fast progress in computer architecture and code development, is not yet feasible because of the enormous complexity of the systems, which would render calculations extremely costly. However, useful information about biomolecule/silica surface

systems at an ab initio level can be obtained by using drastically simplified biosystems, for example, amino acids, small peptides, nucleobases, base pairs, etc. Additionally, this procedure allows focusing the problem in a more oriented way, for instance, from a set of amino acids, determining those more prone to interact with a particular silica surface feature.

Among biomolecules, proteins are by far the most studied systems, and thus, results involving proteinaceous-based systems have significant presence in this section. This section is organized as follows. First, a review of the results concerning amino acid interaction with silica surfaces will be provided, both at the gas phase–silica and solution–silica interfaces, paying particular attention to glycine, the simplest amino acid. Second, we will focus on peptides and proteins adsorbed on silica, and finally, we will address the interaction of other biomolecules (i.e., DNA derivatives), drugs, and natural products with silica surfaces.

9.1. Interaction with Amino Acids

9.1.1. The Glycine Case. **9.1.1.1. Gas-Phase Interaction.** Glycine (shown in Figure 60), is the simplest amino acid and is

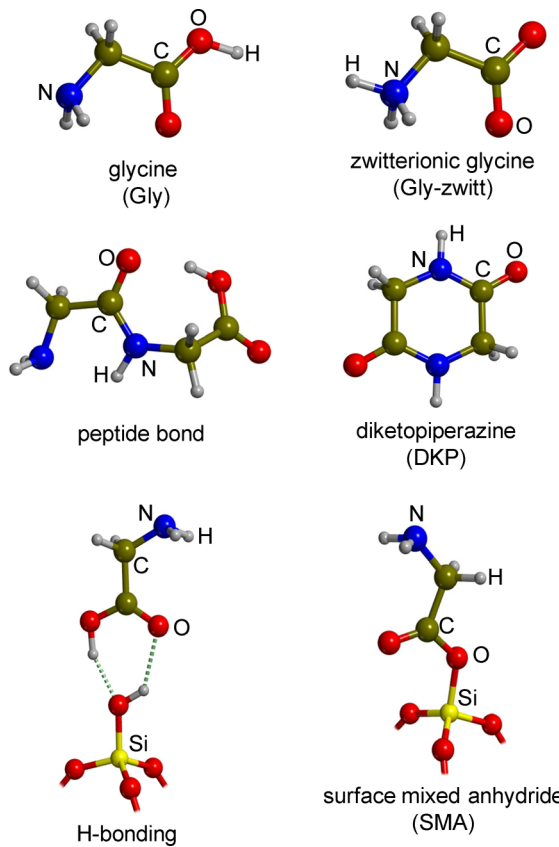


Figure 60. Chemical systems relevant for glycine adsorption mentioned in this review.

ideal to model AA/silica systems because the defining functionalities of an amino acid are not obscured by the lateral substituent. For years, glycine was the only known natural amino acid to sublime before decomposing so that chemical vapor deposition (CVD) on silica (and on other solid surfaces as well) allowed experimental study of the intrinsic glycine/silica surface features, free from the influence of water, which resulted in a fertile ground for a fruitful interplay between theory and experiments. Currently, fast thermal heating

techniques allow neutral amino acids to be obtained in the gas phase.^{644,645}

The works of Groenewegen et al.⁶⁴⁶ and Basiuk et al.⁶⁴⁷ are two seminal studies focused on the interaction of glycine vapors with silica surfaces outgassed at 650–700 °C using IR spectroscopy measurements. More recently, Lomenech et al.²²³ reported the FTIR spectrum of the adsorption of glycine by CVD on a silica sample pretreated at 100 °C. Because some of the glycine IR absorption modes strongly overlap with vibrational modes of silica or residual water (in particular, the $\nu(\text{OH})_{\text{COOH}}$ and the $\delta(\text{HNH})$ glycine modes are obscured by the $\nu(\text{OH})$ of Si–OH and the $\delta(\text{HOH})$ of water, respectively), the $\nu(\text{C=O})$ mode is usually used as fingerprint to characterize glycine adsorption onto silica surfaces due to its sharp and intense band. The experimental $\nu(\text{C=O})$ vibrational mode for glycine in the gas phase was measured by Stepanian et al.⁶⁴⁸ by entrapping glycine in a cold Ar matrix, resulting in a value of 1784 cm⁻¹. Table 13 collects the $\nu(\text{C=O})$ registered in these works and the assignments made by the authors.

Table 13. Reported Stretching $\nu(\text{C=O})$ Values (in cm⁻¹) and the Assignments Made by the Authors^a

authors	$\nu(\text{C=O})$	assignment according to the authors
Groenewegen et al. ⁶⁴⁶	1740	“surface mixed anhydride”
	1670	H-bonding
Basiuk et al. ⁶⁴⁷	1760	“surface mixed anhydride”
	1720	H-bonding
Lomenech et al. ²²³	1670	peptide bond
	1699	H-bonding

^aFigure 60 shows the chemical systems associated to these assignments.

Both Groenewegen et al.⁶⁴⁶ and Basiuk et al.⁶⁴⁷ observed one band at 1720 and 1740 cm⁻¹ region, respectively, which was associated to the formation of the “surface mixed anhydride”, that is, of grafted glycine $\equiv\text{Si}_{\text{surf}}-\text{O}-\text{C}(\text{=O})-\text{CH}_2\text{NH}_2$ (SMA, see Figure 60). As mentioned in section 3, this kind of surface feature should form if glycine condenses with a silanol surface group releasing water; that is, $\equiv\text{Si}-\text{OH} + \text{HOOC}-\text{CH}_2\text{NH}_2 \rightarrow \equiv\text{Si}_{\text{surf}}-\text{O}-\text{C}(\text{=O})-\text{CH}_2\text{NH}_2 + \text{H}_2\text{O}$. In contrast, Lomenech et al.²²³ did not observe any band at this region. The three works assigned $\nu(\text{C=O})$ bands corresponding to glycine interacting with SiOH groups via H-bonding, although discrepancies concerning the position were also reported. Finally, a value of 1670 cm⁻¹ was found only in the Basiuk's spectra, which was interpreted as the C=O stretch corresponding to a peptide bond (see Figure 60), suggesting that silica surfaces catalyzed the peptide bond formation.

The FTIR spectra recorded by Lomenech et al.,²²³ both for the naked silica powder and for the glycine/silica prepared by CVD within the 2000–1300 cm⁻¹ region are shown in Figure 61. In addition to the above-mentioned 1699 cm⁻¹ band, two sharper bands at 1423 and 1371 cm⁻¹, probably resulting from the $\delta(\text{HCH})$ and $\delta(\text{CCH})$ modes, respectively, were attributed to glycine adsorption, because they were not present in the spectrum of bare silica. The other two bands present in the two spectra (1861 and 1630 cm⁻¹) were assigned to the $\nu_{\text{as}}(\text{SiOSi})$ and $\delta(\text{HOH})$ frequencies of adsorbed water, respectively, although in the latter a contribution from the $\delta(\text{HNH})$ mode was also tentatively assigned. No bands associated with SMA were observed.

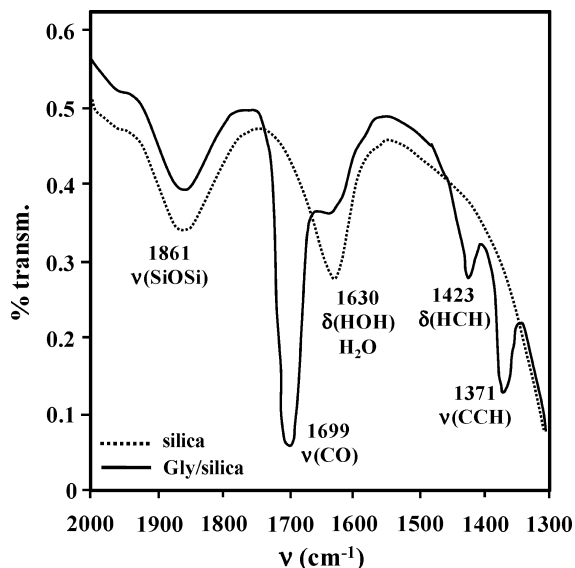


Figure 61. FTIR spectra of the naked silica powder (dotted line spectrum) and glycine/silica prepared by CVD (solid line spectrum). Adapted with permission from ref 223. Copyright 2005 John Wiley and Sons.

It was suggested that fully hydroxylated silica surfaces may act as solid solvents, since the presence of a large amount of Si–OH groups may have the same effect as a large number of water molecules. This can be checked by analyzing the presence of adsorbed glycine zwitterion, $^+{\text{H}_3\text{NCH}_2\text{COO}}^-$ (Gly-zwitt, see Figure 60) in the glycine/silica spectrum of Figure 61. Results indicated no signs of adsorbed Gly-zwitt. Indeed, neither the bending modes of NH_3^+ , at approximately 1617 and 1523 cm⁻¹, nor the COO^- stretching modes, which appear at lower values than those in C=O(OH) , were present in the spectrum. Thus, from the gas phase, glycine adsorbs in its canonical form (Gly-can), indicating that the silanol groups present at the surface are not sufficient to make silica behave as a solid solvent and transform Gly-can into Gly-zwitt.

A final interesting point to analyze in Lomenech's spectra (Figure 61) is whether other transformed forms of glycine are present. The $\nu(\text{C=O})$ bands due to a peptide bond and the diketopiperazine (DKP, shown in Figure 60) cycle were not present. The formation of DKP, which takes place by cyclodimerization of two glycine molecules at 150–200 °C with the emission of two H_2O molecules, could be ruled out because the ring stretching mode at 1471 cm⁻¹, the most conspicuous sign for DKP, was not present. Both absences indicate that no glycine condensation proceeds on the surfaces in the conditions used.

Despite the very interesting results provided by these IR data, several questions still remain open: (i) What is the actual picture of glycine adsorbed on a silica surface at a molecular level? (ii) why are there discrepancies in the $\nu(\text{C=O})$ value for the H-bonding interacting form between the different works? (iii) Why is the surface mixed anhydride observed in some works and not in others? Answers to these questions have been provided in works based on quantum mechanics.

In the same work of Lomenech et al.,²²³ B3YLP calculations on the glycine interaction with minimal clusters (H_3SiOH , $\text{H}_2\text{Si}(\text{OH})_2$ and $\text{H}_4\text{Si}_2\text{O}(\text{OH})_2$ simulating isolated, geminal, and vicinal sites, respectively) were also reported. Calculations allowed performance of a complete search for all possible H-

bonded complexes between one single glycine and a variable number of silanol groups, representing the complex distribution of OH groups at the surface of amorphous silica. On the other hand, Rimola et al.^{74,309} simulated at the B3LYP level the adsorption of glycine on the (001) surface of edingtonite terminated with isolated hydroxyl groups, using both a cluster approach and a full periodic treatment. The structures that best match the experimental results as well as the computed adsorption energies (ΔE_{ads}) are shown in Figure 62. Table 14 summarizes the comparison between the computed and the experimental $\nu(\text{C}=\text{O})$ values.

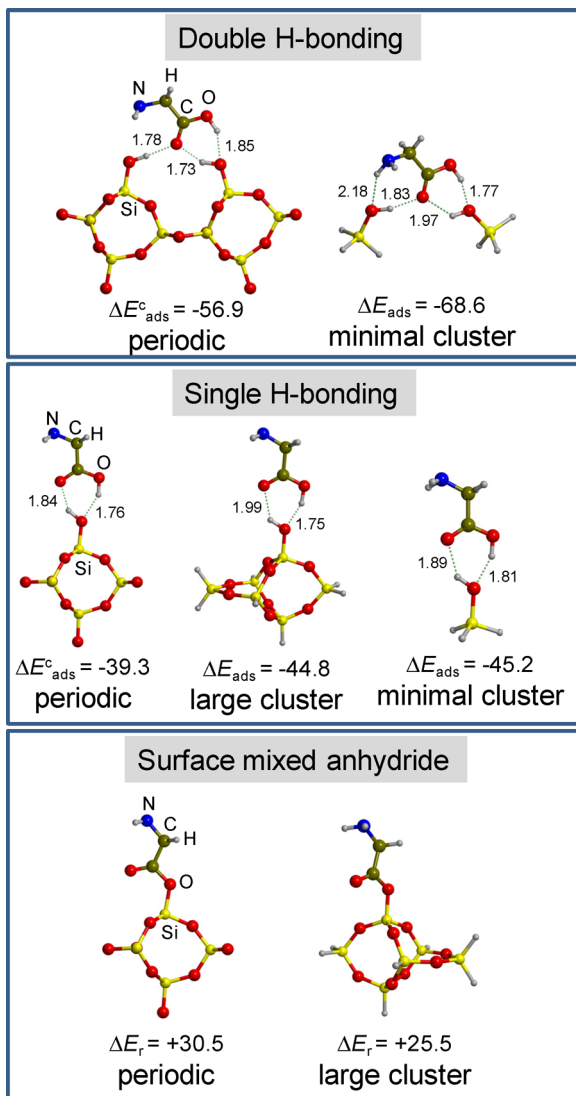


Figure 62. Different glycine/silica surface complexes obtained from ab initio calculations: “periodic” means calculations performed at the B3LYP/double- ζ level using a periodic silica surface model; “minimal cluster” means calculations performed at the B3LYP/6-31++G(d,p) level using minimal cluster models; “large cluster” means calculations performed at the B3LYP/6-31+G(d,p) level using a larger cluster model than the minimal ones. Computed adsorption energies (in kJ mol^{-1}) are also reported: ΔE_{ads} and $\Delta E_{\text{ads}}^{\text{c}}$ refer to adsorption energies without and with the basis set superposition error corrected, respectively. ΔE_r refers to the reaction energy (in kJ mol^{-1}) for the formation of the surface mixed anhydride ($\equiv \text{Si}_{\text{surf}}-\text{OH} + \text{HOOC}-\text{CH}_2-\text{NH}_2 \rightarrow \equiv \text{Si}_{\text{surf}}-\text{O}(\text{=O})-\text{CH}_2-\text{NH}_2 + \text{H}_2\text{O}$). The bond distances reported are in Å. Drawn from data of refs 74 and 223.

Table 14. Comparison between the Experimental and Computed $\nu(\text{C}=\text{O})$ Values (in cm^{-1}) Reported in the Literature^a

experimental	computed	interaction pattern/model	authors
1699	1694 ^a	double H-bonding/periodic	Rimola et al. ³⁰⁹
	1701 ^b	double H-bonding/minimal cluster	Lomenech et al. ²²³
1720	1717 ^a	single H-bonding/periodic	Rimola et al. ³⁰⁹
	1724 ^c	single H-bonding/large cluster	Rimola et al. ³⁰⁹
	1723 ^b	single H-bonding/minimal cluster	Lomenech et al. ²²³
1760	1767 ^c	surface mixed anhydride/large cluster	Rimola et al. ⁷⁴
	1769 ^a	surface mixed anhydride/periodic	Rimola et al. ⁷⁴

^aThe structural interpretation made by the authors is defined in the “interaction pattern/model” column and shown in Figure 62.

^bComputational details for B3LYP/double- ζ and a scaling factor of 0.957. ^bComputational details for B3LYP/6-31++G(d,p) and a scaling factor of 0.961. ^cComputational details for B3LYP/6-31+G(d,p) and a scaling factor of 0.975.

The value of 1699 cm^{-1} represents the maximum bathochromic shift (-85 cm^{-1}) of the $\nu(\text{C}=\text{O})$ fingerprint mode and results from the H-bonding with two different terminal silanol groups (see “double H-bonding” interaction pattern in Figure 62). Theoretical results indicate that the interaction of glycine with silica surfaces may also take place with only one SiOH group through the “single H-bonding” interaction pattern (see Figure 62). The computed $\nu(\text{C}=\text{O})$ values for glycine adopting this adsorption mode (1717, 1724, and 1723 cm^{-1} , for periodic, minimal, and large cluster models, respectively) agree fairly well with the experimental value of 1720 cm^{-1} . Noticeably, the “single H-bonding” interaction pattern corresponds to a cooperative H-bond similar to that commonly found for carboxylic acid dimers; that is, the COOH group is envisaged in two H-bonds with one silanol group, one in which the glycine OH group acts as a H-bond donor and another one in which the C=O group acts as a H-bond acceptor. Such a cooperative effect is responsible for the significant bathochromic shift observed for $\nu(\text{C}=\text{O})$ (experimentally, -64 cm^{-1}). Remarkably, the computed glycine/silica complexes that exhibit these two H-bond patterns were found to be the most stable adducts. Differences between the experimental results of Basiuk et al.⁶⁴⁷ and those of Lomenech et al.²²³ can be related to the different pretreatment of the silica surfaces. The latter authors pretreated the silica sample at 100°C overnight, while the former ones outgassed the silica sample at about 700°C . Silanol population is smaller in the silica sample treated at 700°C because at high temperatures silica surfaces undergo silanol condensations. Thus, isolated silanol groups are predominant in Basiuk’s silica, and the interaction with glycine takes place via the “single H-bonding” interaction pattern. In contrast, Lomenech’s silica, richer in silanol groups (both in amount and diversity), is able to adsorb glycine via two contiguous surface silanol groups adopting the “double H-bonding” interaction pattern.

Basiuk et al.⁶⁴⁷ also observed a band at 1760 cm^{-1} , which was associated with the $\nu(\text{C}=\text{O})$ mode of the SMA bond. Calculations addressed to check whether this band could correspond to this surface functionality indicated that this is indeed the case. The computed $\nu(\text{C}=\text{O})$ values using both the “large cluster” and the “periodic” surface models were found at

1767 and 1769 cm^{-1} , respectively (see Table 14).³⁰⁹ Nonetheless, theoretical calculations also revealed that SMA formation from reacting glycine with an isolated SiOH has a reaction free energy ($T = 298 \text{ K}$) of $+25.5 \text{ kJ mol}^{-1}$; that is, the reaction is thermodynamically disfavored. However, as already discussed in a previous section, a pretreatment of the silica sample at $700 \text{ }^\circ\text{C}$ causes silanol condensation processes, which as we have previously explained may result in the formation of some strained surface defects such as $(\text{SiO})_2$ or S2R and $(\text{SiO})_3$ or S3R. Rimola et al.⁵⁴¹ have theoretically studied the reactivity of S2R defects with glycine to give the SMA. Calculations indicated that this reaction is indeed feasible because the computed free energy barrier and reaction free energy were found to be about 54 and -63 kJ mol^{-1} , respectively. This is probably due to the opening of the very strained S2R ring. Moreover, these results provide a plausible explanation of why Basiuk et al.⁶⁴⁷ observed the formation of the silica SMA whereas Lomenech et al.²²³ did not. That is, in Basiuk's surfaces, after pretreatment at $700 \text{ }^\circ\text{C}$, some S2R defects were probably present, which reacted with vapors of glycine during the CVD experiments to form the SMA bond; in contrast, Lomenech's silica surface was pretreated at $100 \text{ }^\circ\text{C}$ so that such strained defects were probably not produced and consequently SMAs were not able to form.

Noticeably, calculations agree with the experimental observations about the fact that the glycine/silica surface interactions do not induce the preferential adsorption of Gly-zwitt over Gly-can. Figure 63a,b shows that attempts to optimize Gly-zwitt with the presence of one SiOH group (structures on the left) evolved toward Gly-can (structures of the right).^{309,556} In fact, adsorption of Gly-zwitt is only determined to be favorable at large coverages³⁰⁹ due to stabilizing lateral interactions (Figure 63c), similarly to what

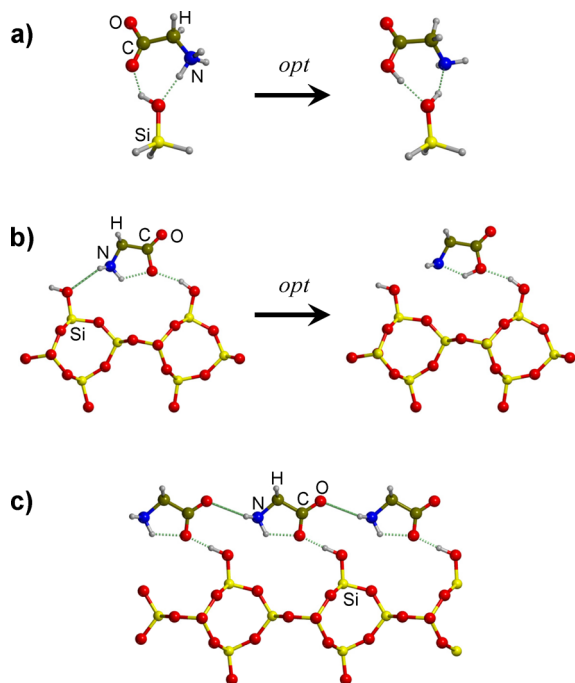


Figure 63. (a, b) Attempts to optimize glycine in its zwitterionic state when interacting with one SiOH group. Results indicated that glycine evolved toward its canonical state. (c) Zwitterionic glycine found as a stable form only when considering a high loading adsorption. Drawn from data of refs 309 and 556.

occurs in the glycine molecular crystal.^{649,650} This brings about a rather strong H-bond cooperativity between adsorbed glycine molecules that helps to increase the electrostatic interactions between them up to a limit in which adsorbed zwitterionic forms are stable. It is worth mentioning that this structure can only be found with a periodic treatment; otherwise the lateral interactions between adjacent glycine molecules, crucial for the stabilization of Gly-zwitt, cannot be accounted for.

Similarly, from theoretical results in refs 223 and 556, it is confirmed that an increment of the SiOH groups interacting with glycine induces a significant stabilization of Gly-zwitt over Gly-can (see Figure 64). It is expected that with four SiOH

$(\text{SiOH})_n$	Canonical systems	Zwitterionic systems	ΔE_{rel}
$n = 1$			-
$n = 2$			41.8
$n = 3$			15.5

Figure 64. Relative energies (ΔE_{rel} , in kJ mol^{-1}) between canonical glycine and zwitterionic glycine, as a function of the number of SiOH groups. Drawn from data of ref 223. Computed at B3LYP/6-31+G(d,p).

groups Gly-zwitt would become more stable than the canonical form. However, a glycine molecule interacting with four SiOH groups is not physically sound, because it would mean a silica surface with an unreasonably high density of silanols. Along this line, Han and Sholl⁶⁵¹ found that Gly-zwitt adsorbed on a periodic model of a fully hydroxylated α -quartz (0001) surface, featured to exhibit H-bonded geminal SiOH groups, was practically isoenergetic with the analogous canonical system, in both cases four SiOH groups were involved in the glycine binding.

All of the structures shown above simulate the interaction of glycine with silica surfaces considering isolated, vicinal, and interacting silanol groups. However, geminal silanols are also present on silica surfaces. Geminal silanol groups, although being present in a lesser degree than the others, have been reported to exhibit a slightly more acidic character (see sections 3.1.2 and 8.2.6) and because of that the interaction of glycine with these silanol groups also deserves to be studied. Adopting the minimal $\text{Si}(\text{OH})_4$ cluster model, Lomenech et al.²²³ computed at B3LYP/6-31++G(d,p) level the complex shown in Figure 65a, as a first attempt to picture the glycine/SiOH geminal interface, in which the COOH establishes a cooperative H-bond with two geminal OH groups.

Han and Sholl⁶⁵¹ also calculated at the PBE level the most stable structure of glycine adsorbed on the hydroxylated α -

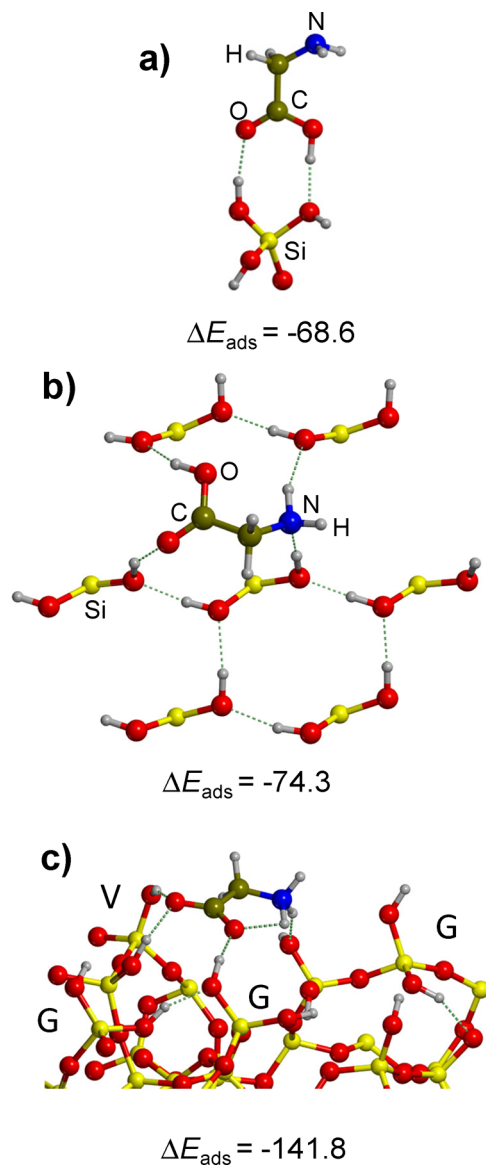


Figure 65. (a) Optimized structure and computed adsorption energy (ΔE_{ads} , in kJ mol^{-1}) at B3LYP/6-31++G for glycine interacting with a minimal cluster ($\text{Si}(\text{OH})_4$) model representing geminal silanol groups (drawn with data from ref 223). (b) Optimized structure and computed adsorption energy at PBE for glycine interacting with the hydroxylated (0001) α -quartz surface (drawn with data from ref 651). (c) The dominant configuration obtained from several ab initio molecular dynamics simulations (PBE method and $T = 300$ K) for glycine interacting with a silica surface model rich in geminal silanol groups (drawn with data from ref 641). The computed adsorption energy (ΔE_{ads} , in kJ mol^{-1}) was obtained by performing a geometry optimization onto this configuration at the B3LYP/6-311++G(d,p) level. V and G refer to vicinal and geminal silanol groups, respectively.

quartz (0001) surface (see Figure 65b). For this case, two H-bonds present on the pristine surface were destroyed in order to form the four H-bonds that bind glycine onto the surface. In a more recent work, Costa et al.⁶⁴¹ computed the interaction of glycine on a highly hydroxylated amorphous silica surface (7.66 OH nm^{-2}) particularly dominated by geminal SiOH groups (5.1 nm^{-2} , with a ratio of about 66% of the total surface SiOH). Calculations were based on ab initio molecular dynamics simulations carried out at $T = 300$ K using the PBE density functional method. The most stable configuration obtained is

represented in Figure 65c. As one can observe, glycine was found as Gly-zwitt, the carboxylate groups being engaged by the surface through two vicinal and one geminal SiOH groups (labeled as V and G, respectively) and the ammonium being H-bonded to the O atom of a geminal SiOH. The authors interpreted that the stabilization of the Gly-zwitt could be due to two factors: (i) the large amount of silanol groups present on the surface, which facilitated the formation of several H-bonds with glycine (about 4); (ii) the increased acidic character of the geminal SiOH, which enabled it to form more favorable electrostatic interactions with negative charge densities, as the one present in the carboxylate group. Therefore, according to these theoretical results, it seems that highly hydroxylated silica surfaces ($7\text{--}8 \text{ OH nm}^{-2}$) may indeed act as solid solvents. However, this statement should be taken with caution considering that it is generally accepted that the silanol density for fumed silica is approximately $4\text{--}5 \text{ nm}^{-2}$ and the geminal silanol density is considerably lower than the one exhibited by the surface model used by Costa et al.⁶⁴¹ In fact, no traces of Gly-zwitt were found in the experimental glycine/silica IR spectrum. Despite that, these results are relevant for studies using silicas formed in conditions of high water activity such as the biogenic ones, in which a density of 6.2 OH nm^{-2} has been quoted. Additionally, precipitated silica, where SiOH densities between 7 and 8 nm^{-2} have been reported, might be the most relevant materials present in the prebiotic earth so that these results gain significance in a prebiotic context.

9.1.1.2. Interaction in the Presence of Water. All the works commented so far dealt with the adsorption of glycine under strict gas phase conditions; namely, in absence of water. Nonetheless, water is ubiquitous in biological media so the adsorption of glycine in wet conditions is of great relevance. Lambert and co-workers have investigated in depth^{210,224,247,652} glycine adsorption on amorphous silica from aqueous solutions at different initial concentrations and pHs, by means of different spectroscopic techniques such as XRD, diffuse reflectance infrared Fourier transform spectroscopy (DRIFTS), solid state nuclear magnetic resonance (ssNMR), and thermoproduced desorption coupled to mass spectrometry (TPD-MS). From these works, three main conclusions can be drawn, which are exposed below.

9.1.1.2.1. A Molecularly Adsorbed Glycine Species Coexists with the α - and β -Glycine Crystalline Forms. Glycine is known to crystallize as three polymorphs: α -, β -, and γ -glycine (those other forms found only in extreme conditions are not included). In these three polymorphs, glycine is found in its zwitterionic state and the local environments of these zwitterions differ only by specific H-bonding arrangements. The ¹³C NMR chemical shifts in the carboxylate region (170–178 ppm) for the α -, β -, and γ -glycines are well differentiated: 176.4, 175.4 and 174.5, respectively. Considering that the reproducibility of the chemical shifts is better than 0.05 ppm, ssNMR is therefore a suitable technique to discriminate between these and other glycine forms.

The obtained ¹³C cross-polarization magic angle spinning (CP-MAS) NMR spectra focused on the carboxylate region for glycine/silica with low and high glycine concentrations (pH 6–7) are shown in Figure 66a.

At high glycine concentrations, three characteristic signals were observed, among which two were assigned to the α - and β -glycine forms (176.45 and 175.4 ppm, respectively). When the glycine loading was decreased, these two signals vanished while the one at 173 ppm remained present with the same

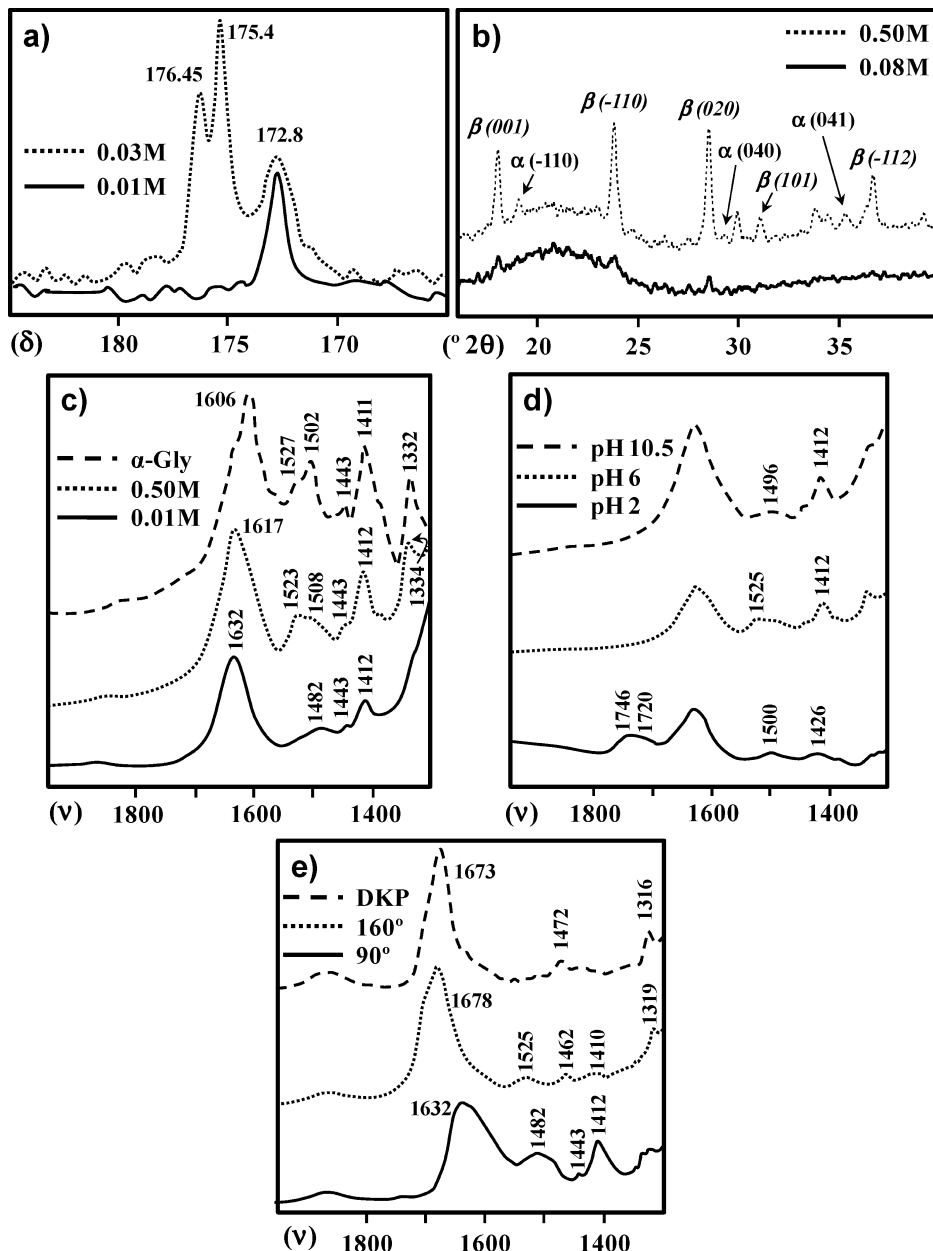


Figure 66. (a) ^{13}C CP-MAS NMR (in ppm) spectra in the carboxylate region for glycine/silica at low (solid line spectrum) and high (dotted line spectrum) glycine concentrations (pH 6–7). (b) XRD diffractograms for glycine/silica at low (solid line spectrum) and high (dotted line spectrum) glycine concentrations. (c) FTIR spectra (in cm^{-1}) for glycine/silica at low (solid line spectrum) and high (dotted line spectrum) glycine concentrations (pH 6) and for the α -glycine polymorph (broken line spectrum). (d) FTIR spectra for glycine/silica (in cm^{-1}) at different pH values. (e) DRIFTS spectra (in cm^{-1}) for glycine/silica at 90 and 160 °C (solid and dotted line spectra, respectively) and for DKP/silica (broken line spectrum). Adapted with permission from refs 210, 224, and 247. Copyright 2004, 2009 American Chemical Society and Copyright 2007 Schweizerbart Science Publishers (<http://www.schweizerbart.de/>).

intensity, indicating that it does not belong to any bulk polymorph but to a form of glycine interacting with silica surface groups, hereafter called “molecularly adsorbed glycine”. Additionally, it was noted that the change in the chemical shift of this form with respect to the bulk zwitterionic ones was of the same order as the difference in δ between the polymorphs, which suggested modifications by H-bonding to the surface (formation of covalent bonds would result in at least two times larger shifts). Accordingly, the authors suggested that the “molecularly adsorbed glycine” was defined by the formation of H-bond networks with the silica surfaces in the line of a typical “surface adduct”. The registered XRD diffractograms shown in

Figure 66b confirmed the precipitation of bulk glycine crystals at high glycine concentrations. Additionally, FTIR spectra (Figure 66c) clearly indicated that at high glycine concentration the observed bands matched perfectly well those for pure α -glycine (assignments available in Table 15). Therefore, at low concentrations glycine was specifically adsorbed on silica surface sites, presumably interacting through H-bonds yielding a “molecularly adsorbed glycine” form, whereas at higher concentrations the α - and β -glycine bulk polymorphs were also present.

The authors highlighted the formation of the β polymorph in addition to the α one (see the intensities of the XRD

Table 15. Assignments of the Bands Observed in the Spectra Shown in Figure 66c,d,e

Assignments for Figure 66c (cm^{-1})			
vibrational mode	[Gly] = 0.01 M	[Gly] = 0.50 M	pure α -glycine
$\delta_{\text{as}}(\text{NH}_3^+)$	1632	1617	1606
$\delta_s(\text{NH}_3^+)$	1482	1523, 1508	1527, 1502
$\delta_s(\text{CH}_2)$	1443	1443	1443
$\nu_s(\text{COO}^-)$	1412	1412	1411
$\rho_w(\text{CH}_2)$		1334	1332
Assignments for Figure 66d (cm^{-1})			
species	vibrational mode	pH 2	pH 6
Gly-can	$\nu(\text{C}=\text{O})$	1746, 1720	
Gly-zwitt	$\delta_s(\text{NH}_3^+)$	1500	1525
	$\nu_s(\text{COO}^-)$	1426	1412
Assignments for Figure 66e (cm^{-1})			
species	vibrational mode	90 °C	160 °C
Gly-zwitt	$\delta_{\text{as}}(\text{NH}_3^+)$	1632	
	$\delta_s(\text{NH}_3^+)$	1482	1525
	$\delta_s(\text{CH}_2)$	1443	
	$\nu_s(\text{COO}^-)$	1412	1410
DKP	$\nu(\text{C}=\text{O})$		1678
	DKP ring breathing		1462
	$\rho_w(\text{CH}_2) + \nu(\text{C}-\text{C})$	1319	1316

diffractogram of the Figure 66b), an unexpected fact because the latter normally precipitates from saturated solutions. Based on the observations in which precipitation of different glycine allomorphs from a concentrated solution can be controlled by polarization effects using laser light,⁶⁵³ the authors proposed that the electric field gradients imposed by the negative charges present on the silica surface are strong enough to cause specific orientations of the molecules, although they also pointed out that other structuring effects such as H-bonding with surface groups could be operating as well.

Based on these results, the authors suggested that the most likely picture of glycine adsorption consists in an initial specific adsorption on a limited number of surface sites followed by surface precipitation in the vicinity of the silica surface, or possibly on the selectively adsorbed glycine molecules.

9.1.1.2.2. At Low pH Glycinum Cation and Zwitterion Species Coexist; at Higher pH Only Zwitterions Are Present. Figure 66d shows the recorded FTIR spectra of the glycine/silica system as a function of adsorption pH, while Table 15 summarizes the assignments of the bands. At pH 2, the two bands at 1720 and 1746 cm^{-1} due to $\nu(\text{C}=\text{O})$ of protonated COOH and the band at 1500 cm^{-1} due to $\delta_s(\text{NH}_3^+)$ indicated that the glycinium cation was present in the sample. Moreover, Gly-zwitt also seemed to be present since the band for the $\nu_s(\text{COO}^-)$ mode appeared at 1426 cm^{-1} . With the solution pH increase (see the pH 6 spectra) the $\nu(\text{C}=\text{O})$ modes totally disappeared while the $\nu_s(\text{COO}^-)$ mode considerably increased, thus indicating that only Gly-zwitt was present. The $\nu_s(\text{COO}^-)$ and $\delta_s(\text{NH}_3^+)$ modes changed to 1412 and 1525 cm^{-1} , respectively, almost the same as that for the zwitterion in the α -glycine polymorph. At pH 10.5, the registered spectrum was very similar to the one at pH 6 so that Gly-zwitt was still present, and contrary to what one would expect no evidence of the glycinate anion was observed. Interestingly, the band at 1525 cm^{-1} was shifted to 1496 cm^{-1} , which closely resembled the one observed at pH 6 for low coverage samples. Concerning the presence of only zwitterions instead of

glycinate anions at pH 10.5, the authors suggested that the speciation of glycine could be governed by local values of pH close to the surface rather than its bulk value. That is, at this pH the silica surface bears a strong negative charge and, accordingly, the solution neighboring the surface forms a diffuse layer of opposite charge, which automatically produces a local pH lower than the value in the solution bulk. Therefore, the speciation at the interface may be different than that in the bulk, and for this particular case, the lower local pH might justify the observed higher percentages of zwitterions.

Interestingly, the authors also indicated that no covalent bonds between glycine and the silica surface occurred, a fact which allowed ruling out any “surface acylation”. In other words, the SMA form was not present. This strengthened the thesis that the “molecularly adsorbed glycine” was formed by specific H-bonds with the surface, rather than by covalent bonds.

9.1.1.2.3. Thermal Treatments of Adsorbed Glycine Molecules Induce the Formation of DKP. Figure 66e shows the in situ DRIFT spectra of the glycine/silica system as a function of heating temperature with a sample that mostly contained the “molecularly adsorbed glycine” form (pH 6 and concentration of 0.08 M). Table 15 collects the assignments of the bands observed. At $90\text{ }^\circ\text{C}$, no changes were observed in comparison to FTIR spectra at room temperature (Figure 66c). At $160\text{ }^\circ\text{C}$, the spectra underwent strong modifications and became quite similar to that of the DKP/silica system. In particular, the transformation was suggested by the presence of the intense absorption band at 1678 cm^{-1} due to the $\nu(\text{C}=\text{O})$ of the adsorbed DKP, by the small sharp band at 1462 cm^{-1} corresponding to the DKP ring-breathing and by an increase in intensity of the $\rho_w(\text{CH}_2)$ mode due to the contribution of the C–C stretching vibrations at approximately the same frequency (1316 cm^{-1}). The presence of small bands at 1410 and 1525 cm^{-1} ($\nu_s(\text{COO}^-)$ and $\delta_s(\text{NH}_3^+)$, respectively) also suggested small amounts of residual adsorbed Gly-zwitt. Conversely, the bands associated with the linear Gly-Gly dimer (for instance, its strongest band at 1598 cm^{-1}) were not observed. Additionally, TPD-MS experiments (not shown here) revealed H_2O^+ signals (18 amu) between 160 and $200\text{ }^\circ\text{C}$, in agreement with DKP formation, because the reaction is accompanied by the production of two water molecules. Therefore, the authors concluded that adsorption of Gly-zwitt on silica surfaces activates the formation of amide bonds, contrary to glycine on Pt(111),⁶⁵⁴ graphite,⁶⁵⁵ and Cu(110).²¹⁹

In addition to this set of works, Ben Shir et al.²²⁸ also studied the binding of glycine on silica surfaces using multinuclear ssNMR-techniques (section 3.2.5). For this case, SBA-15, a mesoporous silica material with a high surface area (pore diameters of 5 – 30 nm), was used as silica surface model. The effect of the amount of water present in the system was also considered, adopting both low and high hydration states. In low hydration conditions, the presence of a single population of surface-bound glycine species was observed. Despite the low H atom density ($<4\text{ H nm}^{-2}$), it was possible to determine, by means of ^{15}N { ^1H } separated local field (SLF) NMR experiments, that the glycine amine moiety was protonated (i.e., $-\text{NH}_3^+$). Cross-polarization (CP) ^{15}N { ^{29}Si } and ^{29}Si { ^{15}N } REDOR measurements allowed the geometry, stoichiometry, and specificity of glycine to the silica surface binding sites to be established. In particular, it was found that the $-\text{NH}_3^+$ moiety was positioned above a plane formed by 3 or 4 Si surface atoms, predominantly Q³ Si species arranged in a

triangular or square geometry, with an internuclear N···Si distance of 4.1 ± 0.3 Å. In addition to the high abundance of Q³ silanol sites, Q² and Q⁴ Si species were also observed on the SBA-15 surface in lesser amounts. Moreover, ¹⁵N {¹³C} REDOR data indicated that the COO⁻ had a very restricted motion, which practically indicated no contribution to surface binding. For the high hydration state (estimated surface hydrogen density of 6–12 H atoms nm⁻²), the presence of two different surface-bound glycine populations, plus a third population with “free” (non-surface-bound) glycine molecules was determined. One interacting species was identified to be the same as the one present in the low hydration state; the other bound population was found to have the same binding stoichiometry and geometry, but the COO⁻ group experienced a larger amplitude motion. The “free” population was interpreted as glycine being completely solvated by water molecules because glycine exhibited large libration motions. The physical picture suggested by the authors for the three populations detected, emerging from the accumulated data, is shown in Figure 67.

The H-bonding network between the ammonium H atoms and the lone pair electrons of the oxygens atoms of the SiOH and of H₂O (for bound and nonbound populations) was postulated to be the chemical driving force that underlay glycine/silica surface specific interactions. Confirming the results of Lambert and co-workers,^{210,224,247} surface-induced crystallization of α and β polymorphs was also observed.

Despite these very interesting results, important aspects, however, still remain unclear. An important issue is to determine whether the interaction between glycine and the silica surface takes place through an actual direct contact or is mediated by solvent water molecules. Moreover, for the former case, it is also of interest to know which are the preferred groups (COO⁻ or NH₃⁺) responsible of the contact, although, as shown above, sophisticated ssNMR techniques can provide some clues.²²⁸ Additionally, it is relevant to establish the number of OH groups (both from SiOH and water) needed to stabilize the zwitterionic form over the canonical one. Although these points were not fully resolved by the previous spectroscopic works, some ab initio studies were devoted to providing information on these aspects.

Costa et al.⁵⁵⁶ and Rimola et al.³²² simulated the interaction of glycine in its zwitterionic state with silica surfaces terminated by isolated SiOH groups in a microsolvated state, that is, accounting for a small number of water molecules. The former authors used the minimal H₃SiOH clusters in the presence of one and two water molecules and the B3LYP/6-31++G(d,p) level of theory. The most stable complexes found are shown in Figure 68. Results indicated that with one water molecule the interaction of glycine with one isolated SiOH group can take place directly through the NH₃⁺ group, the COO⁻ interaction being mediated by the water molecule (Figure 68a), or adopting the reverse situation (Figure 68b) because both complexes were found to be energetically almost degenerate. Additionally, with two H₂O molecules and two isolated SiOH groups, the most stable adduct is the structure shown in Figure 68c, in which the COO⁻ moiety interacts directly with the silanols whereas waters bridge the interaction with NH₃⁺. Rimola et al.³²² used a periodic model of the (001) edingtonite silica surface with two independent SiOH groups per unit cell to study at the B3LYP/triple- ζ level the successive addition of water molecules (from 1 to 5) at the glycine/silica interface. The most stable adducts found are shown in Figure 69.

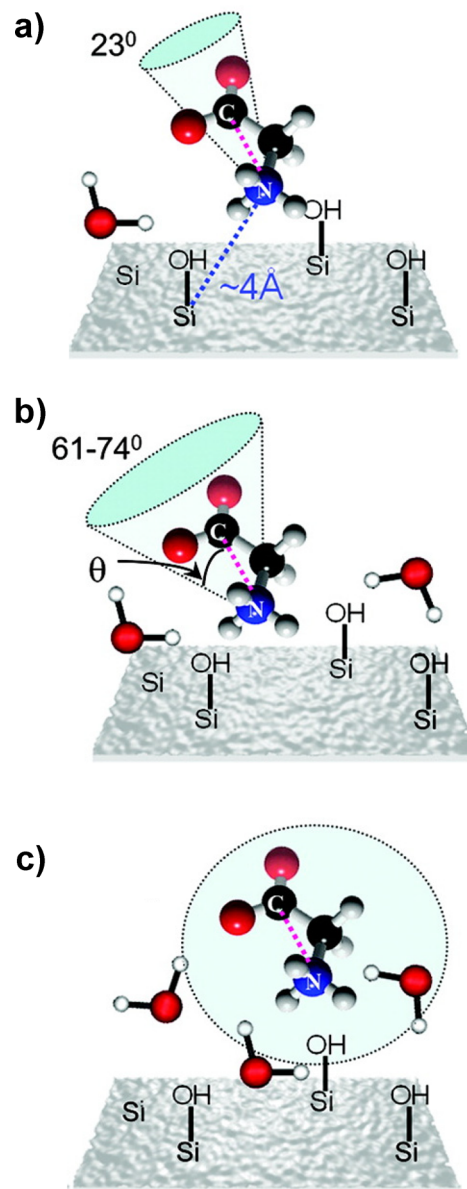


Figure 67. Picture of the three populations (bound, a and b, and free, c) for glycine/SBA-15 detected by multinuclear ssNMR experiments. Adapted with permission from ref 228. Copyright 2012 American Chemical Society.

Interestingly, with one water molecule (Figure 69a), the direct contact of glycine with the silica surface occurred through the COO⁻ group, whereas water interacted with NH₃⁺. With two and three water molecules (Figure 69b,c, respectively), COO⁻ still was found to be involved in the direct contact with SiOH, while it interacted with two water molecules. However, for four and five water molecules (Figure 69d,e, respectively) such a direct contact disappeared, and the glycine/silica interaction was mediated by water. This progressive microsolvation procedure indicates that the direct contact between glycine and the silica surface becomes lost upon increasing the number of water molecules until reaching a situation in which the glycine/silica interface is completely dominated by water. It is worth mentioning that this situation was not observed by Costa et al.⁵⁵⁶ due to the limited number of water molecules considered. In the work of Rimola et al.,³²² the vibrational frequencies of the structure shown in Figure 69e were also

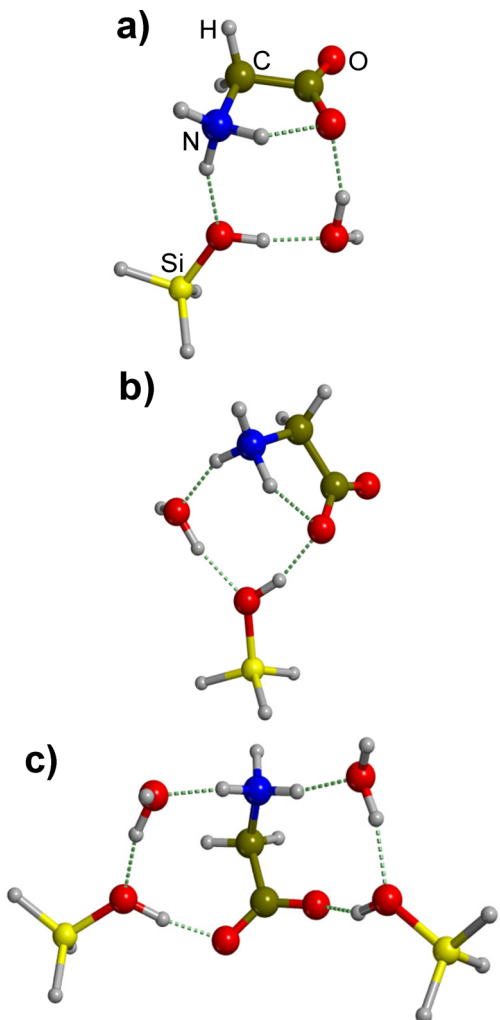


Figure 68. Stable structures found in ref 556 for the interaction of zwitterionic glycine with minimal silanol clusters in the presence of one and two explicit water molecules. Optimized at the B3LYP/6-31+G(d,p) level.

computed and compared with the experimental IR results of Meng et al.²¹⁰ (data shown in Table 16). In this case, the $\nu_{as}(\text{COO}^-)$ and $\nu(\text{NH}_3^+)$ modes useful for comparison are hidden by the stretching and bending modes of solvent water, which cover the 3900–3500 cm^{-1} and 1700–1600 cm^{-1} regions. Because of that, the $\delta(\text{CCH}) + \nu_s(\text{COO}^-)$, $\delta(\text{HCH})$, and $\delta_{as}(\text{NH}_3^+)$ were used, because they do not interfere with water bands. The comparison between the experimental measurements and the B3LYP data is fairly good, with a maximum deviation of 30 cm^{-1} . Indeed, the B3LYP $\delta_{as}(\text{NH}_3^+)$ and $\delta(\text{CCH}) + \nu_s(\text{COO}^-)$ values are in very good agreement with the experimental ones, thus supporting the view that NH_3^+ and COO^- are completely solvated by H_2O .

The analysis focused on the Gly-zwitt–Gly-can relative stability as a function of the number of OH groups (shown in Figure 70) is also of interest. Results indicated that, as expected, the larger the number of OH, the higher the stability of Gly-zwitt. Rameakers et al.⁶⁵⁶ found that, for the glycine/ $(\text{H}_2\text{O})_n$ system, with $n = 2$, Gly-zwitt was metastable (i.e., Gly-zwitt did not reverse to Gly-can) whereas Gly-can was the dominating form. With $n = 4$, Gly-zwitt was found to be more stable than Gly-can. When silica surface is present, results show the same trend, even though in this case the OH groups belong to water

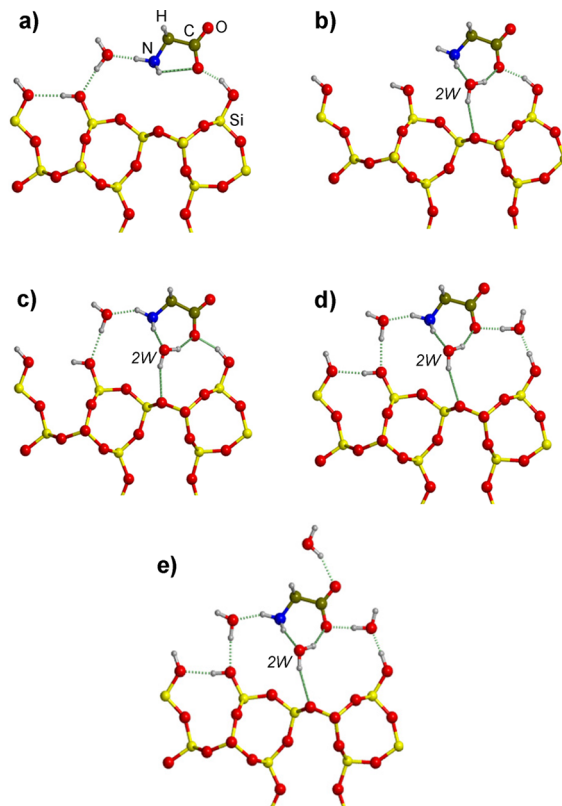


Figure 69. The most stable structures found in ref 322 for the successive addition of water (from one to five, a–e, respectively) at the Gly-zwitt/silica surface interface. Periodic systems optimized at the B3LYP/triple- ζ level. Adapted with permission from ref 322. Copyright 2008 American Chemical Society.

Table 16. Comparison between the Experimental and Harmonic B3LYP Frequencies (cm^{-1}) for the Glycine/Silica System

vibrational mode	experiments ^a (pH 6)	B3LYP ^b
$\delta(\text{CCH}) + \nu_s(\text{COO}^-)$	1412	1405
$\delta(\text{HCH})$	1443	1422
$\delta_{as}(\text{NH}_3^+)$	1617	1619

^aThe experimental values are at pH 6 (taken from Figure 66c). ^bThe computed frequencies correspond to the structure shown in Figure 69e.

and silanols. That is, with two OH groups in direct contact with glycine, Gly-zwitt becomes stable, although the canonical form is the preferred configuration, whereas when glycine is in contact with four OH groups Gly-zwitt becomes the most stable form.

As mentioned, these theoretical results only addressed the interaction of glycine with isolated SiOH groups and not with geminal ones, which due to their more acidic behavior are expected to be different. Because of that, Costa et al.⁶⁴¹ and Zhao et al.³²³ studied the adsorption of glycine on silica surfaces rich in geminal silanol groups in the presence of water, both works using first-principles molecular dynamics simulations. In the work of Costa et al.,⁶⁴¹ the adsorption was simulated considering a microsolvated environment constituted by five water molecules (enough to ensure the stabilization of Gly-zwitt over Gly-can). Several MD runs at the PBE level and $T = 300$ K with evolution times of 1500 fs indicated that in the

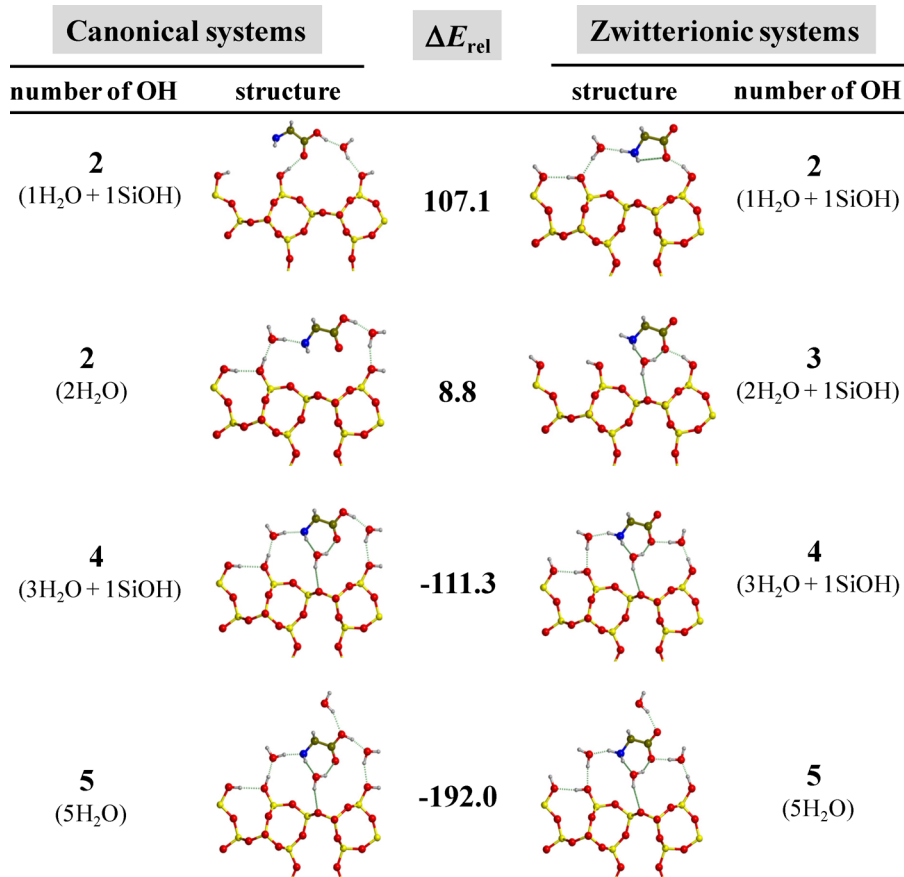


Figure 70. Relative electronic energies (ΔE_{rel} , in kJ mol^{-1}) of the zwitterionic systems with respect to the canonical ones as a function of the number of OH groups interacting with glycine, with different H₂O loadings (one, two, three, and five water molecules). Adapted with permission from ref 322. Copyright 2008 American Chemical Society.

dominant conformation (shown in Figure 71a), the COO[−] moiety was in direct contact with the surface through one geminal SiOH group, whereas NH₃⁺ was interacting with water molecules far from the surface.

Zhao et al.³²³ also studied glycine adsorption, but unlike this previous work, they included 140 water molecules in order to simulate the bulk solvent effects and carried out MD simulations based on the self-consistent charge density functional tight binding (SCC-DFTB) method (see section 5.6.2 for details of the method). After running several MD simulations at $T = 300$ K with evolution times of 20 ps for different initial guess structures, the results obtained did not differ much from those found by Costa et al.⁶⁴¹ Indeed, they found that the dominant configuration (shown in Figure 71b) exhibited the COO[−] group pointing toward the surface and establishing direct contact with geminal SiOH groups, while NH₃⁺, though they were able to establish direct H-bonds with geminal SiOH groups, preferred to interact with bulk water, away from the surface. These trends can be seen in the time evolution of the distance between the functional COO[−] and NH₃⁺ groups of Gly-zwitt and the surface silanols obtained for one MD run (see Figure 71c): COO[−] was close to the surface during all the MD simulation while NH₃⁺ only interacted with the surface for short lapses of time, being far from the surface the rest of the time. Analysis of the Mulliken charges after the MD simulations showed that the interaction involved a considerable charge transfer, because the surface carried a negative charge (from −0.381 to −1.09 electrons) whereas

glycine and water molecules hold a positive charge (from +0.0719 to +0.0124 electrons, for glycine). Moreover, the authors indicated that, because the surface exhibited a negative charge, the low affinity of NH₃⁺ to the surface could not be explained using the conventional acid–base (proton) theory, but considering that the large positive net charge on the geminal H must repel any incoming NH₃⁺, which would explain the great affinity of the COO[−] group for the surface. Remarkably, these two works coincide in estimating the adsorption energy of Gly-zwitt on the geminal silanol groups to about −140/−150 kJ mol^{-1} .

9.1.2. Other Amino Acids. *9.1.2.1. Alanine.* The side chain of alanine is the −CH₃ group, and therefore, it is reasonable to consider that no significant changes will occur compared with glycine because the side chain cannot establish H-bonds with free silanol groups, although dispersive interactions are larger for alanine than for glycine due to the presence of the CH₃ group. Despite that, there are some theoretical and experimental works addressed exclusively to the interaction of alanine with silica surfaces.

The gas-phase interaction of alanine with a large cluster model simulating the (001) edingtonite surface that contains four isolated SiOH groups has been reported by Rimola et al.³²¹ Calculations were carried out using the ONIOM2 strategy with B3LYP/6-311++G(d,p) as high level and MNDO as low level. It was found that the interaction through the backbone chain followed the same features as for glycine; that is, adsorption in the canonical state and engaging at least two H-bonds between

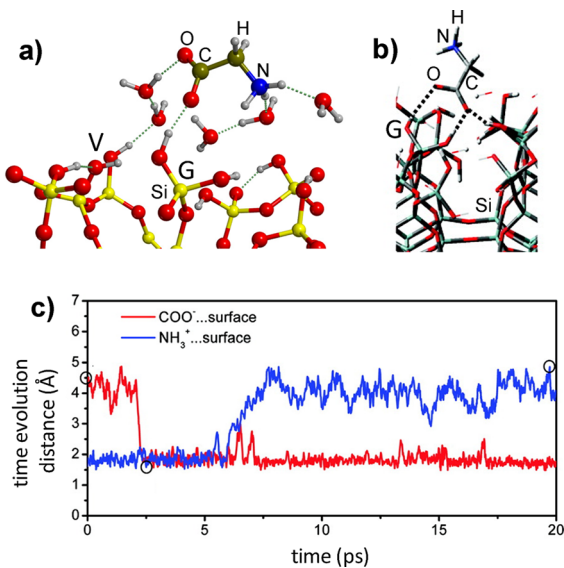


Figure 71. Interaction between glycine and a silica surface rich in geminal silanols with the presence of water. (a) Dominant configuration obtained by means of ab initio MD simulations with five explicit water molecules (PBE density functional method, $T = 300$ K, and evolution times of 1500 fs; drawn with data from ref 641). (b) Dominant configuration obtained by means of SCC-DFTB simulations with 140 explicit water molecules ($T = 300$ K and evolution times of 20 ps). The water molecules have been removed for the sake of clarity. (c) Time evolution of the distance of the COO⁻ and NH₃⁺ moieties with the surface (red and blue lines, respectively) for the MD run associated with the configuration shown in panel b. Panels b and c reprinted with permission from ref 323. Copyright 2011 American Chemical Society.

the SiOH groups and the C=O alanine group. The optimized structure is shown in Figure 72a.

Nonella et al.³²⁴ also studied alanine/silica interactions but in this case by means of first-principles MD simulations at the PBE level considering both vacuum conditions and the presence of explicit water molecules. In vacuo adsorption simulations, carried out at $T = 100$ K and with evolution times of 2.5 ps, showed that the dominant configuration is the one given in Figure 72b. This is notably different from the one previously observed (Figure 72a) because in this case there is a rather strong H-bond between the NH₂ and one SiOH group and the H-bonds between SiOH and COOH adopt a different pattern. Although in both cases the silica surface model is based on edingtonite, these differences are probably because Nonella's model is richer in SiOH surface groups than Rimola's one (eight vs four SiOH groups per unit cell, respectively). This higher SiOH density probably favors the formation of the additional interaction with the NH₂ moiety and the different H-bonding patterns in the COOH group. Furthermore, in Nonella's model, the SiOH's are interacting whereas in Rimola's one they are isolated. MD simulations carried out in the presence of 63 explicit water molecules at $T = 300$ K converged into a picture in which alanine is adsorbed as a zwitterion on the neutral surface (i.e., with no evidence of negatively charged SiO⁻ surface groups) through indirect H-bonds mediated by water molecules (see Figure 72c). Notably, NH₃⁺ eventually established direct H-bond interactions with O atoms of silanols (see Figure 72d). Additionally, the results indicated that the NH₃⁺ group interacted more strongly with

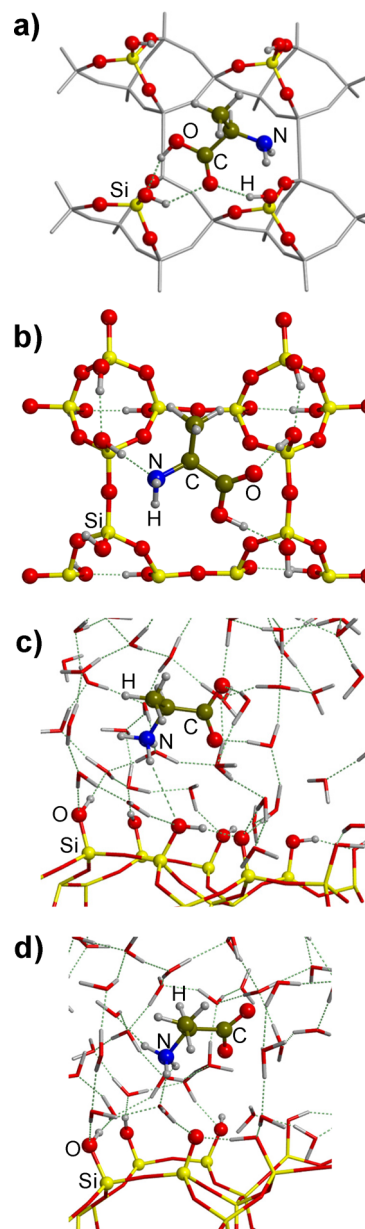


Figure 72. (a) Optimized structure for the alanine/silica system in gas phase at the ONIOM(B3LYP/6-311++G(d,p):MNDO) level (drawn with data from ref 321), (b) dominant configuration for the alanine/silica system in gas phase by means of ab initio MD simulations (PBE method, $T = 100$ K), (c) dominant configuration for the alanine/silica system in aqueous solvent (63 water molecules) by means of ab initio MD simulations (PBE method, $T = 300$ K), and (d) eventual configuration observed during the same MD simulation that yielded panel c. Panels b–d drawn from data of ref 324.

the surface than the COO⁻ one, which was reflected by the orientation of alanine (NH₃⁺ pointing toward the surface).

From an experimental point of view, Ben Shir et al.²²⁷ have also reported ssNMR results focused on the alanine/SBA-15 interface, in a procedure similar to that used later for the glycine/SBA-15 system²²⁸ (see above). The results obtained are, as expected, very similar between the two works. That is, the low hydration state was found to be dominated by a surface-bound alanine population, with the protonated NH₃⁺ moiety close to three to four Q³ silicon centers with an internuclear Si…N distance of 4.0–4.2 Å and the COO⁻ moiety

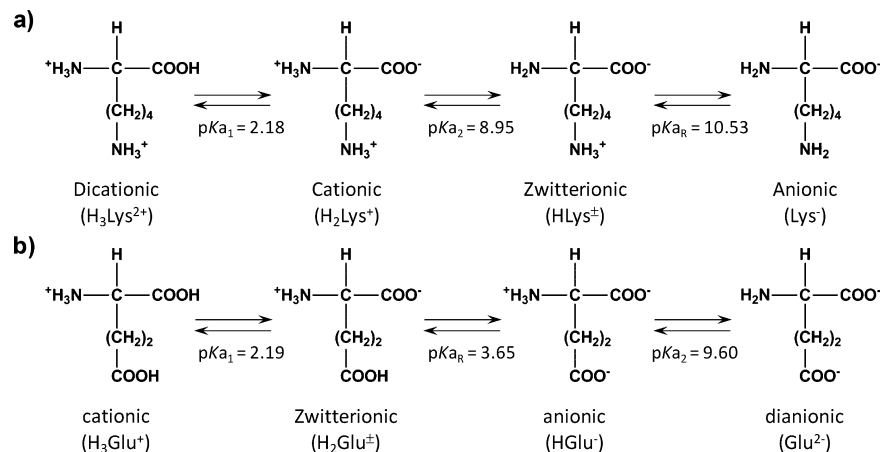


Figure 73. Different protonated states for lysine (a) and glutamic acid (b), including corresponding pK_a values.

not showing contributions to surface binding, whereas in the high hydration state three populations were found, two of them surface-bound and one “free”. The only significant difference found between the two works is that surface-induced crystallization was not observed for the alanine case. Remarkably, this view of transforming a surface immobilized alanine into a “free” alanine molecule solvated by water when the hydration conditions are increased is in full agreement with the results of Amitay-Rosen et al.,²²⁵ in which they observed, by means of dynamic MAS NMR measurements, that a single water molecule was enough to remove the bound alanine molecules from the SBA-15 surface. This behavior is moreover consistent with the calculations of Nonella et al.³²⁴ (see above) where it was observed that the adsorption of alanine on a silica surface is not direct through the NH_3^+ or COO^- groups but bridged by solvent water molecules.

9.1.2.2. Lysine and Glutamic Acid. The side chains of lysine and glutamic acid are the $-(\text{CH}_2)_4-\text{NH}_2$ and $-(\text{CH}_2)_2-\text{COOH}$ groups, respectively, and thus, these amino acids are of interest because they exhibit different protonated forms depending on the pH. Figure 73 shows the different states as well as respective pK_a values.

The adsorption of lysine on amorphous silica in the 7.1–9.8 pH range was measured by Kitadai et al.²¹⁷ by means of attenuated total reflectance infrared (ATR-IR) spectroscopy. At $\text{pH} < 7$, the absorbance of adsorbed lysine was found to be small because nonadsorbed lysine was predominant, and therefore at these values, the ATR-IR spectra were not recorded. Figure 74 shows the spectra of lysine in solution (a) and when adsorbed on silica (b) over the whole range of pH values tested.

Spectra in Figure 74a indicated that, as expected, lysine changes its protonation state from the zwitterionic to the cationic state upon pH decrease. This was clearly demonstrated by the disappearance of the NH_2 scissoring ($\delta_{sc}(\text{NH}_2)$) band at 1559 cm^{-1} , only present in the zwitterionic state, and by the increase in intensity of those bands involving NH_3^+ , due to the protonation of the α -amino group when the pH decreased. In contrast, it was observed that the spectra for the adsorbed lysine on silica remained mostly invariable upon pH change (see Figure 74b). Quantitative spectral analysis based on calibration lines for lysine in solution indicated that, regardless of the pH, $81\% \pm 5\%$ of the adsorbed lysine was present in the cationic state and $19\% \pm 5\%$ in the zwitterionic state. With these results and considering that the point of zero charge of

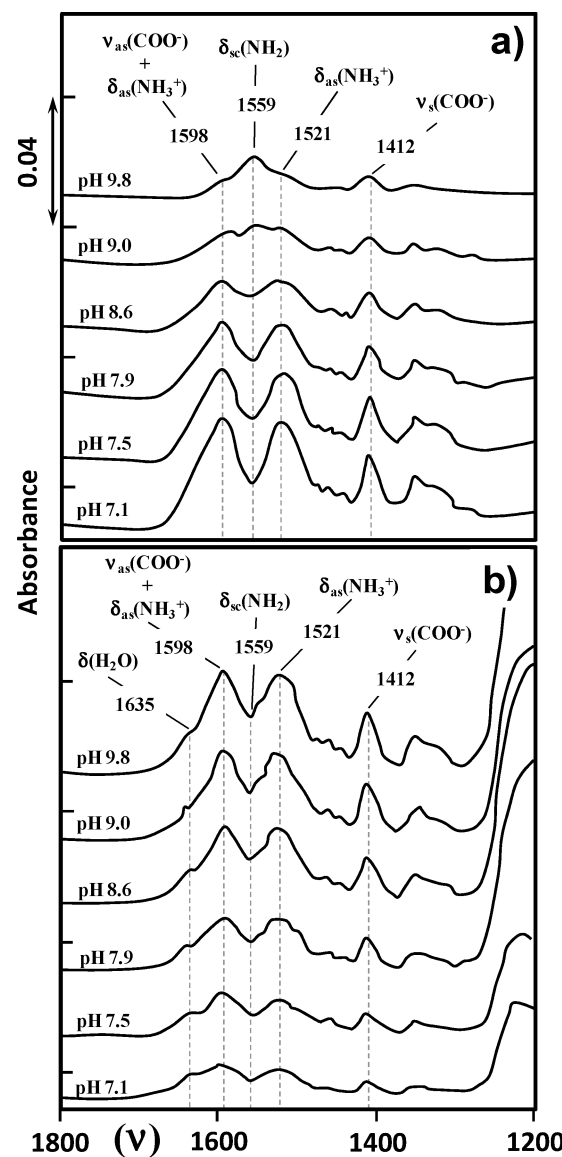


Figure 74. ATR-IR spectra (cm^{-1}) for lysine in solution (a) and when adsorbed on silica surface (b) as a function of pH. Adapted with permission from ref 217. Copyright 2009 Elsevier.

the used silica sample is about 2, the authors interpreted that adsorption of lysine was mainly driven by electrostatic interactions between the negatively charged silica surface and the protonated NH_3^+ groups, although hydrophobic interactions between lysine and siloxane bridges were not ruled out. Remarkably, this binding mechanism based on electrostatic forces agrees with the isothermal experiments of O'Connor et al.²¹⁵ on the adsorption of lysine on siliceous MCM-41 and is consistent with the experimental findings of Stievano et al.,²⁴⁷ which showed a preferential adsorption of lysine from an equimolar mixture of glycine and lysine. Indeed, considering that at pH 7 glycine is in its zwitterionic state, lysine is predominantly in its cationic state, and silica bears a significant negative charge, lysine adsorption should certainly be more favorable than glycine adsorption.

As far as glutamic acid is concerned, Bouchoucha et al.²¹¹ recorded the IR spectrum for the glutamic acid/silica system, results showing that at pH 3 the predominant species was the H_2Glu^\pm zwitterionic state, because the dominant bands were those involving the backbone NH_3^+ and COO^- groups and the protonated side chain COOH (see Figure 75a).

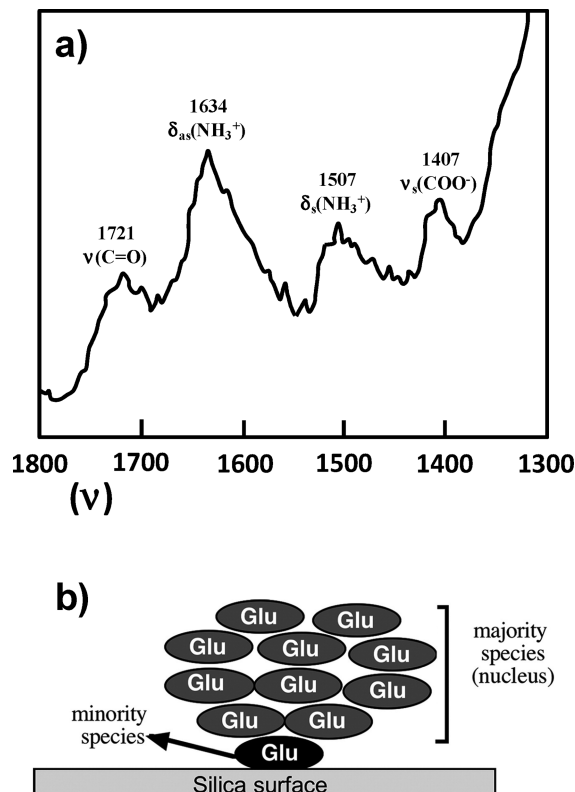


Figure 75. (a) IR spectrum (in cm^{-1}) for glutamic acid when adsorbed on silica at pH 3 (adapted with permission from ref 211, Copyright 2011 American Chemical Society). (b) Schematic representation of the glutamic acid/silica interface where two forms of glutamic acid (the molecularly adsorbed and the precipitated ones, as minority and majority species, respectively) were found to coexist.

As expected, at pH 8–9, the $\text{C}=\text{O}$ band associated with COOH was absent indicating that the predominant species was the HGlu^- anion. Similar IR features were obtained for free glutamic acid in solution at these pH values, thereby confirming that the contact with silica does not significantly modify glutamic acid speciation. Additionally, quantitative adsorption

data from HPLC suggested a weak affinity between glutamic acid species and the hydrated silica surfaces and therefore that the interaction mainly takes place via H-bonding rather than electrostatic forces. On the other hand, the obtained XRD diffractograms showed the formation of bulk glutamic acid crystallites at concentrations lower than saturation. This phenomenon was comparable to what geochemists sometimes call “surface precipitation” or better “surface-induced precipitation”, that is, the precipitation of a mineral exclusively on the surface adsorbent under conditions where the bulk solution is undersaturated. Such a growth has also been reported for the glycine/ $\text{TiO}_2(110)$ system,⁶⁵⁷ and this “surface-induced precipitation” has been even used in several procedures of preparation of supported heterogeneous catalysts.⁶⁵⁸ Incidentally, the glutamic acid crystallite formation is different compared with the glycine one. For glutamic acid, the shape of the adsorption isotherm suggests that nucleation of a bulk glutamic acid phase does indeed occur at the silica–solution interface whereas for glycine bulk crystallites can be formed from nonspecifically retained solution during the drying step. However, for glutamic acid, the bulk phase that precipitated was the same that would be obtained from a concentrated aqueous solution of glutamic acid, that is, the β -polymorph. Solid-state NMR measurements confirmed the presence of these two glutamic acid populations; i.e., the molecularly adsorbed form and the precipitated one, as minority and majority species, respectively, (see the schematic picture of Figure 75b) and also suggested that at the interface the adsorbed species compete with a few water molecules to directly interact with the silica surface.

From a theoretical point of view, lysine and glutamic acid adsorptions considering strict gas-phase conditions were simulated by Rimola et al.³²¹ using a (001) edingtonite-based surface cluster model that contains four isolated SiOH groups and the ONIOM2(B3LYP/6-311++G(d,p):MNDO) level of theory. As expected, the computed adduct exhibited a rather strong H-bond between the proton of one SiOH and the N atom of the amine side chain (see structure of Figure 76a). A similar H-bonding pattern was found by Han et al.⁶⁵⁹ when studying the adsorption of methylamine (considered as a model of the side chain of lysine) on the hydroxylated (0001) surface of α -quartz, although in this case the H of the NH_2 group also established a H-bond with an O atom of one surface SiOH group. Glutamic acid holds a COOH group at the end of the side chain and thus the most stable adduct found for this amino acid exhibits the cooperative H-bonding pattern between the COOH and one SiOH group (see Figure 76b). To the best of our knowledge, calculations accounting for water solvent effects have only been carried out for the lysine case by Gambino et al.,⁶⁶⁰ who modeled by means of classical MD simulations the adsorption of lysine on a hydroxylated quartz surface with the presence of 350 explicit water molecules. At variance with the ATR-IR results, they found HLys^\pm as the most stable state, over the cationic one. Despite that, the results obtained are likewise of valuable interest because it was found that lysine interacts adopting an end-on orientation with the protonated NH_3^+ side chain group pointing toward the surface (see schematic structure of Figure 76c). Moreover, it was observed that water provides an indirect cooperative contribution to the lysine/quartz interactions, decreasing the solvation shell around the charged NH_3^+ and SiO^- groups and in turn strengthening the lysine/quartz interactions.

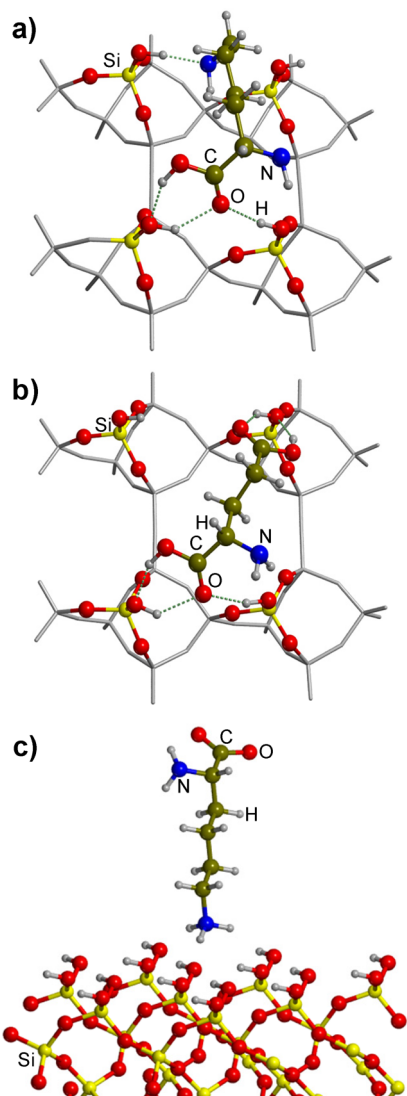


Figure 76. Interaction of lysine (a) and glutamic acid (b) with a hydroxylated (001) edingtonite surface model (drawn from data of ref 321) computed at the ONIOM2(B3LYP/6-311++G(d,p):MNDO level). (c) Schematic representation of the dominant configuration obtained for zwitterionic lysine interacting with a hydroxylated α -quartz surface model in aqueous solution using classical MD simulations (drawn from data of ref 660). Water molecules have been omitted for the sake of clarity.

9.1.3. General Trends Found in Amino Acid Adsorption on Silica Surfaces. Static quantum chemical calculations have the advantage that they allow computation of binding adsorption energies straightforwardly and efficiently. This is important because by computing the adsorption energies of a set of AAs on silica surfaces one may establish a scale of relative stability of the AA/silica adducts and hence obtain trends on the affinity of AAs for silica. This was actually performed by Rimola et al.,³²¹ who presented a comprehensive computational study for the gas-phase adsorption of 15 AAs (Table 17 shows some selected cases) in their canonical state on a model cluster of hydroxylated silica surface based on the (001) edingtonite surface terminated by four isolated SiOH groups.

Geometry optimizations were performed at the ONIOM2-(B3LYP/6-311++G(d,p):MNDO) level and adsorption energies were determined after including Grimme's correction for

Table 17. BSSE-Corrected Adsorption Energies ($\Delta E_{\text{ads}}^{\text{C}}$), Free Energies ($\Delta G_{\text{ads}}^{\text{C}}$, $T = 298$ K) Including Dispersion (D) (units in kJ mol^{-1}) for Several Amino Acids Interacting with Hydroxylated Silica Surface from Ref 321

amino acid	side chain behavior	$\Delta E_{\text{ads}}^{\text{C}}$	$\Delta G_{\text{ads}}^{\text{C}}$	$\Delta G_{\text{ads}}^{\text{C}} + D$
Gly	nonpolar	-48.5	18.4	-13.0
Ala	nonpolar	-46.4	18.8	-7.5
Phe	nonpolar	-43.1	29.7	-15.9
Ser	polar/neutral	-56.1	25.1	-20.5
Glu	polar/acidic	-76.6	7.5	-36.0
Gln	polar/amide function	-72.8	14.2	-33.5
Lys	polar/basic	-73.6	7.1	-37.2
Arg	polar/basic	-72.4	11.7	-41.0

dispersion.⁴²⁰ It is worth mentioning that in all cases the adsorbed complexes showed the same interactions observed for glycine (see Figure 62) plus those derived from the AA side chain with the available free SiOH groups. This ensured that differences in the adsorption energies were due to the AA side chain interactions with silica. The computed adsorption energies (Table 17) indicated that $\Delta E_{\text{ads}}^{\text{C}}$ become more favorable as the number of polar groups in the AA side chain increases due to the formation of stronger H-bonds with the surface. Interestingly, the computed $\Delta G_{\text{ads}}^{\text{C}}$ were found to be all positive due to the unfavorable entropic terms. However, since the dispersive forces play a fundamental role on the adsorption energy, when adding the correction for dispersion, final free adsorption energies ($\Delta G_{\text{ads}}^{\text{C}} + D$) become all negative. Overall, the authors pointed out that the adsorption processes were mainly dictated by both H-bonding and dispersion. That is, while the former interactions seemed to determine the relative silica affinity for the different AAs, the latter ones mainly contributed by greatly lowering the adsorption energies. From the $\Delta G_{\text{ads}}^{\text{C}} + D$ values, the authors established the following relative scale for AA affinity toward silica surfaces of moderate hydroxylation degree: polar/basic > polar acidic \approx polar/amidic > polar/neutral > nonpolar.

Sholl and co-workers^{651,661} have reported theoretical results addressed to the enantiospecific adsorption of AAs. All natural α -AAs with the exception of glycine are intrinsically chiral and only one of the two possible enantiomers is naturally found in proteins. The existence of this biological homochirality raises profound questions about the origins of life. Furthermore, in nature, not only biomolecules are chiral, but also naturally occurring minerals may present chirality. Some authors have invoked the possibility that naturally occurring chiral surfaces may discriminate one enantiomer over the other, which in turn is controlled by the enantiospecific interactions between the two partners. Quartz is chiral, and because of that, Sholl and co-workers calculated the adsorption energies of the two possible enantiomers of several AAs on the chiral (0001) and (010) α -quartz surfaces. The results obtained are summarized in Table 18. The authors highlighted that measurable energy differences were obtained between the two enantiomers of serine and cysteine, and for serine, aspartic acid and asparagine when adsorbed on the (0001) and (010) surfaces, respectively, while for the other amino acids negligible energy differences were computed. They also mentioned, however, that the largest enantiospecific energy difference, given by aspartic acid, was the only case comparable to the computed enantiospecific energy differences reported on metal chiral surfaces, which are indeed able to carry out chiral recognition.^{662,663}

Table 18. Computed Electronic Adsorption Energies (ΔE_{ads} , kJ mol^{-1}) and Those Including ZPE Corrections (ΔU_{ads} , kJ mol^{-1}) for the Adsorption of the R and S Enantiomers of Alanine, Serine, Cysteine, Aspartic Acid, and Asparagine on the (0001) and (010) α -Quartz Surfaces

chiral AA	(0001) ⁶⁵¹		(010) ⁶⁶¹	
	ΔE_{ads}	ΔU_{ads}	ΔE_{ads}	ΔU_{ads}
R-Ala	-74.3	-68.5	-70.4	-69.5
S-Ala	-73.3	-66.5	-72.4	-72.4
R-Ser	-85.9	-76.2	-73.3	-70.4
S-Ser	-90.7	-83.9	-69.5	-67.5
R-Cys	-83.2/-83.0	-75.0/-75.5	-78.1	-75.3
S-Cys	-79.2/-78.7	-71.6/-70.9	-78.1	-75.3
R-Asp			-75.3	-73.3
S-Asp			-84.9	-81.0
R-Asn			-69.5	-64.6
S-Asn			-73.3	-68.5

Data obtained from refs 651 and 661.

To the best of our knowledge, systematic studies focused on the adsorption of AAs on silica surfaces in solution to obtain an affinity scale have not been reported yet, which is unfortunate since experimental data exist for comparison (ref 207; see section 3.2.2). However, Walsh and co-workers^{591,595} have reported the binding of several AA analogues (i.e., small molecules that resemble the side chain of an AA) on the (001), (100), and (011) hydroxylated α -quartz surfaces under aqueous conditions (Table 19 reports some selected cases). It is worth

Table 19. PMF Free Adsorption Energies (in kJ mol^{-1}) for Some Amino Acid Analogue Molecules Interacting with the (001), (100), and (011) α -Quartz Surfaces from Ref 595.

molecule	AA	(001)	(100)	(011)
CH_4	Ala	-4.6	-5.0	-6.7
CH_3OH	Ser	-4.2	-3.8	-5.9
$\text{CH}_3(\text{CH}_2)_3\text{NH}_3^+$	Lys	-2.1	-2.9	-4.2
C_6H_6	Phe	-7.1	-8.8	-11.7
CH_3COO^-	Glu	-6.7	-5.4	-12.1

noting that, because of the aqueous environment, the butyl ammonium and ethanoate molecules (as analogues for lysine and glutamic acid, respectively) were considered as charged forms, that is, carrying NH_3^+ and COO^- moieties, respectively. In this work, free energies of adsorption were obtained using the potential of mean force (PMF) method. This method allows running of MD simulations for a fixed distance between the center of mass of the adsorbate and the surface. By modifying this distance over a certain range one can get the PMF free energy profile of adsorption and the binding free energy. For this case, the MD simulations were based on classical force fields. Results obtained (see Table 19) indicated that, in general, the PMF free energy of adsorption did not correlate with the surface silanol density (which ranges, from highest to lowest, as (001) > (100) > (011)), suggesting that the surface topology, and in particular the interstitial spaces between silanol groups, was important. Indeed, visual inspection of the typical configurations of the AA analogues adsorbed on the α -quartz surfaces (see Figure 77) showed that molecules tended to be inserted within the interstitial grooves.

Accordingly, the authors interpreted that hydrophobic interactions between aliphatic chains and the surfaces

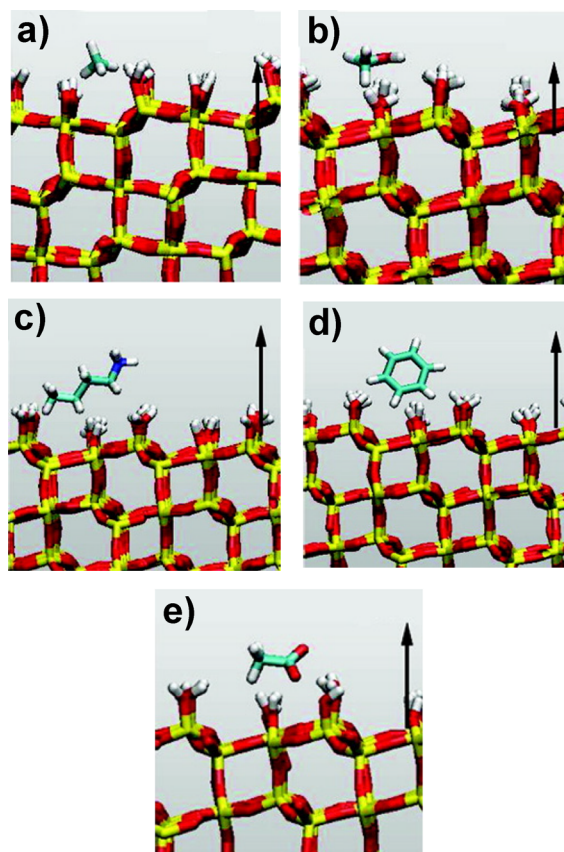


Figure 77. PMF typical configurations of methane (a), methanol (b), butyl ammonium (c), benzene (d), and ethanoate (e) interacting with the (011) α -quartz surface in aqueous solution. Water molecules have been removed for the sake of clarity. Adapted with permission from ref 595. Copyright 2012 American Chemical Society.

contributed significantly to the surface binding. For those AA analogues that bear polar groups, however, it was observed that H-bonding is also relevant for the binding. The obtained PMF adsorption free energies revealed the following trend in the binding: nonpolar/aromatic > polar/negatively charged > nonpolar/aliphatic > polar/neutral > polar/positively charged. The authors also mentioned the limitations of the biomolecule models used. That is, for most residues, the alkyl parts of their side chains will be restrained to point away from the surface (not within or in close proximity to the interstitial spaces) by the backbone chains of amino acids and peptides, so their contribution to the binding energy is limited. This is, for instance, the case for methanol and ethanoate (to model serine and glutamic acid, respectively), in which the methyl groups were found to lie in an interstitial groove, which is not possible if the full amino acid residue is accounted for due to geometry constraints.

The previous results were obtained considering that the silica surfaces did not bear any surface charge; namely, they were neutral. However, silica surfaces may exhibit net electrical surface charges, the sign of which strongly depends on the pH of the solution when silica is immersed. As stated in section 3.1.2, at solution pH values above or below the PZC, the mineral displays a negative or positive surface charge, respectively. Obviously, the higher the difference between the solution pH and the PZC, the more charges the surface exhibits. The PZC marks a changeover in the electrochemical properties of the silica surfaces; however, since it is quite low

for silica (about 2), pH values below the PZC are not very relevant. Analogously, as shown for the lysine and glutamic acid cases, AAs can be found in different charged states depending on the pH of the medium. The isoelectric point (pI) of one AA is the solution pH at which the AA carries equal amounts of positive and negative charges; that is, it is found as zwitterion. In fact, if there are no ionizable groups in the side chains, the pI is simply the mean value of the pK_a 's that involve the carboxylic acid and the ammonium functions, pK_{a_1} and pK_{a_2} , respectively. When there is an ionizable group in the side chain, its pK_a value (pK_{a_R}) also intervenes. Accordingly, at pH values above or below the pI , the AA is found to be anionic or cationic. Due to these pH-dependent electrical properties shown by silica surfaces and AAs, the charged states of the two partners in the adsorption processes may determine the strength of the AA/silica interactions, which in this case will be mainly dictated by electrostatic forces. As already mentioned in section 3.1.2, Churchill et al.¹⁰⁵ have studied the influence of the PZC of quartz surfaces and the pI of some amino acids in the adsorption processes. The PZC of the quartz surfaces was determined using the atomic force microscope (AFM) technique to be ~ 2.8 , whereas the amount of the adsorbed AA on quartz was analyzed with liquid chromatography techniques. Table 20 shows the results obtained, jointly with pK_a and pI values of the AA tested.

Table 20. Relative Adsorption of Amino Acids Analyzed by High-Performance Liquid Chromatography (HPLC) and Reverse-Phase Liquid Chromatography (RPLC) on Quartz and pK_a 's and Isoelectric Points (pI) of the Amino Acids Tested^a

amino acid	relative adsorption		pK_a values			pI
	HPLC ^b	RPLC ^c	pK_{a_1}	pK_{a_2}	pK_{a_R}	
Lys	1.00		2.18	8.95	10.53	9.74
Tyr	<0.20	1.00	2.20	9.11	10.07	5.66
Ala	<0.05	0.81	2.34	9.69		6.01
Gly	<0.05	0.51	2.34	9.60		5.97
Glu	<0.05	0.12	2.19	9.67	4.25	3.22
Asp	<0.05	0.12	1.88	9.60	3.65	2.77

^a pK_{a_1} , pK_{a_2} , and pK_{a_R} refer to pK_a values for backbone COOH and NH_3^+ and side chain R groups, respectively. ^bMeasurements normalized with respect to lysine. ^cMeasurements normalized with respect to Tyr.

AAs with pI values that greatly differ from the PZC of quartz adsorbed in greater abundance than AAs for which pI values and the PZC are similar. That is, lysine was found to be the most adsorbed AA (it is indeed the amino acid that exhibits the largest difference between pI and PZC, 9.74 vs 2.8, respectively), while aspartic acid and glutamic acid are the least adsorbed amino acids (with pI values similar to PZC, 2.80 and 3.04 vs 2.8, respectively). This could be understood considering that at pH values above the PZC of quartz but below the pI of the AA the quartz surface and AA have opposite charge and, thus, electrostatic interaction is attractive and large. For instance, at pH 5, quartz has a moderate negative charge density on the surfaces, but lysine is mostly found in its cationic state, so that attractive electrostatic interactions occur between them, thus favoring adsorption. In contrast, aspartic acid is mostly found as anion (like quartz) so that repulsive electrostatic interactions are established, thereby giving rise to

poor adsorption of aspartic acid. This can be visualized in Figure 78.

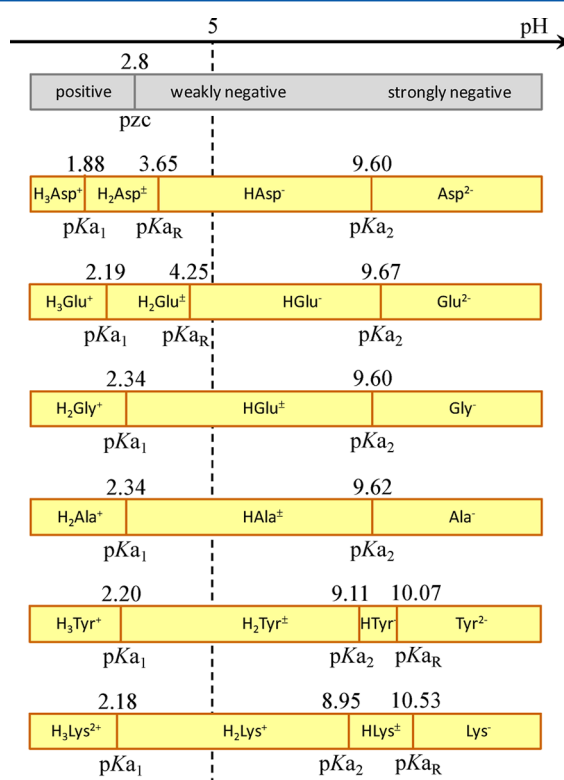


Figure 78. Theoretical acid–base speciation of α -quartz and AAs tested in ref 105 as a function of pH. pK_{a_1} , pK_{a_2} , and pK_{a_R} refer to pK_a values for backbone COOH and NH_3^+ and side chain R groups, respectively.

Interestingly, the greater the separation between the PZC and the pI values, the greater the charge difference between the mineral surface and the amino acid and thus, the more favorable the electrostatic interaction. This pH-dependent adsorption has been also observed by other authors via acid–base titration experiments. Bouchoucha et al.²¹¹ and Gao et al.²⁵³ also observed low amounts of glutamic acid adsorption on amorphous silica and SBA-15, respectively, which was attributed to the negligible difference in pH between the pI of glutamic acid and the PZC of these silica materials (around 3). In the same line, both Gao et al.²⁵³ and Vlasova et al.²¹⁴ observed that adsorption of arginine ($pI = 10.76$) readily occurred on SBA-15 and on surfaces of highly dispersed silica particles, respectively, and that the adsorption amounts quickly increased from pH 3 to 9 because, while the amount of positively charged arginine was kept almost constant within this range, the silica surfaces became more and more negatively charged.

All these facts support that electrostatic forces play an important role in the adsorption processes, especially in the pH regions that correspond to changes in the speciation of the AA and silica surfaces. In the work of Gao et al.,²⁵³ the adsorption of AAs with nonpolar side chains (phenylalanine, leucine, and alanine) was also studied. For the particular case of phenylalanine, the mean charge per molecule was approximately zero in the pH 4–8 range (that is, it was present as zwitterion), but phenylalanine was intensively adsorbed on the surfaces of the SBA-15 and the amount adsorbed was insensitive to pH

variation since the acid-base speciation of phenylalanine was hardly affected. Furthermore, these authors also found that the adsorption amounts of these three amino acids increased with the increased of the size of their side chains (i.e., phenylalanine > leucine > alanine). These facts led them to interpret that the adsorption of phenylalanine was mainly driven by hydrophobic interactions between the nonpolar side chain and the siloxane Si—O—Si surface groups. Along this line, it has been recently demonstrated that hydrophobic interactions indeed play an essential role, which is clearly revealed when electrostatic and H-bonding interactions can be considered as constant.⁴²⁶

In summary, it seems clear that the adsorption mechanism of AAs on silica surfaces may be driven by three main kinds of contributions: (i) electrostatic forces between AA ions and negatively charged $\equiv\text{SiO}^-$ surface groups, which become particularly favorable when the silica surfaces and AA exhibit a net charge of opposite sign achieved by modulating the pH; (ii) H-bonding interactions between AAs (either as neutral molecules or ions) and neutral $\equiv\text{SiOH}$ groups; (iii) hydrophobic interactions between the AA side chains and the siloxane $\equiv\text{Si—O—Si}\equiv$ groups.

9.1.4. Thermally Induced Transformations of Adsorbed Amino Acids on Silica Surfaces. Upon adsorption, amino acids may react to give DKP (vide supra). Indeed, early experiments of Basiuk et al. (ref 241) developed a synthetic procedure for obtaining DKP derivatives from simple amino acids by means of their sublimation in the presence of silica gel. This was the starting point for further very extensive studies of silica-catalyzed thermal transformations of amino acids. Even though DKPs are usually major products, the catalytic activity of silica is so high that DKPs can be further singly or even doubly N-acylated to form imidazopyrazine systems.^{664–667} Formation of DKP derivatives via silica-catalyzed dehydrocyclization of linear dipeptides has also been reported.⁶⁶⁸ These examples show that thermal transformations of amino acids in the presence of silica is the gateway to a very rich chemistry that has not yet been fully investigated.

Experiments in water solution with glycine, alanine, lysine, and glutamic acid, carried out by Lambert et al.,⁶⁵² have shown that upon thermal activation at moderate temperatures (150–160 °C), clean polymerization events occur, which can easily be observed by thermogravimetric analysis. Figure 79 shows the differential thermogravimetric (DTG) analysis for these AA/silica systems.

At least two clear regions were differentiated: (i) one around 150 °C, which was attributed to amide bond formation, and (ii) another one around 300 °C, which corresponded to the degradation of the adsorbed organic matter. Noticeably, the peak at 150 °C was not present for the DKP/silica system as no amide bond formation could occur (there are no free amine or carboxylic groups in this molecule). Despite these general similarities between AAs, the case of glutamic acid has been studied in more detail by Bouchoucha et al.²¹¹ because, in addition to the peak at 150–160 °C, another well-defined peak at 110–120 °C was also detected in some conditions (see Figure 80a).

Experimental measurements performed with FTIR, ssNMR, and ESI-MS (electrospray ionization-mass spectrometry) techniques clearly indicated that this first peak was due to an intramolecular lactam ring closure of glutamic acid to yield pyroglutamic acid (PyroGlu, see Figure 80b). The evidence, however, was less clear for the second peak. Thermogravimetric results indicated that this second step could also be associated

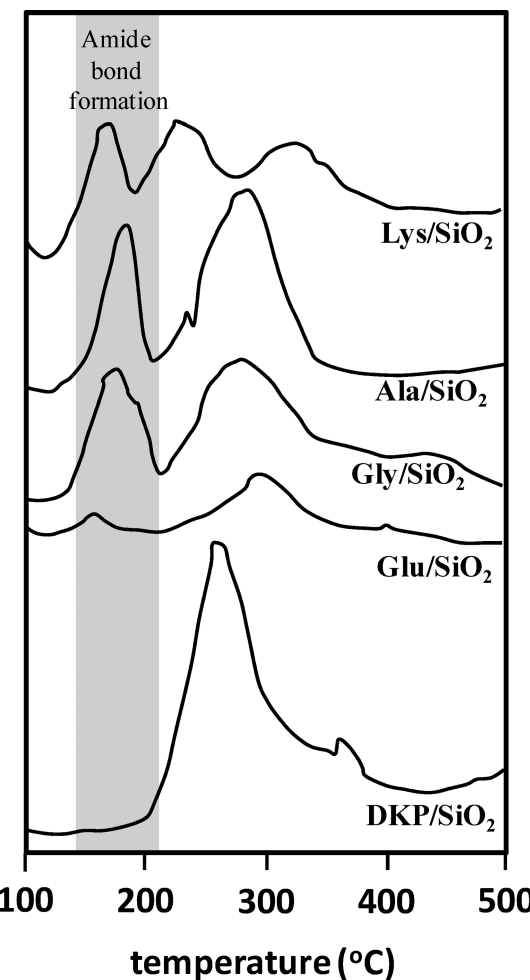


Figure 79. Differential thermogravimetric analysis of several AAs and DKP on amorphous silica. The temperature region where amide bond formation seems to occur is highlighted in gray. Adapted with permission from ref 652. Copyright 2009 Elsevier.

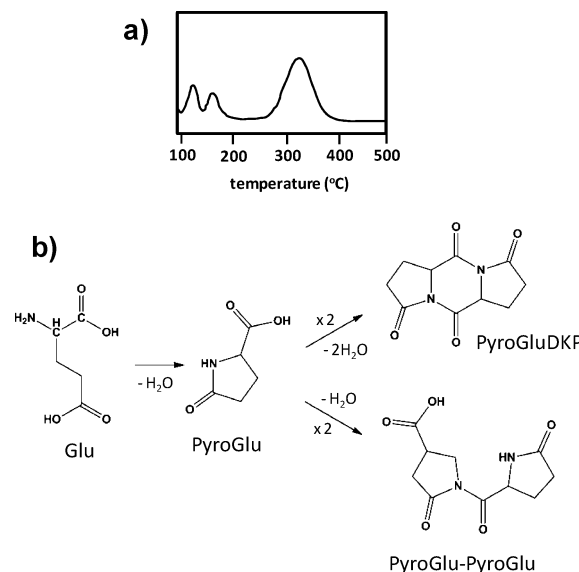


Figure 80. (a) Thermogram (DTG) of glutamic acid on amorphous silica. (b) Schematic representation of the thermal events suggested in ref 211.

with the loss of one water molecule per glutamic acid. Additionally, *in situ* IR showed that the product formed had some bands attributable to the imide functions. These two facts led the authors to deduce that the product formed was the PyroGluDKP (see Figure 80b), which was formed via cyclic condensation of two PyroGlu molecules with the subsequent release of two water molecules. ESI-MS experiments also showed the presence of a peptide constituted by two PyroGlu moieties; that is, PyroGlu–PyroGlu, which also bears an imide bond (see Figure 80b). However, the peptide could itself be the result of a very quick hydrolysis of previously extant PyroGluDKP upon exposure to water in ESI conditions. Irrespective of that, these results provided evidence of the capability of silica surfaces to act as activators of condensation events. In water solutions, the internal cyclization to give PyroGlu is known to be thermodynamically disfavored. In the absence of water, the process becomes thermodynamically favorable but may be kinetically slow; in the form of bulk crystalline glutamic acid, it does indeed occur but only at 197 °C, whereas when supported on silica the condensation was observed to take place at 118 °C. Therefore, the silica surface exerts a kinetic effect on the reaction by working as a catalyst.

9.2. Interaction with Peptides

The works available in literature addressed to study the interaction of peptides with silica surfaces pursue common objectives (section 3.2.7). Most of them focus on determining the binding forces that dictate the peptide/silica interactions; other works aim at unraveling the amino acidic residues most prone to interact with silica surfaces, and just a few evaluate the behavior of peptides upon adsorption. In this review, some details of these works will be provided. It is worth underlining that a great number of works concerning the immobilization of proteins in mesoporous silicates are also available in the literature. These works are of great interest because of their potential applications in the areas of biotechnology and biocatalysis. They have been recently reviewed by Hudson et al.⁶⁶⁹ and therefore will not be addressed in this review.

As far as the first group of works is concerned, a very recent study of Patwardhan et al.²⁷³ emerges as a landmark on the chemistry of aqueous silica nanoparticle surfaces and the mechanism of peptide adsorption. In this work, three types of amorphous silica nanoparticles with 15, 82, and 450 nm diameter were synthesized and by means of base titrations and ζ potential measurements, it was found that the acidity of the silica nanoparticles increased with the particle size. The authors stated that such a dependence of the acidity with the nanoparticle size was due to the adoption of a modified Stöber synthesis^{670,671} for the nanoparticle preparation. In this procedure, the concentration of ammonia was varied to control the particle size, and higher ammonia concentration precipitated larger particles in such a way that more silanol groups became ionized. The PZC decreased from 4.2 to 2.4 as the size of the silica particles increased from 15 to 450 nm and by means of classical MD dynamics the authors estimated that between 5% and 20% (corresponding to 15–450 nm size) of silanol groups were ionized in the form of $\equiv\text{Si}-\text{O}^-$ at pH 7. Peptide binding assays with seven different dodecapeptides were performed using different synthetic peptides by means of ζ potential measurements. It was shown that peptides with higher pI values (i.e., those that contained lysine and arginine residues) were attracted more strongly for those surfaces that exhibited larger surface density of negatively charged $\equiv\text{Si}-\text{O}^-$

groups, thus indicating electrostatic contribution to binding. This was also observed by Chen et al.,²³³ who showed that two peptides enriched with basic amino acid residues had a great binding affinity to SiO_2 supports, and this is also in line with the trend observed by Churchill et al.¹⁰⁵ using AAs instead of peptides (see section 9.1.3). Contribution of electrostatic forces in the peptide/silica interaction was also demonstrated by the fact that at low initial concentration (less than 0.2 mg/L) cationic peptides (namely, those with higher pI) were immediately attracted by silica nanoparticles, presumably via ion pairing, whereas for noncationic peptides (namely, those with lower pI) weak or no adsorption occurred, since the electrostatic interaction was not favorable. However, these noncationic peptides indeed adsorbed after overcoming a certain initial peptide concentration threshold value. Since these peptides contained polar amino acidic residues such as serine, threonine, and tyrosine (with $\text{R}=\text{CH}_2\text{OH}$, $\text{CH}(\text{CH}_3)\text{-OH}$, and PhOH , respectively), the authors interpreted that H-bonding directed the interaction of these peptides with silica nanoparticles. Additionally, at high concentrations, adsorption of cationic peptides seemed to level off due to saturation of $\equiv\text{Si}-\text{O}^-$ sites (Langmuir adsorption, monolayer), whereas for noncationic peptides the adsorption increased even after further elevation of the initial concentration, in support of the formation of H-bonded peptide multilayers. The authors stated that these two binding mechanisms were consistent with the different initial concentrations of the two peptide groups needed to reach significant adsorption. That is, since H-bonds are weaker than electrostatic interactions, the adsorption of cationic peptides required less peptide concentration than for noncationic peptides.

In this same work,²⁷³ classical MD simulations using polymer consistent force field augmented for silica (PCFF-SILICA) at $T = 300$ K were also carried out. Simulations addressed the interaction of a cationic and a noncationic peptide on neutral and partially ionized silica surfaces. Results showed that the former peptide was found within a distance <3 Å from the superficial $\text{SiOH}/\text{Si}-\text{O}^-$ layer during 80% of simulation time while the noncationic one remained separated from the same surface by several water layers. In the bound conformations, NH_3^+ moieties from the N-terminus and side chains tended to be close to surface $\equiv\text{Si}-\text{O}^-$, thereby confirming the formation of ion pairs. Despite that, it was also observed that polar groups established intermittent contacts with SiOH through H-bonds. Figure 81 shows snapshots of the MD that reflect these situations.

In view of these results, the authors concluded that the major contributions to binding are ion pairing via electrostatic forces and H-bonds, although they were aware that less energetic ion–dipole, dipole–dipole, and van der Waals interactions must be also present and that the balance of these two major contributions depends on the acidity of the silica and on the pI and conformational flexibility of the peptides.

Results obtained from classical MD simulations carried out by Nonella et al.,³²⁵ in this case using the CHARMM-modified force field, are also along this line. In this work, the peptide model was the Ala-Lys-Lys-Lys-Ala sequence (AKKKA, charge of +3) and the silica surface was based on the edingtonite structure with some deprotonated silanol groups (charge of -19), the electroneutrality of the system being completed by the inclusion of Cl^- or Na^+ ions. After several MD runs authors observed that the interaction occurred through direct peptide/surface and indirect peptide/water/surface H-bonds, which in

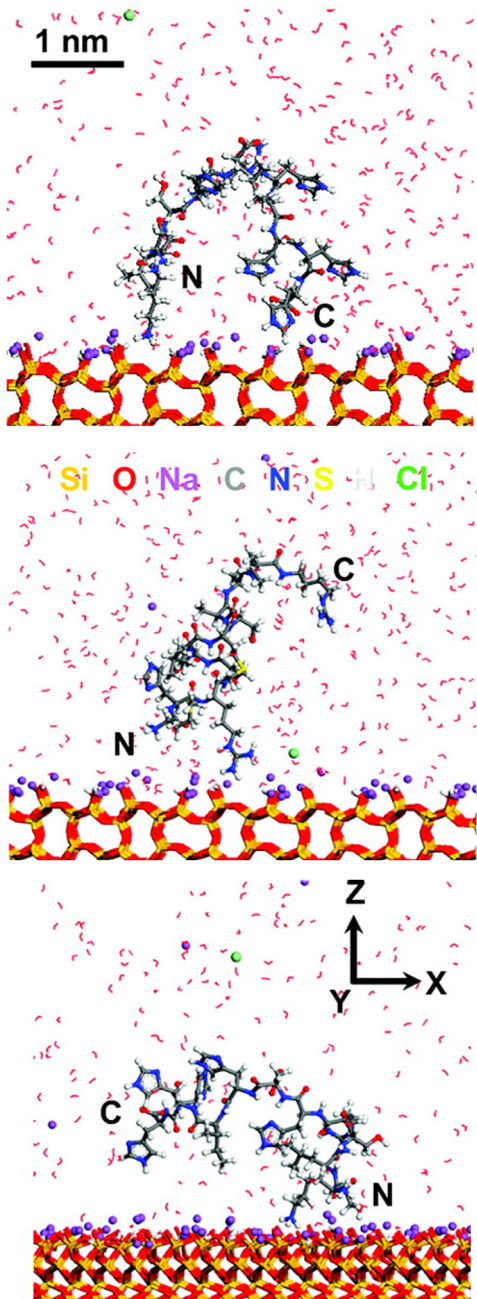


Figure 81. Snapshots of the peptides adsorbed on silica surfaces during classical MD simulations (PCFF-SILICA force field, $T = 300$ K). Interaction with a neutral silica surface (top and middle) and with a negatively charged silica surface (bottom) due to the presence of SiO^- surface groups. The N- and C-terminus have been labeled. Adapted with permission from ref 273. Copyright 2012 American Chemical Society.

turn were continuously formed and broken during the trajectories. Such a peptide/surface interaction variability caused the peptide to exhibit a certain mobility, both in terms of diffusion along the surface and of internal conformational changes, a fact that led the authors to interpret that the “adsorbate state” showed strong dynamical features and, accordingly, an ensemble of different adsorbed structures should exist. Figure 82 shows two MD snapshots in which the peptide interacts directly through five H-bonds with the surface (a) or indirectly bridged by water solvent (b).

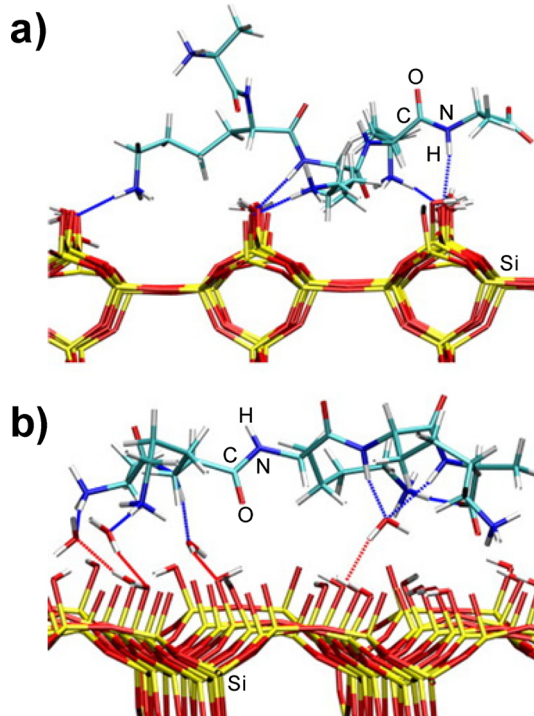


Figure 82. Snapshots of the peptide/silica system during classical MD simulations in aqueous solvent (CHARMM-type force field, $T = 300$ K): (a) direct H-bonds between peptide and silica; (b) indirect H-bonds between peptide and silica bridged by water. Only water molecules involved in H-bonds are shown. Redrawn with permission from data of ref 325. Copyright 2010 Elsevier.

Remarkably, it was found that direct H-bonds all adopted the $\text{Lys-NH}_3^+ \cdots \text{OSi}^-$ pattern, thus including a strong electrostatic component, whereas indirect H-bonds adopted either $\text{NH} \cdots \text{OH} \cdots \text{OSi}^-$ or $\text{NH} \cdots \text{O} \cdots \text{HOSi}^-$, where NH can either belong to Lys-NH_3^+ group, to the terminal NH_3^+ group, or to the backbone NH moiety and O or OH belong to a water molecule.

It seems clear that electrostatic interactions between charged peptides and silica surfaces play a significant role in peptide binding. This adsorption driving force has been exploited by Jonsson and co-workers^{672,673} in order to induce helical peptide structures when adsorbed on silica particles, as already mentioned in section 3.2.6. Indeed, the authors beautifully showed that designed peptides, which were unconstructed in solution, adopted a well-defined helix structure upon silica adsorption due to the electrostatic interaction between the two partners (see Figure 83a).

In these works, several peptides were synthesized with the particularity that basic amino acidic residues such as arginine were precisely placed at strategic positions in such a way that when adopting an α -helix structure they were positioned on the same side of the helix (see Figure 83b). Since at pH 8–10 the basic residues and the surfaces of the silica nanoparticles exhibited net positive and negative charges, respectively, the electrostatic complementarity induced the formation of helical structures upon adsorption. Additionally, the addition of acidic residues such as glutamic acid, which were deprotonated at these pH values, at positions that pointed away the surface when adopting helix structure (i.e., facing the solution, see Figure 83b) resulted in a significant increase of the helical content of the peptide upon silica adsorption, probably due to

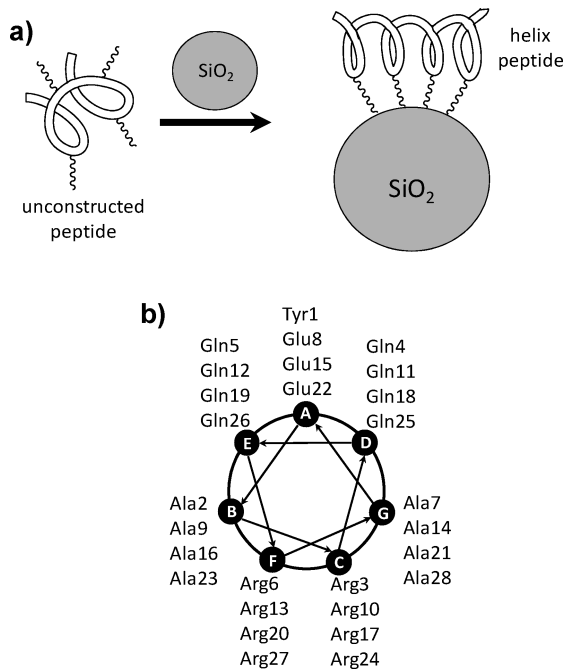


Figure 83. (a) Schematic representation of the silica surface-induced helix formation. (b) Amino acid sequence of a peptide presented in ref 673 that folds as an α -helix in the presence of silica surfaces, depicted as a helical wheel, where each point gives rise to a row of amino acids.

both electrostatic repulsion with the surface and attraction to water solvent. Interestingly, Bolivar et al.²⁰⁹ have demonstrated that proteins that in solution exhibited helix conformations constituted by arginine residues, which in turn were exposed on one side of the helix, retained the very same conformation upon silica surface adsorption. This was due to the large affinity between the arginine-rich helix regions and the surface, hence opening up a potential way to immobilize enzymes on silica surfaces, which usually tends to cause denaturation.

Despite these findings, Manyar et al.⁶⁷⁴ observed that during the enzyme pepsin immobilization in SBA-15, the maximum loading was achieved when both the enzyme and the matrix were negatively charged. Because of these surprising results, Giussani et al.⁶⁷⁵ have recently presented a theoretical study to understand this behavior. The work was carried out by means of classical MD simulations (CHARMM22 force field) where a complete solvated pepsin with a -6 charge interacted with a flat silica surface exhibiting negatively charged SiO^- groups in the presence of either Na^+ and K^+ cation to ensure electro-neutrality. Results indicated that, irrespective of the counterion, solvated pepsin adhered to the surface regions where the SiO^- groups were located because of the mediation of the cations and solvent. It was found that the actual pepsin/silica interaction depended on the nature of the cosolvating cation. That is, K^+ was found to coordinate the SiO^- oxygen atom dragging the solvated pepsin on top of the negative surface, whereas Na^+ showed more affinity toward water than SiO^- , forcing water molecules that surround pepsin to stick via H-bonding to silanolates, thereby approaching pepsin toward the surface.

Related to the question of which residues are more prone to interact with silica surfaces, Sarikaya and co-workers^{271,272,676} have reported results that provide clues to understand the connection between the amino acid content, the sequence, and the molecular structure of peptides on the one hand and their

interaction and affinity to silica on the other hand. Remarkably, this has been achieved by combining bioinformatics, experiments, and theoretical simulations. They first developed a bioinformatic approach²⁷¹ that allowed them to identify and select available peptides according to their inorganic-solid binding properties (section 3.2.6), so that a classification from strong- to weak-binding peptides sequences was established. Interestingly, the binding properties of these selected peptides toward quartz experimentally measured using surface plasmon resonance spectroscopy very well matched those predicted by bioinformatic tools. Among the different selected peptides, it was found that the strong-binding ones contained hydrophobic regions characterized by the presence of proline along with other hydrophobic residues such as tryptophan and leucine, whereas the weak-binding sequences did not. In order to evaluate the role of these residues in the interaction, classical MD simulations (CHARMM force field) of three peptides (two strong binders and one weak binder) in interaction with quartz (100) surface were carried out.^{272,676} It was found that the strong-binding peptides exhibited the proline-rich regions in close proximity to silica surface, and visual inspection revealed that these residues were buried at interstitial sites of quartz, whereas polar groups (serine, histidine and C-terminal carboxylate) were involved in H-bonds with the surface (see Figure 84a,b).

For the weak-binding peptide, it was observed that the interaction occurred through valine ($R = \text{CH}(\text{CH}_3)_2$), alanine, and arginine (see Figure 84c), the former two residues being attracted to the hydrophobic quartz interstices, while the arginine/quartz contact was attributed to a combination of electrostatic and H-bonding. Therefore, it seems that hydrophobic regions are prone to interact with quartz surfaces due to the presence of hydrophobic cavities. This had already been suggested and shown using amino acid analogues (see above, section 9.1.3). The authors also stated that the proline-rich region plays a second role to favor the interaction. That is, analysis of internal H-bonds (namely, intrapeptide and peptide–water H-bonds) both in solution alone and in interaction with quartz revealed that the two strong-binding peptides do not change the number of internal H-bonds, while the weak-binding one loosens a certain number of its internal H-bonds upon adsorption. This suggested that the proline-rich regions might have hindered the formation of internal H-bonds in the sense that their internal stability remained constant between the solution and contact with the surface, whereas for the other peptide the internal stability decreased when adsorbed due to the loss of internal H-bonds, rendering the peptide/silica complex globally less stable.

According to these results, the propensity of certain residues to interact more or less favorably with silica surfaces, which ultimately leads to the specific recognition of a given silica surface by a given peptide sequence, arises from the complex interplay of interactions such as electrostatic interactions, directional H-bonding, and hydrophobic (dispersive) forces. However, a very recent work of Schneider et al.³⁰⁸ highlighted that the peptide-sequence/silica surface recognition may also be helped by the structuring of the water solvent when in contact with the silica surface features; that is, amino acid side chains are able to “sense” the molecular solvent structure and, in particular, the local solvent density variations at the solid/liquid interface with atomic scale precision, similarly to the lock-and-key recognition mechanism typical in biological systems. The authors performed several classical MD simulations (AMBER

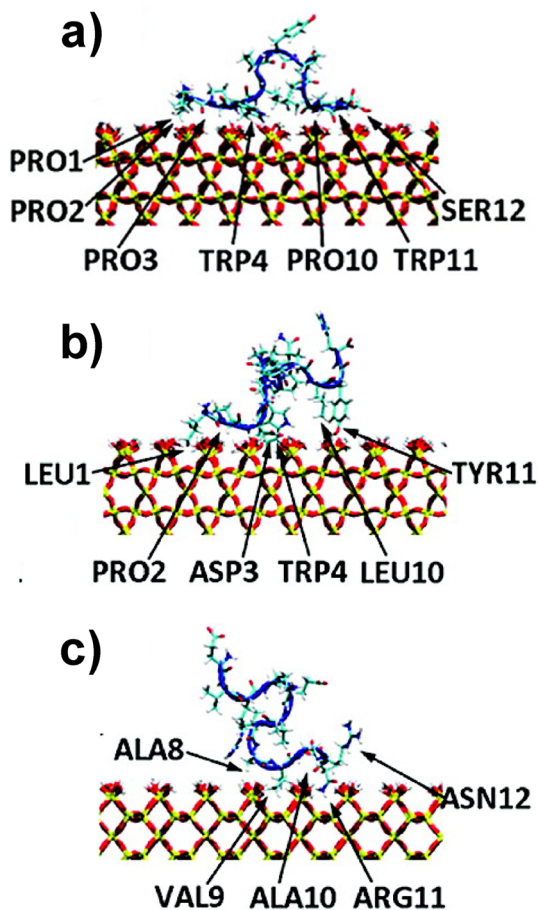


Figure 84. Snapshots of the peptide/silica systems during classical MD simulations in aqueous solvent (CHARMM-type force field, $T = 300$ K) for strong-binding peptides (a, b) and the weak-binding peptide (c). Water molecules have been omitted for the sake of clarity. Adapted with permission from ref 272. Copyright 2010 American Chemical Society.

force field) for the adsorption of Arg-Lys-Leu-Pro-Asp-Ala (AKLPDA) onto an oxidized silicon surface that contained SiOH and SiO^- surface groups. Results indicated that the arginine and lysine residues remained close to the surface during most of the simulation time (see Figure 85a), the computed adsorption free energy being -15 and -7 kJ mol^{-1} for arginine and lysine, respectively.

The authors also analyzed the water structuring during the simulations by examining the density profiles of water oxygen atoms along the direction normal to the surfaces, and they observed the presence of a first broad water layer as well as patches of reduced water density (see Figure 85b). The most interesting point was that the aliphatic parts of the side chains spread almost flat within regions of low water density while the charged moieties occupied high-density positions (namely, the first broad water layer) seeking the proximity of SiOH and SiO^- to establish H-bonds. This was confirmed by computing the free energy profile of a spherical hydrophobic solute from the surface to the bulk water along the normal direction of the surface ($\Delta G(z)$), in which the maximal values of $\Delta G(z)$ were correlated with those positions with low water density (see Figure 85c). These findings pointed out that the local solvent density variations near heterogeneous rough surfaces, such as the silica ones, may be sensed by the side chains in a way that

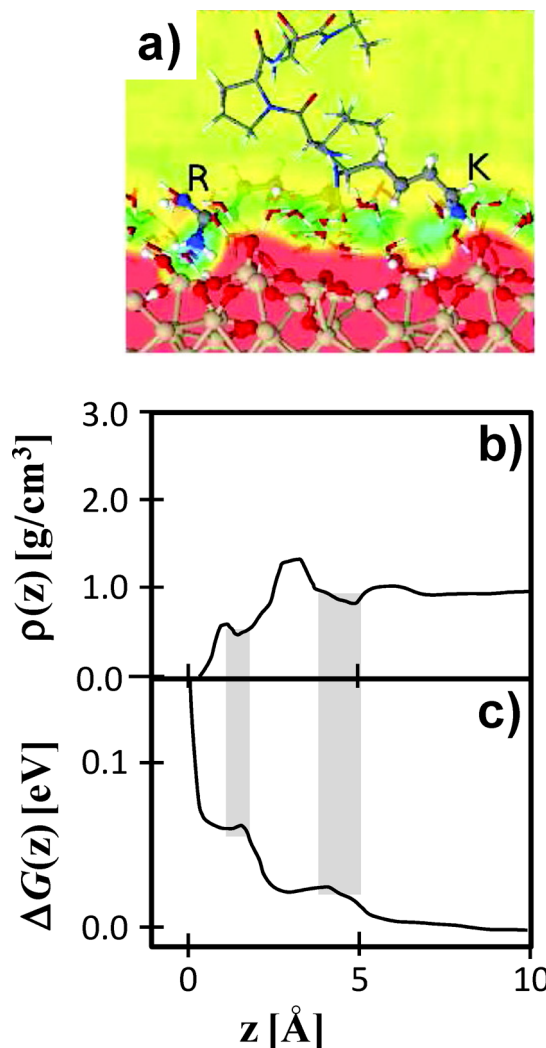


Figure 85. (a) Snapshot of the peptide/oxidized silicon surface system during classical MD simulations in aqueous solvent (AMBER force field, $T = 300$ K). Arginine (R) and lysine (K) residues have been labeled. (b) Density profile of water oxygen on the oxidized silicon surface. (c) Free energy profile of a spherical hydrophobic solute on the oxidized silicon surface. Gray regions indicate that positions with low water density on the surface match with maxima of $\Delta G(z)$. Adapted with permission from ref 308. Copyright 2012 American Chemical Society.

bears many features characteristic of the specific recognition in biomolecular aggregates. In this particular study, the alternation between hydrophobic and hydrophilic residues optimized the matching with the solvent density oscillations.

Finally the experimental works carried out by Somorjai and co-workers^{235,677} and already mentioned in section 3.2.6 are also of interest because they show the evolution of peptides once they are adsorbed on silica surfaces. In these works, the adsorption of peptides with XY composition (X hydrophobic and Y cationic) on hydrophilic silica were studied *in situ*. QCM measurements indicated that all peptides tested adsorbed onto silica. However, the most interesting peptide was the 14-AA sequence containing leucine and lysine (sequence of Ac-LKKLLKLLKKLL-NH₂) since SFG results indicated that it was the only peptide that, when adsorbed on silica, showed an NH stretching band (3300 cm^{-1}) due to an amide peptide and the absence of CH stretching modes in the spectrum,

suggesting a different orientational distribution of the peptide at the solid/water interface compared with that in solution. For this peptide, the results obtained by AFM are also of interest, since the authors monitored the changes of the adsorbed peptide on the silica with time of adsorption. In general (see Figure 86, left column), it was observed that the peptide

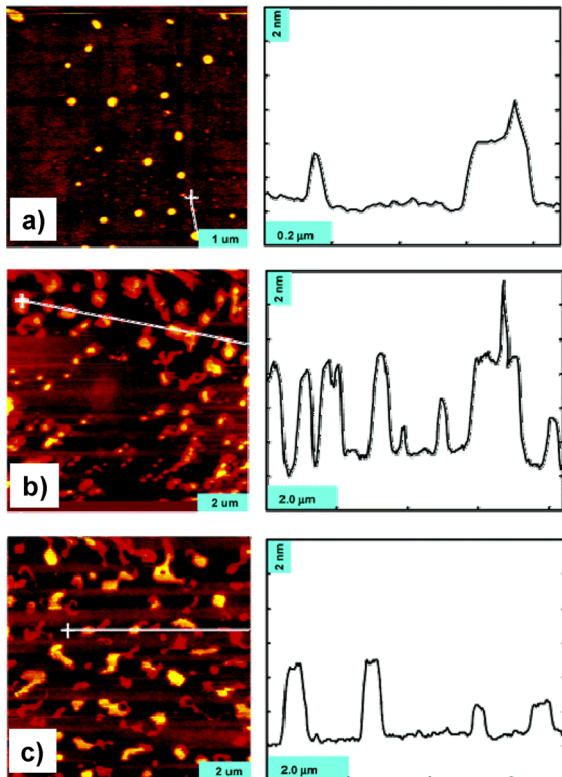


Figure 86. AFM topographical features of a peptide based on the leucine and lysine residues in interaction with silica imaged at <5 min (a), 5–10 min (b), and >30 min (c). In the right column it is observed that the topographic heights do not dramatically change with adsorption time. Adapted with permission from ref 235. Copyright 2006 American Chemical Society.

underwent a gradual morphological transition on silica from small spherical islands (~ 200 nm wide) to much larger laterally aggregated domains (up to $1.5\ \mu\text{m}$) between $t < 5$ min to >30 min. Despite that, the authors observed that the lateral expansion was not accompanied by an incremental growth in feature height, since topographic heights of 2.5 and 5.0 nm remained constant (see Figure 86, right column). Interestingly, QCM results indicated that adsorption took place in a multistep fashion. These data, along with AFM observations, suggested that the process involved an initial rapid adsorption on top of several nucleation sites on the surface, followed by subsequent slower reorganization, which included island growth, and spreading over silica, to form large laterally coalesced domains.

9.3. Interaction with Nucleic Acid-Related Biomolecules

Understanding the adsorption of nucleic-acid derivatives (i.e., nucleobases, base-pairs, DNA and RNA sequences, etc.) to solid surfaces has important applications in DNA microarrays,^{678–680} gene therapy,^{681,682} DNA-based devices,^{683,684} high-quality DNA purification by chromatographic techniques,^{685,686} and DNA hybridization.^{687,688} The initial stage of

biofilm formation is facilitated by the attachment of extracellular DNA on the substrate surface⁶⁸⁹ so that a thorough understanding of DNA adsorption to surfaces is of great relevance to control the formation of bacterial biofilms. Additionally, it has been reported⁶⁹⁰ that adsorbed extracellular DNA on mineral surfaces may retain its ability to transform competent microorganisms (namely, microorganisms adapted for easier receiving of heterogeneous DNA) via horizontal gene transfer, thus giving rise to microbial diversity. In this context, the interaction with nucleic-acid derivatives becomes of particular relevance due to the capability of silica nanoparticles, especially those of mesoporous silica, to load and deliver genetic material, a fundamental process in gene therapy.⁶⁹¹ Indeed, the prospect of gene therapy and genetic engineering as a new medical technique implies transferring custom genetic material into cellular environments to correct genetic diseases via loading and transport of the genetic material on carrier bodies. The most common and simplest method of gene delivery is the viral vector system,⁶⁹² in which the genetic material is carried into nonpathogenic viruses. However, the risks involved in the expression of the viral genetic code and its nonspecificity have promoted the development of synthetic systems for these purposes, among which mesoporous silica nanoparticles are attractive candidates due to their ability to confine genetic material into their porous space, their high chemical resistance to microbial attack, low toxicity, thermal stability, and ease of modifications.

Organizing this section adopting the “bottom up” scheme, in terms of size and complexity of the systems (similarly to what has been done for amino acids and peptides) has shown that much less data are available in the literature compared with that for AAs and peptides. Indeed, to the best of our knowledge, only one work dealing with single nucleobases interacting with bare silica surfaces has been reported, while works involving functionalized silica surfaces can be found in the literature due to the relevance of these modified phases in chromatography. Even if we include modified silicas, all the works available are based on experimental measurements, while no computational studies have been found.

In this single work devoted to nucleobase/silica interactions, Plekan et al.²⁵⁸ studied the adsorption of adenine on SiO_2 by means of photoemission and soft X-ray photoabsorption. The photoemission spectrum was found to be quite similar to that of adenine multilayer, but some striking differences were observed, which led the authors to propose that adenine chemisorption had occurred.

As regards polymeric nucleic acids, clear evidence of the fact that mesoporous silica can load DNA sequences into the pores was provided by Solberg et al.⁶⁹³ In this work, experiments of X-ray diffraction, nitrogen physisorption, UV-visible spectroscopy, and fluorescence confocal microscopy performed before and after pore filling were used to demonstrate that double-stranded linear DNA sequences were certainly taken up into the pores of acid-prepared mesoporous silica (APMS). Powder XRD patterns (see Figure 87a) indicated that APMS alone adsorbed certain amount of DNA.

The presence of a single broad diffraction peak of the parent material alone (dashed-line peak) is typical of ordered mesoporous silica due to the amorphous nature of the walls, while the decrease in intensity (solid-line peak) was claimed to be indicative of the presence of a guest molecule inside the pores.⁶⁹⁴ Clearer evidence of this is provided by the fluorescence confocal scanning laser microscopy images (see

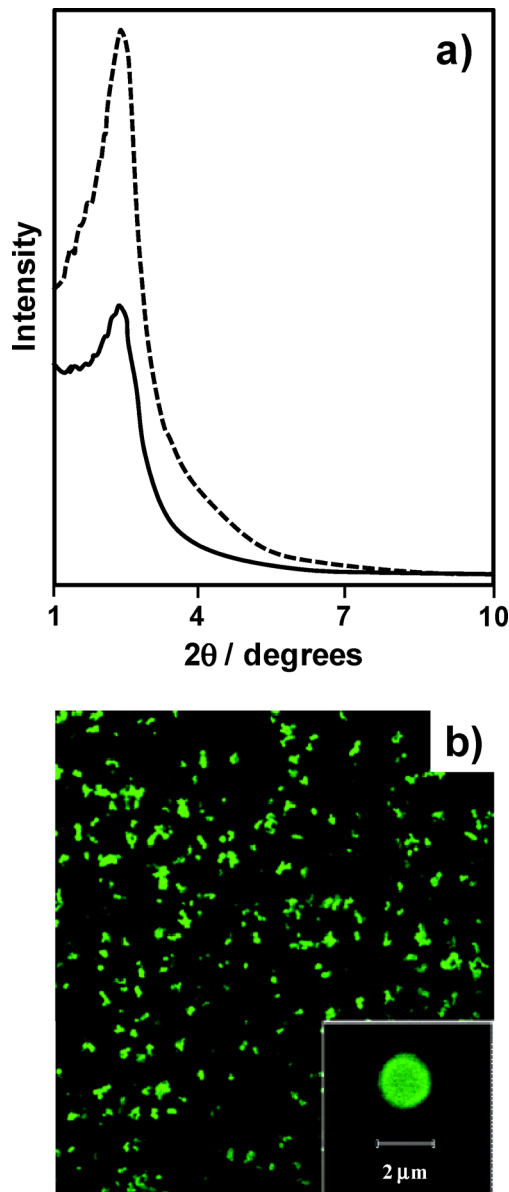


Figure 87. (a) Powder XRD patterns before (dashed-line) and after (solid line) DNA filling. (b) Fluorescence confocal scanning laser microscopy image of APMS after DNA adsorption. Adapted with permission from ref 693. Copyright 2006 American Chemical Society.

Figure 87b), which also indicated DNA penetration of the bulk of the micrometric particles.

This view that DNA can be loaded within the pores of mesoporous silica nanoparticles has been recently strengthened by Li et al.^{695,696} In these two works, the adsorption behavior of a short salmon DNA in the presence of either a mesoporous silica nanoparticle or a nonmesoporous silica nanoparticle was compared. DNA adsorption isotherms produced a typical Langmuir shape (see Figure 88) suggesting that monolayer adsorption at the DNA/silica interface occurred, but differences on the maximum adsorption capacity between the two materials were detected, that is, 121.6 and 48.3 mg DNA/mg nanoparticle for mesoporous and nonporous silica nanoparticles, respectively.

The most remarkable finding of these works was that two desorption events were observed: one at $T = 0.5\text{ }^{\circ}\text{C}$, in which a very small fraction of adsorbed DNA was released and a second

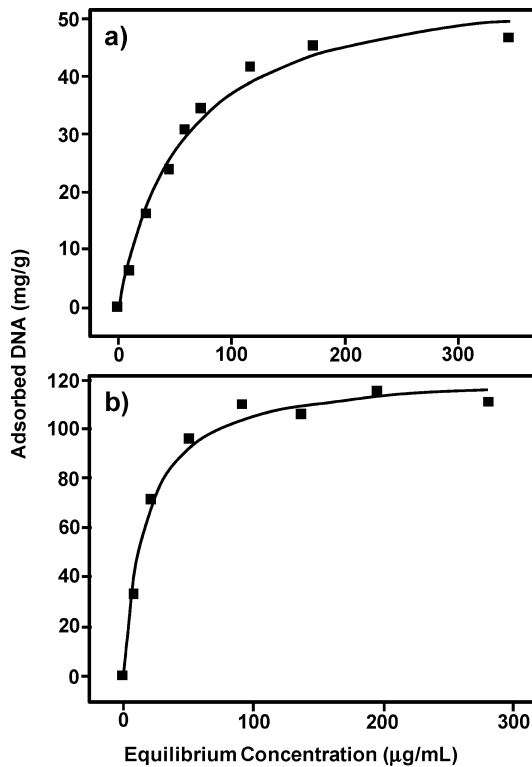


Figure 88. Ascending adsorption isotherms measured for salmon DNA with nonporous (a) and mesoporous (b) silica nanoparticles. Reprinted with permission from ref 696. Copyright 2012 American Chemical Society.

one at $T = 37\text{ }^{\circ}\text{C}$, in which a large amount of adsorbed DNA was released. Supported by dynamic light scattering experiments, the authors interpreted that the first DNA desorption was due to the release of DNA sequences adsorbed on the external surfaces of the mesoporous silica particles, whereas the second one corresponded to DNA located within the pores.

Thus, it seems clear that DNA indeed adsorbs on pure silica surfaces. However, an interesting question arises: considering that at physiological pH, both silica surfaces and DNA sequences have a net negative charge because of the presence of SiO^- and phosphate groups, respectively, what are the driving forces for DNA adsorption? The same question was formulated by several authors.^{690,696–699} Summarizing the results of these different works, one may conclude that the energetic contributions to DNA interaction with a silica surface can be categorized into three parts: (i) the electrostatic effect (repulsive); (ii) the dehydration effect; (iii) DNA/silica H-bonding. As regards point i, it was observed that an increase of the salt concentration (namely, the ionic strength) led to an increase of adsorption, which was more pronounced for divalent than for monovalent cations. The authors interpreted that the increase of salt concentration shielded to a greater extent the negative charges on DNA and silica surfaces, thus reducing the electrostatic repulsion. Dehydration effects were also considered as a binding mechanism based on the fact that an increase in concentration of a chaotropic salt (that is, a salt that tends to disrupt the structure of macromolecules and that can intensively capture free water molecules) also yielded an increase in adsorption.^{696,697} This was explained by considering that the reaction of DNA adsorption actually involves the release of water: $\text{DNA}(\text{hydrated}) + \text{silica}(\text{hydrated}) \rightarrow \text{DNA-silica complex} + \text{water}$.

conterions \Leftrightarrow DNA/silica + water. The formation of H-bonds between DNA and silica was confirmed by two findings. The first one was that a pH decrease resulted in an increase of adsorption, which led the authors to interpret that at low pH some of the phosphate groups became protonated, hence enabling H-bonding. The second evidence was that isothermal titration calorimetry for DNA injected into binding solution with silica indicated that its adsorption was exothermic.⁶⁹⁶ The overall picture for the adsorption mechanism of DNA derivatives onto silica must thus consider the presence of cations to shield the unfavorable electrostatic interactions between the negative charges present in silica and DNA, as well as the dehydration effects and the formation of intermolecular H-bonds.

An interesting point concerning DNA/silica interactions is the conformation changes undergone by DNA due to adsorption. This was addressed by Scholes et al.,⁷⁰⁰ who explored, by means of resonance energy transfer-based techniques, the conformation changes occurring within the helical structure of a well-defined oligonucleotide upon silica adsorption from aqueous solution. Results obtained via evanescent wave-induced time-resolved Förster resonance energy transfer (EW-TRFRET) measurements showed a dependence of the nucleotide conformational state on the electrolyte concentration. That is, at high electrolyte concentrations, an increase in the flexibility of the oligonucleotide was observed, which led to an unwinding of the helix and to a separation of the two strands, allowing the oligonucleotide to bind directly to the silica surfaces. In contrast, at low electrolyte concentrations, the rigidity of the oligonucleotide prevented an unwinding of the double helix upon adsorption, which resulted in only small segments directly contacting silica. These two situations are depicted in Figure 89.

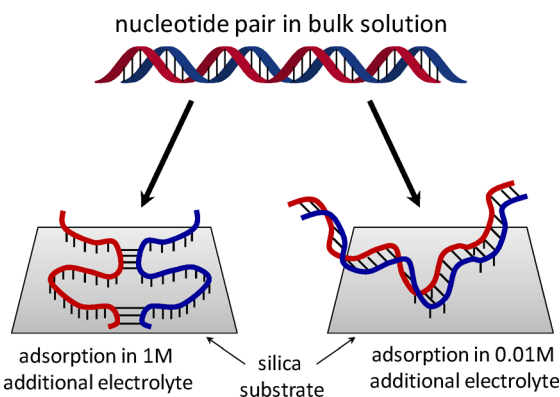


Figure 89. Schematic representation of the conformational changes of oligonucleotides upon silica adsorption depending on the electrolyte concentration. Reprinted with permission from ref 700. Copyright 2011 American Chemical Society.

9.4. Interaction with Drugs and Natural Products

A thorough characterization of the interface between silica surfaces and drugs or natural products is of prime relevance due to the growing interest in the field of drug delivery systems. Indeed, ordered mesoporous materials such as the ones based on silica (e.g., MCM-41, SBA-15) can be loaded with different organic molecules that would be released afterward in a controlled fashion inside a living body. This potential route for drug intake is motivated by the lack of long-term efficiency for certain therapies when the drug is administrated orally or via

injection or their negative effects when conventionally administered. Because of their lack of toxicity, their furtivity (they easily become invisible to the immune system), and their porosity, silica-based ordered mesoporous materials have shown to be excellent candidates to act as drug delivery systems, since they are able to incorporate high dosages of drugs into the mesopores.¹⁷ Moreover, the silanol-containing walls can be functionalized allowing a better control over drug release.⁷⁰¹ In the last 10 years, great efforts have been devoted to the confinement and storing of drugs in mesoporous silicas, as well as to the kinetics of the drug release. Along this line works devoted to several drug/mesoporous silica systems are available in literature: ibuprofen in MCM-41,^{17,702} MCM-48,⁷⁰³ and SBA-15,⁷⁰² gentamicin in SBA-15,⁷⁰⁴ erythromycin in MCM-41,⁷⁰⁵ MCM-48,⁷⁰³ and SBA-15,⁷⁰⁵ alendronate in SBA-15,⁷⁰⁶ and amoxicillin in SBA-15.⁷⁰⁷ Moreover, Vallet-Regí and co-workers have recently authored two excellent reviews focused on this topic.^{15,708} For conciseness, in this section, we will focus on studies that aim to provide a detailed picture at a molecular scale (either with spectroscopic methods or via theoretical calculations) of the actual drug/silica interface. A proper understanding of the drug/silica interactions is fundamental to understand the loading and delivery capability of a given system, since this ultimately depends on the chemical nature of the functionalities of the two partners.

Within the present context, it is worth mentioning the works of Azaïs et al.^{709,710} who studied, by means of sophisticated ss-NMR techniques, the behavior of ibuprofen (IB)⁷⁰⁹ and benzoic acid (BA)⁷¹⁰ when encapsulated within different MCM-41 silica matrices, which differed by the pore diameters (for IB, 35 and 116 Å, hereafter referred as MCM-41₃₅ and MCM-41₁₁₆, respectively; for BA, 30 and 100 Å, hereafter referred as MCM-41₃₀ and MCM-41₁₀₀, respectively). The ¹H MAS NMR spectra at ambient temperature of IB and BA were recorded both in their crystalline bulk forms and when confined in the MCM-41 matrices (shown in Figure 90a,b).

Contrary to the bulk crystalline forms, the spectra for the confined molecules were found to be extremely sharp, a fact that confirmed the high mobility behavior of IB and BA within the pores, in fact the NMR spectra look more like liquid phase than solid-phase. For both molecules the signals of the protons corresponding to alkyl and phenyl groups as well as of SiOH were unambiguously assigned (labeled in Figure 90a,b). The proton signals coming from the COOH group of IB and BA were not visible, contrary to the bulk forms, whereas they appeared in the spectra recorded at low temperatures. These findings suggested that at ambient temperature the proton of the COOH groups was in fast exchange with other environmental protons, namely, SiOH or H₂O. Additional evidence for the involvement of the COOH group in the interaction with the silica walls was provided by FTIR measurements (only for IB, see Figure 90c), which demonstrated an important bathochromic shift of the $\nu(\text{C}=\text{O})$ (from 1721 to 1709 cm⁻¹). Measurements of apparent transverse relaxation times $T_2'(^1\text{H})$ were carried out through solid echo sequence experiments using monoexponential time decay in order to determine the mobility of IB and BA within the pores (the higher the mobility, the longer the $T_2'(^1\text{H})$ value). Unusually long values were obtained (2.4–16.6 and 14.7–20.2 ms for IB and BA, respectively) compared with crystalline forms (for bulk BA $T_2'(^1\text{H}) \approx 150 \mu\text{s}$) although shorter compared with, for instance, BA in CDCl₃ (around 600–700 ms), suggesting a viscous (i.e., liquid-like) behavior of the confined molecules.

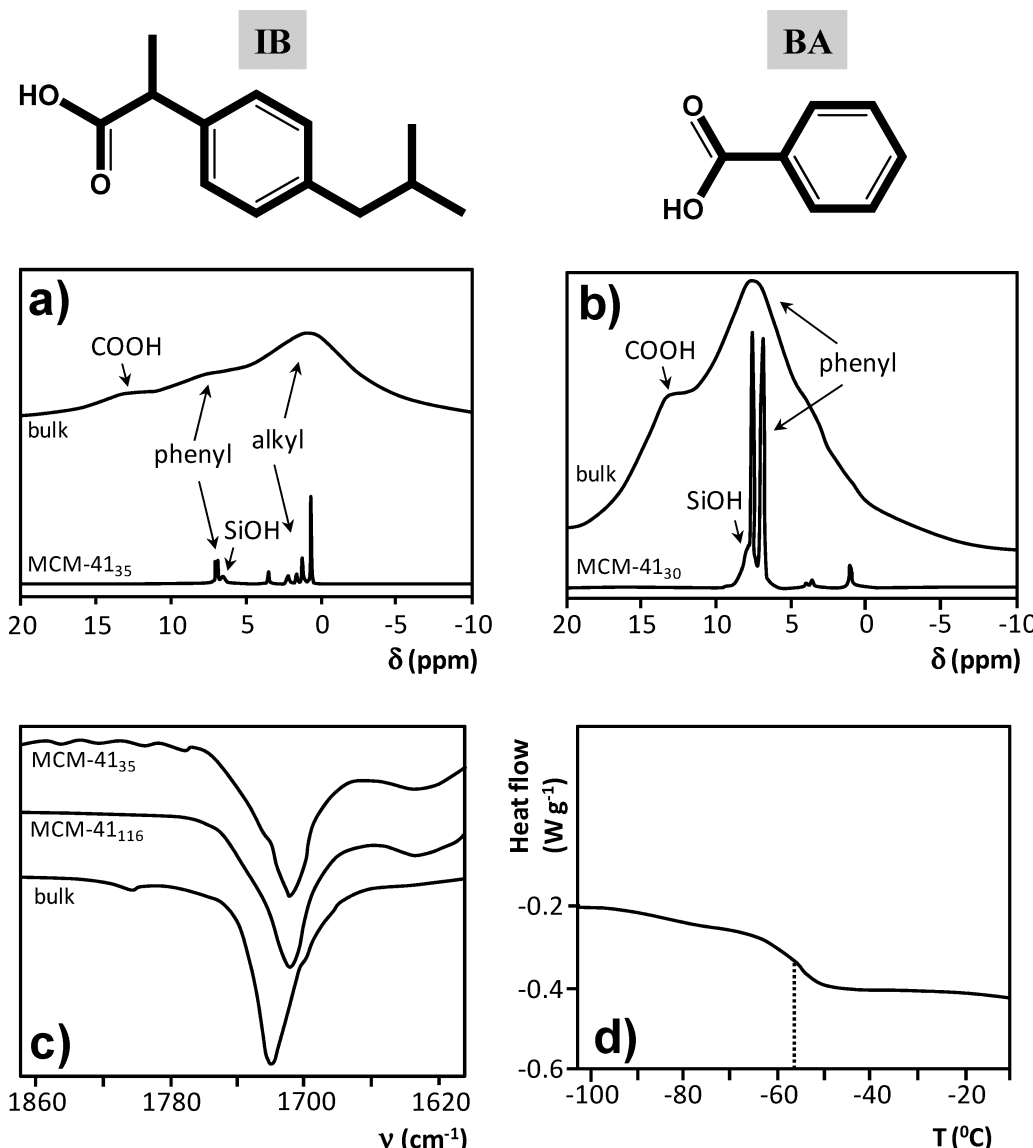


Figure 90. Recorded spectra for confined ibuprofen (IB) and benzoic acid (BA): (a, b) ^1H MAS NMR spectra of IB and BA, respectively, in their bulk states and in MCM-41 matrices; (c) FTIR spectra of IB in the $\nu(\text{C}=\text{O})$ region in its bulk state and in MCM-41 matrices; (d) DSC measurements of BA within MCM-41. Adapted with permission from refs 709 and 710. Copyright 2006, 2010 American Chemical Society.

For both IB and BA, ^1H MAS NMR experiments indicated that a liquid–solid phase transition took place when the temperature decreased (at -50 and -55 °C, respectively), which intriguingly occurred at significantly lower temperatures than respective bulk melting points (76 and 125 °C, respectively). In order to get a deeper insight onto this phase transition, differential scanning calorimetry (DSC) measurements were carried out since they allow elucidation of the physical state of confined molecules. The occurrence of phase transitions permits differentiation of glassy from crystalline states, while absence is indicative of molecular deposition onto the surfaces. DSC measurements (shown in Figure 90d) for BA in MCM-41₃₀ clearly showed a variation of the heat flow at -55 °C, which was not detected on unloaded MCM-41₃₀ and on pure BA. Such depression of the phase transition temperatures has been reported in the literature to be characteristic of confined molecules in porous materials.^{711–716} Remarkably, IB solidified in a glassy state and in a crystalline form when confined in MCM-41₃₅ and MCM-41₁₁₆, respectively. Authors attributed

these two radically different behaviors to steric effects; that is, crystalline ibuprofen is a dimer with a total length of ~ 26 Å so that pores of 116 Å diameter were large enough to allow nucleation of crystallites, whereas pores of 35 Å diameter, even if the dimer fit inside, were exceedingly constrained, thus inducing a vitrification process. In contrast, BA solidified in a glassy state when confined in both MCM-41 silicas (no entrapped crystallites of BA were observed), a fact that led the authors to suggest that the minimal critical size needed for crystallization of BA in MCM-41 might be greater than 100 Å.

The studies of Mellaerts et al.^{717,718} are focused on investigating the loading and the molecular interactions of the itraconazole (ITR) drug into SBA-15 using a combination of DSC, XPS, DRS UV-vis, FTIR, and ^1H MAS NMR spectroscopic techniques. DSC measurements allowed the authors to elucidate the phase transition of ITR occurring within the SBA-15 pores. Bulk crystalline ITR melts at 168 °C, while it undergoes a glass transition at 60 °C. These phase

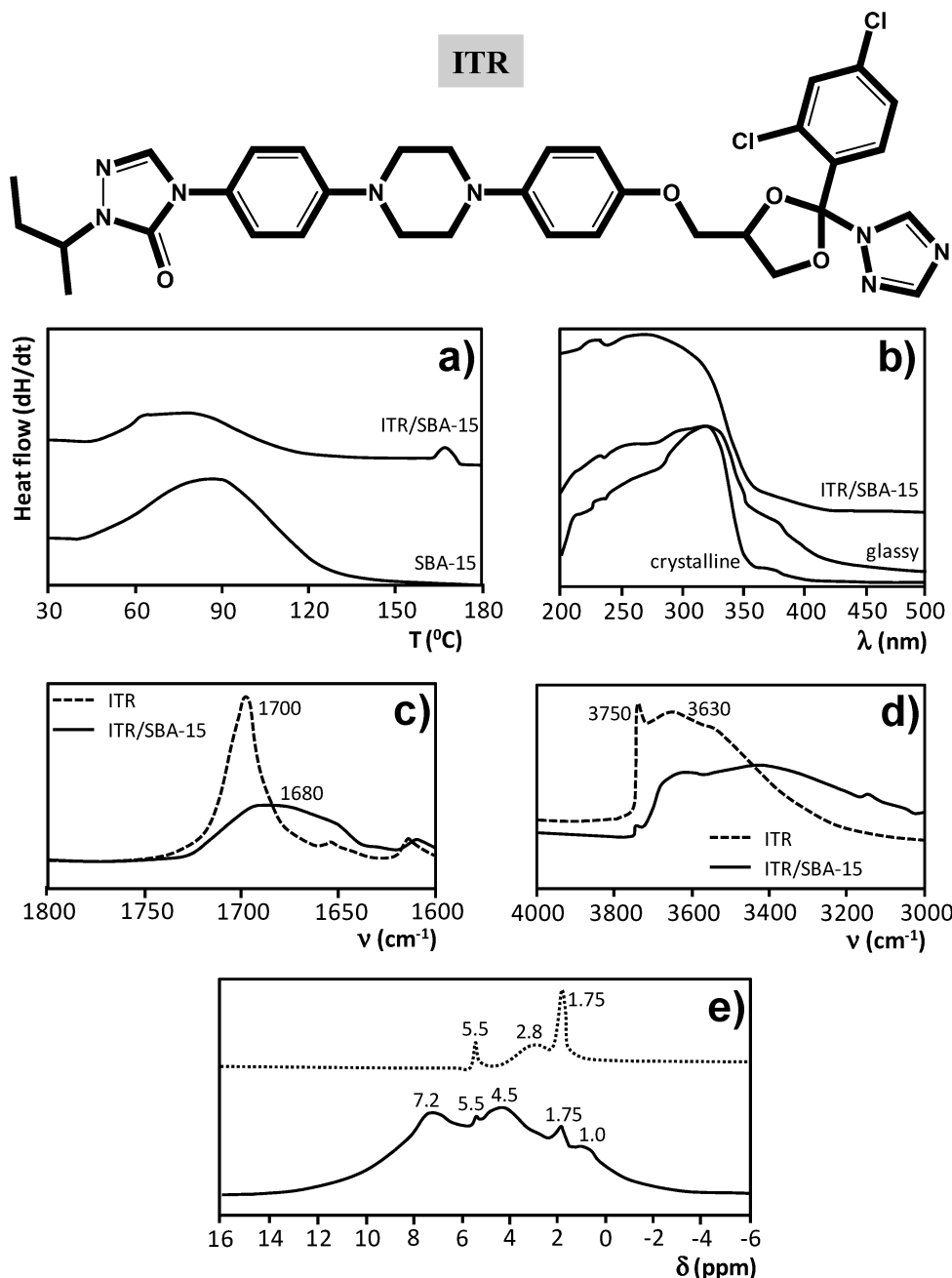


Figure 91. Recorded spectra for confined itraconazole (ITR): (a) DSC measurements of pure SBA-15 and loaded with ITR; (b) DRS-UV spectra of crystalline and glassy ITR and in SBA-15; (c, d) FTIR spectra of free ITR and in SBA-15 in the C=O and OH stretching regions, respectively; (e) ¹H MAS NMR spectra of confined ITR in SBA-15 (solid line and dashed-line spectra belong to single pulse excitation and spin echo spectra, respectively). Adapted with permission from refs 717 and 718. Copyright 2008 American Chemical Society and 2011 Royal Society of Chemistry.

transitions were also observed (see Figure 91a) for ITR within the pores, which revealed the formation of an ITR bulk phase.

XPS techniques allowed determination that ITR was deposited as a film or layer-wise along the pore walls. In order to preliminarily define the molecular environment of the confined ITR, a set of DRS UV-vis experiments were performed. Figure 91b shows the recorded spectra for glassy, crystalline, and confined ITR. The band at 320 nm (also present in the pure bulk forms) and the shoulder between 350 and 400 nm revealed an aggregation of ITR molecules. Additionally, the band featured at 200–245 nm, according to the authors, was indicative of the contact of glassy ITR particles with the silica carrier. In order to have a deeper insight into the

actual contact between ITR and SBA-15, FTIR and ¹H MAS NMR measurements were also carried out. Concerning FTIR, it was observed that in the carbonyl stretching region (see Figure 91c), the band at 1700 cm⁻¹ of the isolated ITR underwent a bathochromic shift to 1680 cm⁻¹ upon adsorption, indicating a H-bonding between the C=O and the SiOH groups. Noticeably, similar IR shifts were also observed by Qu et al. for captopril confined in the MCM-41 pores.⁷¹⁹ Consistently, the absorption bands of isolated SBA-15 at 3750 and 3630 cm⁻¹ due to isolated and H-bonded silanol groups, respectively, became red-shifted in the ITR/SBA-15 system (see Figure 91d). However, according to the authors, such shifts were caused not only by the interaction with the

$\text{C}=\text{O}$ group but also by the interaction with the O ether and the N piperazine atoms, since significant spectral shifts in the CH stretching region of the neighboring ether and piperazine groups were also detected. Concerning ^1H MAS NMR (spectra shown in Figure 91e), the broad signals at 4.5 and 7.2 ppm were assigned to aliphatic and aromatic protons of ITR. The sharp signal at 1.75 ppm was due to protons of isolated SiOH, while the signal around 1 ppm was due to silanolic hydroxyl protons but with different acid strength or location from the isolated ones. The authors highlighted the considerable intensity of the 1.75 ppm signal, despite the high ITR loading and the ITR/SiOH contact evidenced by FTIR. Due to that, the authors interpreted that large part of the SiOH groups did not find a binding partner in the ITR monolayer due to the inaccessibility of the bulky adsorbed ITR molecules, probably because of the roughness of the SBA-15 walls. The authors assigned the signal at 5.5 ppm to H-bonded silanols, which were not bonded to H_2O molecules (the SiOH... H_2O bonding gave rise the signal at \sim 2.8 ppm due to the chemical exchange process between the chemically equivalent protons⁷²⁰), in particular to the interactions with adsorbed ITR. Since SiOH... H_2O clustering was also observed, the picture the authors proposed was ITR in contact with the SBA-15 surfaces with some H_2O molecules positioned between the two partners.

As far as theoretical works on this subject are concerned, to the best of our knowledge, only one theoretical work focused on the interaction of drugs with silica surfaces has been published so far. This work⁷²¹ addresses the adsorption of aspirin (ASP) on a periodic model of the fully hydroxylated (001) α -quartz surface, using the PBE density functional method and a linear combination of numerical atomic orbitals as implemented in the SIESTA code. The most stable adsorbed geometry found by the authors is shown in Figure 92.

The interaction between ASP and the surface was found to be dictated by three H-bonds. In two of them, two surface SiOH groups acted as donor H-bonding groups, the $\text{C}=\text{O}$ groups of ASP being the acceptors, while the third H-bond involved the proton of the COOH group and the O atom of another SiOH group. As for glycine interacting with the same surface (see section 9.1.1.1 and Figure 65b), the H-bonding network exhibited by the pristine α -quartz surface was broken in order to form the ASP/silica adduct, suggesting a competition between the SiOH...ASP and SiOH...SiOH H-bond interactions. The adsorption energy was calculated to be -107 kJ mol^{-1} , similar to the values obtained for some amino acids.

Concerning theoretical works on the interaction of natural products with silica surfaces, several works devoted to the adsorption of benzenediol compounds are available in the literature, in particular, for catechol (1,2-benzenediol)^{722,723} and hydroquinone (1,4-benzenediol).⁴²⁶ Small amounts of catechol occur naturally in fruits, vegetables, and some mushrooms. Moreover, the catechol moiety is present in proteins of marine mussels, which have an unusual high content of 3,4-dihydroxy-L-phenylalanine (the catechol functionality). These residues have been suggested to be the responsible for the strong adhesion of mussels in wet surfaces such as mineral oxides. Hydroquinone may be found as an active toxin in the *agaricus* mushrooms family and is one of the primary reagents in the defensive glands of bombardier beetles.

Mian et al.⁷²² have theoretically studied, at the PBE level, the gas-phase adsorption of catechol onto periodic models of the

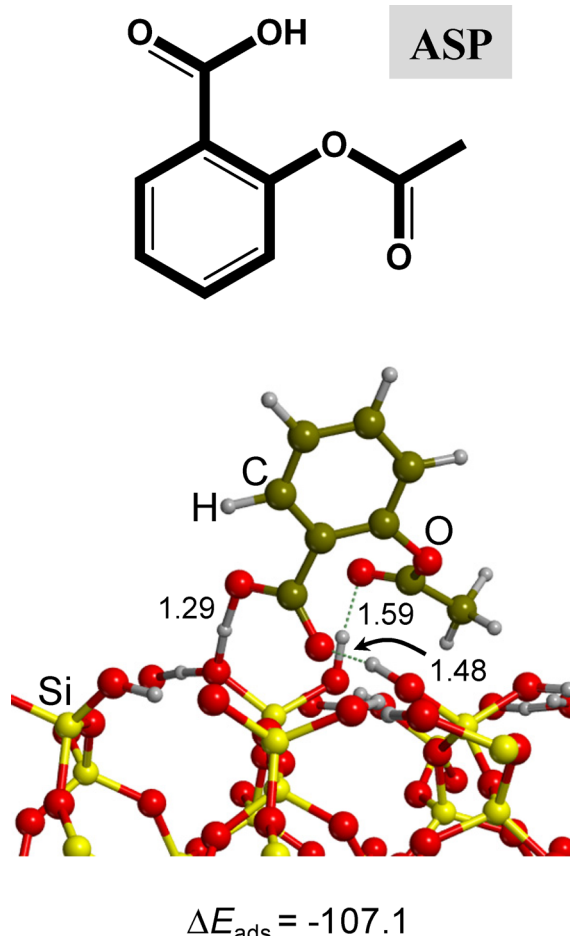


Figure 92. Structure of aspirin (ASP) and the optimized most stable structure of the ASP adsorbed on the (001) α -quartz surface in gas-phase at the PBE level. The computed adsorption energy (ΔE_{ads} , in kJ mol^{-1}) is also reported. Bond distances in \AA . Drawn from data of ref 721.

(001) α -cristobalite and (111) β -cristobalite surfaces, which only present geminal and isolated SiOH groups, respectively. The most stable adducts found are shown in Figure 93.

On (001) α -cristobalite, catechol forms four H-bonds with the geminal SiOH groups, the OH catechol functions acting both as donor and as acceptor H-bonding groups (see Figure 93a). Once again these H-bonds were formed at the expense of partial destruction of the H-bonding network of the pristine surface. Catechol on (111) β -cristobalite was found to form three H-bonds (see Figure 93b), in which one catechol OH acts as H-bond acceptor solely whereas the other one acts as both H-bond donor and acceptor. Consistent with the number of H-bonds formed, the BSSE-corrected adsorption energies ($\Delta E_{\text{ads}}^{\text{C}}$) for catechol on the (001) α -cristobalite and (111) β -cristobalite surfaces were computed to be -59 and -49 kJ mol^{-1} , respectively. Rimola et al.⁴²⁶ have studied the gas-phase adsorption of hydroquinone on periodic surface models based on the sanidine feldspar framework with hydrophobic and hydrophilic surface features at the B3LYP-D level. The most stable structures found considering low surface loading (i.e., with no lateral interactions between adsorbed molecules belonging to adjacent unit cells) are shown in Figure 94.

Hydroquinone in interaction with the hydrophobic surface shows weak H-bonds between the hydroquinone OH

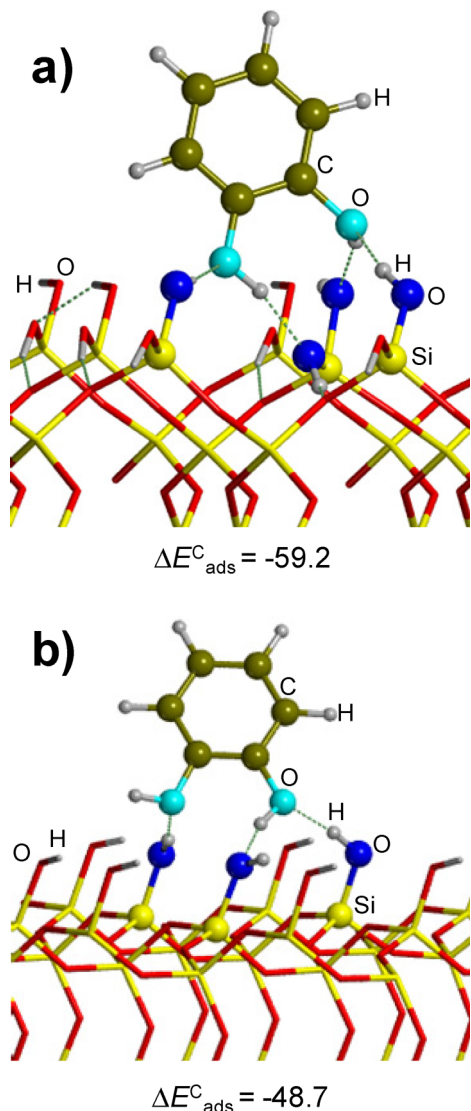


Figure 93. Optimized most stable structures of the catechol adsorbed on the (001) α -cristobalite (a) and (111) β -cristobalite surfaces (b) in gas phase at the PBE level. The computed BSSE-corrected adsorption energies ($\Delta E_{\text{ads}}^{\text{C}}$, in kJ mol^{-1}) are also reported. Drawn from data of ref 722.

functionalities and the O atoms of siloxane groups (see Figure 94a). The computed $\Delta E_{\text{ads}}^{\text{C}}$ value at B3LYP-D is -42 kJ mol^{-1} . The role of dispersive forces in the adsorption was found to be crucial since ΔE_{ads} computed at the pure B3LYP level was -2 kJ mol^{-1} . In the most stable adduct found for hydroquinone interacting with the hydrophilic surface (see Figure 94b), only one of the hydroquinone OH groups was engaged in a H-bond with the surface. Interestingly, the SiOH group that interacts with hydroquinone is the one that exhibits the largest acidity among the different SiOH groups available in the unit cell, as indicated by the potential electrostatic maps of the naked surface. The $\Delta E_{\text{ads}}^{\text{C}}$ was computed to be -84 kJ mol^{-1} at B3LYP-D level, twice more negative than for hydroquinone adsorbed on the hydrophobic surface. Remarkably, although the adduct was significantly H-bonded, dispersion also played a major role since the computed $\Delta E_{\text{ads}}^{\text{C}}$ value at pure B3LYP was only -30 kJ mol^{-1} .

As noted, these works dealt with the adsorption of benzenediol compounds under strict gas-phase conditions, so

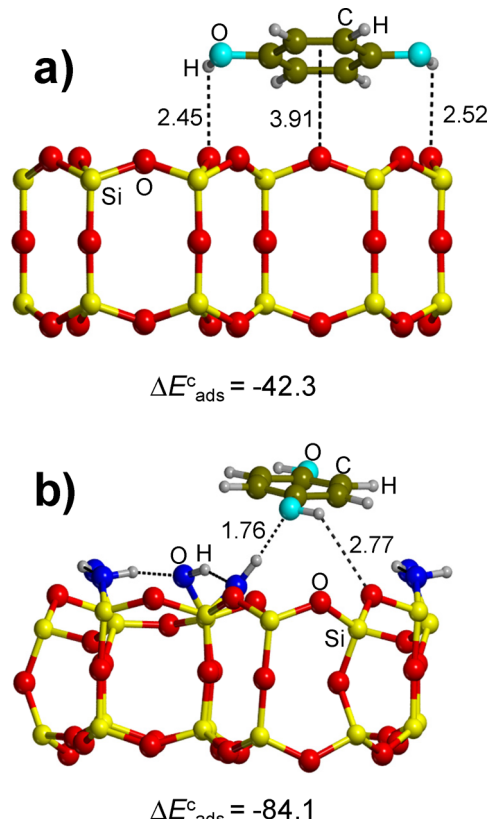


Figure 94. Optimized most stable structures of hydroquinone adsorbed on models of hydrophobic (a) and hydrophilic (b) silica surfaces based on the sanidine feldspar framework at the B3LYP-D level. The computed BSSE-corrected adsorption energies ($\Delta E_{\text{ads}}^{\text{C}}$, in kJ mol^{-1}) are also reported. Bond distances in Å. Drawn from data of ref 426.

no effects from the bulk water were accounted for. Aware of this limitation, Mian et al.,⁷²³ in a subsequent work, studied catechol adsorption onto the (001) α -cristobalite surface model in the presence of 25 explicit water molecules and ran a set of static calculations and ab initio MD simulations at the PBE level. The static calculations were used to proceed with a progressive microsolvation of the catechol/silica interface (i.e., progressive addition of water molecules arising from the wet environment) in a similar fashion to what has been already reported in the literature.⁷²⁴ By means of these calculations, the authors determined that the more water molecules at the interface bridging catechol and silica, the more unstable the system was, suggesting that catechol and the silica surface preferred to establish direct contact. In order to further confirm this finding, ab initio MD simulations were carried out, results showing that, starting from a configuration in which water molecules were fully occupying the catechol/silica interface region, after 10 ps of MD evolution, direct interactions between catechol and the surface were already established (see Figure 95).

10. SUMMARY AND PERSPECTIVES

Hopefully this review has highlighted the complexity and subtleties of silica in its crystalline and amorphous forms already as a bare material. The rather subtle nature of the different functionalities present at the silica surface is discussed in section 2, and their characterization by experimental

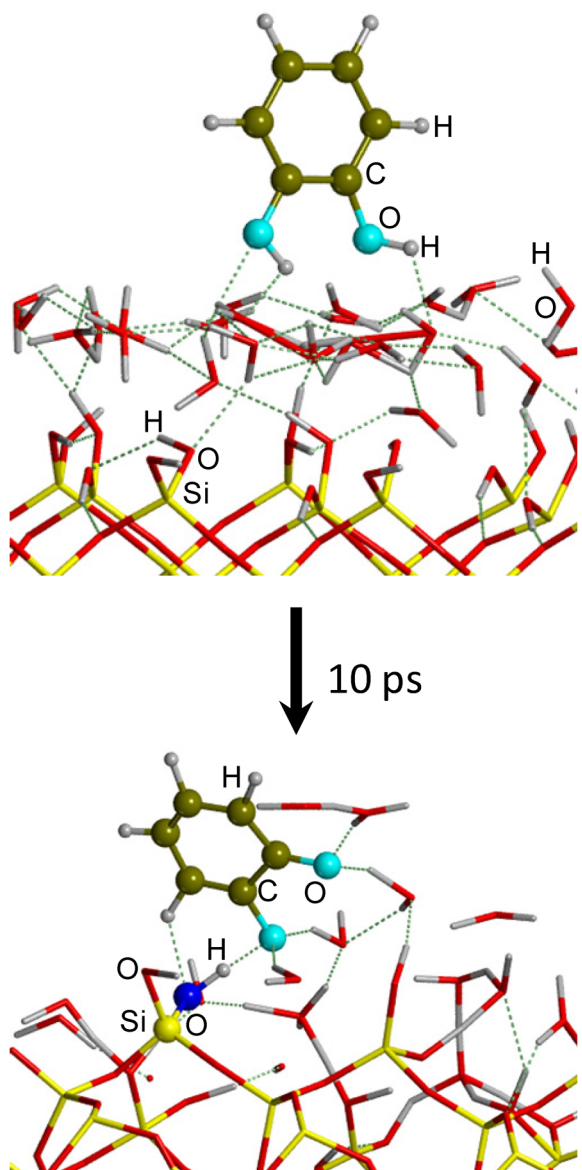


Figure 95. Initial configuration (top) and snapshot taken after 10 ps of evolution (bottom) of ab initio MD simulations (PBE level) for catechol adsorption on the (001) α -cristobalite surface with 25 explicit waters. Drawn from data of ref 723.

techniques reviewed in section 3. In essence, for silica exposed to atmospheric moisture, the dominant surface features are silanol (SiOH) groups and siloxane bridges ($\text{Si}=\text{O}-\text{Si}$), the relative ratio between them being dictated by the thermal history suffered by the silica sample. Siloxanes are rather unreactive unless highly strained, but silanols show diverse types of reactivity. They are weakly acidic and can be deprotonated in the presence of a solution. They readily engage in H-bonding, either between themselves or with Lewis basic molecules from their environment. Further structural distinctions can be made that have consequences on silanol reactivity. First, on the basis of bond connectivity, geminal silanols, Q^2 , are different from terminal ones, Q^3 . Some experimental data suggest that the acidity of these two types of silanols may be different, but in opposition, quantum mechanical calculations reveal that, when isolated, Q^2 and Q^3 sites have almost the same acidity. In other words, it is difficult to conceive differences in reactivity with respect to the

interaction of biomolecules to Q^2 sites compared with Q^3 ones, and for instance, there is no definite indication that a Q^2 -rich surface could be connected to toxicity of crystalline silica. Second, on the basis of spatial proximity, silanols that are close enough to be associated by H-bonding exhibit a different reactivity from isolated ones. The terminal SiOH group belonging to a chain of mutually H-bonded SiOH groups is much more acidic than isolated Q^3 or Q^2 groups. The acidity is modulated by the H-bond strength which, in turn, results from the topology and chain length of the interacting SiOH . This is perhaps the real reason why in some cases the presence of Q^2 sites, which induce a local increase of silanol density, has been put in relation with a specific reactivity. On surfaces derived from crystalline silica polymorphs, the H-bond cooperativity extends to infinity, whereas for amorphous silica surfaces only short chains are possible due to the uneven distribution of the OH groups. This is, in our opinion, the reason that brings about the existence of two acidic sites on amorphous silica surfaces ($\text{pK}_a = 8.5$ and 4.5, respectively) as resulted from experimental measurements: the first acidity would be associated with isolated silanol species (Q^2 or Q^3), the second one being due to the terminal silanols of H-bonded chains. Longer-range distinctions may be significant, but this is still hypothetical. In regards to siloxanes, it is important to know what kind of $(-\text{Si}-\text{O}-)_n$ rings (also called SnR) they form. Experimental data are not precise so far, but it is estimated that S4R and smaller rings are unstable. Two-silicon rings, S2R or $(\text{SiO})_2$, may be present in samples treated at high T as a minor surface feature, as their concentration is typically about 1 order of magnitude smaller than that of isolated SiOH .

Through these surface functionalities, silica interacts with adsorbed (bio)molecules and, ultimately, with living organisms. The nature of the sites implies that H-bonds (with the SiOH) and dispersive interactions (with $\text{Si}-\text{O}-\text{Si}$) are the key forces behind localized adsorption of (bio)molecules, while chemical reactions involving these groups are less common. Therefore, experimental methods capable of tracking the changes in the SiOH spectroscopic features, which are sensitive to H-bonding interactions, are particularly useful (infrared, Raman, and NMR). Unfortunately, the amorphous nature of most silica materials adopted in technological applications renders the elucidation of the atomic details difficult because diffraction-based techniques, such as LEED and electron diffraction microscopy, are not applicable. Therefore, although amorphous silicas have been studied experimentally for at least 50 years, progress in site identification has been exceedingly slow and many features of the silica surfaces are still debated. This is also why SiO_2 surface chemistry is a field where the contribution of theoretical chemistry methods has always been highly valued. Only the advent of powerful computers, together with highly efficient programs, allowed researchers to overcome the intrinsic limits of experimental techniques, because the primary objective of computer modeling is to provide atomistic details of the system under investigation.

Strategies to efficiently model silica surfaces have been covered in section 4, and the computational methods apt to describe with different level of accuracy their physicochemical features and the adsorption of (bio)molecules have been briefly reviewed in section 5. Clearly, techniques based on solving the electronic Schrödinger equation (either based on the wave function or the electron density) can be adopted if high accuracy and generality are sought, provided that density functional methods based on standard exchange–correlation

functionals are supplemented with dispersion interaction correction. While these methods are, in principle, the best approach one can use, the complexity of the systems of interest (size, amorphous nature, role of water, etc.) and the need to account for temperature effects by molecular dynamics simulations forces adopting of more approximated methods based on classical force fields in a molecular mechanics approach.

Sections 6 and 7 provide an overview of the properties of bare silica surfaces determined by the above computational methods. In general, we realize that there is no specific force field able to "accurately" mimic all the features of both bulk and surfaces of silica. The best attempt to date is FFSiOH,⁴⁶⁷ which is definitely able to reproduce structure, dynamic properties, and H-bond features of silica-based materials, not restricted to dense silica ones. Much work needs, however, to be done to extend this promising force field toward the interaction with molecules, water being the most urgent one. Force fields were proven essential to allow for a multiscale approach, using a specific method according to a given system size, in order to arrive at a number of definite and realistic models of the amorphous silica surface, as described in section 7. The complexity of the possible cases of interest when (bio)-molecules interact with silica surfaces has been divided in logical pieces of increasing complexity, namely, the case of H₂O adsorption (section 8), because water is the most ubiquitous molecule in a biological environment, followed by the cases of monomers (mainly amino acids), and then of the corresponding polymers, peptides and nucleic acid related biomolecules (section 9). The adsorption of other molecules, which are not rigorously biomolecules, has also been addressed in section 9, because their behaviors mimic that of residues to be found in real proteins. From the methodological point of view, only methods able to properly handle relatively weak intermolecular interactions should be adopted. Because the interaction of biomolecules with silica surfaces is driven by H-bond and dispersion forces, this excludes DFT methods based on standard GGA functionals because they completely miss the dispersion component of the interaction. Also, care should be exerted when choosing a specific functional because those based on Perdew formulation of the exchange (PBE, PW91) tend to give too long OH bond length. Functionals based on the Becke formulation of the exchange (BLYP, BP86) or even hybrid ones (B3LYP) when coupled to empirical corrections to recover dispersion interactions, as suggested recently, have been shown to provide a more balanced behavior. As a perspective, semiempirical methods based on the new PM7 method, which includes H-bond and dispersion corrections, appear to be very promising. Because semiempirical methods favorably scales with the system size, we look forward to seeing new applications in the silica/biomolecules context. The main "take home message" from the results of section 9 is that computer simulation can provide excellent support to experimental interpretation providing that adsorption is carried out at the gas/solid interface. In the particular case of amino acids, this is indeed feasible, because they sublime without decomposing and can be condensed on well-defined silica surfaces; few teams have studied such experimental setups until now, however. The situation is much more intricate when experiments envisage adsorption from water solution. In this case, the adsorption is strongly pH-dependent because both the silica surface and the amino acids change their protonation state accordingly, greatly affecting the sign of the electrostatic

interaction. More precisely, pH values higher than the point of zero charge of silica surfaces will cause deprotonation of SiOH groups with dramatic consequences for the adsorption of amino acids. The latter also exhibit different charge speciations (between zwitterionic, anionic, and cationic forms) as a function of their pK_a values; according to this speciation, they undergo strong electrostatic interactions (attraction or repulsion, as the case may be) with the silica surface, which often dominate the adsorption energetics. Carrying out adsorption from water solutions is experimentally less complex than from the gas phase: the opposite is true for the modeling approach. There, the need to account for the presence of significant amounts of water in order to bring the system to be stabilized in a different protonation state compared with the canonical forms in gas phase renders the simulation a daunting task in terms of the requested computational resources. Resorting to microsolvation (few water molecules located at strategic points) is a clever idea, but the applicability of this approach should not be overstated because many of the sought properties result from the presence of a large quantity of water (entropic factors, structuring of the second solvation shell, etc.). In that respect, one of the key issue is to understand whether the (bio)molecule is directly attached to the surface functionalities or its interaction is mediated by the presence of preadsorbed water. This is not easily addressed by experiments or by simulations. Experimentally, it is hard to detect spectral features that can be unambiguously attributed to a "first layer of adsorbed water" and discriminate them from the features for bulk water, although vibrational sum frequency spectroscopy⁷²⁵ can indeed help in obtaining such data. For the latter, the relatively long residence time of a protein residue or a water molecule attached to the surface requires rather sophisticated and expensive metadynamics procedures⁷²⁶ to bring the time scale of molecular dynamics simulations down to acceptable values.

More generally, there are not many techniques that allow characterization of *in situ* molecules at "buried interfaces", including the silica/solution interface. An extensive review of these techniques, concerning solid/solution interfaces in general, has recently appeared; a significant number of the examples provided concern biomolecule adsorption, but mostly their application is not yet routine.⁷²⁷

Gathering precise experimental data on even a single biomolecule/silica system is a long, protracted endeavor. It can be seen from section 9 that only for the simplest amino acid has the amount of experimental data reached a "critical mass" where systematic comparisons between experiment and theory become fruitful, and even in the case of glycine/silica, many experimental data are still missing. On the other hand, the progress of spectroscopic techniques (especially vibrational and NMR) now allows us to reach an unprecedented level of detail in the molecular characterization of adsorbed biomolecules. If close cooperation of experimentalists and theoreticians on well-focused systems can be undertaken, future progress could be fast.

During the search for papers focusing on the present topic, we discovered that nothing has been done to model the interaction of DNA bases with silica, while few works have appeared addressing their interactions with montmorillonites.^{412,728} The same is also true for studies dealing with phospholipids as a model of cell membranes in which only one paper has been published.⁷²⁹ Both fields should be explored in depth, among other reasons because of the importance of DNA

in developing nanodevices within a bottom-up approach.⁷³⁰ For instance, in a way similar to nanolithography, one could pattern ordered DNA to the desired positions on a substrate that includes hydrophilicity and covalent attachment as provided by silica surfaces.⁷³¹ On the other hand, cell membranes are the main “contact surfaces” between a living organism and a biomaterial and, as a perspective, we believe that understanding the process of membrane lipid adhesion is key to ultimately improve the design of biocompatible materials.⁷³² Despite the difficulties described above, we are confident that new technological improvements in the high-performance computing machines, as well as in experimental methods will widen our possibility to address problems in the “biological surface science”⁷³³ context, like understanding how conformational changes are induced in peptides by adsorption at oxides surface or better drug protection and delivery using mesoporous materials, to mention just two of them. Hopefully, these basic research advances will provide the grounds and the driving force needed for rapid developments in a wide range of applications including tissue engineering, biosensors, drug delivery, and medical diagnosis.

AUTHOR INFORMATION

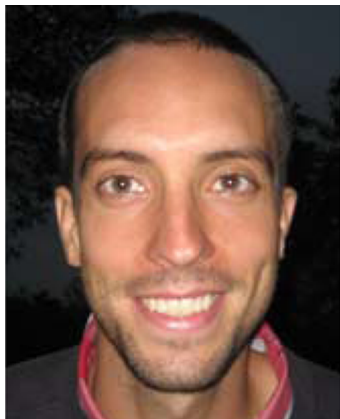
Corresponding Author

*E-mail: piero.ugliengo@unito.it.

Notes

The authors declare no competing financial interest.

Biographies



Dr. Albert Rimola received his B.S. in Chemistry from the Autonomous University of Barcelona (UAB), where he completed in 2007 his Ph.D. in Theoretical and Computational Chemistry under the supervision of Prof. Mariona Sodupe addressed to metal ion gas phase chemistry. He continued his studies as a postdoctoral researcher at the University of Torino for two years with Prof. Piero Ugliengo, focusing his research on modeling the interaction and reactivity of biomolecules with inorganic biomaterials. In 2010, he returned to UAB to work on chemical processes of prebiotic interest, focused in more detail on gas-grain astrochemical processes. He is co-author of 36 papers in peer-reviewed international journals.



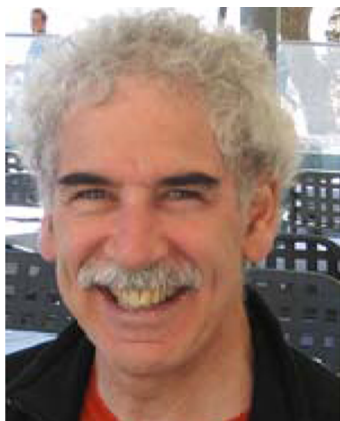
Dr. Dominique Costa obtained her Ph.D. in 1989 in UPMC, Paris. After a postdoctoral stay at University of Torino, where she focused on silica surface reactivity, she entered CNRS at Laboratoire de Physico-Chimie des Surfaces, LPCS, Paris, where she specialized in XPS analysis for corrosion resistance and biomolecules adsorption. From 1997, she converted to ab initio calculations, and since then, she studies the reactivity of functional surfaces of interest for catalysis (at Laboratoire de Réactivité de Surfaces and Institut Français du Pétrole), biointerfaces (at LRS and LPCS), or corrosion resistance (at LPCS) and is now developing solid–liquid interface ab initio studies. She is co-author of 60 papers in peer-reviewed international journals.



Prof. Mariona Sodupe received her Ph.D. in Chemistry from the Autonomous University of Barcelona (UAB) in 1990. Then she continued her studies as postdoctoral researcher at NASA Ames Research Center (California) for two years. In 1992, she returned to UAB where she is now full professor in the Department of Chemistry. Current research areas of interest are metal–ligand systems of biological interest and surface properties of silica-based materials. Recent projects focus on the role of mineral surfaces in prebiotic chemistry. She is co-author of 145 papers in peer-reviewed international journals.



Prof. Jean-François Lambert obtained a Ph.D. from the UCL (Louvain-la-Neuve) in 1987. He spent 2 years as a postdoctoral associate at the University of Wisconsin (Milwaukee) and another year at the Soil Science laboratory at the INRA-Versailles. He joined the LRS (Laboratory for Surface Reactivity) at the UPMC in 1990 and worked on the rationalization of supported catalysts synthesis with M. Che. In 2004, after obtaining a full professorship, he founded the research group on “interfaces in biological environments” with C.-M. Pradier. His current research interests include biocompatibility, hybrid materials, and prebiotic chemistry.



Prof. Piero Ugliengo graduated in chemistry from the University of Torino where he is associate professor of physical chemistry. His main collaborations are at Daresbury Laboratory (U.K.), Humboldt University of Berlin (DE), Universitat Autònoma de Barcelona (ES), and UPMC Paris (FR). The main scientific interests are on ab initio modeling of hydrogen-bond interactions in solids and at their surfaces with focus on silica and zeolites. Recent interests are on modeling the role of minerals in prebiotic chemistry and adsorption of biomolecules at the surface of inorganic biomaterials. He is co-author of 180 papers in peer-reviewed international journals.

ACKNOWLEDGMENTS

Part of the Introduction and section 2 have been derived from the Ph.D. thesis by Federico Musso, “Theoretical Study of the surface properties of crystalline and amorphous silica polymorphs”, 2011, Universitat Autònoma de Barcelona and University of Torino. P.U. is grateful to the Ministerio de Educacion Cultura y Deporte del Gobierno de España for supporting his stage (SAB2011-0033) at the UAB during the writing of this review and to Progetti di Ricerca di Ateneo-Compagnia di San Paolo-2011-Linea 1A, progetto ORTO11RRTS for funding. Fruitful discussion and support with Dr. M. Corno and M. Delle Piane of the Dipartimento di

Chimica, Università di Torino, are also acknowledged. P.U. acknowledges the invaluable and continuous scientific support provided by Prof. Vera Bolis on silica topics. Many of the results reported in this review would have not been possible without allowance of the massive parallel version of the CRYSTAL09 code provided by the Theoretical Chemistry group at Dipartimento di Chimica, Università di Torino. M.S. gratefully acknowledges support through 2011 ICREA Academia award. Financial support from MICINN and the DIUE of the Generalitat de Catalunya through the CTQ2011-24847/BQU and 2009SGR638 projects, respectively, is also acknowledged. A.R. is indebted to Ministerio de Economía y Competitividad for a Juan de la Cierva contract. The authors are also grateful to Prof. Lucio Colombi Ciacchi (University of Bremen) for providing the coordinates of the amorphous silica surface from which Figure 20 has been made and Prof. G. Magnacca (University of Turin) for IR spectra of Figure 9. D.C. thanks B. Diawara for graciously providing the Modelview software, which has allowed the construction and analyses of some data reported here. D.C. and J.F.L. thank Frederik Tielens for discussion on many aspects of amorphous silica models.

REFERENCES

- (1) Brown, G. E.; Henrich, V. E.; Casey, W. H.; Clark, D. L.; Eggleston, C.; Felmy, A.; Goodman, D. W.; Grätzel, M.; Maciel, G.; McCarthy, M. I.; Nealson, K. H.; Sverjensky, D. A.; Toney, M. F.; Zachara, J. M. *Chem. Rev.* **1999**, *99*, 77.
- (2) Clayton, D. C. *Principles of Stellar Evolution and Nucleosynthesis*; The University of Chicago Press: Chicago, IL, 1983.
- (3) Iler, R. K. *The Chemistry of Silica*, 2nd ed.; John Wiley & Sons, Inc.: New York, Chichester, Brisbane, Toronto, 1979.
- (4) *The Surface Properties of Silica*; Legrand, A. P., Ed.; John Wiley & Sons: Chichester, 1998.
- (5) *Adsorption on Silica Surfaces*; Papirer, E., Ed.; Marcel Dekker Inc.: New York, 2000; Vol. 90.
- (6) El Shafei, G. M. S. In *Adsorption on Silica Surfaces*; Papirer, E., Ed.; CRC Press, Taylor & Francis Group: Santa Barbara, CA, 2000; Vol. 90, p 35.
- (7) Morrow, B. A.; Gay, I. D. In *Adsorption on Silica Surfaces*; Papirer, E., Ed.; CRC Press, Taylor & Francis Group: Santa Barbara, CA, 2000; Vol. 90, p 9.
- (8) Davydov, V. Y. In *Adsorption on Silica Surfaces*; Papirer, E., Ed.; CRC Press, Taylor & Francis Group: : Santa Barbara, CA, 2000; Vol. 90, p 63.
- (9) *Characterization and Chemical Modification of the Silica Surface*; Vansant, E. F., van der Voort, P., Vrancken, K. C., Eds.; Elsevier Science B.V.: Amsterdam, 1995; Vol. 93.
- (10) Vallee, A.; Humblot, V.; Pradier, C. M. *Acc. Chem. Res.* **2010**, *43*, 1297.
- (11) Nawrocki, J. *J. Chromatogr. A* **1997**, *779*, 29.
- (12) Hench, L. L.; Splinter, R. J.; Allen, W. C.; Greenlee, T. K. *J. Biomed. Mater. Res. Symp.* **1971**, *2*, 117.
- (13) Hench, L. L. *Sol-Gel Silica. Properties, Processing and Technology Transfer*; Noyes Publications: Westwood, NJ, 1998.
- (14) Colla, M.; Izquierdo-Barba, I.; Vallet-Regí, M. *Expert Opin. Ther. Pat.* **2008**, *18*, 639.
- (15) Vallet-Regí, M.; Balas, F.; Arcos, D. *Angew. Chem., Int. Ed.* **2007**, *46*, 7548.
- (16) Barbe, C.; Bartlett, J.; Kong, L. G.; Finnie, K.; Lin, H. Q.; Larkin, M.; Calleja, S.; Bush, A.; Calleja, G. *Adv. Mater.* **2004**, *16*, 1959.
- (17) Vallet-Regí, M.; Rámila, A.; del Real, R. P.; Pérez-Pariente, J. *Chem. Mater.* **2001**, *13*, 308.
- (18) Castner, D. G.; Ratner, B. D. *Surf. Sci.* **2002**, *500*, 28.
- (19) Lai, C. Y.; Trewyn, B. G.; Jeftinija, D. M.; Jeftinija, K.; Xu, S.; Jeftinija, S.; Lin, V. S.-Y. *J. Am. Chem. Soc.* **2003**, *125*, 4451.
- (20) Slowing, I.; Trewyn, B. G.; Lin, V. S.-Y. *J. Am. Chem. Soc.* **2006**, *128*, 14792.

- (21) Fubini, B. In *The Surface Properties of Silicas*; Legrand, A. P., Ed.; John Wiley & Sons: West Sussex, U.K., 1998; pp 415–458.
- (22) Fubini, B. *Ann. Occup. Hyg.* **1998**, *42*, 521.
- (23) Fubini, B.; Otero Areán, C. *Chem. Soc. Rev.* **1999**, *28*, 373.
- (24) Merget, R.; Bauer, T.; Kupper, H. U.; Philippou, S.; Bauer, H. D.; Breitstadt, R.; Bruening, T. *Arch. Toxicol.* **2002**, *75*, 625.
- (25) Groppo, E.; Lamberti, C.; Bordiga, S. S., G.; Zecchina, A. *Chem. Rev.* **2005**, *105*, 115.
- (26) Shahriari, M. R. In *Optical Fiber Sensors Technology*; Grattan, K. T. V., Meggitt, B. T., Eds.; Kluwer Academic: Dordrecht, the Netherlands, 1999; Vol. 4.
- (27) Cho, E. J.; Bright, F. V. *Anal. Chem.* **2001**, *73*, 3289.
- (28) Shughart, E. L.; Ahsan, K.; Detty, M. R.; Bright, F. V. *Anal. Chem.* **2006**, *78*, 3165.
- (29) Lichtenstein, L.; Buchner, C.; Yang, B.; Shaikhutdinov, S.; Heyde, M.; Sierka, M.; Włodarczyk, R.; Sauer, J.; Freund, H. J. *Angew. Chem., Int. Ed.* **2012**, *51*, 404.
- (30) Berman, H. M.; Westbrook, J.; Feng, Z.; Gilliland, G.; Bhat, T. N.; Weissig, H.; Shindyalov, I. N.; Bourne, P. E. *Nucleic Acids Res.* **2000**, *28*, 235.
- (31) *Water in Biomaterials Surface Science*; Morra, M., Ed.; John Wiley & Sons Ltd: Chichester, 2001.
- (32) Young, G. J. *J. Colloid Sci.* **1958**, *13*, 67.
- (33) Morrow, B. A.; Cody, I. A.; Lee, L. S. M. *J. Phys. Chem.* **1976**, *80*, 2761.
- (34) Blum, J.; Avnir, D. In *Handbook of Sol-Gel Science and Technology*; Sakka, S., Ed.; Springer: New York, 2003; Vol. III.
- (35) Pagliaro, M. *Silica-Based Materials for Advanced Chemical Applications*; RSC Publishing: Cambridge, U.K., 2009.
- (36) Corno, M.; Rimola, A.; Bolis, V.; Ugliengo, P. *Phys. Chem. Chem. Phys.* **2010**, *12*, 6309.
- (37) Tilcock, A. *Proc. - R. Soc. Edinburgh, Sect. A: Math. Phys. Sci.* **2009**, *465*, 1003.
- (38) Knözinger, H. In *The Hydrogen Bond. Recent Developments in Theory and Experiments*; Schuster, P., Zundel, G., Sandorfy, C., Eds.; North-Holland: Amsterdam, 1976; Vol. 3, p 1263.
- (39) Sauer, J.; Ugliengo, P.; Garrone, E.; Saunders, V. R. *Chem. Rev.* **1994**, *94*, 2095.
- (40) Burneau, A.; Gallas, J. P. In *The Surface Properties of Silicas*; Legrand, A. P., Ed.; John Wiley & Sons: Chichester, 1998; pp 145–234.
- (41) Zachariasen, W. H. *J. Am. Chem. Soc.* **1932**, *54*, 3841.
- (42) Bruckner, R. *Encycl. Appl. Phys.* **1997**, *18*, 101.
- (43) Catlow, C. R. A.; Cormack, A. N. *Int. Rev. Phys. Chem.* **1987**, *6*, 227.
- (44) Chao, E. C. T.; Shoemaker, E. M.; Madsen, B. M. *Science* **1960**, *132*, 220.
- (45) Stishov, S. M.; Popova, S. V. *Geokhimiya* **1961**, *10*, 837.
- (46) Ross, N. L.; Shu, J.-F.; Hazen, R. M. *Am. Mineral.* **1990**, *75*, 739.
- (47) Nicholas, J. B.; Winans, R. E.; Harrison, R. J.; Iton, L. E.; Curtiss, L. A.; Hopfinger, A. J. *J. Phys. Chem.* **1992**, *96*, 7958.
- (48) Bär, M. R.; Sauer, J. *Chem. Phys. Lett.* **1994**, *226*, 405.
- (49) Luke, B. T. *J. Phys. Chem.* **1993**, *97*, 7505.
- (50) Tielens, F.; De Proft, F.; Geerlings, P. *J. Mol. Struct. THEOCHEM* **2001**, *542*, 227.
- (51) West, R.; Whatley, L. S.; Lake, K. J. *J. Am. Chem. Soc.* **1961**, *83*, 761.
- (52) Baerlocher, C.; McCusker, L. B. Database of Zeolite Structures. <http://www.iza-structure.org/databases/>.
- (53) *Diffusion Mechanisms in Crystalline Materials*; Catlow, C. R. A., Cowern, N. E. B., Farkas, D., Mishin, Y., Eds.; Material Research Society: Warrendale, PA, 1999; Vol. 527.
- (54) *Computer Modelling of Microporous Materials*; Catlow, C. R. A., van Santen, R. A., Smit, B., Eds.; Elsevier Ltd.: London, 2004.
- (55) Weiss, A.; Weiss, A. Z. *Anorg. Allg. Chem.* **1954**, *276*, 95.
- (56) Hamann, D. R. *Phys. Rev. B* **1997**, *55*, 14784.
- (57) Sing, K. S. W. *Pure Appl. Chem.* **1985**, *57*, 603.
- (58) Brunauer, S.; Emmett, P. H.; Teller, E. *J. Am. Chem. Soc.* **1938**, *60*, 309.
- (59) Avnir, D.; Farin, D. *Nature* **1984**, *308*, 261.
- (60) Hench, L. L.; Ulrich, D. B. *Ultrastructure Processing of Ceramics Glasses and Composites*; Wiley: New York, 1984.
- (61) Depradel, A. C.; Imelik, B. C. *R. Hebd. Seances Acad. Sci.* **1956**, *242*, 122.
- (62) Kresge, C. T.; Leonowicz, M. E.; Roth, W. J.; Vartuli, J. C.; Beck, J. S. *Nature* **1992**, *359*, 710.
- (63) Beck, J. S.; Vartuli, J. C.; Roth, W. J.; Leonowicz, M. E.; Kresge, C. T.; Schmitt, K. D.; Chu, C. T.-W.; Olson, D. H.; Sheppard, E. W.; McCullen, S. B.; Higgins, J. B.; Schlenker, J. L. *J. Am. Chem. Soc.* **1992**, *114*, 10834.
- (64) Hatton, B.; Landskron, K.; Whitnall, W.; Perovic, D.; Ozin, G. A. *Acc. Chem. Res.* **2005**, *38*, 305.
- (65) Ehrlich, H.; Demadis, K. D.; Pokrovsky, O. S.; Koutsoukos, P. G. *Chem. Rev.* **2010**, *110*, 4656.
- (66) Dickerson, M. B.; Sandhage, K. H.; Naik, R. R. *Chem. Rev.* **2008**, *108*, 4935.
- (67) D'Souza, A. S.; Pantano, C. G. *J. Am. Ceram. Soc.* **1999**, *82*, 1289.
- (68) Li, I.; Bandara, J.; Shultz, M. J. *Langmuir* **2004**, *20*, 10474.
- (69) Zhou, F.; Head, J. D. *J. Phys. Chem. B* **2000**, *104*, 9981.
- (70) Mondal, B.; Ghosh, D.; Das, A. K. *Chem. Phys. Lett.* **2009**, *478*, 115.
- (71) Eyre, R. J.; Goss, J. P.; Macleod, R. M.; Briddon, P. R. *Phys. Chem. Chem. Phys.* **2008**, *10*, 4495.
- (72) Maciel, G. E.; Sindorf, D. W. *J. Am. Chem. Soc.* **1980**, *102*, 7606.
- (73) Tarini, M.; Cignoni, P.; Montani, C. *IEEE Trans. Vis. Comput. Graph.* **2006**, *12*, 1237.
- (74) Rimola, A.; Tosoni, S.; Sodupe, M.; Ugliengo, P. *ChemPhysChem* **2006**, *7*, 157.
- (75) Rimola, A.; Ugliengo, P. *J. Chem. Phys.* **2008**, *128*, 204702.
- (76) Mathias, J.; Wannemacher, G. *J. Colloid Interface Sci.* **1988**, *125*, 61.
- (77) Zhuravlev, L. T.; Potapov, V. V. *Russ. J. Phys. Chem.* **2006**, *80*, 1119.
- (78) Zhuravlev, L. T. *Colloids Surf., A* **2000**, *173*, 1.
- (79) Zhuravlev, L. T. *Colloids Surf., A* **1993**, *74*, 71.
- (80) Zhuravlev, L. T. *Langmuir* **1987**, *3*, 316.
- (81) Bolis, V.; Cavenago, A.; Fubini, B. *Langmuir* **1997**, *13*, 895.
- (82) Bolis, V.; Fubini, B.; Marchese, L.; Martra, G.; Costa, D. *J. Chem. Soc., Faraday Trans.* **1991**, *87*, 497.
- (83) Trebosc, J.; Wiench, J. W.; Huh, S.; Lin, V. S. Y.; Pruski, M. *J. Am. Chem. Soc.* **2005**, *127*, 3057.
- (84) Landmesser, H.; Kossheck, H.; Storek, W.; Fricke, R. *Solid State Ionics* **1997**, *101–103*, 271.
- (85) Jal, P. K.; Sudarshan, M.; Saha, A.; Patel, S.; Mishra, B. K. *Colloids Surf., A* **2004**, *240*, 173.
- (86) Lesnichin, S. B.; Kamdem, N.; Mauder, D.; Denisov, G. S.; Shenderovich, I. G. *Russ. J. Gen. Chem.* **2010**, *80*, 2027.
- (87) Taylor, D. E.; Runge, K.; Cory, M. G.; Burns, D. S.; Vasey, J. L.; Hearn, J. D.; Henley, M. V. *J. Phys. Chem. C* **2011**, *115*, 24734.
- (88) Chuang, I. S.; Maciel, G. E. *J. Phys. Chem. B* **1997**, *101*, 3052.
- (89) Bolt, G. H. *J. Phys. Chem.* **1957**, *61*, 1166.
- (90) Abendroth, R. P. *J. Colloid Interface Sci.* **1970**, *34*, 591.
- (91) Duval, Y.; Mielczarski, J. A.; Pokrovsky, O. S.; Mielczarski, E.; Ehrhardt, J. J. *J. Phys. Chem. B* **2002**, *106*, 2937.
- (92) Sverjensky, D. A.; Sahai, N. *Geochim. Cosmochim. Acta* **1998**, *62*, 3703.
- (93) Dixit, S.; Van Cappellen, P. *Geochim. Cosmochim. Acta* **2002**, *66*, 2559.
- (94) Hiemstra, T.; DeWit, J. C. M.; VanRiemsdijk, W. H. *J. Colloid Interface Sci.* **1989**, *133*, 91.
- (95) Schwarz, J. A. *J. Colloid Interface Sci.* **1999**, *218*, 1.
- (96) Ong, S. W.; Zhao, X. L.; Eisenthal, K. B. *Chem. Phys. Lett.* **1992**, *191*, 327.
- (97) Ostroverkhov, V.; Waychunas, G. A.; Shen, Y. R. *Phys. Rev. Lett.* **2005**, *94*, No. 046102.
- (98) Schnippering, M.; Neil, S. R. T.; Mackenzie, S. R.; Unwin, P. R. *Chem. Soc. Rev.* **2011**, *40*, 207.

- (99) O'Reilly, J. P.; Butts, C. P.; I'Anson, I. A.; Shaw, A. M. *J. Am. Chem. Soc.* **2005**, *127*, 1632.
- (100) Fisk, J. D.; Batten, R.; Jones, G.; O'Reilly, J. P.; Shaw, A. M. *J. Phys. Chem. B* **2005**, *109*, 14475.
- (101) Fan, H.-F.; Li, F.; Zare, R. N.; Lin, K.-C. *Anal. Chem.* **2007**, *79*, 3654.
- (102) Hiemstra, T.; Venema, P.; VanRiemsdijk, W. H. *J. Colloid Interface Sci.* **1996**, *184*, 680.
- (103) Bickmore, B. R.; Tadanier, C. J.; Rosso, K. M.; Monn, W. D.; Eggett, D. L. *Geochem. Cosmochim. Acta* **2004**, *68*, 2025.
- (104) Machesky, M. L.; Predota, M.; Wesolowski, D. J.; Vlcek, L.; Cummings, P. T.; Rosenqvist, J.; Ridley, M. K.; Kubicki, J. D.; Bandura, A. V.; Kumar, N.; Sofo, J. O. *Langmuir* **2008**, *24*, 12331.
- (105) Churchill, H.; Teng, H.; Hazen, R. M. *Am. Mineral.* **2004**, *89*, 1048.
- (106) Alexander, G. B.; Iler, R. K. *J. Phys. Chem.* **1953**, *57*, 932.
- (107) Sonnenfeld, J. *J. Colloid Interface Sci.* **1996**, *183*, 597.
- (108) Behrens, S. H.; Grier, D. G. *J. Chem. Phys.* **2001**, *115*, 6716.
- (109) Charlet, L.; Schindler, P. W.; Spadini, L.; Furrer, G.; Zyss, M. *Aquat. Sci.* **1993**, *55*, 291.
- (110) Sahai, N.; Sverjensky, D. A. *Geochem. Cosmochim. Acta* **1997**, *61*, 2801.
- (111) Foissy, A.; Persello, J. In *The Surface Properties of Silicas*; Legrand, A. P., Ed.; J. Wiley & Sons: Chichester, 1998; pp 147–234.
- (112) Marmier, N.; Delisée, A.; Fromage, F. *J. Colloid Interface Sci.* **1999**, *212*, 228.
- (113) Turov, V. V.; Leboda, R.; Bogillo, V. I.; Skubiszewska-Zieba, J. *Langmuir* **1997**, *13*, 1237.
- (114) Turov, V. V.; Mironyuk, I. F. *Colloids Surf, A* **1998**, *134*, 257.
- (115) Morrow, B. A.; McFarlan, A. J. *Langmuir* **1991**, *7*, 1695.
- (116) Kamiya, H.; Mitsui, M.; Takano, H.; Miyazawa, S. *J. Am. Ceram. Soc.* **2000**, *83*, 287.
- (117) Bolis, V.; Busco, C.; Bordiga, S.; Ugliengo, P.; Lamberti, C.; Zecchina, A. *Appl. Surf. Sci.* **2002**, *196*, 56.
- (118) Hoffmann, P.; Knozinger, E. *Surf. Sci.* **1987**, *188*, 181.
- (119) McFarlan, A. J.; Morrow, B. A. *J. Phys. Chem.* **1991**, *95*, 5388.
- (120) Takei, T.; Kato, K.; Meguro, A.; Chikazawa, M. *Colloids Surf, A* **1999**, *150*, 77.
- (121) Bocuzzi, F.; Coluccia, S.; Ghilotti, G.; Morterra, C.; Zecchina, A. *J. Phys. Chem.* **1978**, *22*, 1298.
- (122) Queeney, K. T.; Weldon, M. K.; Chang, J. P.; Chabal, Y. J.; Gurevich, A. B.; Sapjeta, J.; Opila, R. L. *J. Appl. Phys.* **2000**, *87*, 1322.
- (123) Queeney, K. T.; Herbots, N.; Shaw, J. M.; Atluri, V.; Chabal, Y. *J. Appl. Phys. Lett.* **2004**, *84*, 493.
- (124) Olsen, J. E.; Shimura, F. *Appl. Phys. Lett.* **1988**, *53*, 1934.
- (125) Nagai, N.; Hashimoto, H. *Appl. Surf. Sci.* **2001**, *172*, 307.
- (126) Pasternack, R. M.; Rivillon Amy, S.; Chabal, Y. *J. Langmuir* **2008**, *24*, 12963.
- (127) Kim, J.; Seidler, P.; Fill, C.; Wan, L. S. *Surf. Sci.* **2008**, *602*, 3323.
- (128) Kim, J.; Seidler, P.; Wan, L. S.; Fill, C. *J. Colloid Interface Sci.* **2009**, *329*, 114.
- (129) Kim, J.; Cho, J.; Seidler, P. M.; Kurland, N. E.; Yadavalli, V. K. *Langmuir* **2010**, *26*, 2599.
- (130) Aissaoui, N.; Bergaoui, L.; Landoulsi, J.; Lambert, J.-F.; Boujday, S. *Langmuir* **2012**, *28*, 656.
- (131) Brinker, C. J.; Brow, R. K.; Tallant, D. R. *J. Non-Cryst. Solids* **1990**, *120*, 26.
- (132) Maniar, P. D.; Navrotsky, A. *J. Non-Cryst. Solids* **1990**, *120*, 20.
- (133) Humbert, B.; Burneau, A.; Gallas, J. P.; Lavalle, J. C. *J. Non-Cryst. Solids* **1992**, *143*, 75.
- (134) Riegel, J. o. N.-C. S.; Hartmann, I.; Kiefer, W.; Gross, J.; Fricke, J. *J. Non-Cryst. Solids* **1997**, *211*, 294.
- (135) Wallace, S.; West, J. K.; Hench, L. L. *J. Non-Cryst. Solids* **1993**, *152*, 101.
- (136) Chakoumakos, B. C.; Hill, R. J.; Gibbs, G. V. *Am. Mineral.* **1981**, *66*, 1237.
- (137) Morrow, B. A.; Cody, I. A. *J. Phys. Chem.* **1976**, *80*, 1995.
- (138) Michalske, T. A.; Bunker, B. C. *J. Appl. Phys.* **1984**, *56*, 2686.
- (139) Bunker, B. C.; Haaland, D. M.; Ward, K. J.; Michalske, T. A.; Smith, W. L.; Binkley, J. S.; Melius, C. F.; Balfe, C. A. *Surf. Sci.* **1989**, *210*, 406.
- (140) Grabbe, A.; Michalske, T. A.; Smith, W. L. *J. Phys. Chem.* **1995**, *99*, 4648.
- (141) Inaki, Y.; Yoshida, H.; Yoshida, T.; Hattori, T. *J. Phys. Chem. B* **2002**, *106*, 9098.
- (142) Chiang, C.-M.; Zegarski, B. R.; Dubois, L. H. *J. Phys. Chem.* **1993**, *97*, 6948.
- (143) Zarubin, D. P. *J. Non-Cryst. Solids* **2001**, *286*, 80.
- (144) West, J. K.; LaTorre, G.; Hench, L. L. *J. Non-Cryst. Solids* **1996**, *195*, 45.
- (145) Engelhardt, G.; Michel, D. *High Resolution Solid State NMR of Silicates and Zeolites*; Wiley & Sons: New York, 1987.
- (146) Boujday, S. Ph.D. Thesis, UPMC Paris 6, 2002.
- (147) Zhao, H.; Chen, Q.; Zhang, S. *Microporous Mesoporous Mater.* **2012**, *155*, 240.
- (148) Rossini, A. J.; Zagdoun, A.; Lelli, M.; Gajan, D.; Rascon, F.; Rosay, M.; Maas, W. E.; Coperet, C.; Lesage, A.; Emsley, L. *Chem. Sci.* **2012**, *3*, 108.
- (149) Spearing, D. R.; Farnan, I.; Stebbins, J. F. *Phys. Chem. Miner.* **1992**, *19*, 307.
- (150) van Eck, E. R. H.; Smith, M. E.; Kohn, S. C. *Solid State Nucl. Magn. Reson.* **1999**, *15*, 181.
- (151) Hu, J. Z.; Kwak, J. H.; Herrera, J. E.; Wang, Y.; Peden, C. H. F. *Solid State Nucl. Magn. Reson.* **2005**, *27*, 200.
- (152) d'Espinose de la Caillerie, J.-B.; Aimeur, M. R.; Kortobi, Y. E.; Legrand, A. P. *J. Colloid Interface Sci.* **1997**, *197*, 434.
- (153) Liu, C. H. C.; Maciel, G. E. *J. Am. Chem. Soc.* **1996**, *118*, 5103.
- (154) Hughes, C. E. *Prog. Nucl. Magn. Reson. Spectrosc.* **2004**, *45*, 301.
- (155) Baum, J.; Munowitz, M.; Garroway, A. N.; Pines, A. *J. Chem. Phys.* **1985**, *83*, 2015.
- (156) Hwang, S.-J.; Uner, D. O.; King, T. S.; Pruski, M.; Gerstein, B. C. *J. Phys. Chem.* **1996**, *99*, 3697.
- (157) Shantz, D. F.; Schmedt auf der Günne, J.; Koller, H.; Lobo, R. F. *J. Am. Chem. Soc.* **2000**, *122*, 6659.
- (158) Fubini, B.; Giannello, E.; Volante, M.; Bolis, V. *Toxicol. Ind. Health* **1990**, *6*, 571.
- (159) Stathis, J. H.; Kastner, M. A. *Phys. Rev. B* **1984**, *29*, 7079.
- (160) Pacchioni, G.; Vitiello, M. *J. Non-Cryst. Solids* **1999**, *245*, 175.
- (161) Mashkovtsev, R. I.; Pan, Y. M. *Phys. Chem. Miner.* **2012**, *39*, 79.
- (162) Buscarino, G.; Vaccaro, G.; Agnello, S.; Gelardi, F. M. *J. Non-Cryst. Solids* **2009**, *355*, 1092.
- (163) Feng, P. B.; Wang, Y.; Rong, X.; Su, J. H.; Ju, C. Y.; Du, J. F. *Phys. Lett. A* **2012**, *376*, 2195.
- (164) Romanelli, M.; Di Benedetto, F.; Bartali, L.; Innocenti, M.; Fornaciai, G.; Montegrossi, G.; Pardi, L. A.; Zoleo, A.; Capacci, F. *Phys. Chem. Miner.* **2012**, *39*, 479.
- (165) Fenoglio, I.; Fubini, B.; Ghibaudo, E. M.; Turci, F. *Adv. Drug Delivery Rev.* **2011**, *63*, 1186.
- (166) Zelenak, V.; Zelenakova, A.; Kovac, J. *Colloids Surf, A* **2010**, *357*, 97.
- (167) Lercher, J. A.; Grundling, C.; EderMirth, G. *Catal. Today* **1996**, *27*, 353.
- (168) Marchese, L.; Gianotti, E.; Maschmeyer, T.; Martra, G.; Coluccia, S.; Thomas, J. *Nuovo Cimento D* **1997**, *19*, 1707.
- (169) Armandi, M.; Bolis, V.; Bonelli, B.; Arean, C. O.; Ugliengo, P.; Garrone, E. *J. Phys. Chem. C* **2011**, *115*, 23344.
- (170) Bonelli, B.; Cozzolino, M.; Tesser, R.; Di Serio, M.; Piumetti, M.; Garrone, E.; Santacesaria, E. *J. Catal.* **2007**, *246*, 293.
- (171) Parry, E. P. *J. Catal.* **1963**, *2*, 371.
- (172) Trombetta, M.; Busca, G.; Rossini, S.; Piccoli, V.; Cornaro, U.; Guercio, A.; Catani, R.; Willey, R. *J. Catal.* **1998**, *179*, 581.
- (173) Fubini, B.; Bolis, V.; Cavenago, A.; Garrone, E.; Ugliengo, P. *Langmuir* **1993**, *9*, 2712.
- (174) Borello, E.; Zecchina, A.; Morterra, C. *J. Phys. Chem.* **1967**, *71*, 2938.
- (175) Borello, E.; Zecchina, A.; Morterra, C. *J. Phys. Chem.* **1967**, *71*, 2945.

- (176) Natal-Santiago, M. A.; Dumesic, J. A. *J. Catal.* **1998**, *175*, 252.
- (177) Luts, T.; Katz, A. *Top. Catal.* **2012**, *55*, 84.
- (178) Bunker, B. C.; Haaland, D. M.; Michalske, T. A.; Smith, W. L. *Surf. Sci.* **1989**, *222*, 95.
- (179) Natal-Santiago, M. A.; Hill, J. M.; Dumesic, J. A. *J. Mol. Catal. A* **1999**, *140*, 199.
- (180) Brunel, D.; Cauvel, A.; Di Renzo, F.; Fajula, F.; Fubini, B.; Onida, B.; Garrone, E. *New J. Chem.* **2000**, *24*, 807.
- (181) Srinivasan, S.; Datye, A. K.; Smith, M. H.; Peden, C. H. F. *J. Catal.* **1994**, *145*, 565.
- (182) Sindorf, D. W.; Maciel, G. E. *J. Phys. Chem.* **1982**, *86*, 5208.
- (183) Koltsov, S. I.; Malygin, A. A.; Volkova, A. N.; Aleskovskii, V. B. *Russ. J. Inorg. Chem.* **1973**, *47*, 988.
- (184) Fleischman, S. D.; Scott, S. L. *J. Am. Chem. Soc.* **2011**, *133*, 4847.
- (185) Dong, Y.; Pappu, S. V.; Xu, Z. *Anal. Chem.* **1998**, *70*, 4730.
- (186) Boujday, S.; Lambert, J.-F.; Che, M. *J. Phys. Chem. B* **2003**, *107*, 651.
- (187) Boujday, S.; Lambert, J.-F.; Che, M. *ChemPhysChem* **2004**, *5*, 1003.
- (188) Schroeder, T.; Adelt, M.; Richter, B.; Naschitzki, M.; Bäumer, M.; Freund, H.-J. *Surf. Rev. Lett.* **2000**, *7*, 7.
- (189) Wendt, S.; Frerichs, M.; Wei, T.; Chen, M. S.; Kempter, V.; Goodman, D. W. *Surf. Sci.* **2004**, *565*, 107.
- (190) Chen, M. S.; Santra, A. K.; Goodman, D. W. *Phys. Rev. B* **2004**, *69*, No. 155404.
- (191) Yu, X.; Yang, B.; Boscoboinik, J. A.; Shaikhutdinov, S.; Freund, H.-J. *Appl. Phys. Lett.* **2012**, *100*, No. 151608.
- (192) Mirji, S. A.; Halligudi, S. B.; Mathew, N.; Ravi, V.; Jacob, N. E.; Patil, K. R. *Colloids Surf., A* **2006**, *287*, 51.
- (193) Takahashi, T.; Fukatsu, S.; Itoh, K. M.; Uematsu, M.; Fujiwara, A.; Kageshima, H.; Takahashi, Y.; Shiraishi, K. *J. Appl. Phys.* **2003**, *93*, 3674.
- (194) Chang, C.-C.; Shu, M.-C. *J. Phys. Chem. B* **2003**, *107*, 7076.
- (195) Wu, W. L.; Wallace, W. E.; Lin, E. K.; Lynn, G. W.; Glinka, C. J.; Ryan, E. T.; Ho, H. M. *J. Appl. Phys.* **2000**, *87*, 1193.
- (196) Chiba, K.; Takenaka, Y. *Appl. Surf. Sci.* **2008**, *254*, 2534.
- (197) Chandrasekhar, V.; Boomishankar, R.; Nagendran, S. *Chem. Rev.* **2004**, *104*, 5847.
- (198) Feher, F. J.; Newman, D. A.; Walzer, J. F. *J. Am. Chem. Soc.* **1989**, *111*, 1741.
- (199) Abbenhuis, H. C. L.; Burrows, A. D.; Kooijman, H.; Lutz, M.; Palmer, M. T.; van Santen, R. A.; Spek, A. L. *Chem. Commun.* **1998**, 2627.
- (200) Dijkstra, T. W.; Duchateau, R.; van Santen, R. A.; Meetsma, A.; Yap, G. P. A. *J. Am. Chem. Soc.* **2002**, *124*, 9856.
- (201) Gun'ko, V. M.; Turov, V. V.; Zarko, V. I.; Voronin, E. F.; Tischenko, V. A.; Dudnik, V. V.; Pakhlov, E. M.; Chuiko, A. A. *Langmuir* **1997**, *13*, 1529.
- (202) Totland, C.; Steinkopf, S.; Blokhus, A. M.; Nerdal, W. *Langmuir* **2011**, *27*, 4690.
- (203) Basiuk, V. A. In *Encyclopedia of Surface and Colloid Science*; Marcel Dekker: New York, 2002; pp 277–293.
- (204) Parida, S. K.; Dash, S.; Patel, S.; Mishra, B. K. *Adv. Colloid Interface Sci.* **2006**, *121*, 77.
- (205) Lambert, J.-F. *Origins Life Evol. Biospheres* **2008**, *38*, 211.
- (206) Popat, A.; Hartono, S. B.; Stahr, F.; Liu, J.; Qiao, S. Z.; Lu, G. Q. *Nanoscale* **2011**, *3*, 2801.
- (207) Basiuk, V. A. *Surfactant Sci. Ser.* **1998**, *75*, 55.
- (208) Hartmann, M. *Chem. Mater.* **2005**, *17*, 4577.
- (209) Bolivar, J. M.; Nidetzky, B. *Langmuir* **2012**, *26*, 10040.
- (210) Meng, M.; Stievano, L.; Lambert, J.-F. *Langmuir* **2004**, *20*, 914.
- (211) Bouchoucha, M.; Jaber, M.; Onfroy, T.; Lambert, J.-F.; Xue, B. *J. Phys. Chem. C* **2011**, *115*, 21813.
- (212) Janossy, I.; Menyhard, M. *Surf. Sci.* **1974**, *25*, 647.
- (213) Clegg, M. L.; Morales de la Garza, L.; Karakatsani, S.; King, D. A.; Driver, S. M. *Top. Catal.* **2012**, *19–20*, 1429.
- (214) Vlasova, N. N.; Golovkova, L. P. *Colloid J.* **2004**, *66*, 657.
- (215) O'Connor, A. J.; Hokura, A.; Kisler, J. M.; Shimazu, S.; Stevens, G. W.; Komatsu, Y. *Sep. Purif. Technol.* **2006**, *48*, 197.
- (216) Basiuk, V. A.; Gromovoy, T. Y. *Colloids Surf., A* **1996**, *118*, 127.
- (217) Kitadai, N.; Yokoyama, T.; Nakashima, S. *J. Colloid Interface Sci.* **2009**, *329*, 31.
- (218) Paszti, Z.; Keszthelyi, T.; Hakkel, O.; Guczi, L. *J. Phys.: Condens. Matter* **2008**, *20*, No. 224014.
- (219) Barlow, S. M.; Kitching, K. J.; Haq, S.; Richardson, N. V. *Surf. Sci.* **1998**, *401*, 322.
- (220) Holinga, G. J.; York, R. L.; Onorato, R. M.; Thompson, C. M.; Webb, N. E.; Yoon, A. P.; Somorjai, G. A. *J. Am. Chem. Soc.* **2011**, *133*, 6243.
- (221) Macklin, J. W.; White, D. H. *Spectrochim. Acta A* **1985**, *41A*, 851.
- (222) Basiuk, V. A.; Gromovoy, T. Y. *React. Kinet. Catal. Lett.* **1993**, *50*, 297.
- (223) Lomenech, C.; Bery, G.; Costa, D.; Stievano, L.; Lambert, J.-F. *ChemPhysChem* **2005**, *6*, 1061.
- (224) Lopes, I.; Piao, L.; Stievano, L.; Lambert, J.-F. *J. Phys. Chem. C* **2009**, *113*, 18163.
- (225) Amitay-Rosen, T.; Kababya, S.; Vega, S. *J. Phys. Chem. B* **2009**, *113*, 6267.
- (226) Amitay-Rosen, T.; Vega, S. *Phys. Chem. Chem. Phys.* **2010**, *12*, 6763.
- (227) Ben Shir, I.; Kababya, S.; Amitay-Rosen, T.; Balazs, Y. S.; Schmidt, A. *J. Phys. Chem. B* **2010**, *114*, 5989.
- (228) Ben Shir, I.; Kababya, S.; Schmidt, A. *J. Phys. Chem. C* **2012**, *116*, 9691.
- (229) Stievano, L.; Tielen, F.; Lopes, I.; Folliet, N.; Gervais, C.; Costa, D.; Lambert, J.-F. *Cryst. Growth Des.* **2010**, *10*, 3657.
- (230) Mirau, P. A.; Naik, R. R.; Gehring, P. *J. Am. Chem. Soc.* **2011**, *133*, 18243.
- (231) Wolny, P. M.; Spatz, J. P.; Richter, R. P. *Langmuir* **2010**, *26*, 1029.
- (232) Satriano, C.; Fragala, M. E.; Forte, G.; Santoro, A. M.; La Mendola, D.; Kasemo, B. *Soft Matter* **2012**, *8*, 53.
- (233) Chen, H.; Su, X.; Neoh, K.-G.; Choe, W.-S. *Anal. Chem.* **2006**, *78*, 4872.
- (234) Phillips, D. C.; York, R. L.; Mermut, O.; McCrea, K. R.; Ward, R. S.; Somorjai, G. A. *J. Phys. Chem. C* **2007**, *111*, 255.
- (235) Mermut, O.; Phillips, D. C.; York, R. L.; McCrea, K. R.; Ward, R. S.; Somorjai, G. A. *J. Am. Chem. Soc.* **2006**, *128*, 3598.
- (236) York, R. L.; Holinga, G. J.; Somorjai, G. A. *Langmuir* **2009**, *25*, 9369.
- (237) Wei, Y.; Latour, R. A. *Langmuir* **2008**, *24*, 6721.
- (238) Thypambil, A. A.; Wei, Y.; Latour, R. A. *Langmuir* **2012**, *28*, 5687.
- (239) Landoulsi, J.; Dupres, V. *ChemPhysChem* **2011**, *12*, 1310.
- (240) Cha, P.; Krishnan, A.; Fiore, V. F.; Vogler, E. A. *Langmuir* **2008**, *24*, 2553.
- (241) Basiuk, V. A. *Russ. J. Theor. Exp. Chem.* **1990**, *26*, 89, 97 original Russian.
- (242) Basiuk, V. A.; Gromovoy, T. Y.; Glukhoy, A. M.; Golovaty, V. G. *Origins Life Evol. Biospheres* **1991**, *21*, 129.
- (243) Basiuk, V. A.; Gromovoy, T. Y.; Chuiko, A. A.; Soloshonok, V. A.; Kukhar, V. P. *Synthesis* **1992**, *5*, 449.
- (244) Basiuk, V. A.; Gromovoy, T. Y.; Khil'chevskaya, E. G. *Origins Life Evol. Biospheres* **1995**, *25*, 375.
- (245) Bujdák, J.; Rode, B. M. *React. Kinet. Catal. Lett.* **1997**, *62*, 281.
- (246) Bujdák, J.; Rode, B. M. *Origins Life Evol. Biospheres* **1999**, *29*, 451.
- (247) Stievano, L.; Yu Piao, L.; Lopes, I.; Meng, M.; Costa, D.; Lambert, J.-F. *Eur. J. Mineral.* **2007**, *19*, 321.
- (248) Kunota, L. T.; Gamero, A.; Santana Santos, A.; Granjeiro, J. M. *J. Colloid Interface Sci.* **1996**, *185*, 453.
- (249) Alaeddine, S.; Nygren, H. *Colloids Surf., B* **1996**, *6*, 71.
- (250) Vlasova, N. N. *Colloid J.* **2005**, *67*, 537.
- (251) Palit, D.; Moulik, S. P. *J. Colloid Interface Sci.* **2001**, *239*, 20.

- (252) Pizzanelli, S.; Kababya, S.; Frydman, V.; Landau, M.; Vega, S. *J. Phys. Chem. B* **2005**, *109*, 8029.
- (253) Gao, Q.; Xu, W.; Xu, Y.; Wu, D.; Sun, Y.; Deng, F.; Shen, W. *J. Phys. Chem. B* **2008**, *112*, 2261.
- (254) Goering, J.; Sah, S.; Burghaus, U.; Street, K. W., Jr. *Surf. Interface Anal.* **2008**, *40*, 1423.
- (255) Casado, C.; Castán, J.; Gracia, I.; Yus, M.; Mayoral, A. I.; Sebastián, V.; López-Ram-de-Viu, P.; Uriel, S.; Coronas, J. *Langmuir* **2012**, *28*, 6638.
- (256) Shin, J. H.; Park, S. S.; Selvaraj, M.; Ha, C.-S. *J. Porous Mater.* **2012**, *19*, 29.
- (257) Kim, J.; Desch, R. J.; Thiel, S. W.; Gulants, V. V.; Pinto, N. G. *Microporous Mesoporous Mater.* **2012**, *149*, 60.
- (258) Plekan, O.; Feyer, V.; Sutara, F.; Skála, T.; Svec, M.; Cháb, V.; Matolín, V.; Prince, K. C. *Surf. Sci.* **2007**, *603*, 1973.
- (259) Poeckh, T.; Lopez, S.; Fuller, A. O.; Solomon, M. J.; Larson, R. G. *Anal. Biochem.* **2008**, *373*, 253.
- (260) Nakanishi, K.; Sakiyama, T.; Imamura, K. *J. Biosci. Bioeng.* **2001**, *91*, 233.
- (261) Gray, J. J. *Curr. Opin. Struct. Biol.* **2004**, *14*, 110.
- (262) Lundqvist, M.; Sethson, I.; Jonsson, B.-H. *Langmuir* **2005**, *21*, 5974.
- (263) Greenfield, N. J. *Anal. Biochem.* **1996**, *235*, 1.
- (264) Giacomelli, C. E.; Bremer, M. G. E. G.; Norde, W. *J. Colloid Interface Sci.* **1999**, *220*, 13.
- (265) Xia, N.; May, C. J.; McArthur, S. L.; Castner, D. G. *Langmuir* **2002**, *18*, 4090.
- (266) Han, S.; Xu, W.; Meiwen, C.; Jiqian, W.; Xia, D.; Xu, H.; Zhao, X.; Lu, J. R. *Soft Matter* **2012**, *8*, 645.
- (267) Burkett, S. L.; Read, M. J. *Langmuir* **2001**, *17*, 5059.
- (268) Read, M. J.; Burkett, S. L. *J. Colloid Interface Sci.* **2003**, *261*, 255.
- (269) Sethuraman, A.; Vedantham, G.; Imoto, T.; Przybycien, T.; Belfort, G. *Proteins: Struct., Funct., Bioinf.* **2004**, *56*, 669.
- (270) Felsovalyi, F.; Mangiagalli, P.; Bureau, C.; Kumar, S. K.; Banta, S. *Langmuir* **2011**, *27*, 11873.
- (271) Oren, E. E.; Tamerler, C.; Sahin, D.; Hnilova, M.; Seker, U. O. S.; Sarikaya, M.; Samudrala, R. *Bioinformatics* **2007**, *23*, 2816.
- (272) Oren, E. E.; Notman, R.; Kim, I. W.; Evans, J. S.; Walsh, T. R.; Samudrala, R.; Tamerler, C.; Sarikaya, M. *Langmuir* **2010**, *26*, 11003.
- (273) Patwardhan, S. V.; Emami, F. S.; Berry, R. J.; Jones, S. E.; Naik, R. R.; Deschaume, O.; Heinz, H.; Perry, C. C. *J. Am. Chem. Soc.* **2012**, *134*, 6244.
- (274) Ikeda, T.; Kuroda, A. *Colloids Surf., B* **2011**, *85*, 359.
- (275) Dovesi, R. In *Quantum-Mechanical Ab-initio Calculation of the Properties of Crystalline Materials*; Pisani, C., Ed.; Springer: Berlin, 1996; Vol. 67, p 31.
- (276) Pisani, C. In *Quantum-Mechanical Ab-initio Calculation of the Properties of Crystalline Materials*; Pisani, C., Ed.; Springer: Berlin, 1996; Vol. 67, p 47.
- (277) Pisani, C.; Dovesi, R.; Roetti, C. In *Lecture Notes in Chemistry*; Springer-Verlag: Berlin, 1988; Vol. 48, p 193.
- (278) Bergerhoff, G.; Hundt, R.; Sievers, R.; Brown, I. D. *J. Chem. Inf. Comput. Sci.* **1983**, *23*, 66.
- (279) Giacovazzo, C.; Monaco, H. L.; Artioli, G.; Viterbo, D.; Ferraris, G.; Gilli, G.; Zanotti, G.; Catti, M. *Fundamentals of Crystallography*, 2nd ed.; Oxford University Press: New York, 2002.
- (280) Bakos, T.; Rashkeev, S. N.; Pantelides, S. T. *Phys. Rev. Lett.* **2002**, *88*, No. 055508.
- (281) Malavasi, G.; Menziani, M. C.; Pedone, A.; Segre, U. *J. Non-Cryst. Solids* **2006**, *352*, 285.
- (282) Pedone, A.; Malavasi, G.; Menziani, M. C.; Segre, U.; Cormack, A. N. *Chem. Mater.* **2008**, *20*, 4356.
- (283) Pedone, A. *J. Phys. Chem. C* **2009**, *113*, 20773.
- (284) Colombi Ciacchi, L.; Payne, M. C. *Phys. Rev. Lett.* **2005**, *95*, No. 196101.
- (285) Butenuth, A.; Moras, G.; Schneider, J.; Koleini, M.; Koppen, S.; Meissner, R.; Wright, L. B.; Walsh, T. R.; Colombi Ciacchi, L. *Phys. Status Solidi B* **2012**, *249*, 292.
- (286) Sarnthein, J.; Pasquarello, A.; Car, R. *Phys. Rev. B* **1995**, *52*, 12690.
- (287) Sarnthein, J.; Pasquarello, A.; Car, R. *Phys. Rev. Lett.* **1995**, *74*, 4682.
- (288) Haworth, R.; Mountjoy, G.; Corno, M.; Ugliengo, P.; Newport, R. *J. Phys. Rev. B* **2010**, *81*, No. 060301.
- (289) Corno, M.; Pedone, A.; Dovesi, R.; Ugliengo, P. *Chem. Mater.* **2008**, *20*, 5610.
- (290) Dracinsky, M.; Benda, L.; Bour, P. *Chem. Phys. Lett.* **2011**, *512*, 54.
- (291) Dovesi, R.; Civalleri, B.; Orlando, R.; Roetti, C.; Saunders, V. R. In *Reviews in Computational Chemistry*; Lipkowitz, K. B., Larter, R., Cundari, T. R., Eds.; Wiley-VCH, Inc: New York, 2005; Vol. 21, pp 1–125.
- (292) Tasker, P. W. *J. Phys. C: Solid State Phys.* **1979**, *12*, 4977.
- (293) Meyer, B.; Marx, D. *Phys. Rev. B* **2003**, *67*, No. 035403.
- (294) Murashov, V. *J. Mol. Struct.* **2003**, *650*, 141.
- (295) Murashov, V. V. *J. Phys. Chem. B* **2005**, *109*, 4144.
- (296) Radzig, V. A. In *Defects in SiO₂ and Related Dielectrics: Science and Technology*; Pacchioni, G.; Skuja, L.; Griscom, D. L., Eds.; Kluwer Academic Publishers: Dordrecht, the Netherlands, 2000; Vol. 2, pp 339–370.
- (297) Radzig, V. A.; Berestetskaya, I. V.; Kostritsa, S. N. *Kinet. Catal.* **1998**, *39*, 863.
- (298) Pacchioni, G.; Ferrari, A. M.; Ierano, G. *Faraday Discuss.* **1997**, *106*, 155.
- (299) Pacchioni, G.; Ierano, G. *Phys. Rev. Lett.* **1997**, *79*, 753.
- (300) Pacchioni, G.; Ierano, G. *Phys. Rev. B* **1998**, *57*, 818.
- (301) Pacchioni, G.; Ierano, G.; Marquez, A. M. *Phys. Rev. Lett.* **1998**, *81*, 377.
- (302) Zwijnenburg, M. A.; Sokol, A. A.; Sousa, C.; Bromley, S. T. J. *Chem. Phys.* **2009**, *131*, No. 034705.
- (303) Boero, M.; Pasquarello, A.; Sarnthein, J.; Car, R. *Phys. Rev. Lett.* **1997**, *78*, 887.
- (304) Rudra, J. K.; Fowler, W. B. *Phys. Rev. B* **1987**, *35*, 8223.
- (305) Vaccaro, G.; Buscarino, G.; Agnello, S.; Sporea, A.; Oproiu, C.; Sporea, D. G.; Gelardi, F. M. *J. Phys. Chem. C* **2012**, *116*, 144.
- (306) Musso, F.; Sodupe, M.; Corno, M.; Ugliengo, P. *J. Phys. Chem. C* **2009**, *113*, 17876.
- (307) Cole, D. J.; Payne, M. C.; Csanyi, G.; Spearing, S. M.; Colombi Ciacchi, L. *J. Chem. Phys.* **2007**, *127*, No. 204704.
- (308) Schneider, J.; Colombi Ciacchi, L. *J. Am. Chem. Soc.* **2012**, *134*, 2407.
- (309) Rimola, A.; Sodupe, M.; Tosoni, S.; Civalleri, B.; Ugliengo, P. *Langmuir* **2006**, *22*, 6593.
- (310) Corno, M.; Busco, C.; Bolis, V.; Tosoni, S.; Ugliengo, P. *Langmuir* **2009**, *25*, 2188.
- (311) Rimola, A.; Corno, M.; Garza, J.; Ugliengo, P. *Philos. Trans. R. Soc., A* **2012**, *370*, 1478.
- (312) Rimola, A.; Corno, M.; Zicovich-Wilson, C. M.; Ugliengo, P. *J. Am. Chem. Soc.* **2008**, *130*, 16181.
- (313) Rozanska, X.; Delbecq, F.; Sautet, P. *Phys. Chem. Chem. Phys.* **2010**, *12*, 14930.
- (314) Peri, J. B.; Hensley, J. A. *L. J. Phys. Chem.* **1968**, *72*, 2926.
- (315) Vigne-Maeder, F.; Sautet, P. *J. Phys. Chem. B* **1997**, *101*, 8197.
- (316) Civalleri, B.; Casassa, S.; Garrone, E.; Pisani, C.; Ugliengo, P. *J. Phys. Chem. B* **1999**, *103*, 2165.
- (317) Tosoni, S.; Civalleri, B.; Pascale, F.; Ugliengo, P. *J. Phys.: Conf. Ser.* **2008**, *117*, No. 012026.
- (318) Civalleri, B.; Ugliengo, P. *J. Phys. Chem. B* **2000**, *104*, 9491.
- (319) Goumans, T. P. M.; Catlow, C. R. A.; Brown, W. A. *J. Chem. Phys.* **2008**, *128*, No. 134709.
- (320) Goumans, T. P. M.; Wander, A.; Catlow, C. R. A.; Brown, W. A. *Mon. Not. R. Astron. Soc.* **2007**, *382*, 1829.
- (321) Rimola, A.; Sodupe, M.; Ugliengo, P. *J. Phys. Chem. C* **2009**, *113*, 5741.
- (322) Rimola, A.; Civalleri, B.; Ugliengo, P. *Langmuir* **2008**, *24*, 14027.

- (323) Zhao, Y. L.; Koppen, S.; Frauenheim, T. *J. Phys. Chem. C* **2011**, *115*, 9615.
- (324) Nonella, M.; Seeger, S. *ChemPhysChem* **2008**, *9*, 414.
- (325) Nonella, M.; Seeger, S. *Chem. Phys.* **2010**, *378*, 73.
- (326) Orlando, R.; Delle Piane, M.; Bush, I. J.; Ugliengo, P.; Ferrabone, M.; Dovesi, R. *J. Comput. Chem.* **2012**, *33*, 2276.
- (327) Pisani, C.; Maschio, L.; Casassa, S.; Halo, M.; Schutz, M.; Usryat, D. *J. Comput. Chem.* **2008**, *29*, 2113.
- (328) Pisani, C.; Schutz, M.; Casassa, S.; Usryat, D.; Maschio, L.; Lorenz, M.; Erba, A. *Phys. Chem. Chem. Phys.* **2012**, *14*, 7615.
- (329) Paier, J.; Ren, X.; Rinke, P.; Scuseria, G. E.; Gruneis, A.; Kresse, G.; Scheffler, M. *New J. Phys.* **2012**, *14*, No. 043002.
- (330) Hafner, J. *J. Comput. Chem.* **2008**, *29*, 2044.
- (331) Maschio, L.; Civalleri, B.; Ugliengo, P.; Gavezzotti, A. *J. Phys. Chem. A* **2011**, *115*, 11179.
- (332) Maschio, L. *J. Chem. Theory Comput.* **2011**, *7*, 2818.
- (333) Sherrill, C. D. *J. Chem. Phys.* **2010**, *132*, No. 110902.
- (334) Tomasi, J.; Persico, M. *Chem. Rev.* **1994**, *94*, 2027.
- (335) Sauer, J. *Chem. Rev.* **1989**, *89*, 199.
- (336) Meier, W. M.; Olson, D. H.; Baerlocher, C. *Zeolites* **1996**, *17*, 1.
- (337) Sauer, J.; Hill, J. R. *Chem. Phys. Lett.* **1994**, *218*, 333.
- (338) Civalleri, B.; Garrone, E.; Ugliengo, P. *Chem. Phys. Lett.* **1998**, *294*, 103.
- (339) Civalleri, B.; Garrone, E.; Ugliengo, P. *Chem. Phys. Lett.* **1999**, *299*, 443.
- (340) Civalleri, B.; Garrone, E.; Ugliengo, P. *Langmuir* **1999**, *15*, 5829.
- (341) Bordiga, S.; Roggero, I.; Ugliengo, P.; Zecchina, A.; Bolis, V.; Artioli, G.; Buzzoni, R.; Marra, G.; Rivetti, F.; Spano, G.; Lamberti, C. *J. Chem. Soc., Dalton Trans.* **2000**, 3921.
- (342) Bolis, V.; Busco, C.; Ugliengo, P. *J. Phys. Chem. B* **2006**, *110*, 14849.
- (343) Bolis, V.; Busco, C.; Aina, V.; Morterra, C.; Ugliengo, P. *J. Phys. Chem. C* **2008**, *112*, 16879.
- (344) Koch, W.; Holthausen, M. C. *A Chemist's Guide to Density Functional Theory*, 2nd ed.; Wiley-VCH Verlag GmbH: Weinheim, Germany, 2002.
- (345) Musso, F.; Ugliengo, P.; Solans-Monfort, X.; Sodupe, M. *J. Phys. Chem. C* **2010**, *114*, 16430.
- (346) Yang, J. J.; Meng, S.; Xu, L. F.; Wang, E. G. *Phys. Rev. Lett.* **2004**, *92*, No. 146102.
- (347) Bakowies, D.; Thiel, W. *J. Phys. Chem.* **1996**, *100*, 10580.
- (348) Zhang, Y.; Lee, T.-S.; Yang, W. *J. Chem. Phys.* **1999**, *110*, 46.
- (349) Poteau, R.; Alary, F.; Abou El Makarim, H.; Heully, J. L.; Barthelat, J. C.; Daudey, J. P. *J. Phys. Chem. A* **2001**, *105*, 206.
- (350) Poteau, R.; Ortega, I.; Alary, F.; Solis, A. R.; Barthelat, J. C.; Daudey, J. P. *J. Phys. Chem. A* **2001**, *105*, 198.
- (351) Taylor, C. E.; Cory, M. G.; Bartlett, R. J.; Thiel, W. *Comput. Mater. Sci.* **2003**, *27*, 204.
- (352) Taylor, D. E.; Bunte, S. W.; Runge, K. *J. Phys. Chem. A* **2006**, *110*, 6279.
- (353) Mallik, A.; Taylor, D. E.; Runge, K.; Dufty, J. W. *Int. J. Quantum Chem.* **2004**, *100*, 1019.
- (354) Maseras, F.; Morokuma, K. *J. Comput. Chem.* **1995**, *16*, 1170.
- (355) Frisch, M. J.; Trucks, G. W.; Schlegel, H. B.; Scuseria, G. E.; Robb, M. A.; Cheeseman, J. R.; Zakrzewski, V. G.; Montgomery, J. A., Jr.; Stratmann, R. E.; Burant, J. C.; Dapprich, S.; Millam, J. M.; Daniels, A. D.; Kudin, K. N.; Strain, M. C.; Farkas, O.; Tomasi, J.; Barone, V.; Cossi, M.; Cammi, R.; Mennucci, B.; Pomelli, C.; Adamo, C.; Clifford, S.; Ochterski, J.; Petersson, G. A.; Ayala, P. Y.; Cui, Q.; Morokuma, K.; Salvador, P.; Dannenberg, J. J.; Malick, D. K.; Rabuck, A. D.; Raghavachari, K.; Foresman, J. B.; Cioslowski, J.; Ortiz, J. V.; Baboul, A. G.; Stefanov, B. B.; Liu, G.; Liashenko, A.; Piskorz, P.; Komaromi, I.; Gomperts, R.; Martin, R. L.; Fox, D. J.; Keith, T.; Al-Laham, M. A.; Peng, C. Y.; Nanayakkara, A.; Challacombe, M.; Gill, P. M. W.; Johnson, B.; Chen, W.; Wong, M. W.; Andres, J. L.; Gonzalez, C.; Head-Gordon, M.; Replogle, E. S.; Pople, J. A. *Gaussian98*; Gaussian, Inc.: Pittsburgh, PA, 1998.
- (356) Svensson, M.; Humbel, S.; Froese, R. D. J.; Matsubara, T.; Sieber, S.; Morokuma, K. *J. Phys. Chem.* **1996**, *100*, 19357.
- (357) Humbel, S.; Sieber, S.; Morokuma, K. *J. Chem. Phys.* **1996**, *105*, 1959.
- (358) Dapprich, S.; Komaromi, I.; Byun, K. S.; Morokuma, K.; Frisch, M. J. *J. Mol. Struct. THEOCHEM* **1999**, *461*, 1.
- (359) Eichler, U.; Kolmel, C. M.; Sauer, J. *J. Comput. Chem.* **1997**, *18*, 463.
- (360) Vreven, T.; Morokuma, K. *J. Comput. Chem.* **2000**, *21*, 1419.
- (361) Roggero, I.; Civalleri, B.; Ugliengo, P. *Chem. Phys. Lett.* **2001**, *341*, 625.
- (362) Bolis, V.; Barbaglia, A.; Broyer, M.; Busco, C.; Civalleri, B.; Ugliengo, P. *Origins Life Evol. Biospheres* **2004**, *34*, 69.
- (363) Bordiga, S.; Ugliengo, P.; Damin, A.; Lamberti, C.; Spoto, G.; Zecchina, A.; Spano, G.; Buzzoni, R.; Dalloro, L.; Rivetti, F. *Top. Catal.* **2001**, *15*, 43.
- (364) Sauer, J.; Sierka, M. *J. Comput. Chem.* **2000**, *21*, 1470.
- (365) Brandle, M.; Sauer, J. *J. Am. Chem. Soc.* **1998**, *120*, 1556.
- (366) Nachtigalova, D.; Nachtigall, P.; Sierka, M.; Sauer, J. *Phys. Chem. Chem. Phys.* **1999**, *1*, 2019.
- (367) Tuma, C.; Sauer, J. *Phys. Chem. Chem. Phys.* **2006**, *8*, 3955.
- (368) Sillar, K.; Hofmann, A.; Sauer, J. *J. Am. Chem. Soc.* **2009**, *131*, 4143.
- (369) Svelle, S.; Tuma, C.; Rozanska, X.; Kerber, T.; Sauer, J. *J. Am. Chem. Soc.* **2009**, *131*, 816.
- (370) Vreven, T.; Byun, K. S.; Komaromi, I.; Dapprich, S.; Montgomery, J. A.; Morokuma, K.; Frisch, M. J. *J. Chem. Theory Comput.* **2006**, *2*, 815.
- (371) Cramer, C. *Essentials of Computational Chemistry: Theories and Models*, 2nd ed.; Wiley: Chichester, U.K., 2004.
- (372) Jensen, F. *Introduction to Computational Chemistry*, 2nd ed.; Wiley: Chichester, U.K., 2006.
- (373) Szabo, A.; Ostlund, N. S. *Modern Quantum Chemistry: Introduction to Advanced Electronic Structure Theory* Dover: Mineola, NY, 1996.
- (374) Pyykkö, P.; Stanton, J. F. *Chem. Rev.* **2012**, *112*, 1.
- (375) Crawford, T. D.; King, R. A. *Chem. Phys. Lett.* **2002**, *366*, 611.
- (376) Lee, M. S.; Maslen, P. E.; Head-Gordon, M. *J. Chem. Phys.* **2000**, *112*, 3592.
- (377) Maslen, P. E.; Head-Gordon, M. *Chem. Phys. Lett.* **1998**, *283*, 102.
- (378) Saebo, S.; Pulay, P. *Chem. Phys. Lett.* **1985**, *113*, 13.
- (379) Saebo, S.; Pulay, P. *J. Chem. Phys.* **1988**, *88*, 1884.
- (380) Saebo, S.; Pulay, P. *Annu. Rev. Phys. Chem.* **1993**, *44*, 213.
- (381) Schutz, M. *J. Chem. Phys.* **2002**, *116*, 8772.
- (382) Scuseria, G. E.; Ayala, P. Y. *J. Chem. Phys.* **1999**, *111*, 8330.
- (383) Werner, H. J.; Manby, F. R.; Knowles, P. J. *J. Chem. Phys.* **2003**, *118*, 8149.
- (384) Pisani, C.; Busso, M.; Capecci, G.; Casassa, S.; Dovesi, R.; Maschio, L.; Zicovich-Wilson, C.; Schutz, M. *J. Chem. Phys.* **2005**, *122*, No. 094113.
- (385) Sousa, S. F.; Fernandes, P. A.; Ramos, M. J. *J. Phys. Chem. A* **2007**, *111*, 10439.
- (386) Musso, F. Ph.D. Thesis, Universitat Autònoma de Barcelona and Università di Torino, 2011.
- (387) Tucker, M. G.; Keen, D. A.; Dove, M. T. *Mineral. Mag.* **2001**, *65*, 489.
- (388) Schmahl, W. W.; Swainson, I. P.; Dove, M. T.; Graeme-Barber, A. Z. *Kristallogr.* **1992**, *201*, 125.
- (389) Kihara, K.; Matsumoto, T.; Imamura, M. Z. *Kristallogr.* **1986**, *177*, 27.
- (390) Saxena, S. K.; Chatterjee, N.; Fei, Y.; Shen, G. *Thermodynamic Data on Oxides and Silicates*; Springer-Verlag: Berlin, 1993.
- (391) Goumans, T. P. M.; Wander, A.; Brown, W. A.; Catlow, C. R. A. *Phys. Chem. Chem. Phys.* **2007**, *9*, 2146.
- (392) Zicovich-Wilson, C. M.; Pascale, F.; Roetti, C.; Saunders, V. R.; Orlando, R.; Dovesi, R. *J. Comput. Chem.* **2004**, *25*, 1873.
- (393) Sicolio, S.; Palma, G.; Di Valentini, C.; Pacchioni, G. *Phys. Rev. B* **2007**, *76*, No. 075121.

- (394) Giordano, L.; Sushko, P. V.; Pacchioni, G.; Shluger, A. L. *Phys. Rev. Lett.* **2007**, *99*, No. 136801.
- (395) Giordano, L.; Sushko, P. V.; Pacchioni, G.; Shluger, A. L. *Phys. Rev. B* **2007**, *75*, No. 024109.
- (396) Raghavachari, K.; Ricci, D.; Pacchioni, G. *J. Chem. Phys.* **2002**, *116*, 825.
- (397) Sodupe, M.; Bertran, J.; Rodriguez-Santiago, L.; Baerends, E. J. *J. Phys. Chem. A* **1999**, *103*, 166.
- (398) Braida, B.; Hiberty, P. C.; Savin, A. *J. Phys. Chem. A* **1998**, *102*, 7872.
- (399) Gilli, G.; Gilli, P. *J. Mol. Struct.* **2000**, *552*, 1.
- (400) Kim, K.; Jordan, K. D. *J. Phys. Chem.* **1994**, *98*, 10089.
- (401) Tuma, C.; Boese, A. D.; Handy, N. C. *Phys. Chem. Chem. Phys.* **1999**, *1*, 3939.
- (402) Novoa, J. J.; Sosa, C. *J. Phys. Chem.* **1995**, *99*, 15837.
- (403) Civalleri, B.; Garrone, E.; Ugliengo, P. *J. Mol. Struct. THEOCHEM* **1997**, *419*, 227.
- (404) Ugliengo, P.; Civalleri, B.; Garrone, E. *Nuovo Cimento D* **1997**, *19*, 1765.
- (405) Thanthiriwatte, K. S.; Hohenstein, E. G.; Burns, L. A.; Sherrill, C. D. *J. Chem. Theory Comput.* **2011**, *7*, 88.
- (406) Ireta, J.; Neugebauer, J.; Scheffler, M. *J. Phys. Chem. A* **2004**, *108*, 5692.
- (407) Ugliengo, P.; Pascale, F.; Merawa, M.; Labeguerie, P.; Tosoni, S.; Dovesi, R. *J. Phys. Chem. B* **2004**, *108*, 13632.
- (408) Hobza, P.; Sponer, J.; Reschel, T. *J. Comput. Chem.* **1995**, *16*, 1315.
- (409) Allen, M. J.; Tozer, D. J. *J. Chem. Phys.* **2002**, *117*, 11113.
- (410) Kristyan, S.; Pulay, P. *Chem. Phys. Lett.* **1994**, *229*, 175.
- (411) Perezjorda, J. M.; Becke, A. D. *Chem. Phys. Lett.* **1995**, *233*, 134.
- (412) Mignon, P.; Ugliengo, P.; Sodupe, M. *J. Phys. Chem. C* **2009**, *113*, 13741.
- (413) Mignon, P.; Ugliengo, P.; Sodupe, M.; Hernandez, E. R. *Phys. Chem. Chem. Phys.* **2010**, *12*, 688.
- (414) Lin, I. C.; Seitsonen, A. P.; Coutinho-Neto, M. D.; Tavernelli, I.; Rothlisberger, U. *J. Phys. Chem. B* **2009**, *113*, 1127.
- (415) Grossman, J. C.; Schwiegles, E.; Draeger, E. W.; Gygi, F.; Galli, G. *J. Chem. Phys.* **2004**, *120*, 300.
- (416) Sit, P. H. L.; Marzari, N. *J. Chem. Phys.* **2005**, *122*, No. 204510.
- (417) Todorova, T.; Seitsonen, A. P.; Hutter, J.; Kuo, I. F. W.; Mundy, C. J. *J. Phys. Chem. B* **2006**, *110*, 3685.
- (418) Elstner, M.; Hobza, P.; Frauenheim, T.; Suhai, S.; Kaxiras, E. *J. Chem. Phys.* **2001**, *114*, 5149.
- (419) Grimme, S. *J. Comput. Chem.* **2004**, *25*, 1463.
- (420) Grimme, S. *J. Comput. Chem.* **2006**, *27*, 1787.
- (421) Grimme, S.; Antony, J.; Ehrlich, S.; Krieg, H. *J. Chem. Phys.* **2010**, *132*, No. 154104.
- (422) Civalleri, B.; Zicovich-Wilson, C. M.; Valenzano, L.; Ugliengo, P. *CrystEngComm* **2008**, *10*, 405.
- (423) Jurecka, P.; Cerny, J.; Hobza, P.; Salahub, D. R. *J. Comput. Chem.* **2007**, *28*, 555.
- (424) Kabelac, M.; Valdes, H.; Sherer, E. C.; Cramer, C. J.; Hobza, P. *Phys. Chem. Chem. Phys.* **2007**, *9*, 5000.
- (425) Morgado, C.; Vincent, M. A.; Hillier, I. H.; Shan, X. *Phys. Chem. Chem. Phys.* **2007**, *9*, 448.
- (426) Rimola, A.; Civalleri, B.; Ugliengo, P. *Phys. Chem. Chem. Phys.* **2010**, *12*, 6357.
- (427) Tkatchenko, A.; Scheffler, M. *Phys. Rev. Lett.* **2009**, *102*, No. 073005.
- (428) von Lilienfeld, O. A.; Tavernelli, I.; Rothlisberger, U.; Sebastiani, D. *Phys. Rev. Lett.* **2004**, *93*, No. 153004.
- (429) von Lilienfeld, O. A.; Tavernelli, I.; Rothlisberger, U.; Sebastiani, D. *Phys. Rev. B* **2005**, *71*, No. 195119.
- (430) Torres, E.; DiLabio, G. A. *J. Phys. Chem. Lett.* **2012**, *3*, 1738.
- (431) Dion, M.; Rydberg, H.; Schroder, E.; Langreth, D. C.; Lundqvist, B. I. *Phys. Rev. Lett.* **2004**, *92*, No. 246401.
- (432) Zhao, Y.; Truhlar, D. G. *J. Chem. Theory Comput.* **2007**, *3*, 289.
- (433) Zhao, Y.; Truhlar, D. G. *Acc. Chem. Res.* **2008**, *41*, 157.
- (434) Boys, S.; Bernardi, F. *Mol. Phys.* **1970**, *19*, 553.
- (435) Goltl, F.; Hafner, J. *J. Chem. Phys.* **2012**, *136*.
- (436) Civalleri, B.; Zicovich-Wilson, C. M.; Ugliengo, P.; Saunders, V. R.; Dovesi, R. *Chem. Phys. Lett.* **1998**, *292*, 394.
- (437) Tosoni, S.; Tuma, C.; Sauer, J.; Civalleri, B.; Ugliengo, P. *J. Chem. Phys.* **2007**, *127*, No. 154102.
- (438) Paier, J.; Hirschl, R.; Marsman, M.; Kresse, G. *J. Chem. Phys.* **2005**, *122*, No. 234102.
- (439) Leach, A. R. *Molecular Modelling. Principles and Applications*, 2 ed.; Pearson Education Limited: Dorchester, U.K., 2001.
- (440) Alder, B. J.; Wainwright, T. E. *J. Chem. Phys.* **1959**, *31*, 459.
- (441) Rahman, A. *Phys. Rev.* **1964**, *136*, A405.
- (442) Car, R.; Parrinello, M. *Phys. Rev. Lett.* **1985**, *55*, 2471.
- (443) Marx, D.; Hutter, J. *Ab initio Molecular Dynamics: Basic Theory and Advanced Methods*; Cambridge University Press: Cambridge, U.K., 2009.
- (444) Pople, J. A.; Santry, D. P.; Segal, G. A. *J. Chem. Phys.* **1965**, *43*, S129.
- (445) Dewar, M. J. S.; Thiel, W. *J. Am. Chem. Soc.* **1977**, *99*, 4899.
- (446) Stewart, J. P.; MOPAC2012, Ed.; <http://OpenMOPAC.net>: Colorado Springs, CO, USA, 2012.
- (447) Korth, M.; Pitonák, M.; Rezáč, J. *J. Chem. Theory Comput.* **2010**, *6*, 344.
- (448) Rezáč, J.; Hobza, P. *J. Chem. Theory Comput.* **2011**, *8*, 141.
- (449) Slater, J. C.; Koster, G. F. *Phys. Rev.* **1954**, *94*, 1498.
- (450) Elstner, M.; Frauenheim, T.; Kaxiras, E.; Seifert, G.; Suhai, S. *Phys. Status Solidi B* **2000**, *217*, 357.
- (451) Elstner, M.; Frauenheim, T.; Suhai, S. *J. Mol. Struct. THEOCHEM* **2003**, *632*, 29.
- (452) Elstner, M.; Porezag, D.; Jungnickel, G.; Elsner, J.; Haugk, M.; Frauenheim, T.; Suhai, S.; Seifert, G. *Phys. Rev. B* **1998**, *58*, 7260.
- (453) Frauenheim, T.; Seifert, G.; Elstner, M.; Hajnal, Z.; Jungnickel, G.; Porezag, D.; Suhai, S.; Scholz, R. *Phys. Status Solidi B* **2000**, *217*, 41.
- (454) Thomas, F.; Gotthard, S.; Marcus, E.; Thomas, N.; Christof, K.; Marc, A.; Michael, S.; Zoltán, H.; Aldo Di, C.; Sándor, S. *J. Phys.: Condens. Matter* **2002**, *14*, 3015.
- (455) Elstner, M. *Theor. Chem. Acc.* **2006**, *116*, 316.
- (456) Allinger, N. L. *J. Am. Chem. Soc.* **1977**, *99*, 8127.
- (457) van Beest, B. W. H.; Kramer, G. J.; van Santen, R. A. *Phys. Rev. Lett.* **1990**, *64*, 1955.
- (458) Dick, B. G.; Overhauser, A. W. *Phys. Rev.* **1958**, *112*, 90.
- (459) Jackson, R. A.; Catlow, C. R. A. *Mol. Simul.* **1988**, *1*, 207.
- (460) Gale, J. D. Z. *Kristallogr.* **2005**, *220*, 552.
- (461) Schaible, M. *Crit. Rev. Solid State Mater. Sci.* **1999**, *24*, 265.
- (462) Hassanalali, A. A.; Singer, S. *J. J. Phys. Chem. B* **2007**, *111*, 11181.
- (463) Hassanalali, A. A.; Singer, S. *J. J. Comput.-Aided Mater. Des.* **2007**, *14*, 53.
- (464) Garofalini, S. H. *J. Non-Cryst. Solids* **1990**, *120*, 1.
- (465) Mahadevan, T. S.; Garofalini, S. H. *J. Phys. Chem. C* **2008**, *112*, 15037.
- (466) Du, J.; Cormack, A. N. *J. Am. Ceram. Soc.* **2005**, *88*, 2532.
- (467) Pedone, A.; Malavasi, G.; Menziani, M. C.; Segre, U.; Musso, F.; Corno, M.; Civalleri, B.; Ugliengo, P. *Chem. Mater.* **2008**, *20*, 2522.
- (468) van Duin, A. C. T.; Dasgupta, S.; Lorant, F.; Goddard, W. A. *J. Phys. Chem. A* **2001**, *105*, 9396.
- (469) Pauling, L. *J. Am. Chem. Soc.* **1947**, *69*, 542.
- (470) van Duin, A. C. T.; Strachan, A.; Stewman, S.; Zhang, Q. S.; Xu, X.; Goddard, W. A. *J. Phys. Chem. A* **2003**, *107*, 3803.
- (471) Fogarty, J. C.; Aktulga, H. M.; Grama, A. Y.; van Duin, A. C. T.; Pandit, S. A. *J. Chem. Phys.* **2010**, *132*, No. 174704.
- (472) Feuston, B. P.; Garofalini, S. H. *J. Chem. Phys.* **1988**, *89*, 5818.
- (473) Tsuneyuki, S.; Tsukada, M.; Aoki, H.; Matsui, Y. *Phys. Rev. Lett.* **1988**, *61*, 869.
- (474) Schröder, K.-P.; Sauer, J.; Leslie, M.; Richard, C.; Catlow, A.; Thomas, J. M. *Chem. Phys. Lett.* **1992**, *188*, 320.
- (475) Hill, J. R.; Sauer, J. *J. Phys. Chem.* **1994**, *98*, 1238.
- (476) Schroder, K. P.; Sauer, J. *J. Phys. Chem.* **1996**, *100*, 11043.
- (477) Sierka, M.; Sauer, J. *Faraday Discuss.* **1997**, *106*, 41.

- (478) Guillot, B.; Guissani, Y. *J. Chem. Phys.* **2001**, *114*, 6720.
 (479) Skuja, L. N.; Silin, A. R. *Phys. Status Solidi A* **1979**, *56*, K11.
 (480) Griscom, D. L. *J. Non-Cryst. Solids* **1985**, *73*, 51.
 (481) Skuja, L. *J. Non-Cryst. Solids* **1994**, *179*, 51.
 (482) Skuja, L.; Suzuki, T.; Tanimura, K. *Phys. Rev. B* **1995**, *52*, 15208.
 (483) Skuja, L.; Tanimura, T.; Itoh, N. *J. Appl. Phys.* **1996**, *80*, 3518.
 (484) Skuja, L.; Naber, A. In *Proceedings of the 13th International Conference on Defects in Insulating Materials - Icdim 96*; Matthews, G. E., Williams, R. T., Eds.; Metallurgical Society of AIME: Warrendale, PA, 1997; Vol. 239, pp 25–28.
 (485) Vaccaro, L.; Cannas, M.; Radzig, V.; Boscaino, R. *Phys. Rev. B* **2008**, *78*, No. 075421.
 (486) Vaccaro, L.; Cannas, M.; Radzig, V. *J. Non-Cryst. Solids* **2009**, *355*, 1020.
 (487) Zyubin, A. S.; Mebel, A. M.; Lin, S. H.; Glinka, Y. D. *J. Chem. Phys.* **2002**, *116*, 9889.
 (488) Griscom, D. L. *J. Non-Cryst. Solids* **1978**, *31*, 241.
 (489) Stapelbroek, M.; Griscom, D. L.; Friebele, E. J.; Sigel, G. H. *J. Non-Cryst. Solids* **1979**, *32*, 313.
 (490) Griscom, D. L.; Friebele, E. *J. Phys. Rev. B* **1981**, *24*, 4896.
 (491) Griscom, D. L. *J. Non-Cryst. Solids* **2011**, *357*, 1945.
 (492) Glinka, Y. D.; Lin, S. H.; Chen, Y. T. *Phys. Rev. B* **2002**, *66*, No. 035404.
 (493) Raghavachari, K.; Pacchioni, G. *J. Chem. Phys.* **2001**, *114*, 4657.
 (494) Murashov, V. V.; Demchuk, E. *Surf. Sci.* **2005**, *595*, 6.
 (495) Murashov, V. V.; Demchuk, E. *J. Phys. Chem. B* **2005**, *109*, 10835.
 (496) Koudriachova, M. V.; Beckers, J. V. L.; de Leeuw, S. W. *Comput. Mater. Sci.* **2001**, *20*, 381.
 (497) Rignanese, G. M.; De Vita, A.; Charlier, J. C.; Gonze, X.; Car, R. *Phys. Rev. B* **2000**, *61*, 13250.
 (498) Lopes, P. E. M.; Demchuk, E.; Mackerell, A. D., Jr. *Int. J. Quantum Chem.* **2009**, *109*, 50.
 (499) de Leeuw, N. H.; Higgins, F. M.; Parker, S. C. *J. Phys. Chem. B* **1999**, *103*, 1270.
 (500) Rignanese, G. M.; Charlier, J. C.; Gonze, X. *Phys. Chem. Chem. Phys.* **2004**, *6*, 1920.
 (501) Adeagbo, W. A.; Doltsinis, N. L.; Klevakina, K.; Renner, J. *ChemPhysChem* **2008**, *9*, 994.
 (502) Walsh, T. R.; Wilson, M.; Sutton, A. P. *J. Chem. Phys.* **2000**, *113*, 9191.
 (503) Tosoni, S.; Civalleri, B.; Ugliengo, P. *J. Phys. Chem. C* **2010**, *114*, 19984.
 (504) Yang, J. J.; Wang, E. G. *Phys. Rev. B* **2006**, *73*, No. 035406.
 (505) Zyubin, A. S.; Glinka, Y. D.; Mebel, A. M.; Lin, S. H.; Hwang, L. P.; Chen, Y. T. *J. Chem. Phys.* **2002**, *116*, 281.
 (506) Ceresoli, D.; Bernasconi, M.; Iarlori, S.; Parrinello, M.; Tosatti, E. *Phys. Rev. Lett.* **2000**, *84*, 3887.
 (507) Masini, P.; Bernasconi, M. *J. Phys.: Condens. Matter* **2002**, *14*, 4133.
 (508) Mishler, C.; Horbach, J.; Kob, W.; Binder, K. *J. Phys.: Condens. Matter* **2005**, *17*, 4005.
 (509) Ugliengo, P.; Sodupe, M.; Musso, F.; Bush, I. J.; Orlando, R.; Dovesi, R. *Adv. Mater.* **2008**, *20*, 4579.
 (510) Tielens, F.; Gervais, C.; Lambert, J. F.; Mauri, F.; Costa, D. *Chem. Mater.* **2008**, *20*, 3336.
 (511) Pickard, C. J.; Mauri, F. *Phys. Rev. B* **2001**, *63*, No. 245101.
 (512) Thomas, J. M.; Klinowski, J.; Ramdas, S.; Hunter, B. K.; Tennakoon, D. T. B. *Chem. Phys. Lett.* **1983**, *102*, 158.
 (513) Engelhardt, G.; Radeglia, R. *Chem. Phys. Lett.* **1984**, *108*, 271.
 (514) Pedone, A.; Malavasi, G.; Menziani, M. C.; Cormack, A. N.; Segre, U. *J. Phys. Chem. B* **2006**, *110*, 11780.
 (515) Ugliengo, P.; Viterbo, D.; Chiari, G. *Z. Kristallogr.* **1993**, *207*, 9.
 (516) Dovesi, R.; Saunders, V. R.; Roetti, C.; Orlando, R.; Zicovich-Wilson, C. M.; Pascale, F.; Civalleri, B.; Doll, K.; Harrison, N. M.; Bush, I. J.; D'Arco, P.; Llunell, M. *CRYSTAL06 User's Manual*; Università di Torino: Torino, 2006.
 (517) Delle Piane, M.; Corno, M.; Ugliengo, P. Presented at the Satellite Meeting of the World Association of Theoretical and Computational Chemists, WATOC 2011: Theoretical Modeling of Materials, Barcelona, 13–15 July 2011.
 (518) Feuston, B. P.; Garofalini, S. H. *J. Chem. Phys.* **1989**, *91*, 564.
 (519) Berendsen, H. J. C.; Postma, J. P. M.; van Gunsteren, W. F.; Hermans, J. In *Intermolecular Forces*; Pullmann, B., Ed.; Reidel: Dordrecht, the Netherlands, 1981; p 331.
 (520) Bakaev, V. A.; Steele, W. A. *J. Chem. Phys.* **1999**, *111*, 9803.
 (521) Roder, A.; Kob, W.; Binder, K. *J. Chem. Phys.* **2001**, *114*, 7602.
 (522) Mischler, C.; Kob, W.; Binder, K. *Comput. Phys. Commun.* **2002**, *147*, 222.
 (523) Okuno, M.; Kawamura, K. *J. Non-Cryst. Solids* **1995**, *191*, 249.
 (524) Leed, E. A.; Pantano, C. G. *J. Non-Cryst. Solids* **2003**, *325*, 48.
 (525) Mischler, C.; Horbach, J.; Kob, W.; Binder, K. *J. Phys.: Condens. Matter* **2005**, *17*, 4005.
 (526) Cerius2 v.4.9 2003, Accelrys, Inc.
 (527) Brooks, B. R., III; C. L., B., Jr; A. D., M.; Nilsson, L.; Petrella, R. J.; Roux, B.; Won, Y.; Archontis, G.; Bartels, C.; Boresch, S.; Caflisch, A.; Caves, L.; Cui, Q.; Dinner, A. R.; Feig, M.; Fischer, S.; Gao, J.; Hodoscek, M.; Im, W.; Kuczera, K.; Lazaridis, T.; Ma, J.; Ovchinnikov, V.; Paci, E.; Pastor, R. W.; Post, C. B.; Pu, J. Z.; Schaefer, M.; Tidor, B.; Venable, R. M.; Woodcock, H. L.; Wu, X.; Yang, W.; York, D. M.; Karplus, M. *J. Comput. Chem.* **2009**, *30*, 1545.
 (528) Cruz-Chu, E. R.; Aksimentiev, A.; Schulten, K. *J. Phys. Chem. B* **2006**, *110*, 21497.
 (529) Berendsen, H. J. C.; Grigera, J. R.; Straatsma, T. P. *J. Phys. Chem.* **1987**, *91*, 6269.
 (530) Stillinger, F. H.; Weber, T. A. *Phys. Rev. B* **1985**, *31*, 5262.
 (531) Vashishta, P.; Kalia, R. K.; Rino, J. P.; Ebbsjö, I. *Phys. Rev. B* **1990**, *41*, 12197.
 (532) Lerbret, A.; Lelong, G.; Mason, P. E.; Saboungi, M. L.; Brady, J. W. *Food Biophys.* **2011**, *6*, 233.
 (533) Rustad, J. R.; Hay, B. P. *Geochim. Cosmochim. Acta* **1995**, *59*, 1251.
 (534) Bourg, I. C.; Steefel, C. I. *J. Phys. Chem. C* **2012**, *116*, 11556.
 (535) Morrow, B. A.; Cody, I. A. *J. Phys. Chem.* **1975**, *79*, 761.
 (536) Morrow, B. A.; Cody, I. A. *J. Phys. Chem.* **1976**, *80*, 1998.
 (537) Ferrari, A. M.; Garrone, E.; Spoto, G.; Ugliengo, P.; Zecchina, A. *Surf. Sci.* **1995**, *323*, 151.
 (538) Woodcock, L. V.; Angell, C. A.; Cheeseman, P. *J. Chem. Phys.* **1976**, *65*, 1565.
 (539) Wilson, M.; Walsh, T. R. *J. Chem. Phys.* **2000**, *113*, 9180.
 (540) Du, M.-H.; Kolchin, A.; Cheng, H.-P. *J. Chem. Phys.* **2004**, *120*, 1044.
 (541) Rimola, A.; Ugliengo, P. *Phys. Chem. Chem. Phys.* **2009**, *11*, 2497.
 (542) Wander, M. C. F.; Clark, A. E. *J. Phys. Chem. C* **2008**, *112*, 19986.
 (543) Ostroverkhov, V.; Waychunas, G. A.; Shen, Y. R. *Chem. Phys. Lett.* **2004**, *386*, 144.
 (544) Engemann, S.; Reichert, H.; Dosch, H.; Bilgram, J.; Honkimaki, V.; Snigirev, A. *Phys. Rev. Lett.* **2004**, *92*, No. 205701.
 (545) Pelmenschikov, A.; Leszczynski, J.; Pettersson, L. G. M. *J. Phys. Chem. A* **2001**, *105*, 9528.
 (546) Criscenti, L. J.; Kubicki, J. D.; Brantley, S. L. *J. Phys. Chem. A* **2006**, *110*, 198.
 (547) Gautier, J. M.; Oelkers, E. H.; Schott, J. *Geochim. Cosmochim. Acta* **2001**, *65*, 1059.
 (548) Nangia, S.; Garrison, B. J. *J. Phys. Chem. A* **2008**, *112*, 2027.
 (549) Nangia, S.; Garrison, B. J. *Mol. Phys.* **2009**, *107*, 831.
 (550) Gratz, A. J.; Bird, P. *Geochim. Cosmochim. Acta* **1993**, *57*, 977.
 (551) Castagliola, M.; Tellier, C. R.; Vaterkowski, J. L. *J. Mater. Sci.* **1986**, *21*, 3551.
 (552) Zeitler, T. R.; Cormack, A. N. *J. Cryst. Growth* **2006**, *294*, 96.
 (553) Sjoberg, S. *J. Non-Cryst. Solids* **1996**, *196*, 51.
 (554) Yang, J. J.; Wang, E. G. *Curr. Opin. Solid State Mater. Sci.* **2006**, *10*, 33.

- (555) Sauer, J.; Schroder, K. P. *Z. Phys. Chem. (Leipzig)* **1985**, 266, 379.
- (556) Costa, D.; Lomenech, C.; Meng, M.; Stievano, L.; Lambert, J. *F. J. Mol. Struct. THEOCHEM* **2007**, 806, 253.
- (557) Chashchikhin, V.; Rykova, E.; Bagataryants, A. *Phys. Chem. Chem. Phys.* **2011**, 13, 1440.
- (558) Fubini, B.; Bolis, V.; Bailes, M.; Stone, F. S. *Solid State Ionics* **1989**, 32–3, 258.
- (559) Puibasset, J.; Pellenq, R. J. M. *Phys. Chem. Chem. Phys.* **2004**, 6, 1933.
- (560) Fubini, B.; Bolis, V.; Cavenago, A.; Ugliengo, P. *J. Chem. Soc., Faraday Trans.* **1992**, 88, 277.
- (561) Douillard, J. M.; Elwafir, M.; Partyka, S. *J. Colloid Interface Sci.* **1994**, 164, 238.
- (562) Fubini, B. *Thermochim. Acta* **1988**, 135, 19.
- (563) Klier, K.; Shen, J. H.; Zettlemoyer, A. C. *J. Phys. Chem.* **1973**, 77, 1458.
- (564) Du, Q.; Freysz, E.; Shen, Y. R. *Phys. Rev. Lett.* **1994**, 72, 238.
- (565) Garrone, E.; Kazansky, V. B.; Kustov, L. M.; Sauer, J.; Senchenya, I. N.; Ugliengo, P. *J. Phys. Chem.* **1992**, 96, 1040.
- (566) Ferrari, A. M.; Ugliengo, P.; Garrone, E. *J. Phys. Chem.* **1993**, 97, 2671.
- (567) Murashov, V.; Harper, M.; Demchuk, E. *J. Occup. Environ. Hyg.* **2006**, 3, 718.
- (568) Thompson, K. C.; Margey, P. *Phys. Chem. Chem. Phys.* **2003**, 5, 2970.
- (569) Cypryk, M. *J. Organomet. Chem.* **1997**, 545, 483.
- (570) Pelmenschikov, A. G.; Morosi, G.; Gamba, A. *J. Phys. Chem. A* **1997**, 101, 1178.
- (571) Ignatyev, I. S.; Partal, F.; Gonzalez, J. J. L.; Sundius, T. *Spectrochim. Acta, Part A* **2004**, 60, 1169.
- (572) Pelmenschikov, A. G.; Morosi, G.; Gamba, A. *J. Phys. Chem.* **1992**, 96, 7422.
- (573) Yang, J. J.; Meng, S.; Xu, L. F.; Wang, E. G. *Phys. Rev. B* **2005**, 71, 035413.
- (574) Musso, F.; Ugliengo, P.; Sodupe, M. *J. Phys. Chem. A* **2011**, 115, 11221.
- (575) Bandura, A. V.; Kubicki, J. D.; Sofo, J. O. *J. Phys. Chem. C* **2011**, 115, 5756.
- (576) Chen, Y. W.; Chu, I. H.; Wang, Y.; Cheng, H. P. *Phys. Rev. B* **2011**, 84, No. 155444.
- (577) Casarin, M.; Falcomer, D.; Glisenti, A.; Natile, M. M.; Poli, F.; Vittadini, A. *Chem. Phys. Lett.* **2005**, 405, 459.
- (578) Takeuchi, M.; Bertinetti, L.; Martra, G.; Coluccia, S.; Anpo, M. *Appl. Catal. A* **2006**, 307, 13.
- (579) Gallas, J.-P.; Goupil, J.-M.; Vimont, A.; Lavalle, J.-C.; Gil, B.; Gilson, J.-P.; Misserque, O. *Langmuir* **2009**, 25, 5825.
- (580) Lutz, W.; Weber, M.; Bertram, R.; Kurzhals, R.; Kryukova, G. *Z. Anorg. Allg. Chem.* **2011**, 637, 421.
- (581) Behrens, H.; Stuke, A. *Glass Sci. Technol.* **2003**, 76, 176.
- (582) Sulpizi, M.; Gaigeot, M.-P.; Sprik, M. *J. Chem. Theory Comput.* **2012**, 8, 1037.
- (583) Fernandez-Cata, G.; Perez-Gramatges, A.; Alvarez, L. J.; Comas-Rojas, H.; Zicovich-Wilson, C. M. *J. Phys. Chem. C* **2009**, 113, 13309.
- (584) Leung, K.; Nielsen, I. M. B.; Criscenti, L. J. *J. Am. Chem. Soc.* **2009**, 131, 18358.
- (585) Gaigeot, M.-P.; Sprik, M.; Sulpizi, M. *J. Phys.: Condens. Matter* **2012**, 24, 124106.
- (586) Zhao, Y. L. *J. Theor. Comput. Chem.* **2012**, 11, 155.
- (587) Skelton, A. A.; Fenter, P.; Kubicki, J. D.; Wesolowski, D. J.; Cummings, P. T. *J. Phys. Chem. C* **2011**, 115, 2076.
- (588) Skelton, A. A.; Wesolowski, D. J.; Cummings, P. T. *Langmuir* **2011**, 27, 8700.
- (589) Du, Z. M.; de Leeuw, N. H. *Surf. Sci.* **2004**, 554, 193.
- (590) Du, Z. M.; de Leeuw, N. H. *Dalton Trans.* **2006**, 2623.
- (591) Notman, R.; Walsh, T. R. *Langmuir* **2009**, 25, 1638.
- (592) Argyris, D.; Cole, D. R.; Striolo, A. *J. Phys. Chem. C* **2009**, 113, 19591.
- (593) Lopes, P. E. M.; Murashov, V.; Tazi, M.; Demchuk, E.; MacKerell, A. D. *J. Phys. Chem. B* **2006**, 110, 2782.
- (594) Nangia, S.; Washton, N. M.; Mueller, K. T.; Kubicki, J. D.; Garrison, B. J. *J. Phys. Chem. C* **2007**, 111, 5169.
- (595) Wright, L. B.; Walsh, T. R. *J. Phys. Chem. C* **2012**, 116, 2933.
- (596) Zeitler, T. R.; Greathouse, J. A.; Cygan, R. T. *Phys. Chem. Chem. Phys.* **2012**, 14, 1728.
- (597) Xuefen, Z.; Guiwu, L.; Xiaoming, W.; Hong, Y. *Appl. Surf. Sci.* **2009**, 255, 6493.
- (598) Phan, A.; Ho, T. A.; Cole, D. R.; Striolo, A. *J. Phys. Chem. C* **2012**, 116, 15962.
- (599) Greathouse, J. A.; O'Brien, R. J.; Bemis, G.; Pabalan, R. T. *J. Phys. Chem. B* **2002**, 106, 1646.
- (600) Lu, Z. Y.; Sun, Z. Y.; Li, Z. S.; An, L. J. *J. Phys. Chem. B* **2005**, 109, 5678.
- (601) Tosoni, S.; Pascale, F.; Ugliengo, P.; Orlando, R.; Saunders, V. R.; Dovesi, R. *Mol. Phys.* **2005**, 103, 2549.
- (602) Schlegel, M. L.; Nagy, K. L.; Fenter, P.; Sturchio, N. C. *Geochim. Cosmochim. Acta* **2002**, 66, 3037.
- (603) Etzler, F. M.; Fagundus, D. M. *J. Colloid Interface Sci.* **1987**, 115, 513.
- (604) Takei, T.; Chikazawa, M. *J. Colloid Interface Sci.* **1998**, 208, 570.
- (605) Takei, T.; Eriguchi, E.; Fuji, M.; Watanabe, T.; Chikazawa, M. *Thermochim. Acta* **1998**, 308, 139.
- (606) Fubini, B.; Zanetti, G.; Altilia, S.; Tiozzo, R.; Lison, D.; Saffiotti, U. *Chem. Res. Toxicol.* **1999**, 12, 737.
- (607) Heinz, H.; Farmer, B. L.; Pandey, R. B.; Slocik, J. M.; Patnaik, S. S.; Pachter, R.; Naik, R. R. *J. Am. Chem. Soc.* **2009**, 131, 9704.
- (608) Perdew, J. P.; Burke, K.; Ernzerhof, M. *Phys. Rev. Lett.* **1998**, 80, 891.
- (609) Fuerstenau, D. W.; Pradip. *Adv. Colloid Interface Sci.* **2005**, 114, 9.
- (610) Ahmed, S. M.; Vancleav, Ab. *Can. J. Chem. Eng.* **1965**, 43, 23.
- (611) Li, H. C.; Debruyn, P. L. *Surf. Sci.* **1966**, 5, 203.
- (612) Pokrovsky, O. S.; Golubev, S. V.; Mielczarski, J. A. *J. Colloid Interface Sci.* **2006**, 296, 189.
- (613) Eisenthal, K. B. *Chem. Rev.* **2006**, 106, 1462.
- (614) Shen, Y. R.; Ostroverkhov, V. *Chem. Rev.* **2006**, 106, 1140.
- (615) Allen, L. H.; Matijevi, E.; Meties, L. *J. Inorg. Nucl. Chem.* **1971**, 33, 1293.
- (616) Gurau, M. C.; Kim, G.; Lim, S. M.; Albertorio, F.; Fleisher, H. C.; Cremer, P. S. *ChemPhysChem* **2003**, 4, 1231.
- (617) Bertie, J. E.; Labbe, H. J.; Whally, E. *J. Chem. Phys.* **1969**, 50, 4501.
- (618) Scherer, J. R.; Snyder, R. G. *J. Chem. Phys.* **1977**, 67, 4794.
- (619) Lorenz, C. D.; Traverset, A. *Phys. Rev. E: Stat., Nonlinear, Soft Matter Phys.* **2007**, 75, No. 061202.
- (620) Skelton, A. A.; Kubicki, J. D.; Fenter, P.; Van Duin, A. C. T.; Wesolowski, D. J.; Cummings, P. T. *Geochim. Cosmochim. Acta* **2010**, 74, A969.
- (621) Argyris, D.; Cole, D. R.; Striolo, A. *Langmuir* **2009**, 25, 8025.
- (622) Cygan, R. T.; Liang, J. J.; Kalinichev, A. G. *J. Phys. Chem. B* **2004**, 108, 1255.
- (623) Musso, F.; Mignon, P.; Ugliengo, P.; Sodupe, M. *Phys. Chem. Chem. Phys.* **2012**, 14, 10507.
- (624) Kaya, S.; Weissenrieder, J.; Stacchiola, D.; Shaikhutdinov, S.; Freund, H. *J. Phys. Chem. C* **2007**, 111, 759.
- (625) Du, M. H.; Kolchin, A.; Cheng, H. P. *J. Chem. Phys.* **2003**, 119, 6418.
- (626) Chen, Y. W.; Cheng, H. P. *J. Chem. Phys.* **2011**, 134, No. 114703.
- (627) Yates, J. T. *Surf. Sci.* **2004**, 565, 103.
- (628) Branda, M. M.; Montani, R. A.; Castellani, N. J. *Surf. Sci.* **2000**, 446, L89.
- (629) Shchukarev, A.; Sjoberg, S. *Surf. Sci.* **2005**, 584, 106.
- (630) Lee, C. Y.; McCammon, J. A.; Rossky, P. J. *J. Chem. Phys.* **1984**, 80, 4448.
- (631) Lee, S. H.; Rossky, P. J. *J. Chem. Phys.* **1994**, 100, 3334.
- (632) Collins, D. R.; Catlow, C. R. A. *Am. Mineral.* **1992**, 77, 1172.

- (633) deLeeuw, N. H.; Watson, G. W.; Parker, S. C. *J. Chem. Soc., Faraday Trans.* **1996**, 92, 2081.
- (634) Warne, M. R.; Allan, N. L.; Cosgrove, T. *Phys. Chem. Chem. Phys.* **2000**, 2, 3663.
- (635) Hassanali, A. A.; Zhang, H.; Knight, C.; Shin, Y. K.; Singer, S. J. *J. Chem. Theory Comput.* **2010**, 6, 3456.
- (636) Leed, E. A.; Sofo, J. O.; Pantano, C. G. *Phys. Rev. B* **2005**, 72, No. 155427.
- (637) Floess, J. K.; Murad, S. *Chem. Phys. Lett.* **2011**, 516, 216.
- (638) Chai, J. C.; Liu, S. Y.; Yang, X. N. *Appl. Surf. Sci.* **2009**, 255, 9078.
- (639) Feuston, B. P.; Garofalini, S. H. *J. Appl. Phys.* **1990**, 68, 4830.
- (640) Minibaev, R. F.; Zhuravlev, N. A.; Bagatur'yantz, A. A.; Alfimov, M. V. *Russ. Phys. J.* **2009**, 52, 1164.
- (641) Costa, D.; Touretti, A.; Tielens, F.; Gervais, C.; Stievano, L.; Lambert, J. F. *Phys. Chem. Chem. Phys.* **2008**, 10, 6360.
- (642) Duchateau, R.; Dijkstra, T. W.; van Santen, R. A.; Yap, G. P. A. *Chem.—Eur. J.* **2004**, 10, 3979.
- (643) Wächtershäuser, G. *Proc. Natl. Acad. Sci. U.S.A.* **1990**, 87, 200.
- (644) Linder, R.; Nispel, M.; Häber, T.; Kleinermanns, K. *Chem. Phys. Lett.* **2005**, 409, 260.
- (645) Linder, R.; Seefeld, K.; Vavra, A.; Kleinermanns, K. *Chem. Phys. Lett.* **2008**, 453, 1.
- (646) Groenewegen, J. A.; Sachtler, W. M. H. *J. Catal.* **1974**, 33, 176.
- (647) Basiuk, V. A.; Gromovoy, T. Y.; Golovaty, V. G.; Glukhoy, A. M. *Origins Life Evol. Biospheres* **1990**, 20, 483.
- (648) Stepanian, S. G.; Reva, I. D.; Radchenko, E. D.; Rosado, M. T. S.; Duarte, M. L. T. S.; Fausto, R.; Adamowicz, L. *J. Phys. Chem. A* **1998**, 102, 1041.
- (649) Marsh, R. E. *Acta Crystallogr.* **1958**, 11, 654.
- (650) Chowdhry, B. Z.; Dines, T. J.; Jabeen, S.; Withnall, R. *J. Phys. Chem. A* **2008**, 112, 10333.
- (651) Han, J. W.; Sholl, D. S. *Langmuir* **2009**, 25, 10737.
- (652) Lambert, J.-F.; Stievano, L.; Lopes, I.; Gharsallah, M.; Piao, L. *Planet. Space Sci.* **2009**, 57, 460.
- (653) Garetz, B. A.; Matic, J.; Myerson, A. S. *Phys. Rev. Lett.* **2002**, 89, No. 175501.
- (654) Löfgren, P.; Krozer, A.; Lausmaa, J.; Kasemo, B. *Surf. Sci.* **1997**, 370, 277.
- (655) Löfgren, P.; Krozer, A.; Chakarov, D. V.; Kasemo, B. *J. Vac. Sci. Technol., A* **1998**, 16, 2961.
- (656) Ramaekers, R.; Pajak, J.; Lambie, B.; Maes, G. *J. Chem. Phys.* **2004**, 120, 4182.
- (657) Soria, E.; Román, E.; Williams, E. M.; de Segovia, J. L. *Surf. Sci.* **1999**, 433–435, 543.
- (658) Charlet, L.; Manceau, A. A. *J. Colloid Interface Sci.* **1992**, 148, 443.
- (659) Han, J. W.; James, J. N.; Sholl, D. S. *Surf. Sci.* **2008**, 602, 2478.
- (660) Gambino, G. L.; Lombardo, G. M.; Grassi, A.; Marletta, G. *J. Phys. Chem. B* **2004**, 108, 2600.
- (661) Han, J. W.; Sholl, D. S. *Phys. Chem. Chem. Phys.* **2010**, 12, 8024.
- (662) Greber, T.; Šljivančanin, Ž.; Schillinger, R.; Wider, J.; Hammer, B. *Phys. Rev. Lett.* **2006**, 96, No. 056103.
- (663) Bhatia, B.; Sholl, D. S. *Angew. Chem., Int. Ed.* **2005**, 44, 7761.
- (664) Basiuk, V. A.; Navarro-Gonzalez, R.; Basiuk, E. V. *Origins Life Evol. Biospheres* **1998**, 28, 167.
- (665) Basiuk, V. A.; Navarro-Gonzalez, R. *J. Chromatogr., A* **1997**, 776, 255.
- (666) Basiuk, V. A.; Navarro-Gonzales, R.; Basiuk, E. V. *Bioorg. Khim.* **1998**, 24, 842.
- (667) Basiuk, V. A. *Origins Life Evol. Biospheres* **1992**, 22, 333.
- (668) Basiuk, V. A.; Gromovoy, T. Y. *Collect. Czech. Chem. Commun.* **1994**, 59, 461.
- (669) Hudson, S.; Cooney, J.; Magner, E. *Angew. Chem., Int. Ed.* **2008**, 47, 8582.
- (670) Stöber, W.; Fink, A.; Bohn, E. *J. Colloid Interface Sci.* **1968**, 26, 62.
- (671) Roach, P.; Farrar, D.; Perry, C. C. *J. Am. Chem. Soc.* **2006**, 128, 3939.
- (672) Lundqvist, M.; Nygren, P.; Jonsson, B.-H.; Broo, K. *Angew. Chem., Int. Ed.* **2006**, 45, 8169.
- (673) Nygren, P.; Lundqvist, M.; Broo, K.; Jonsson, B.-H. *Nano Lett.* **2008**, 8, 1844.
- (674) Manyar, H. G.; Gianotti, E.; Sakamoto, Y.; Terasaki, O.; Coluccia, S.; Tumbiolo, S. *J. Phys. Chem. C* **2008**, 112, 18110.
- (675) Giussani, L.; Tabacchi, G.; Gianotti, E.; Coluccia, S.; Fois, E. *Philos. Trans. R. Soc., A* **2012**, 370, 1463.
- (676) Notman, R.; Oren, E. E.; Tamerler, C.; Sarikaya, M.; Samudrala, R.; Walsh, T. R. *Biomacromolecules* **2010**, 11, 3266.
- (677) Phillips, D. C.; York, R. L.; Mermut, O.; McCrea, K. R.; Ward, R. S.; Somorjai, G. A. *J. Phys. Chem. C* **2006**, 111, 255.
- (678) Fodor, S. P. A.; Rava, R. P.; Huang, X. C.; Pease, A. C.; Holmes, C. P.; Adams, C. L. *Nature* **1993**, 364, 555.
- (679) Pease, A. C.; Solas, D.; Sullivan, E. J.; Cronin, M. T.; Holmes, C. P.; Fodor, S. P. *Proc. Natl. Acad. Sci. U.S.A.* **1994**, 91, 5022.
- (680) Schena, M.; Shalon, D.; Heller, R.; Chai, A.; Brown, P. O.; Davis, R. W. *Proc. Natl. Acad. Sci. U.S.A.* **1996**, 93, 10614.
- (681) Cheng, L.; Ziegelhoffer, P. R.; Yang, N. S. *Proc. Natl. Acad. Sci. U.S.A.* **1993**, 90, 4455.
- (682) Rädler, J. O.; Koltover, I.; Salditt, T.; Safinya, C. R. *Science* **1997**, 275, 810.
- (683) Sen, T.; Sebastianelli, A.; Bruce, I. J. *J. Am. Chem. Soc.* **2006**, 128, 7130.
- (684) Mannelli, I.; Minunni, M.; Tombelli, S.; Wang, R.; Michela Spiriti, M.; Mascini, M. *Bioelectrochemistry* **2005**, 66, 129.
- (685) Ferreira, G. N. M. *Chem. Eng. Technol.* **2005**, 28, 1285.
- (686) Stellwagen, N. C.; Stellwagen, E. *J. Chromatogr. A* **2009**, 1216, 1917.
- (687) Hook, F.; Ray, A.; Nordén, B.; Kasemo, B. *Langmuir* **2001**, 17, 8305.
- (688) Larsson, C.; Rodahl, M.; Höök, F. *Anal. Chem.* **2003**, 75, 5080.
- (689) Branda, S. S.; Vik, Å.; Friedman, L.; Kolter, R. *Trends Microbiol.* **2005**, 13, 20.
- (690) Romanowski, G.; Lorenz, M. G.; Wackernagel, W. *Appl. Environ. Microbiol.* **1991**, 57, 1057.
- (691) He, X.-x.; Wang, K.; Tan, W.; Liu, B.; Lin, X.; He, C.; Li, D.; Huang, S.; Li, J. *J. Am. Chem. Soc.* **2003**, 125, 7168.
- (692) Verma, I. M.; Somia, N. *Nature* **1997**, 389, 239.
- (693) Solberg, S. M.; Landry, C. C. *J. Phys. Chem. B* **2006**, 110, 15261.
- (694) Marler, B.; Oberhagemann, U.; Vortmann, S.; Gies, H. *Microporous Mater.* **1996**, 6, 375.
- (695) Li, X.; Zhang, J.; Gu, H. *Langmuir* **2011**, 27, 6099.
- (696) Li, X.; Zhang, J.; Gu, H. *Langmuir* **2012**, 28, 2827.
- (697) Melzak, K. A.; Sherwood, C. S.; Turner, R. F. B.; Haynes, C. A. *J. Colloid Interface Sci.* **1996**, 181, 635.
- (698) Gani, S. A.; Mukherjee, D. C.; Chattoraj, D. K. *Langmuir* **1999**, 15, 7130.
- (699) Nguyen, T. H.; Elimelech, M. *Biomacromolecules* **2007**, 8, 24.
- (700) Scholes, C. A.; Millar, D. P.; Gee, M. L.; Smith, T. A. *J. Phys. Chem. B* **2011**, 115, 6329.
- (701) Muñoz, B.; Rámila, A.; Pérez-Pariente, J.; Díaz, I.; Vallet-Regí, M. *Chem. Mater.* **2002**, 15, 500.
- (702) Izquierdo-Barba, I.; Sousa, E.; Doadrio, J.; Doadrio, A.; Pariente, J.; Martínez, A.; Babonneau, F.; Vallet-Regí, M. *J. Sol-Gel Sci. Technol.* **2009**, 50, 421.
- (703) Izquierdo-Barba, I.; Martínez, Á.; Doadrio, A. L.; Pérez-Pariente, J.; Vallet-Regí, M. *Eur. J. Pharm. Sci.* **2005**, 26, 365.
- (704) Doadrio, A. L.; Sousa, E. M. B.; Doadrio, J. C.; Pérez Pariente, J.; Izquierdo-Barba, I.; Vallet-Regí, M. *J. Controlled Release* **2004**, 97, 125.
- (705) Doadrio, J. C.; Sousa, E. M. B.; Izquierdo-Barba, I.; Doadrio, A. L.; Perez-Pariente, J.; Vallet-Regí, M. *J. Mater. Chem.* **2006**, 16, 462.
- (706) Balas, F.; Manzano, M.; Horcajada, P.; Vallet-Regí, M. *J. Am. Chem. Soc.* **2006**, 128, 8116.

- (707) Vallet-Regí, M.; Doadrio, J. C.; Doadrio, A. L.; Izquierdo-Barba, I.; Pérez-Pariente, J. *Solid State Ionics* **2004**, *172*, 435.
- (708) Vallet-Regí, M. *Chem.—Eur. J.* **2006**, *12*, 5934.
- (709) Azaïs, T.; Tourné-Péteilh, C.; Aussénac, F.; Baccile, N.; Coelho, C.; Devoisselle, J.-M.; Babonneau, F. *Chem. Mater.* **2006**, *18*, 6382.
- (710) Azaïs, T.; Hartmeyer, G.; Quignard, S.; Laurent, G.; Babonneau, F. *J. Phys. Chem. C* **2010**, *114*, 8884.
- (711) Alcoutlabi, M.; McKenna, G. B. *J. Phys.: Condens. Matter* **2005**, *17*, R461.
- (712) Morishige, K.; Kawano, K. *J. Chem. Phys.* **2000**, *112*, 11023.
- (713) Morineau, D.; Guegan, R.; Xia, Y.; Alba-Simionescu, C. *J. Chem. Phys.* **2004**, *121*, 1466.
- (714) Takei, T.; Konishi, T.; Fuji, M.; Watanabe, T.; Chikazawa, M. *Thermochim. Acta* **1995**, *267*, 159.
- (715) Gedat, E.; Schreiber, A.; Albrecht, J.; Emmler, T.; Shenderovich, I.; Findenegg, G. H.; Limbach, H. H.; Buntkowsky, G. *J. Phys. Chem. B* **2002**, *106*, 1977.
- (716) Dosseh, G.; Xia, Y.; Alba-Simionescu, C. *J. Phys. Chem. B* **2003**, *107*, 6445.
- (717) Mellaerts, R.; Jammaer, J. A. G.; Van Speybroeck, M.; Chen, H.; Humbeeck, J. V.; Augustijns, P.; Van den Mooter, G.; Martens, J. *A. Langmuir* **2008**, *24*, 8651.
- (718) Mellaerts, R.; Roeffaers, M. B. J.; Houthoofd, K.; Van Speybroeck, M.; De Cremer, G.; Jammaer, J. A. G.; Van den Mooter, G.; Augustijns, P.; Hofkens, J.; Martens, J. A. *Phys. Chem. Chem. Phys.* **2011**, *13*, 2706.
- (719) Qu, F.; Zhu, G.; Huang, S.; Li, S.; Sun, J.; Zhang, D.; Qiu, S. *Microporous Mesoporous Mater.* **2006**, *92*, 1.
- (720) Grünberg, B.; Emmler, T.; Gedat, E.; Shenderovich, I.; Findenegg, G. H.; Limbach, H.-H.; Buntkowsky, G. *Chem.—Eur. J.* **2004**, *10*, 5689.
- (721) Abbasi, A.; Nadimi, E.; Plänitz, P.; Radehaus, C. *Surf. Sci.* **2009**, *603*, 2502.
- (722) Mian, S. A.; Saha, L. C.; Jang, J.; Wang, L.; Gao, X.; Nagase, S. *J. Phys. Chem. C* **2010**, *114*, 20793.
- (723) Mian, S.; Gao, X.; Nagase, S.; Jang, J. *Theor. Chem. Acc.* **2011**, *130*, 333.
- (724) Rimola, A.; Corno, M.; Zicovich-Wilson, C. M.; Ugliengo, P. *Phys. Chem. Chem. Phys.* **2009**, *11*, 9005.
- (725) Richmond, G. L. *Chem. Rev.* **2002**, *102*, 2693.
- (726) Barducci, A.; Bonomi, M.; Parrinello, M. *Wiley Interdiscip. Rev.: Comput. Mol. Sci.* **2011**, *1*, 826.
- (727) Zaera, F. *Chem. Rev.* **2012**, *112*, 2920.
- (728) Mignon, P.; Sodupe, M. *Phys. Chem. Chem. Phys.* **2012**, *14*, 945.
- (729) Murashov, V.; Leszczynski, J. *J. Phys. Chem. A* **1999**, *103*, 1228.
- (730) Biswas, A.; Bayer, I. S.; Biris, A. S.; Wang, T.; Dervishi, E.; Faupel, F. *Adv. Colloid Interface Sci.* **2012**, *170*, 2.
- (731) Kershner, R. J.; Bozano, L. D.; Micheel, C. M.; Hung, A. M.; Fornof, A. R.; Cha, J. N.; Rettner, C. T.; Bersani, M.; Frommer, J.; Rothemund, P. W. K.; Wallraff, G. M. *Nat. Nanotechnol.* **2009**, *4*, 557.
- (732) Kasemo, B. *Curr. Opin. Solid State Mater. Sci.* **1998**, *3*, 451.
- (733) Hook, F.; Kasemo, B.; Grunze, M.; Zauscher, S. *ACS Nano* **2008**, *2*, 2428.
- (734) Leroch, S.; Wendland, M. *J. Phys. Chem. C* **2012**, *116*, 26247.

NOTE ADDED IN PROOF

While this manuscript was in review, an important paper was published⁷³⁴ dealing with the simulation of forces between humid (by H₂O) amorphous silica surfaces. Three different force fields have been tested with respect to their applicability to describe the silica–water interface, namely the ClayFF of Cygan et al.,⁶²² the CWCA from the Schulten group,⁵²⁸ and the ReaxFF by van Duin et al.⁴⁷¹ It was concluded that the ClayFF provides good accuracy for the treated cases and may become the base for further refinement.